Studies for a Time Projection Chamber for the International Linear Collider and Measurement of Beauty Cross Sections in Deep Inelastic Scattering at HERA

Dissertation
zur Erlangung des Doktorgrades
des Fachbereichs Physik
der Universität Hamburg

vorgelegt von

Thorsten Lux

aus Lüneburg

Hamburg
2005

Gutachter der Dissertation	:	Prof. Dr. R.-D. Heuer Prof. Dr. B. Naroska
Gutachter der Disputation	:	Prof. Dr. R.-D. Heuer Prof. Dr. C. Hagner
Datum der Disputation		24.5.2005
Vorsitzender des Prüfungsausschusses	:	Prof. Dr. G. Heinzelmann
Vorsitzender des Promotionsausschusses	:	Prof. Dr. G. Huber
Dekan des Fachbereichs	:	Prof. Dr. G. Huber

Abstract

It is expected, that new physics beyond the Standard Model can be discovered in the energy range up to 1 TeV. A design study of an e^+e^- linear collider, the *International Linear Collider* (ILC), which will give the possibility to investigate this new physics, is currently being performed.
The precise measurement of this new physics, sets as yet unattained requirements on the performance of the detector at the ILC. To ensure this performance the application of new technologies in the detector is necessary. Several studies, which investigate the possible applications of various technologies are currently ongoing. One option under consideration for the main tracking device of the detector at the ILC is a *Time Projection Chamber* (TPC).
In the first part of this thesis a study of the possibility to use *Gas Electron Multipliers* (GEMs) for the readout of a TPC at high magnetic fields is presented. For this study a TPC prototype was designed and built, which allows for measurements in a 5 T magnet. First the functionality of this prototype will be demonstrated by means of a collection of performance measurements. Finally, first results of the point resolution measurements in the presence of high magnetic fields are presented.

In the second part of this thesis the results of the measurements of the total and differential *beauty* cross sections in deep inelastic scattering ($2 < Q^2 < 100$ GeV^2) will be presented. The data used was collected in the years 1999/2000 with the H1 detector at the ep collider HERA and corresponds to an integrated luminosity of 43 pb^{-1}.
The semi-muonic decay channel of the b -flavoured hadrons is chosen for the analysis:

$$ep \rightarrow eb\bar{b}X \rightarrow e\mu j(j)X' \ .$$

Events are selected containing the scattered positron, a muon identified in the central muon system and either one jet in the Breit frame or two jets in the laboratory frame. The fraction of the *beauty* signal in the data sample selected is determined from the distributions of the muon's signed impact parameter and the relative transverse momentum between the muon and the associated jet. The cross sections derived from this are compared with Next-to-Leading order QCD predictions. The measured cross sections are found to be above the NLO QCD calculations.

// Kurzfassung

Es wird erwartet, dass neue Physik jenseits des Standard Modells im Energiebereich bis 1 TeV entdeckt werden kann. Momentan wird eine Design Studie für einen e^+e^- Linearbeschleuniger, dem *International Linear Collider* (ILC), mit einer Schwerpunktsenergie von bis zu 1 TeV durchgeführt, der die Erforschung dieser neuen Physik ermöglichen wird.
Die präzise Vermessung dieser neuen Physik stellt bisher unerreichte Anforderungen an die Leistungsfähigkeit des Detektors am ILC. Um diese zu gewährleisten, ist der Einsatz neuer Technologien notwendig. Momentan werden zahlreiche Studien durchgeführt, die die Einsatzmöglichkeiten der unterschiedlichen Technologien untersuchen. Eine Option für die Hauptspurkammer des Detektors am ILC ist eine *Time Projection Chamber* (TPC).
Im ersten Teil dieser Arbeit wird eine Studie, die sich mit der Einsatzmöglichkeit von *Gas Electron Multipliers* (GEMs) für die Auslese einer TPC in hohen Magnetfeldern beschäftigt, vorgestellt. Für diese Studie wurde eigens ein TPC Prototyp entwickelt und gebaut, der Messungen in einem 5 T Magneten ermöglicht. Zuerst wird die Funktionstüchtigkeit dieses Prototypens anhand einer Auswahl von Kontrollmessungen gezeigt. Anschliessend werden erste Ergebnisse der Messungen der Punktauflösung in hohen Magnetfeldern präsentiert.

Im zweiten Teil dieser Arbeit werden die Ergebnisse der Messungen des totalen und auch einiger differentieller *beauty* Wirkungsquerschnitte in tiefinelastischer Streuung ($2 < Q^2 < 100$ GeV^2) vorgestellt. Die verwendeten Daten wurden in den Jahren 1999/2000 mit dem H1 Detektor am *ep* Beschleuniger HERA aufgezeichnet und entsprechen einer integrierten Luminosität von 43 pb^{-1}.
Der semimyonische Zerfall von b -Hadronen wird für diese Analyse verwendet:

$$ep \rightarrow eb\bar{b}X \rightarrow e\mu j(j)X' \ .$$

Es werden Ereignisse selektiert, die das gestreute Positron, ein im zentralen Myondetektor registriertes Myon und entweder ein Jet im Breit-Bezugssystem oder aber zwei Jets im Labor-Bezugssystem enthalten.
Der Anteil des *beauty* Signals am gesamten selektieren Datensatz wird durch einem 2-dimensionalen Fit aus den Verteilungen des vorzeichenbehafteten Myon-Impaktparameters und des Myon-Transversalimpulses relativ zu einem assozierten Jet bestimmt. Die sich daraus ergebenen b -Wirkungsquerschnitte werden mit QCD Vorhersagen in nächst höherer Ordnung verglichen. Es zeigt sich, dass die gemessenen *beauty* Wirkungsquerschnitte über den QCD-Vorhersagen liegen.

Contents

Preface

Our current knowledge of the world of particle physics is described in the Standard Model (SM). Following this model the fundamental particles are fermions with spin one-half and bosons with integer spin. In total there are 12 different fermions: six quarks and six leptons, which are arranged in three generations (see tab. 1). In addition there is for each particle an anti-particle with opposite charge. The fermions interact with each other by the exchange of vector bosons. These bosons are the photon γ which mediates the electromagnetic force, the $W^{\pm}$ and the Z^0 for the weak interaction and the gluon g as the carrier of the strong force. An overview of the exchange bosons and the corresponding interactions is given in tab. 2. While all fermions take part in the weak force, the electromagnetic force acts only between charged particles and the strong force only between quarks. Gravitation which is the fourth fundamental force is too weak to play a role in the world of the fundamental particles and is until now not included in the SM. The *graviton*, which is expected to mediate gravitation, is also still not experimentally observed.
The SM is based on the concept of local gauge invariance. As a consequence all fermions and bosons should be massless. However, it is observed that both the fermions and the Z and $W^{\pm}$ bosons are massive. In the SM this *electroweak symmetry breaking* is described by the *Higgs mechanism*. This mechanism implies the introduction of a new particle, the *Higgs* boson, which is until now still not observed experimentally. From measurements at the *Large Electron Positron* collider (LEP) a lower limit on the *Higgs* mass of 114.4 GeV is given.
Of course, the question arises, what would happen if no SM *Higgs* particle can be

	1st Generation	2nd Generation	3rd Generation	Electromagnetic charge [e]
Quarks	**u**p (1.5 - 4 MeV)	**c**harm (1.15 - 1.35 GeV)	**t**op ($178.1^{+10.4}_{-8.3}$ GeV)	+2/3
	down (4 - 8 MeV)	**s**trange (80 - 130 MeV)	**b**ottom (4.6 - 4.9 GeV)	-1/3
Leptons	electron (**e**) (0.511 MeV)	muon (μ) (105.6 MeV)	tauon (τ) (1777 MeV)	-1
	ν_e (< 3 eV)	ν_μ (< 0.19 MeV)	ν_τ (< 18.2 MeV)	0

Table 1: *Overview of the fermions of the Standard Model [1]*

Exchange boson	Interaction	Mass [GeV]	Electromagnetic charge [e]
photon γ	electromagnetic	0	0
Z	weak	91.2	0
$W^{\pm}$	weak	80.4	± 1
gluon g	strong	0	0
Higgs		> 114.4	0

Table 2: *Overview of the exchange bosons of the SM [1].*

found at future high energy experiments.
There are models which seek to address this problem, which are an extension of the SM in the sense, that they include the fermions and the exchange bosons of the different forces, but differ in the implementation of the *Higgs* sector to the SM. One such theory is *Supersymmetry* (SUSY).
But also completely different approaches such as *Technicolor*, which introduces a further strong force, are discussed.
Both approaches have in common that they predict new physics. To discover this new physics, directly due to new particles or indirectly due to discrepancies between measured cross sections and SM predictions, and also to search for the SM *Higgs* particle a proton-proton collider is currently under construction. At the *Large Hadron Collider* (LHC) two proton beams, each with an energy of 7 TeV, will collide allowing for the search for new particles over a wide energy range.
If a new particle is found two questions arise: is it the Higgs particle and therefore responsible for the masses of the particles and, if yes, is it the SM Higgs particle or is it consistent with another model, e.g. one of the SUSY models.
The latter question is also important because different theories predict particles with quite similar properties. To answer this question it requires the precise measurement of the production cross section and the decay of these particles.
These measurements can be better performed at an e^+e^- collider than at a hadron collider due to the much cleaner experimental environment at an e^+e^- collider. For a suitable e^+e^- collider simulation and R&D studies are already ongoing in a world wide study, the *International Linear Collider* (ILC) project.
Part I of this thesis includes the presentation of such a R&D study. The goal of this study was to design and build a *Time Projection Chamber* (TPC) prototype for investigating the possibility to use a TPC with *Gas Electron Multiplier* (GEM) readout as central tracking device for a detector at the ILC.

While the search for new particles is probably only successful at the next generation of colliders, the running colliders are used to test the SM. One of these colliders is the *Hadron Elektron Ring Anlage* (HERA) at DESY. There protons and electrons with energies of 920 GeV and 27.5 GeV respectively are brought into collision yielding an excellent environment to investigate the theory of *Quantum Chromodynamics* (QCD). QCD describes the strong interaction within the SM.
Even though the SM can describe the world of particle physics quite well, discrepancies

between measured cross sections and theoretical predictions were found in the past. In Part II a measurement of beauty cross sections in deep inelastic scattering at HERA is presented, which gains from the larger data sample now available compared to previous studies. The larger data sample also allowed, for the first time, to measure differential beauty cross sections.

Part I

A Time Projection Chamber for the International Linear Collider

Chapter 1

The International Linear Collider

As mentioned in the preface various theories are developed to explain electroweak symmetry breaking. Most of them should be revisable in the energy range up to 1 TeV, either due to the discovery of new particles or due to indirect effects such as the measured dependence of the cross sections on the centre-of-mass energy. The investigation of these particles and effects is beyond the capability of current colliders. To gain access to these particles and the new physics two different accelerator approaches are worked out, which are complementary to each other. One, the *Large Hadron Collider* (LHC) [2] is already under construction and will, presumably from 2007 on, bring two proton beams each with a energy of 7 TeV into collision. The LHC will have the capability to open a window to new physics and thus to new particles. However, since protons are composite objects the initial state of the system is not well defined leading to a much more difficult determination of the properties of the new particles. Also some of the new particles might not or only rarely be produced at a hadron machine.

Therefore, also an e^+e^- accelerator with a centre-of-mass energy of up-to 1 TeV is currently being designed. This machine will be well suited for the investigation of the new physics with high precision and in addition it will give access to those particles which can not be produced at significant rate at the LHC.

Historically three different concepts for an e^+e^- collider were developed. The *Next Linear Collider* (NLC) [3] and the *Japanese Linear Collider* (JLC) [4] were based on a normal conducting technology for the cavities, while the *TeV Energy Superconducting Linear Accelerator* (TESLA) [5] foresaw the use of superconducting cavities (fig. 1.1). Due to cost reasons it was obvious that not all three projects could be realised and an international committee was formed to chose the technology. This *International Recommendation Panel* (ITRP) decided in August 2004 that the future e^+e^- collider should be based on the superconducting technology. The decision on a reasonable detector concept on the other hand is completely open. As a next step a *Conceptual Design Report* (CDR) for the now called ILC project will be written, during 2008 the *Technical Design Report* (TDR) has to be finished. The aim is to have first collisions around 2015, if possible in parallel with the operation of the LHC, so that both can gain from each other.

Since the design parameters for the ILC machine and detector still has to be defined, in the following most of the referred parameter values are taken from the TESLA TDR, which will be the starting point of the studies for the ILC.

Figure 1.1: *Superconducting 9-cell niobium cavity (TESLA design) [5]*

1.1 Physics Motivation

Here, a brief overview of the physics programme at the ILC is given. The main focus will be on the *Higgs* mechanism and Supersymmetry.

The *Higgs* Mechanism

Within the *Standard Model* (SM) the mass of the fermions and the Z and W boson is generated by the *Higgs Mechanism.* The underlying idea of this mechanism is, that the masses are generated by the interaction of the particles with a background field, the *Higgs field.* The corresponding boson to this field is the *Higgs* particle. Even though there are strong theoretical requirements for the *Higgs* boson, it has not been observed experimentally. The best limit on its mass comes from direct searches at the *Large Electron Positron collider* (LEP), which shows that the *Higgs* mass m_H should be $m_H > 114.4$ GeV. From combination of the precise measurements at LEP, SLD and Tevatron also a upper limit of the *Higgs* mass can be derived, which is currently $m_H < 280$ GeV (95% confidence level). At the moment the most probable value for its mass is $m_H = 126^{+76}_{-48}$ GeV [6] (fig. 1.2.)

An important production channel of the *Higgs* particle is *Higgstrahlung.* The Feynman diagram of the Higgstrahlung process is shown in fig. 1.3. In the case that the Z boson decays leptonically into e^+e^- or $\mu^+\mu^-$ the basic properties of the Higgs boson, the mass and the width, can be measured very precisely and more importantly model independent. To ensure that the mass resolution of the *Higgs* is only limited by the width of the Z boson ($\Gamma_Z = 2.49$ GeV) the momentum resolution for charged particles of the detector must be better than $\frac{\sigma_{pt}}{p_t^2} \leq 0.5 \cdot 10^{-4}\,(\mathrm{GeV})^{-1}$. The detector concept to achieve this goal is discussed in sec. 1.3 and in sec. 1.4.

Supersymmetry

While the SM describes the particles and their interaction quite well it leaves many questions arising from experimental measurements open. Astrophysical measurements for example indicate that only $\sim 5\%$ of the matter in the universe consists of the particles described by the SM. Therefore, there must be a more fundamental theory which can explain on the one hand this problems, but on the other hand incorporates the SM, changing only the *Higgs* sector.

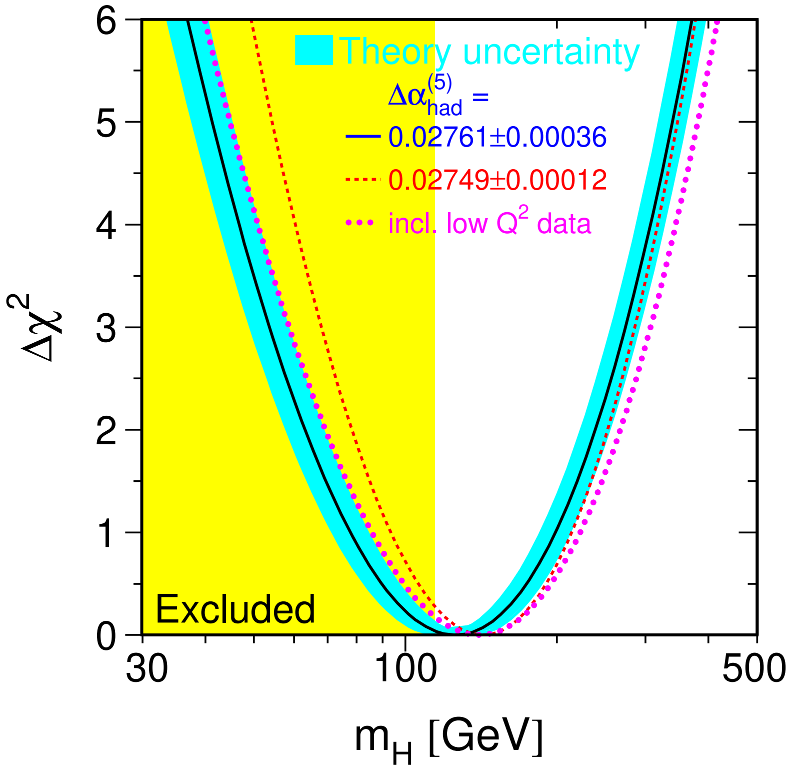

Figure 1.2: *Experimental constraints to the Higgs mass. The yellow area indicates the region which is excluded by direct measurements. The solid line with the blue band (theoretical uncertainties) describes the variation in χ^2 of a fit to the relevant SM parameters [6].*

At the moment the preferred candidate for such an extension of the SM is *Supersymmetry* (SUSY). SUSY introduces for each fermion a new boson and vice versa. If SUSY would be a perfect symmetry the particles of SM and the corresponding supersymmetric partner particles should have the same mass. However, since these partner particles are not observed, there has to be a *SUSY Breaking Mechanism* which leads to different masses of SUSY particles. There are several alternative schemes for the breaking of the symmetry e.g. the incorporation of gravity in SUSY.
All supersymmetric models have in common that they predict a least one light *Higgs* particle with a mass below 200 GeV. Many of these models also predict that a significant fraction of the supersymmetric particles can be found in the energy range of the ILC. If realised in nature the investigation of SUSY is also a good example of the complementarity of LHC and ILC. While at LHC the partner particles of the quarks, the *squarks*, can be in general more precisely measured, the ILC is more appropriate to measure precisely the properties of the *sleptons*. A combination of results from measurements at both machines will even allow to determine the properties of some particles much more precisely than at one machine alone.

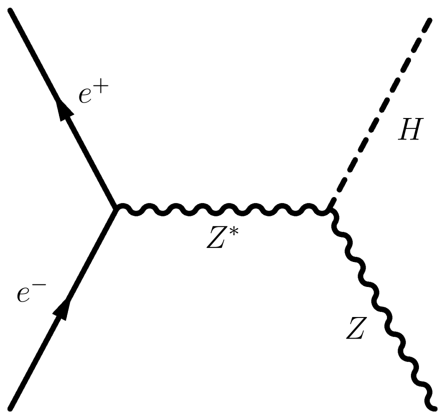

Figure 1.3: *Feynman diagram of the Higgstrahlung process.*

Alternative new Physics and Challenging the SM

Beyond SM and SUSY there are various alternative theories available which can be investigated in the energy range up-to 1 TeV. *Technicolor* which also gives an explanation for the electroweak symmetry breaking for example introduces a new strong interaction. This strong interaction should have an influence on the cross sections measured at the ILC and should be observable in this way.
There exist also theories which show that unification of gravity with the other forces might be realised at much lower energies than thought previously. These theories are based on the introduction of extra space-time dimensions which are curled up. As a result of this events with missing energy would be observed at the ILC.
But even when no direct observation of new physics can be found at the ILC, the very precise measurements of SM parameters will give the possibility to draw conclusions on new physics beyond the energy range of the ILC. An example of this is the prediction of the top mass from the measurements of the Z peak at LEP. The top quark was too heavy to be produced directly at LEP, but contributes to the width of the Z boson by virtual loop corrections.

1.2 The Accelerator

Until now the e^+e^- collider with the highest beam energy ($E_b = 104.5$ GeV) was LEP. The beam energy there was limited by the fact that a accelerated charged particle is losing energy in form of synchrotron radiation. The energy loss E_{loss} per cycle is given by

$$E_{loss} \sim \frac{1}{r}\left(\frac{E}{m}\right)^4 , \tag{1.1}$$

where r is the radius of the collider, E the energy and m the mass of the accelerated particle. For example for LEP, with a radius of ≈ 4.2 km, this results in an energy loss of $E_{loss} = 2$ GeV at a beam energy $E_b = 100$ GeV. For an e^+e^- machine with $\sqrt{s} = 500$ GeV and a comparable energy loss this would lead to a radius of around 1000 km. Therefore, future e^+e^- colliders will need to be built as linear colliders.

Parameter	LEP II	ILC/TESLA (500 GeV)
$\sqrt{s}$	-209 GeV	90 GeV - 1 TeV
$\sigma_x \times \sigma_y$	200 μm $\times$ 2.5 μm	553 nm $\times$ 5 nm
f_b	22 μs	337 ns
N	3×10^{11}	2×10^{10}
$\mathcal{L}$	10^{31} cm^{-2}s^{-1}	3.4×10^{34} cm^{-2}s^{-1}

Table 1.1: *LEP and ILC/TESLA (500 GeV) machine parameters.*

A possible design of such a machine is shown in fig. 1.4 as it was planned for TESLA. One of the main challenges of the ILC is to provide a high luminosity of $\mathcal{L} = 3 \cdot 10^{34}$ cm^{-2}s^{-1} in the whole energy range from 90 GeV - 1 TeV. To achieve this goal for the ILC superconducting cavities will be used. This has the advantage of a smaller power loss compared to the normal conducting technology and allows the accelerator to operate at a rather moderate frequency of $f = 1.3$ GHz. As a consequence of this the cavities can be larger and this reduces the requirements related to alignment. To build an accelerator in the desired energy range the total length of it has to be between 30 and 40 km.

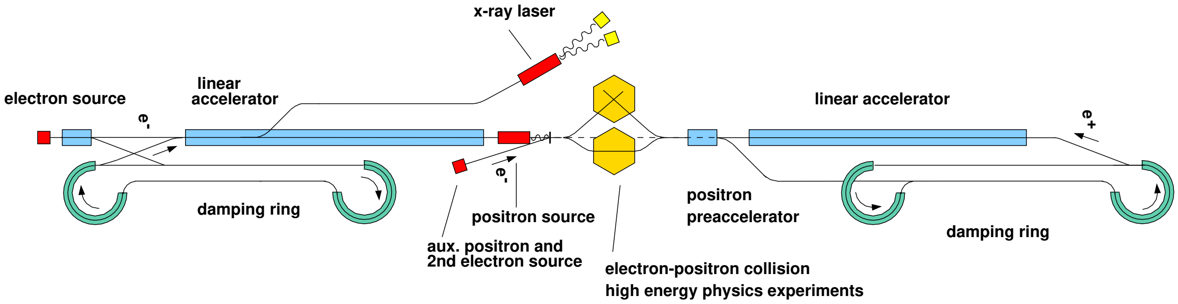

Figure 1.4: *Schematic of the TESLA design for a linear collider [5].*

The electrons and positrons will not be accelerated continuously, but will be grouped in *bunches* with a time between two bunches of 337 ns. About 2000 - 3000 bunches will be combined into a so called *bunch train*. The repetition rate of these trains will be of the order of 5 Hz. The much higher luminosity of the ILC in comparison to LEP will also be achieved by a reduction of the size of the interaction point (IP). In tab. 1.1 some parameters of the ILC and the LEP accelerator are compared. At the moment the collider is planned with two interaction regions, though the final configuration is not yet decided. In addition it is planned to use different polarisations of the beams.

1.3 Detector Requirements and Concept

The large luminosity at the ILC will allow very precise measurements from the statistical point of view. Since it is expected that the background and the radiation damage to the detectors will be relatively low, the design of the detector is purely driven by the physics requirements.

At the moment three different detector concepts are under consideration: the Silicon Detector concept (SiD), the Large Detector concept and the Huge Detector concept. While the former is based on silicon technology, the latter are quite similar and include the use of a gaseous detector for tracking purposes. Here, only the Large Detector concept is presented. For this concept the detector as planned in the TESLA TDR [7] were used as a starting point.

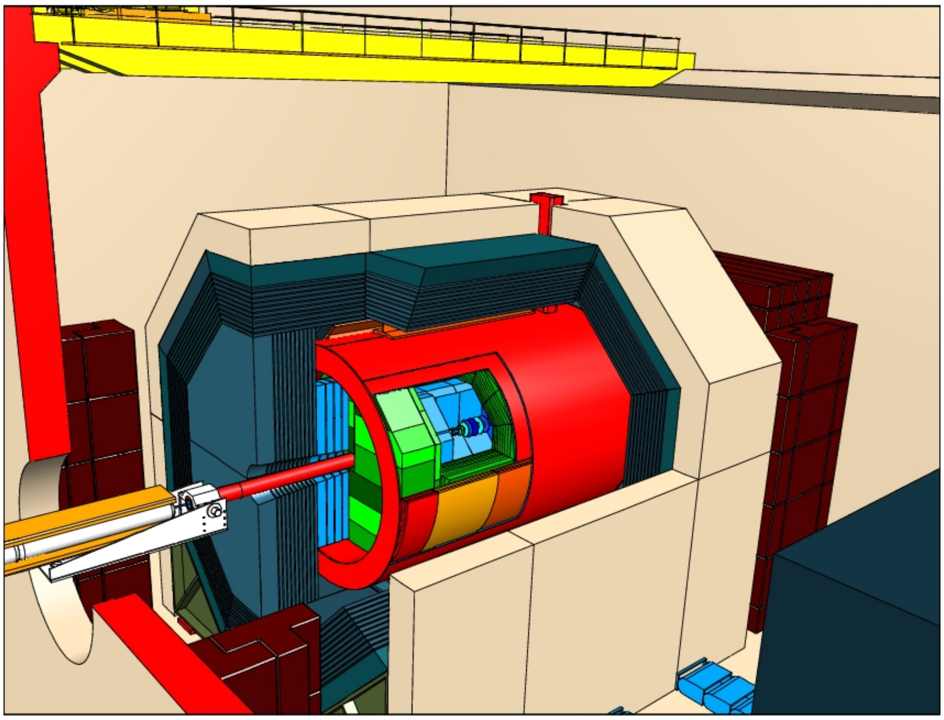

Figure 1.5: *Schematic of a high energy physics detector.*

In the following the most important detector systems are shortly introduced:

Vertexing: To be sure that a discovered particle is the SM Higgs boson the couplings of the Higgs boson to the SM fermions must be measured very precisely. In the SM these couplings are predicted to be proportional to the masses of the fermions. Therefore, it is crucial to be able to distinguish between *b, c* and *uds* flavoured events. Since the average impact parameter for charm flavoured hadrons is only of the order of 100 μm, an impact parameter resolution δ_δ of the vertex detector of

$$\delta_\delta \approx 5\mu\mathrm{m} \tag{1.2}$$

is required to tag c quark decays. This will also give the possibility to assign nearly all tracks to primary, secondary and tertiary vertices allowing for the determination of the vertex mass and charge and thus improving the b / and $f/\overline{f}$ separation.
At the moment several different technologies for the vertex detector, which are CCD [8], CMOS [9], DEPFET [10] and hybrid pixels [11], are under study.

Tracking: The design of the tracking system is driven by various aspects. One of the most important one is to determine precisely the *Higgs* mass from the recoil mass spectrum of the leptonic decay of the Z boson from a Higgsstrahlung process. This sets the requirements on the momentum resolution of:

$$\frac{\sigma_{pt}}{p_t^2} \leq 0.5 \cdot 10^{-5}\,(\mathrm{GeV})^{-1} \quad . \tag{1.3}$$

The influence of the momentum resolution on the recoil mass spectrum is illustrated in fig. 1.6. In addition the tracking system must be able to work within

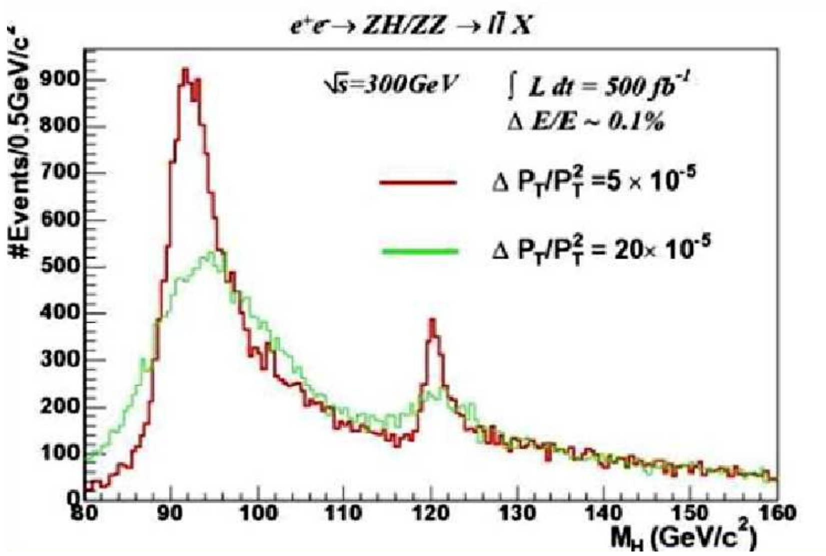

Figure 1.6: *Measurement of the Higgs signal for two different momentum resolutions [12].*

high density track environments and allow for a good separation of the single tracks. For example the production of a $t\bar{t}$ pair leads to up-to 8 jets in the detector. This is also motivated by the concept of particle flow (PFLOW), which is introduced in the next paragraph.

Within the Large Detector concept the tracking system will include the vertex detectors, mentioned above and a *Time Projection Chamber* (TPC) 1.4.

Further detectors based on silicon technology between these are foreseen. They should improve the pattern recognition in linking the tracks found in the TPC with tracks found in the vertex detector and the momentum resolution by the addition of a few very precise space points at comparatively large distance from the interaction point. In the backward and forward direction silicon discs will be placed to cover the angle range down to 7°. These intermediate trackers will also help to identify long-lived particles.

At the end caps of the TPC further detectors will be located giving a precise endpoint for tracks under small angle and thus with only a few space points in the TPC.

All tracking detectors must be able to work in high magnetic fields (4 T).

Calorimetry: To investigate the self-coupling of the SM Higgs boson and also to study the triple gauge coupling such as $e^+e^- \to Z^* \to W^+W^-$ one has to distinguish between ZZ and WW final states. For this a very good jet energy resolution is required:

$$\frac{\sigma_E}{E} \approx \frac{0.3}{\sqrt{E(\mathrm{GeV})}} , \tag{1.4}$$

which is twice as good as at LEP. To achieves this only very little material should be placed in front of the calorimeter. Therefore, it is foreseen, that the calorimeter will be located within the superconducting coil of the magnet. However, also the use of the PFLOW method is required for this jet energy resolution. This concept exploits that $\approx 65\%$ of the jet energy is coming from charged tracks, $\approx 26\%$ from photons and only $\approx 9\%$ from neutrons and neutral long-lived hadrons. The obvious way to measure the jet energy is to use the tracker detectors for the energy determination of the charged tracks, the information of the electromagnetic calorimeter (ECAL) for the energy measurement of the photons and the hadronic calorimeter (HCAL) only for the energy estimation of the neutral hadrons. To be able to disentangle the contributions from charged and neutral particles both a high granularity hadronic calorimeter and also a very good track separation and reconstruction efficiency in the tracker detectors are required. To achieve also a good separation between photons and charged particles an electromagnetic calorimeter with high granularity together with a high magnetic field and, even more important, a large inner radius of the ECAL is necessary. A more detailed introduction to the concept of PFLOW is given in [13].
As a option for the electromagnetic calorimeter with 1 cm^2 cell size and 32 million channels a silicon-tungsten calorimeter is considered. For the hadronic calorimeter there are two different approaches under discussion: A sandwich calorimeter with scintillating tiles and new readout technology (see e.g. [14]) and a digital calorimeter with *Resistive Plate Chambers* (RPC) or wire chamber readout. For both, stainless steel is foreseen as an absorber material.
A further requirement is the large hermeticity of the calorimeter system. In most of the final states with SUSY particles a considerable amount of energy is carried away undetected. To distinguish between these events and events in which energy disappear in form of particles close to the beam pipe, it is required that the forward calorimeter cover the angular range θ down to $\theta \approx 5$ mrad.

Magnet and Muon System To achieve the required momentum resolution a magnetic field of 4 T is foreseen for the Large Detector concept. The superconducting coil should envelope all previously mentioned detector systems. The return yoke of the magnet will be instrumented with RPC or other technologies to detect muons and energy leaking out of the hadronic calorimeter (tail catcher).

1.4 A TPC for a Linear Collider

The theoretical basics of a TPC are presented in sec. 2.5. Here, only a short overview of the design as presented in the TESLA TDR is given. The overall design is driven by the required momentum resolution. The momentum resolution of the TPC alone is given by the Gluckstein formula [15]

$$\frac{\sigma_{pt}}{p_t^2} = \frac{\sigma_{r\phi}}{0.3L^2B}\sqrt{\frac{720}{N+4}} \tag{1.5}$$

and is directly related to the achievable point resolution $\sigma_{r\phi}$. Here, L is the length of the lever arm, B the magnetic field and N the number of points minus 1. To achieve the momentum resolution mentioned above for the whole tracking system the momentum resolution required for the TPC alone is:

$$\left(\frac{\sigma_{pt}}{p_t^2}\right)_{TPC} = 2\cdot 10^{-5}\,(\mathrm{GeV})^{-1} \quad . \tag{1.6}$$

Fig. 1.7 shows one quarter of the TPC as planned for TESLA. The inner radius is 32

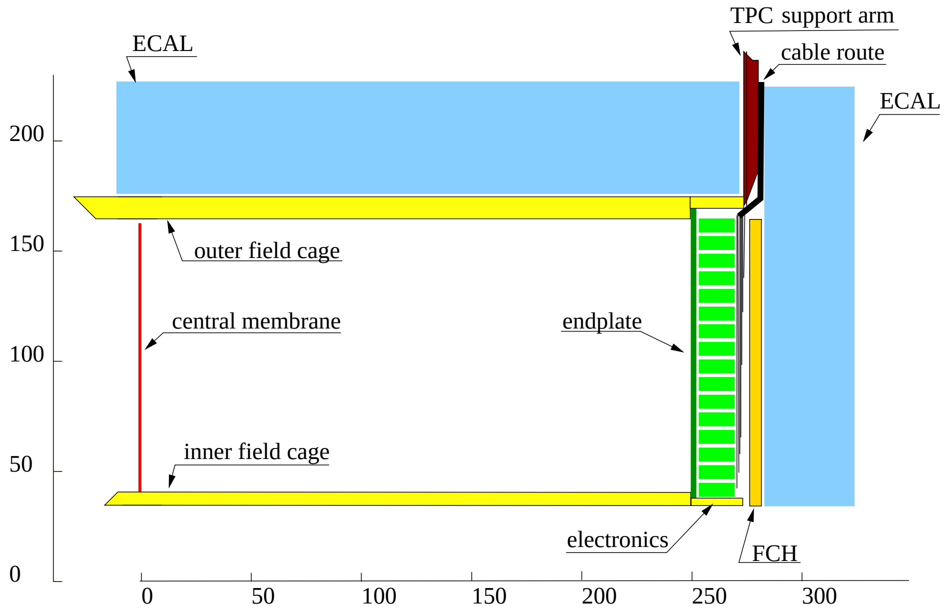

Figure 1.7: *General layout of one quarter of the central tracking system [7].*

cm and the outer 170 cm. The overall length is 2 × 2730 mm leading to a maximal drift distance of 2500 mm. The mechanical parameters of the TPC are summarised in tab. 1.2. A potential candidate for the gas which will act as the sensitive volume for an ILC TPC is a three component mixture of Ar:CO_2 :CH_4 (93:2:5) %. This gas has its maximal drift velocity of $v_D \approx 4.6$ cm/μs at a moderate drift field of 230 V/cm yielding a maximal voltage at the cathode of about 60 kV. As a consequence of the moderate drift velocity up to 160 bunch crossings will be superimposed in the chamber. However, other gas mixtures such as Ar:CH_4 and Ar:CF_4 are under investigation.
Based on simulations using the BRAHMS program package [16] the required single point resolution in $r\phi$ is assumed to be 70 μm for 10 cm drift length and 190 μm for 200 cm. The corresponding z resolution ranges from 6 to 10 mm. Simulations [17] suggested the use of 2×6 mm^2 pads to achieve this goal. Fig. 1.8 shows the result of this simulation. With the suggested pad size each endplate is equipped with

mechanical radii	320 mm inner, 1700 mm outer
overall length	2 × 2730 mm
radii of sensitive volume	362 mm inner, 1618 mm outer
length of sensitive volume	2 × 2500 mm
weight	≈ 4 t
gas volume	38 m^3
radiation length	≈ 0.03 X_0 to outer field cage

Table 1.2: *List of main mechanical parameters of the ILC TPC [7].*

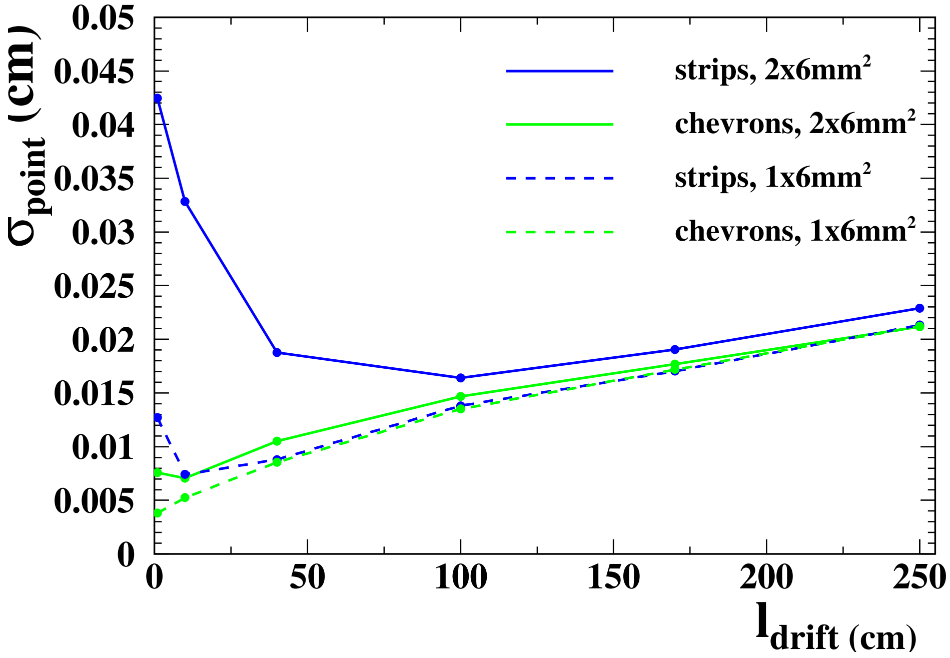

Figure 1.8: *Simulated rϕ resolution as a function of the drift length for different pad geometries and a gas mixture of Ar:CH_4 :CO_2 (93:5:2) [17].*

approximately 600000 readout channels. In addition the TPC should provide a good dE/dx resolution of 4.3% for 200 pad rows. The main performance requirements of the TPC are summarised in tab. 1.3.

1.5 Goal of this Study

Time Projection Chambers are a well established detector type, which has been successfully operated at various experiments e.g. [18–20]. However, the operation of a TPC at the ILC will set much stronger requirements on it than in previous experiments. For example the time between two bunch crossings will only be 337 ns leading to a superposition of up-to 160 bunch crossings in the TPC. As a consequence the space charge in the sensitive volume due to the ions produced in the gas amplification region and then drifting to the cathode may reach a critical amount, if wires, conventionally used for gas amplification close to the endplates of a TPC, are not

Drift distance	10 cm	200 cm
$r\phi$ resolution	70 μm	190 μm
z resolution	0.6 mm	1 mm
double pulse resolution in $r\phi$	≤ 2.3 mm	
double pulse resolution in z	≤ 10 mm	
dE/dx resolution	4.3 % for 200 pad rows	
π/K separation	$> 2\ \sigma$ between 2 and 20 GeV	
momentum resolution ($\lvert\cos\theta\rvert < 0.75$)	1.4×10^{-4} GeV^{-}1	
momentum resolution ($\lvert\cos\theta\rvert < 0.75$)	3.2×10^{-4} GeV^{-}1	

Table 1.3: *Summary of important performance parameters of a TPC at the ILC/TESLA [7].*

replaced by an alternative technology.
An attractive alternative to wires is based on *Micro Pattern Gas Detectors* (MPGDs) namely *Gas Electron Multipliers* (GEMs) [21, 22] (sec. 2.5.2) and *Micromegas* [23]. Apart from the advantage related to the space charge both have further advantages compared to wires which are discussed later.
In a previous study [24] it was already shown that a GEM based readout can be used in principle in a TPC. First measurements of the point resolution without magnetic field were presented in this study. However, it has to be shown that it is also possible to operate a TPC with GEM readout at high magnetic fields of up-to 4 T. Therefore, a new TPC prototype was designed and built during the study presented in this thesis which gives the possibility to measure in a 5.3 T superconducting magnet. In the following the results of the performance studies of this prototype are presented and also first results of point resolution measurements at various magnetic fields and different readout geometries and gases are shown.

This part of the thesis is structured as follows: In Chapter 2 the theoretical basics of gaseous detectors are discussed. In the following chapter, Chapter 3, the new TPC prototype is presented, before in Chapter 4 the performance of the setup is shown. Chapter 5 contains the results of the point resolution study and their discussion. Finally a summary and an outlook are given in Chapter 6.

Chapter 2

Basic Principles of Gaseous Detectors

The principle of all gaseous detectors is based on the fact, that a charged particle at sufficient energy traversing a gas ionises the gas molecules. The released electrons then drift in an applied electric field to the anode, where the signal is read out. In most cases the signal from the primary electrons is too small to be detected. For this reason the primary electrons are multiplied in an avalanche process induced by a high electric field close to the anode.
The *Geiger-Müller Counter* was one of the first detectors based on this principle. It consists of a tube, which acts as a cathode and a thin anode wire, placed in the centre of the tube. A large potential difference between the electrodes leads to electric field high enough for the amplification process to take place close to the wire.
An advancement of this detector is the *Multi Wire Proportional Counter* (MWPC). The MWPC consists of a plane of parallel anode wires between parallel cathode planes and allows for good spatial resolution measurements. Another advantage of the MWPCs is that they are operated in the *proportional mode*, which means that the avalanche size is proportional to the number of primary electrons. This allows a calculation of the deposited energy over a given distance in the gas volume, so that, when the momentum of the particle is measured using a magnetic field, a particle identification via the specific energy loss is possible.

An evolution of this technology is the *Time Projection Chamber* (TPC), which was introduced by Nygren [25] in 1975. This detector type will be presented in detail in sec. 2.5.
In the following a brief overview of the theoretical basics of gaseous detectors is given.

2.1 Detector Gas

In principle all gases with a sufficient small e^- attachment and a stable gas amplification process can be used to operate gaseous detectors. However the choice of the gas or gas mixture respectively depends strongly on the experimental requirements e.g. operational mode, gain, resolution, drift velocity, aging, etc..
Noble gases, e.g. argon, are often chosen as a main component of the chamber gas,

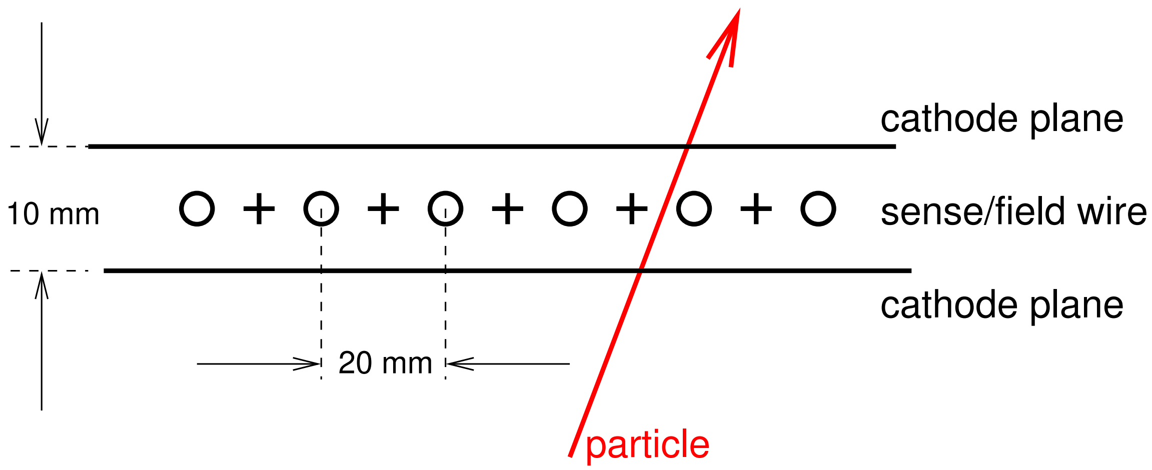

Figure 2.1: *Principle of a multi wire proportional counter.*

because of their chemical properties and their low ionising energies. Since in the amplification process also photons with energies above the ionisation potential are emitted, *quencher gases* have to be added to avoid permanent discharges at quite low gain. Quencher gases have a high cross section for photons in the appropriate energy range. The absorbed energy is dissipated by elastic collisions, vibration, rotation or by dissociation into simpler radicals.

A small amount of quencher gas can dramatically change the properties of the chamber gas: the attainable gas gain may be increased to 10^6, but also the other operational characteristics such as the drift velocity and its dependence on the electric field may change significantly. The choice of the chamber gas is normally supported by Monte Carlo simulations e.g. with the program packages Garfield, MAGBOLTZ and Heed [26–29]. An overview of various gases used in a TPC is given in fig. 2.2 (a).

One must also be aware that gas impurities due to outgasing materials, tightness of the gas system, etc., can change the characteristics of a gas mixture dramatically even when the contamination is only of the order of *ppm*. The fig. 2.2 (b) shows the influence of H_2O contamination on the drift velocity.

Finally the choice of the gas pressure is an important aspect: on one hand a pressure above 1 bar increases the accuracy of the longitudinal resolution, one can achieve a smaller Lorentz angle and also the dE/dx measurements are improved, on the other hand an increased pressure demands a pressure vessel, which adds a considerable amount of material to the detector [30].

2.2 Operational Modes of Gaseous Detectors

All gaseous detectors have in common that their working principle is based on an electric field applied between cathode and anode.

Depending on the strength of the applied electric field several different *operational modes* are distinguished. The so called *ionisation chamber* mode refers to the region, where the applied electric field is strong enough to avoid the recombination of electrons

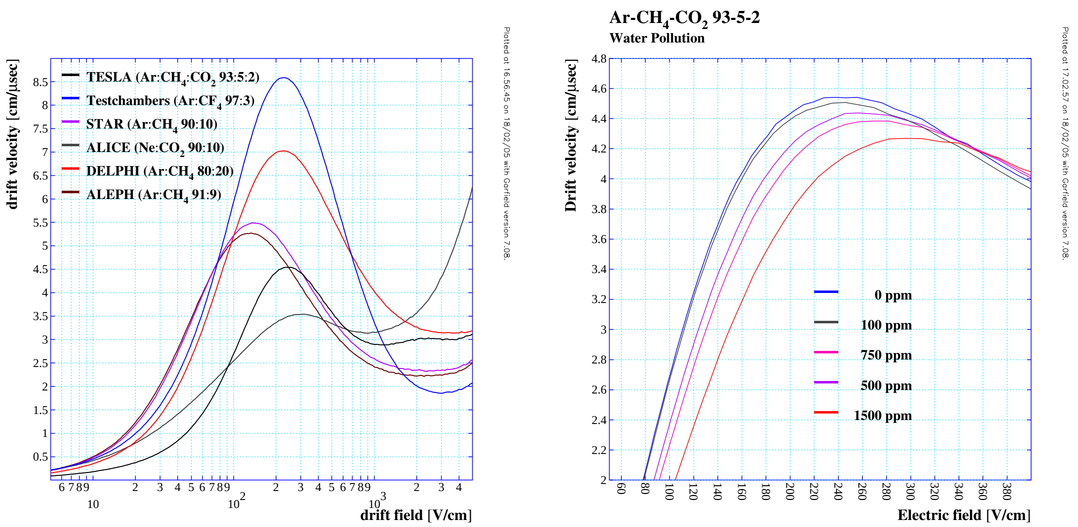

(a) (b)

Figure 2.2: *(a) shows the drift velocity as a function of the applied electric field for various gas mixtures. (b) illustrates the effect of water pollution on the drift velocity. Both were simulated with Garfield.*

and ions, but no gas amplification occurs. If the electric field strength is increased, the primary ionisation electrons are accelerated to energies higher than the first ionisation potential of the gas. These electrons then create electron-ion pairs on their way to the anode. These secondary electrons may also produce further pairs. If the amount of electrons measured at the anode is proportional to the primary ones (see also sec. 2.4.3), the chamber is operated in the *proportional mode*. If the electric field is further increased, space charge effects occur, which change the *effective electric field*. Thus, the proportionality between initial charge and the one measured at the anode is not strictly given anymore. The detector is operated in the *limited proportional mode*. At higher electric fields also photons are produced, which can transverse the gas and produce further ionisation. In this case is the measured charge almost independent from the initial ones. This region is referred to as *Geiger-Müller mode* [31].

2.3 Detection of Charged Particles

Charged particles traversing a gas volume deposit a part of their energy in the gas. The energy transfer occurs mainly via the inelastic scattering of the charged particles at the shell electrons of the gas which is ionised as a result. The specific energy loss dE/dx as a function of β of the charged particle is given by the *Bethe-Bloch-Formula*. But this gives only the mean energy deposition in an absorber of thickness dx. In a given absorber the energy deposition underlies statistical fluctuations. Depending on the thickness of the absorber, this fluctuations are described by various distributions.

2.3.1 Bethe-Bloch-Formula

For the derivation of the *Bethe-Bloch-Formula* two approximations are made: First the shell electrons are free and initially at rest and second the charged particle is much heavier than the electron $m >> m_e$:

$$-\frac{dE}{dx} = \frac{e^2 N_A}{\epsilon_0} z^2 \frac{Z}{A} \frac{1}{\beta^2} \big[\ln \big(\frac{2 m_e c^2 \gamma^2 \beta^2}{I} \big) - \beta^2 \big] \ . \tag{2.1}$$

Here, e denotes the elementary charge, z the charge of the incoming particle in units of e, Z, A are the atomic resp. mass number, m_e the electron mass, ϵ_0 the dielectrical constant of vacuum and N_A the Avogadro number. I is the average ionisation energy of the absorber material. With the relation $\beta = \frac{p}{mc}$ eq. 2.1 splits up for every kind of particle as shown in fig. 2.3. Thus, measuring the momentum p and the specific energy loss dE/dx of the charged particle at the same time allows in this way particle identification on a statistical basis.

2.3.2 Energy Straggling

In general the measured energy deposition in an absorber of thickness dx will not correspond to the mean value given by the *Bethe-Bloch-Formula*. The distribution of the energy loss depends strongly on the thickness of the absorber material. For the calculation of this distribution it is distinguished between thin and thick absorber. In the case of a thin absorber, which is a valid assumption for most gaseous detectors, the energy loss distribution is following a Landau distribution. This distributions differs from a Gaussian due to a large tail, in which a high energy transfer occurs. For thick absorber the energy loss is described by a Gaussian distribution. For the intermediate region the Vavilov model [33] gives a description of the energy loss and also numerical models are available (see e.g. [34]).

2.3.3 Number of Electrons released

The total number of electrons released per unit length n_t is given by:

$$n_t = \frac{dE}{dx} \frac{1}{W} \ . \tag{2.2}$$

Here, W is the average energy to produce a electron-ion-pair, which is larger then ionisation potential, since a part of the deposited energy disappear in excitation energy and the kinetic energy of the electron and the ion. Tab. 2.1 shows the values of W for different gases.
Since energy conservation is an additional condition, the standard deviation is given by:

$$\sigma_{n_t} = \sqrt{n_t F} \ , \tag{2.3}$$

where F donates the Fano factor. In this thesis n_t corresponds to the number of primary electrons.

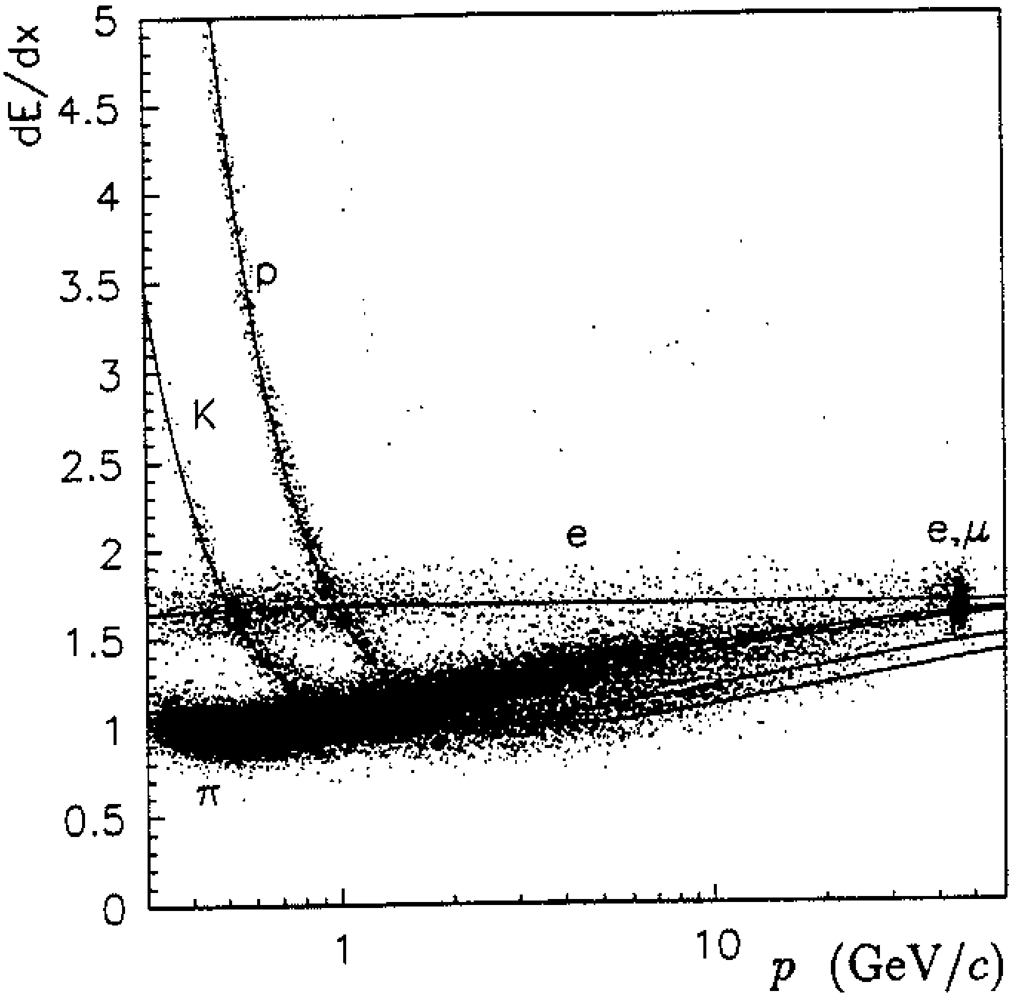

Figure 2.3: *The dE/dx distribution as a function of the particle momentum. The distributions for pions, kaons, protons and electrons are shown as measured with the ALEPH TPC [32].*

2.4 Behaviour of Charges in Gases

For the understanding of the working principle of gaseous detectors the following physical processes are crucial.

2.4.1 Drift

If the molecules of a gas are ionised by a traversing charged particle, the electrons and ions would recombine immediately. Applying an outer electrical field, the *drift field*, this recombination can be avoided. The electrons drift to the anode, while the positive ions drift to the cathode. This motion under the influence of an electric $\vec{E}$ and

Gas	W [eV]
Ar	26.3
Ne	36.4
He	42.3
Xe	21.9
CO_2	32.8
CH_4	27.1

Table 2.1: *Average energy W [eV] needed to produce an electron-ion pair for different gases [30].*

a magnetic $\vec{B}$ field can be described by the following equation:

$$m\frac{dv}{dt} = e\vec{E} + e\vec{v} \times \vec{B} - K\vec{v} \ . \tag{2.4}$$

Here, m denotes the mass of the charged particle, e the electric charge and K a quantity, which describes the viscosity of the gas. The term $-K\vec{v}$ is caused by the scattering of the charged particles on the gas molecules. The ratio $\tau = \frac{m}{K}$ has the dimension of a time and is the average time between two collisions of the charged particle with the gas molecules.
The solution of the Langevin equation for $t \gg \tau$ is:

$$\vec{v} = \frac{e}{m}\tau|\vec{E}|\frac{1}{1+\omega^2\tau^2}(\hat{E} + \omega\tau(\hat{E} \times \hat{B}) + \omega^2\tau^2(\hat{E} \cdot \hat{B})\hat{B}) \ , \tag{2.5}$$

where $\hat{E}$ and $\hat{B}$ denote the unit vectors of the electric and magnetic field respectively and $\omega = \frac{e}{m}B$ is the cyclotron frequency. Eq. 2.5 describes a steady state for which $\frac{dv}{dt} = 0$
Three important cases are distinguishable:

a) If $|B| = 0$ it follows $\omega = 0$ and eq. 2.5 is reduced to

$$\begin{aligned} \vec{v} &= \frac{e}{m}\tau\vec{E} \\ &= \mu\vec{E} \ . \end{aligned} \tag{2.6}$$

The mobility μ depends for electrons on the strength of the electric field due to quantum mechanical effects between the electron and the atomic electrons, while for ions it is constant over a wide range of E.

b) When $\vec{E}$ and $\vec{B}$ are in parallel, eq. 2.6 is also valid, as one can easily see from 2.5.

c) Another very important case is, when there is a significant angle between $\vec{E}$ and $\vec{B}$. In this case the second term in eq. 2.5 dominates and $\vec{v}$ depends also on the magnetic field. An important parameter, on which also the spatial resolution depends, is the *Lorentz angle* α_L. α_L is defined as the angle between $\vec{v}$ and $\vec{E}$. In the extreme case that $\vec{E}$ and $\vec{B}$ are perpendicular, $|\vec{v}|$ is given by:

$$|\vec{v}| = \frac{e\tau}{m\sqrt{1+\omega^2\tau^2}}|\vec{E}| \ . \tag{2.7}$$

One important point is, that in any case the drift velocity depends on the mass of the charged particle, which leads to a much higher drift velocity for electrons than for ions.

2.4.2 Diffusion

Charged particles, which are released in a cloud, will diffuse isotropically away from their place of creation because of their thermal energy. The density distribution of the charged particle after a time t can be described by a Gaussian distribution:

$$n = \left(\frac{1}{\sqrt{4\pi\acute{D}t}}\right)^3 e^{-\frac{r^2}{4\acute{D}t}} \ , \tag{2.8}$$

where r is the radial distance to the creation point and $\acute{D}$ is the diffusion coefficient. The width σ of the distribution is given by:

$$\sigma = \sqrt{2\acute{D}t} \ . \tag{2.9}$$

The diffusion coefficient $\acute{D}$ depends on the chosen gas mixture, temperature T and pressure p by the following formula:

$$\acute{D} = \frac{2}{3\sqrt{\pi}}\frac{1}{p\sigma_{total}}\sqrt{\frac{(kT)^3}{m_{ch}}} \ . \tag{2.10}$$

The total cross section σ_{total} depends also on the chosen gas and the kind of the charged particle. For eq. 2.10 the assumption was made, that the free charges are conserved, this is due to recombination of electrons and ions and in the presence of electro negative molecules, although O_2 not always the case.

Influence of an electric Field

Within an electric field the following definition of the diffusion coefficient is more convenient, whereby the width σ of the distribution can be calculated depending on the drift length L:

$$\sigma_D = D\sqrt{L} \ . \tag{2.11}$$

The quantity D is related to $\acute{D}$ by:

$$D = \sqrt{\frac{2\acute{D}}{v_{drift}}} \ . \tag{2.12}$$

When in the following the diffusion coefficient is mentioned, D is denoted. One would naively expect, that the diffusion of an electron cloud within an electric field is the same along the electric field lines (longitudinal) as for perpendicular to it (transverse), but in 1967 [35] it was shown that the longitudinal diffusion D_l changes significantly in an electric field. The reason for this behaviour is, that the leading and the trailing edge of the cloud have different energies and this, since the collision rate depends on the energy, leads to a change of the diffusion in the longitudinal direction. Fig. 2.4 shows this effect.

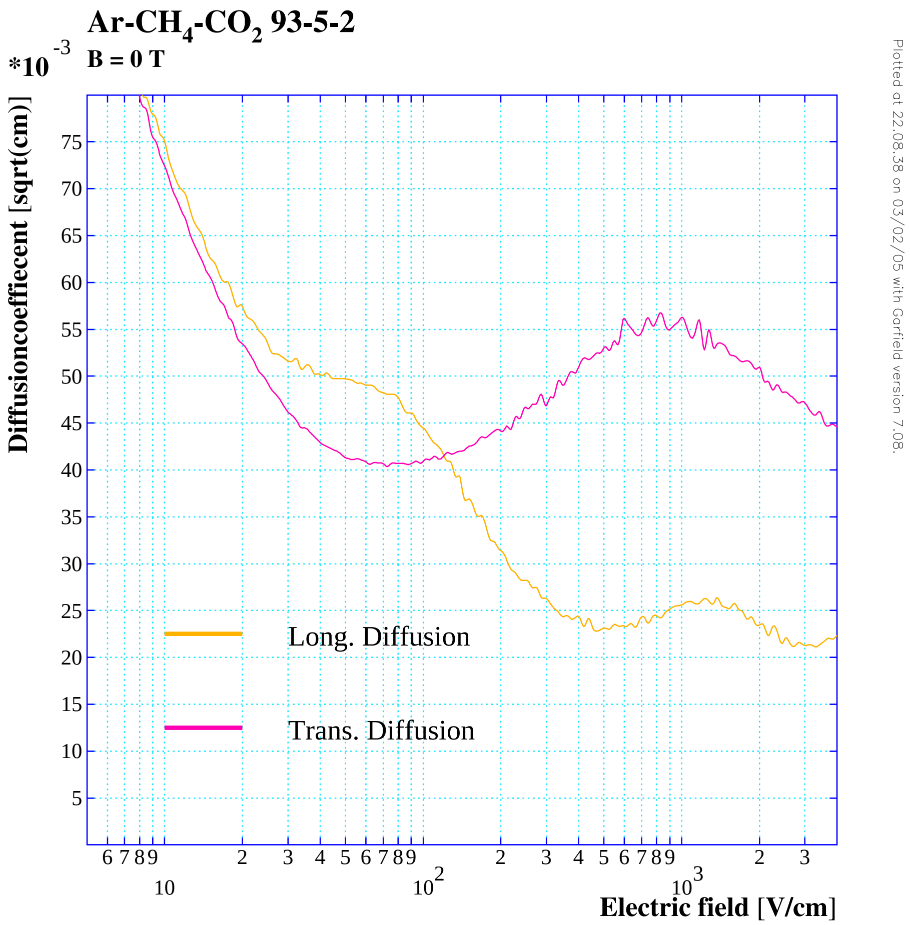

Figure 2.4: *The longitudinal and transverse diffusion at $B = 0$ T depending on the applied electric field. Simulated with Garfield.*

Influence of a magnetic Field

Within a magnetic field the transverse diffusion is strongly suppressed, while the longitudinal diffusion is unchanged. This can be easily explained by the Lorentz force, which influences the particles with a transverse velocity component and forces these on a helical trajectory between two collisions. The diffusion coefficient $D_t(B)$ is given by:

$$D_t(B) = \frac{D_t(0)}{1 + \omega^2\tau^2} \ . \tag{2.13}$$

Here, $D_t(0)$ is the diffusion coefficient in the absence of a magnetic field. Fig. 2.5 shows the effect of a magnetic field on the diffusion coefficients.

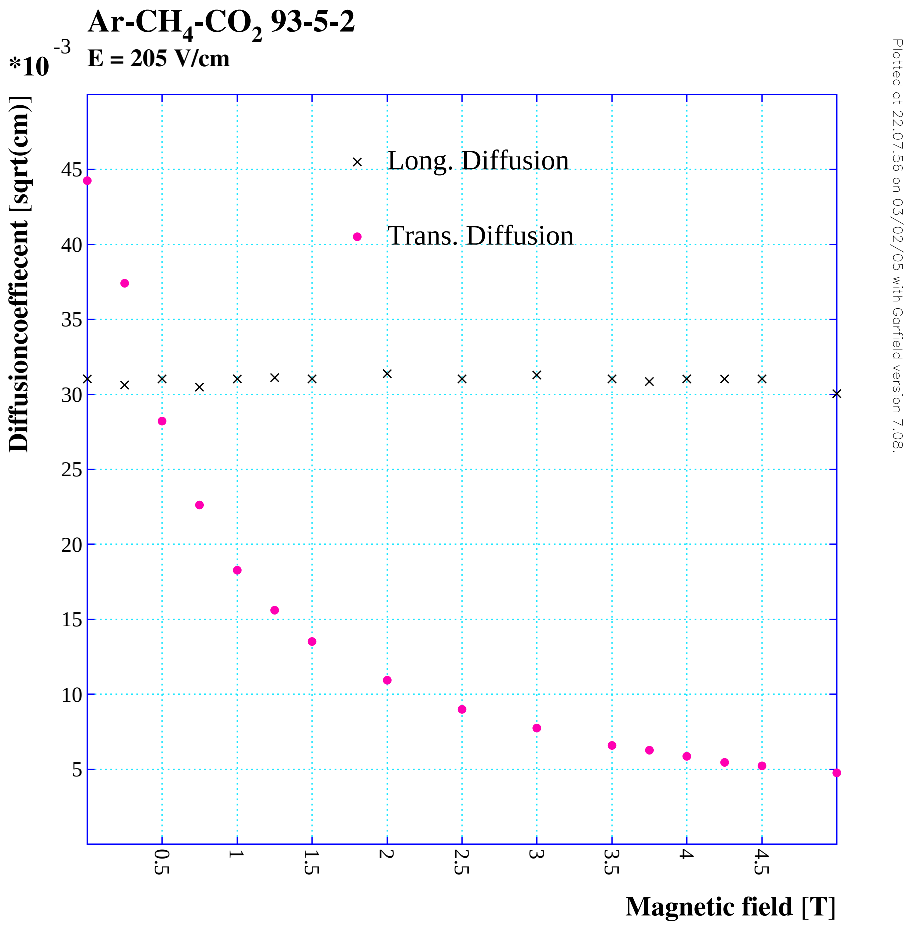

Figure 2.5: *The longitudinal and transverse diffusion at* $E = 205\ \frac{V}{cm}$ *as a function of on the applied electric field. Simulated with Garfield.*

2.4.3 Gas Amplification

At electric field strengths of a few 10 kV/cm the primary electrons are accelerated between two collisions to energies, which are sufficient to ionise the gas. Both, the primary electrons and the in the avalanche process released secondary electrons are again accelerated and ionise the gas. The avalanche continues as long as the field strength is high enough to accelerate the electrons to energies above the ionisation energy of the gas or the electrons are absorbed at an electrode. One important quantity in this process is the first Townsend coefficient α, which is the probability for one ionisation per unit length. α depends on the chosen gas mixture, but also on the strength of the electric field. Since the electric field in the amplification region is usually inhomogeneous, for a detector the gain factor G is an import parameter, if the chamber is operated in the *proportional mode*:

$$G = \frac{N(x)}{N_{x_0}} = \exp\left(\int_{x_0}^{x} \alpha(x)dx\right) . \tag{2.14}$$

Here, x_0 denotes the starting point of the avalanche and x the endpoint, $N(x_0)$ the number of primary electrons and $N(x)$ the number of electrons at the point x.

2.5 Time Projection Chamber

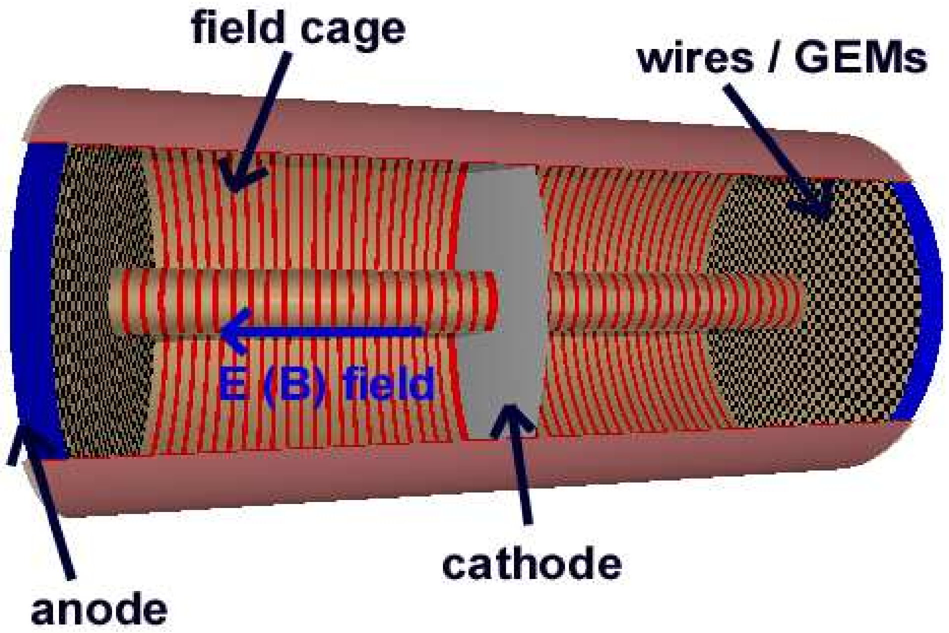

Figure 2.6: *Principle design of a TPC. The various parts of a TPC are shown as explained in the text.*

Fig. 2.6 shows the principle design of a TPC. It usually consists of a cylindrical volume with an outer and, in the case of a colliding experiment, with an inner radius. The endplates of this volume are the anodes, which are at ground potential, while the cathode, which is at a potential of some 10 kV, divides the volume in two identical volumes. Within in the inner radius the beam pipe and the inner detectors, e.g. vertex detectors, are placed. The walls of the volume are the field cage, which ensures a very homogeneous electrical field between the electrodes. The volume contains a gas mixture, which acts as the sensitive material. Fig. 2.7 shows the working principle of a TPC. After a charged particle, e.g. a cosmic muon, has traversed through the gas volume and ionised the gas, the released electrons drift within the electrical field towards the anode, while the ions drift to the cathode. In front of the anode is an amplification device, which creates an electron avalanche. An improvement in contrast to the conventional used wires might be the use of *Micro Patter Gas Detectors* (MPGDs): *Gas Electron Multipliers* (GEMs) or *Micromegas* respectively. An overview of the amplification devices are given in sec. 2.5.2.
The coordinate system is defined in the following way x,y or respectively r,φ are laying in the plane parallel to the anode, while z or respectively θ goes along the chamber.
One advantage of a TPC is the 3 dimensional track reconstruction. The $r\varphi$ information are obtainable from the anode segmented in *pads*, while the z coordinate is delivered by the drift time, which can be calculated by knowing the starting time t_0 from a bunch

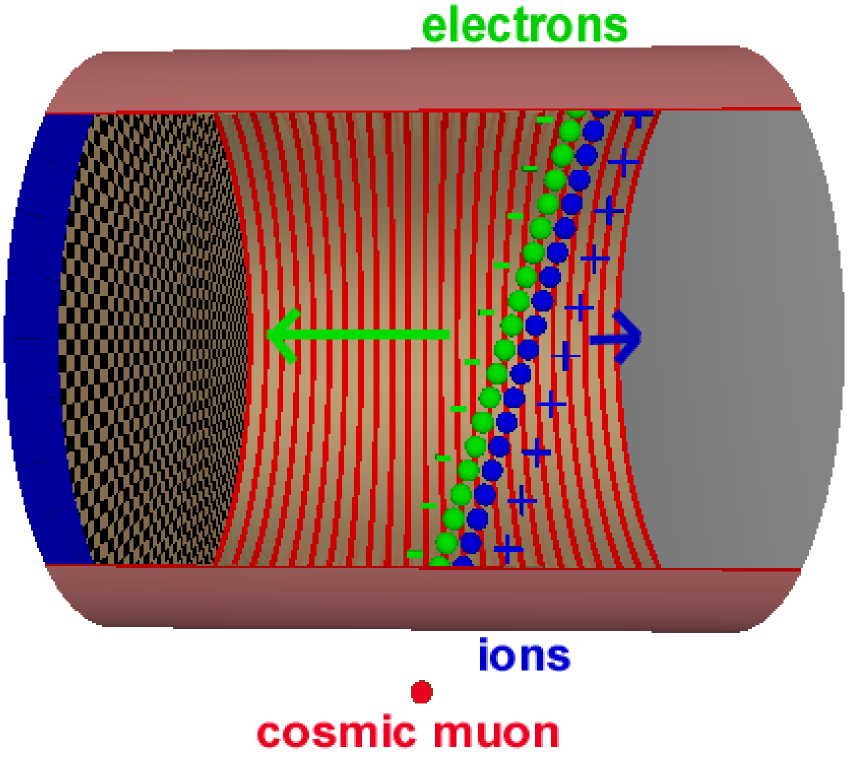

Figure 2.7: *Working principle of a TPC: a charged particle, here a muon (red), traversing the gas volume releases electrons (green) and ions (blue). The electrons drift to the anode (left), while the ions drift, much slower, to the cathode.*

crossing in a colliding experiment or from outer scintillators and the time t_z, when the signal arrives at the anode:

$$z = v_{drift} \cdot (t_z - t_0) \ . \tag{2.15}$$

From eq. 2.15 it follows, that the electric field has to be very homogeneous and that the drift velocity v_{drift} should have only a moderate dependence on the drift field for a given gas mixture. Using a magnetic field it is also possible to determine the transverse momentum p_t of a charged particle, by measuring the radius ρ of the trajectory:

$$p_t[GeV] \approx 0.3 \cdot \rho[m] \cdot B[T] \ . \tag{2.16}$$

With this information and the knowledge of the position of the trajectory in the θ plane it is possible to determine the total momentum of the charged particle.
From the charge deposited on the pads the specific energy loss $\frac{dE}{dx}$ can be extracted, which allows, as mentioned in sec. 2.3 for the identification of the charged particle on a statistical basis. Strong requirements on the electric field and the gas are given. Small variations in the electric and also in the magnetic field can yield large transverse displacements, especially considering that the maximum drift length is of the order of meters for modern TPCs. For TPCs in experiments with large interaction rate it is

also desired, that the gas has a large drift velocity, so that the TPC can be emptied fast. A collection of the drift velocity distribution for various gas mixtures used in a TPC is shown in fig. 2.2 (a). In general the operational drift field is chosen such that it corresponds to the maximum of the drift velocity. Apart from the fast clearance of the TPC this is motivated by the fact, that in this region the effect of temperature, pressure and drift field inhomogeneities on the drift velocity is smallest allowing for a stable operation of the TPC.
Furthermore the attachment coefficient for electrons should be as small as possible to avoid a signal loss that increases with the drift length. Other advantages of a TPC are that there is nearly no material in front of the calorimeters, which surround the TPC. Thus the energy resolution of the calorimeters is only slightly degraded compared to other tracking detectors. It is also and advantage, that $\vec{E}$ and $\vec{B}$ are parallel avoiding so called $\vec{E} \times \vec{B}$ effects. One disadvantage of a TPC is that because of the long drift distances it is a quite slow detector. This is also a problem concerning the ions, which are produced in a large number in the amplification region and drift back to the cathode. They stay much longer in the drift volume than electrons because of their larger mass (see eq. 2.5). This can lead to an accumulation of the positive charges which can result in electric field distortions. Depending on the chosen technology for the amplification different methods to avoid this effect are possible.They are discussed in sec. 2.5.2.

Experiment	Length (m)	Amplification Device	Number of Pads pro Anode	Gas	magnetic Field (T)
ALEPH [18]	2 x 2	Wires	41004	91% Ar 9% CH_4	1.5
DELPHI [36]	2 x 1.3	Wires	20160	80% Ar 20% CO_2	1.2
ALICE [37]		Wires		90% Ne 10% CO_2	?
STAR [20]	2 x 2	Wires	42000	90% Ar 10% CH_4	0.5
TESLA design [7]	2 x 2.5	GEMs Micromegas Wires	600000	93% Ar 5% CH_4 2% CO_2	4.0

Table 2.2: *Overview of various TPCs used in high energy physics detectors.*

2.5.1 Field Cage Design

The field cage normally fulfils a wide range of duties. The most important is to guarantee an electric field, which is as close as possible to the electric field of an infinitely large parallel-plate capacitor. This ensures minimum distortions of the reconstructed tracks. In the ideal case the walls of the TPC could be covered with a highly resistive material to achieve a linear gradient of the potential between anode and cathode. A good approximation can be achieved by covering the walls of the TPC with a large number of parallel conducting strips, which are perpendicular to the field lines and with identical distance between two strips. The cathode, the strips and the anode are connected by a chain of identical resistors and in this way create a nearly linear gradient of the potential. The use of conducting strips with an increasing potential, makes insulators between them unavoidable. Free charges may settle down on these insulators and disturb the electric field. To avoid this several solutions are possible:

Controlled conductivity of the insulator: When the insulator has a conductivity, which leads to an equilibrium between charge deposit and transport to the next electrode, the disturbing effects are reduced.

Retracted insulator surfaces: If the field cage strips have the form as shown in fig. 2.8 the electric field caused by the charge deposited on the insulator between two strips is damped by a factor of the order of $\exp\left(-\frac{\pi d}{s}\right)$ at the top of the strips.

Shielding electrodes: The use of a second layer of electrodes separated from the first one by a thin insulator as shown in fig. 2.8 also helps to reduce distortions. The best results are obtained, if the staggered strips are at an intermediate potential of the two pads.

Depending on the experimental environment the field cage has to satisfy a large number of further requirements. It should also work as a gas vessel, be mechanically stable and self supporting and it has to withstand the high potential difference between the conducting strips and the outer surface, which is of the order of several 10 kV around the cathode. But at the same time the field cage should have as less material as possible. An important quantity related to this point is the radiation length, which is the length by which the electron energy is reduced to $\frac{1}{e} \approx 37\%$. The typical radiation length of TPC field cages was in the past between 7 and 15%, while for modern TPCs at colliding experiments $\approx 3\%$ are desired.

2.5.2 Amplification Devices

It was already mentioned in a previous section that the TPC contains elements, which cause gas amplification. The proportional wires, which are widely used for this purpose, and the GEMs which are investigated in this thesis as an alternative are presented in more detail. An overview of Micromegas are given in [23].

Proportional Wires

Proportional wire chambers were first used in 1948 to detect particles [30]. They were and are used in many high energy experiments for the read out of drift chambers, but there are good reasons to look for alternatives for future experiments. Fig. 2.9 shows how a system of proportional wires as an amplification device in a TPC is build up.
It consists of three layers of wires. The one close to the anode is composed of the amplification and the field wires. At the amplification wires a positive potential is applied. The primary electrons from the drift volume follow the field lines to the wires, close to them the field strength is so high, that gas amplification sets in. This amplification process takes only approximatively 1 ns, then all electrons are collected

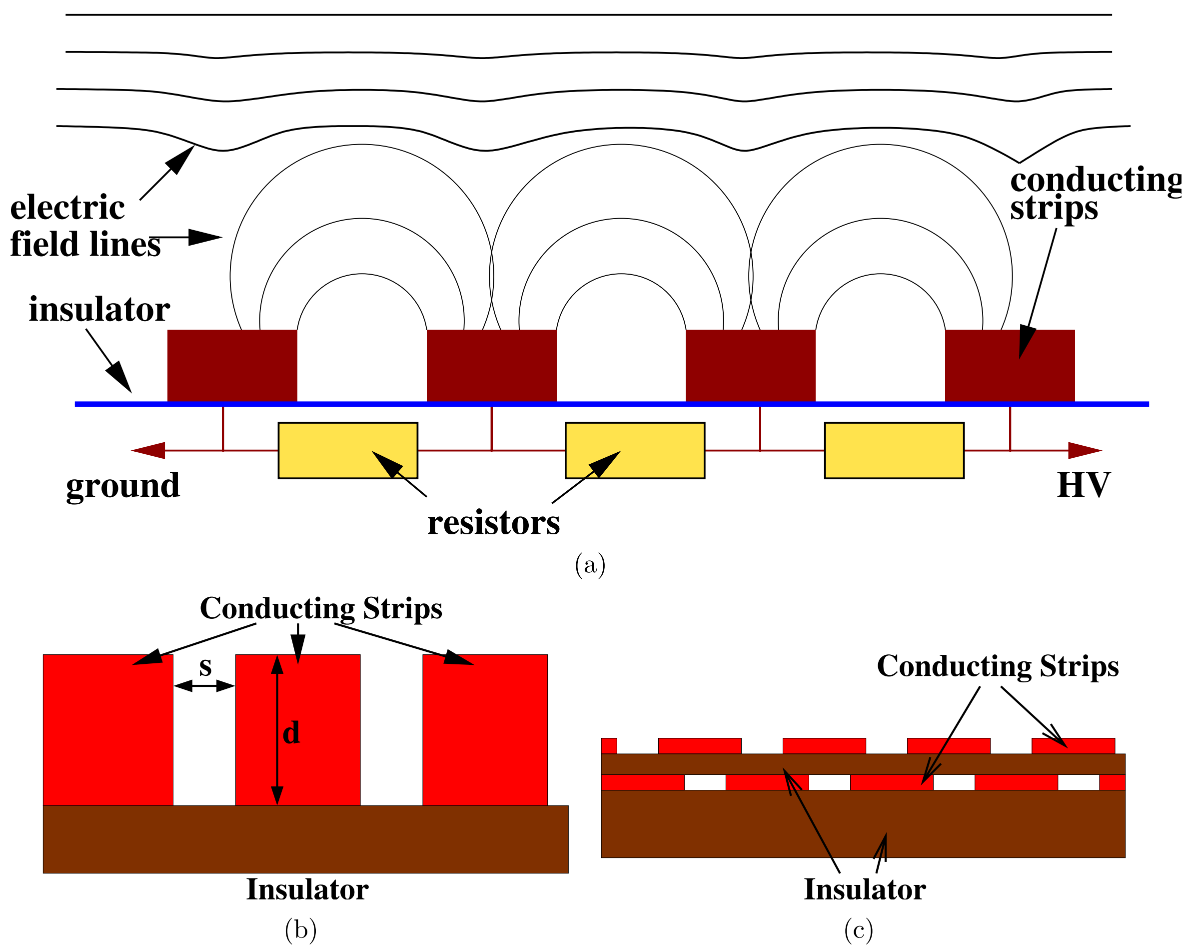

Figure 2.8: *(a) shows the basic principle of the field cage strips. The conducting strips are connected to each other via a resistor. The cathode is located on the right and the anode on the left. (b) illustrates the principle of the retracted insulator surfaces design. (c) is a schematic view of the shielding electrodes design.*

at the wires, while the positive ions start to drift towards the cathode. The change in the energy of the field by the drifting ions is the main component to the signal. Since the ion drift is very slow compared to electrons, the signal is quite long. The signal can be read out at the wires, but the achieved resolution can be improved, when also the signal induced on the anode plane is used. This signal is spread over several pads and allows a good coordinate reconstruction. The field wires are at a lower potential and have a larger diameter than the amplification wires, ensuring that no gas amplification occurs close to them. Their role is to stabilise the electric field. The second wire plane is the shielding plane, which conclude the drift volume. The plane next to the drift volume is the *gating plane*. It has the task to detain the ions, which are also created in the gas amplification process, from drifting back to the sensitive volume. When the gate is open, the applied potential is equivalent to the field potential, while when it is closed, the potential between two neighbouring wires of the gating plane is varied by $\pm(50-100)$ V. The gate is normally closed. With the help of external triggers, e.g. scintillators, it is decided, if a event fulfils the criteria to be interesting physics and the

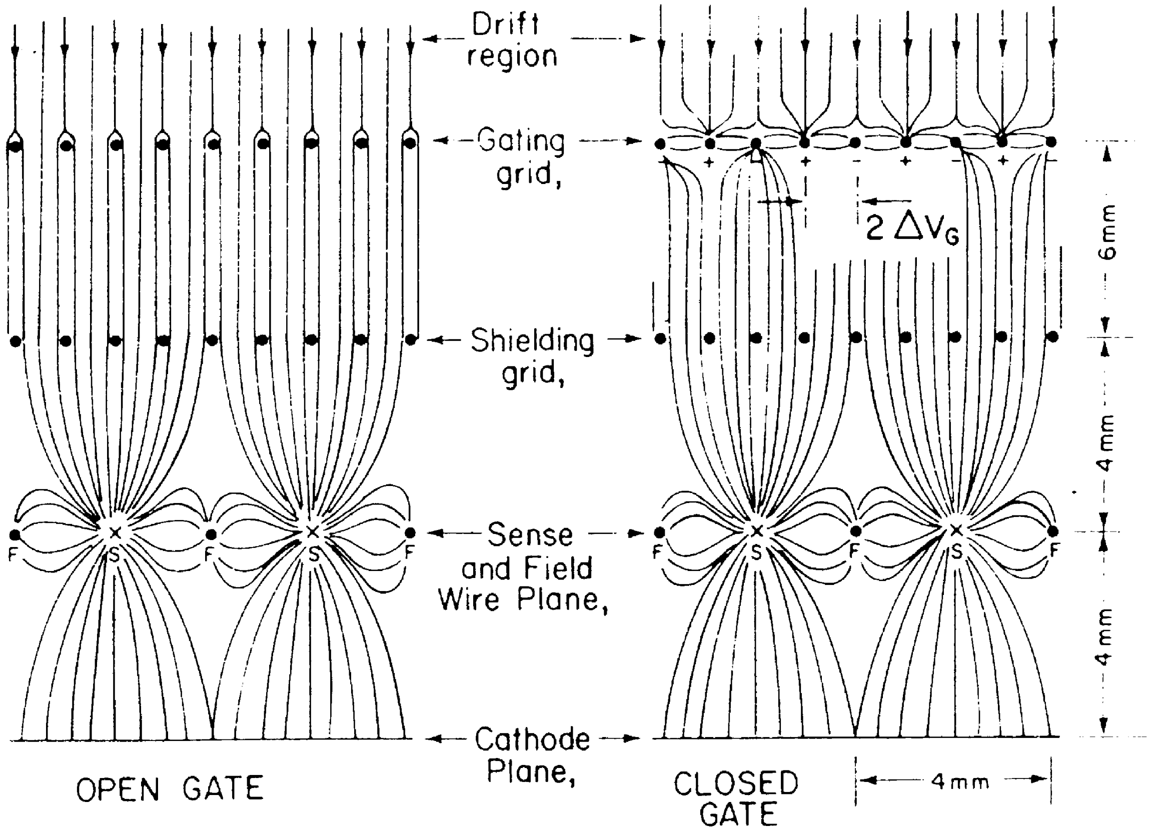

Figure 2.9: *Principle of the gating system in the case of a wire readout. Distribution of the electric field lines, if the gate is "opened" (left) and "closed" (right) [38].*

voltage on the gate is then accordingly applied.

Gas Electron Multiplier

GEMs were introduced the first time by F. Sauli in 1996 as an alternative to the wire amplification system. In the meantime they are not only used in high energy physics, but also in other fields, e.g. medical physics [39].
They consist of a thin Kapton foil coated on both sides with copper and perforated with a high density of holes. Due to the production process (etching) the holes have a double conical shape. A typical GEM has a thickness of 50 μm of the Kapton and 5 μm of the copper layer. The inner diameter of the holes is 55 μm and the outer 70 μm. The holes are arranged hexagonally with a pitch of 140 μm. To achieve a gas amplification with GEMs one has to apply a voltage of a few hundred volts between the two layers of copper. This has the consequence that outer field lines, which are created by the anode and cathode of the detector, are focused into the holes, where the field strength reaches values of the order of several 10 kV/cm, so that the electrons, following the field lines, are accelerated to energies above the ionisation energy of the gas. A positive property of GEMs regarding the suppression of back drifting ions is illustrated in fig. 2.10 (b). The optimisation of the ion feedback is and was the topic of various thesises and publications [40–43]. For the case in which the field between

the cathode and the upper GEM side is significantly lower than the field between the lower side of the GEM and the anode most of the field lines ends on the upper side of the GEM. From this directly follows that a large quantity of the ions, which follow the field lines quite tightly, are collected before they reach the drift volume. Also a part of the field lines end at the lower side of the GEM, so that not all of the electrons are read out at the anode. Because of this the *effective gain* is introduced, which is the ratio between the electrons measured at the anode and the primary ones. When in the following the gain is mentioned, the effective gain is denoted. With one GEM it is possible to archive a gain of up to 10^4, but for stability and flexibility it is useful to arrange the GEMs in a cascade of two or three GEMs at a lower voltage.

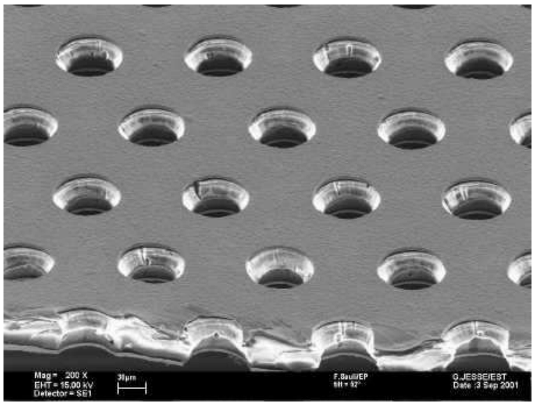

(a)

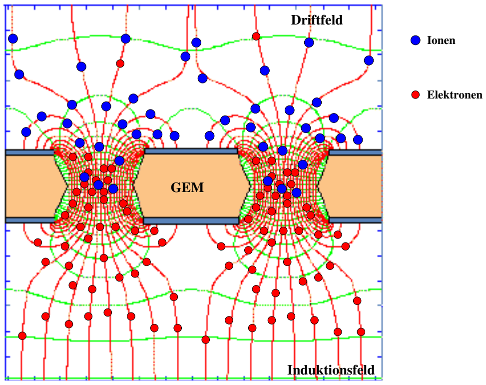

(b)

Figure 2.10: *Layout of a GEM: (a) picture taken with an electron microscope [44]. (b) schematic view which also illustrates the principle of the suppression of the ion feedback (as explained in the text).*

Beside of the intrinsic ion feedback suppression there are more differences between a GEM and a wire readout. A GEM readout uses the direct electron signal, which leads to a better time resolution. On the other hand, since the total number of readout channels are limited, most of the charge is collected on one or two pads in high magnetic fields. This degrades the resolution in the $r\phi$ plane. One solution for this, which is the topic of ongoing studies, is the use of special pad geometries. Fig. 2.11 shows the concept. While on *non-staggered* pads the charge cloud is almost always deposited on one pad, the use of *staggered* pads leads to a charge sharing between two neighbouring pads in every second row. This might be further improved by the use of *chevron* pads, by which a charge sharing in every row should be obtainable. Also, due to the fact that the pitch between the holes in the GEM foil are of the oder of μm, the region, where the electric field $\vec{E}$ and the magnetic field $\vec{B}$ are not parallel, is of the same order. Since, as mentioned in sec. 2.4.1, the motion of the electrons is also influenced by a magnetic field when $\vec{E}$ and $\vec{B}$ are not parallel, this leads to a decreasing of the point resolution. In the case of wires, which have in general a spacing of about a few mm, this effect is much more significant than for GEMs or Micromegas respectively.

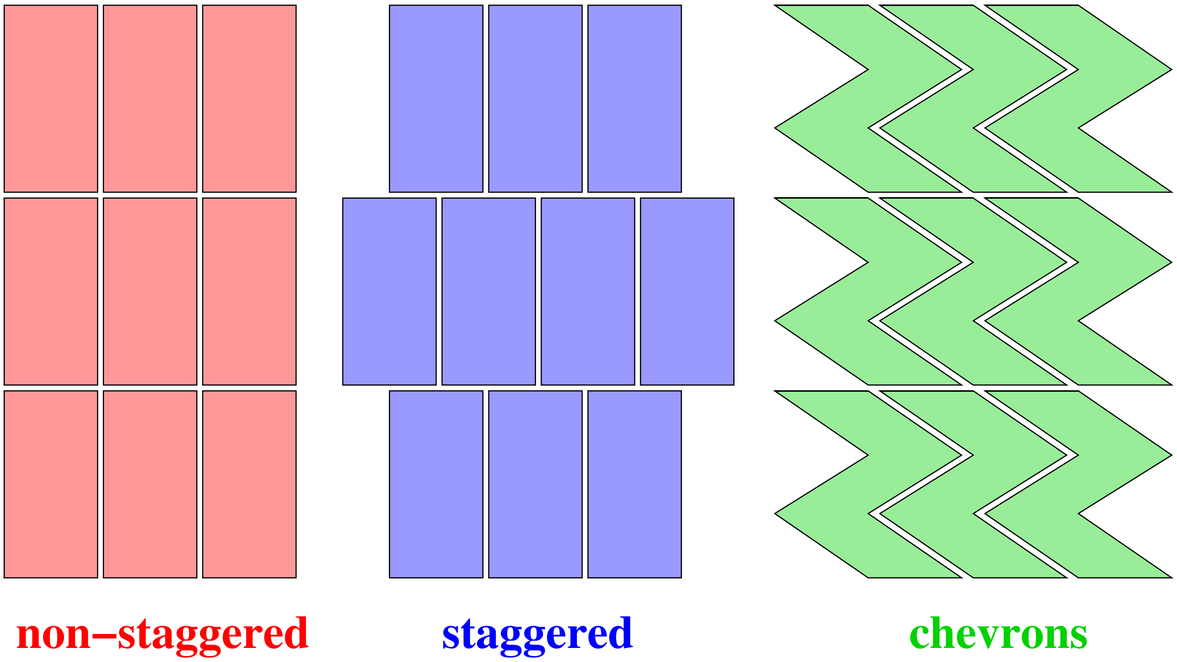

Figure 2.11: *Different possible pad geometries: non-staggered (left), staggered (middle) and one example for a alternative pad shape: chevrons (right).*

2.6 Coordinate Reconstruction limiting Factors

The precision of the track reconstruction is limited by various factors. The most important ones are the geometry of the amplification device and of the pads, the diffusion, the primary ionisation and the readout electronics.
The *Pad Response Function (PRF)* is also an important quantity for point resolution studies. This function gives the average signal height depending on the distance between the track and the middle of the pad. Fig. 2.12 shows the curve for different pad width Δ at a distance G of 4 mm between pads and signal wires. It is clearly visible, that $\Delta \gg G$ leads to a wide flat maximum, which does not allow a precise measurement of the point coordinate. For $\frac{\Delta}{G} \sim 2$ the PRF can be approximated by a Gaussian distribution:

$$P(x) = A \cdot \exp\left(-\frac{(x - x_i)^2}{2\sigma_{PRF}^2}\right) . \tag{2.17}$$

Here, P(x) is the pulse height, x_i the centre of the pad and x the position of the track. The width σ_{PRF} consists of two parts:

$$\sigma_{PRF} = \sqrt{\sigma_0^2 + \sigma_D^2} , \tag{2.18}$$

where σ_0 describes the defocusing within the amplification area, while σ_D is given by eq. 2.11. A further reduction of the pad width is limited by cost and by the fall off of the signal to noise ratio. The PRF of the direct electron signal within GEM amplification system is today a topic of ongoing studies [45, 46].
The transverse point resolution depends also on the number of primary ionisation n_t,

since the error σ_x on the average position is not given by eq. 2.11, but by

$$\sigma_x = \frac{\sigma_D}{\sqrt{n_t}} \tag{2.19}$$

The $r\phi$ point resolution is in addition governed by

- angular pad effects
- $\vec{E} \times \vec{B}$ effect
- signal to noise ratio of the readout electronic

The z coordinate is measured by the drift time of the primary electrons, so that statistical fluctuations has an influence of the longitudinal resolution. Apart from this the z resolution relies also on the longitudinal diffusion and strongly on the readout electronics (shaper, sampling rate, etc.) and therefore will not be considered further within this thesis.

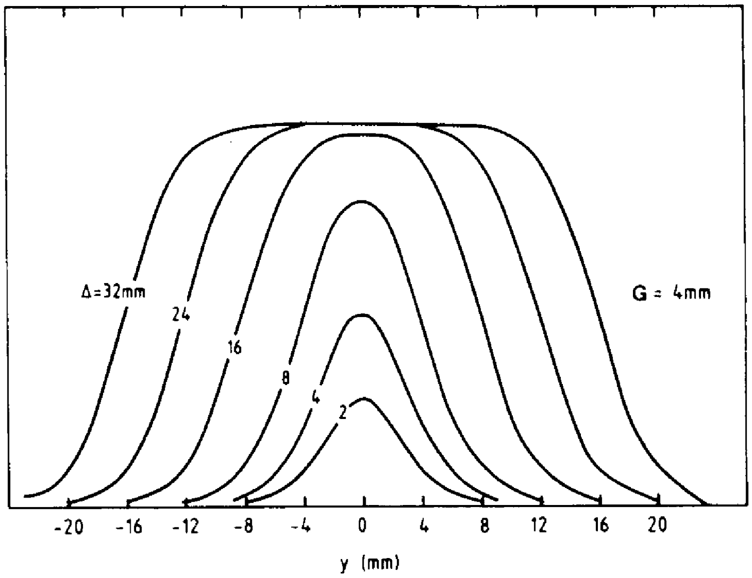

Figure 2.12: *Pad response functions for various pad widths Δ at a fixed distance G of 4 mm between wires and anode.*

Chapter 3

Experimental Setup

In this chapter the design of the TPC prototype is discussed. Furthermore the 5 T magnet, where the measurements were performed, is introduced.

3.1 TPC Prototype

The overall design choice of the TPC prototype was driven by the aim to measure the point resolution as a function of the drift length with different pad geometries. Furthermore a field cage, suitable for a large TPC at a Linear Collider, with a highly homogeneous electric field was desired.
A schematic view of the prototype is shown in fig. 3.1 and a technical drawing of it can be found in Appendix A. The chamber has a cylindrical form of length of 80 cm and

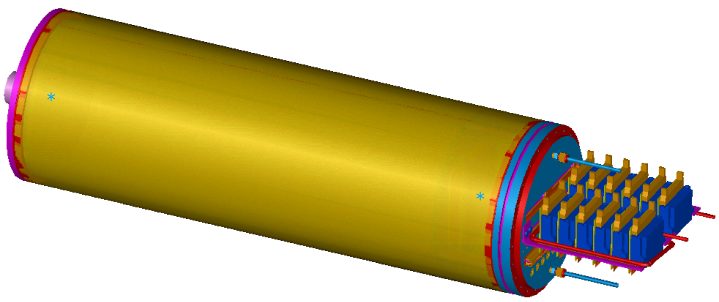

Figure 3.1: *CAD drawing of the TPC prototype.*

is completed by two endplates. The outer diameter of the prototype is 27 cm, driven by the inner diameter of the 5 T magnet of 28 cm. The sensitive volume itself has a length of 66.6 cm. The design parameters are summarised in tab. 3.1. On one side of the sensitive volume the cathode is located, consisting of a copper layer fixed to a G10 plate. This cathode structure is mounted via three support structures on one of the endplates. The other side of the sensitive volume is completed by the *GEM module* surrounded by the *shield*. The function of the shield is to ensure a homogeneous electric field in the sensitive volume, since the GEM module only covers a small part of the cross-sectional area of the chamber. The shield consists of a G10 layer coated with a

total length	80 cm
outer diameter	27 cm
inner diameter	25 cm
length of sensitive volume	66.6 cm
sensitive area	49.6×52.8 mm^2
number of readout channels	192

Table 3.1: *Design parameters of the TPC prototype.*

gold nickel alloy. The GEM module is fixed to the back of the shield, which allows a simpler alignment of the upper GEM surface with the shield surface. The shield again is fixed via three brass and Plexiglas support structures to an intermediate flange. The advantage of this system is, that the chamber can be opened, e.g. to control the HV cables in the case of HV problems, without exposing the GEMs to dust. The shield with GEM module is shown in fig. 3.2. On the cathode endplate the 30 kV HV connector

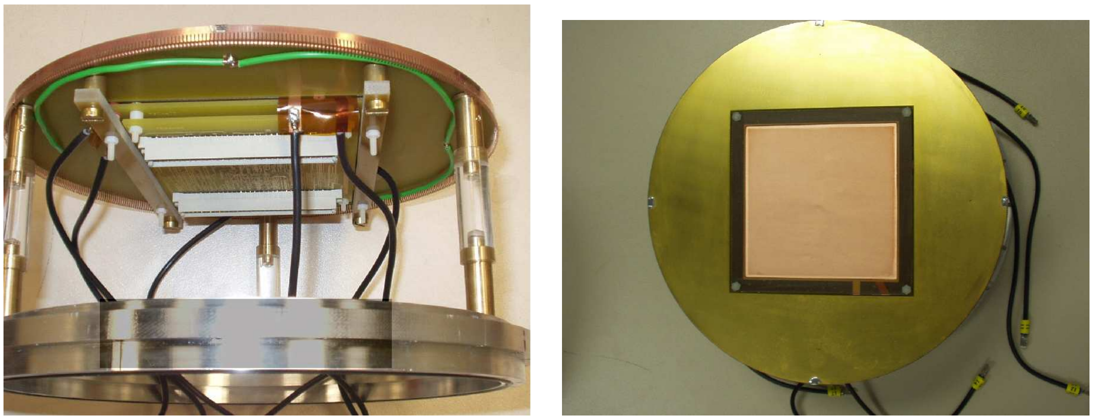

(a) (b)

Figure 3.2: *Shield: (a) from below (b) top view.*

is mounted and connected through a wire to the cathode. The electrical connection between the cathode and the resistor chain over the field cage strips is achieved by springs, which press against the last field cage strip when the cathode is inserted in the chamber. The advantage of this method compared to a soldered connection is, that the cathode can be easily removed and replaced by another one, which e.g. is optimised for laser measurements. There is of course the danger that sparks occur at the springs, which are at a potential of up-to 16 kV, but this was not observed. On the other side of the sensitive volume the shield is connected to the field cage in the same way. In the endplate close to the shield the connectors for the HV and the signal cables are mounted. Onto the endplate the preamplifier tower is fixed. Furthermore two openings for gas are incorporated within the shield endplate and one in the cathode endplate.
The coordinate system is defined in the following way x,y or respectively r,φ are laying in the plane parallel to the anode, while z or respectively θ goes along the chamber.
Fig. 3.3 shows different parts of the TPC prototype. In the following some parts of

the TPC prototype are discussed in more detail, those include the field cage, the GEM module and the gas.

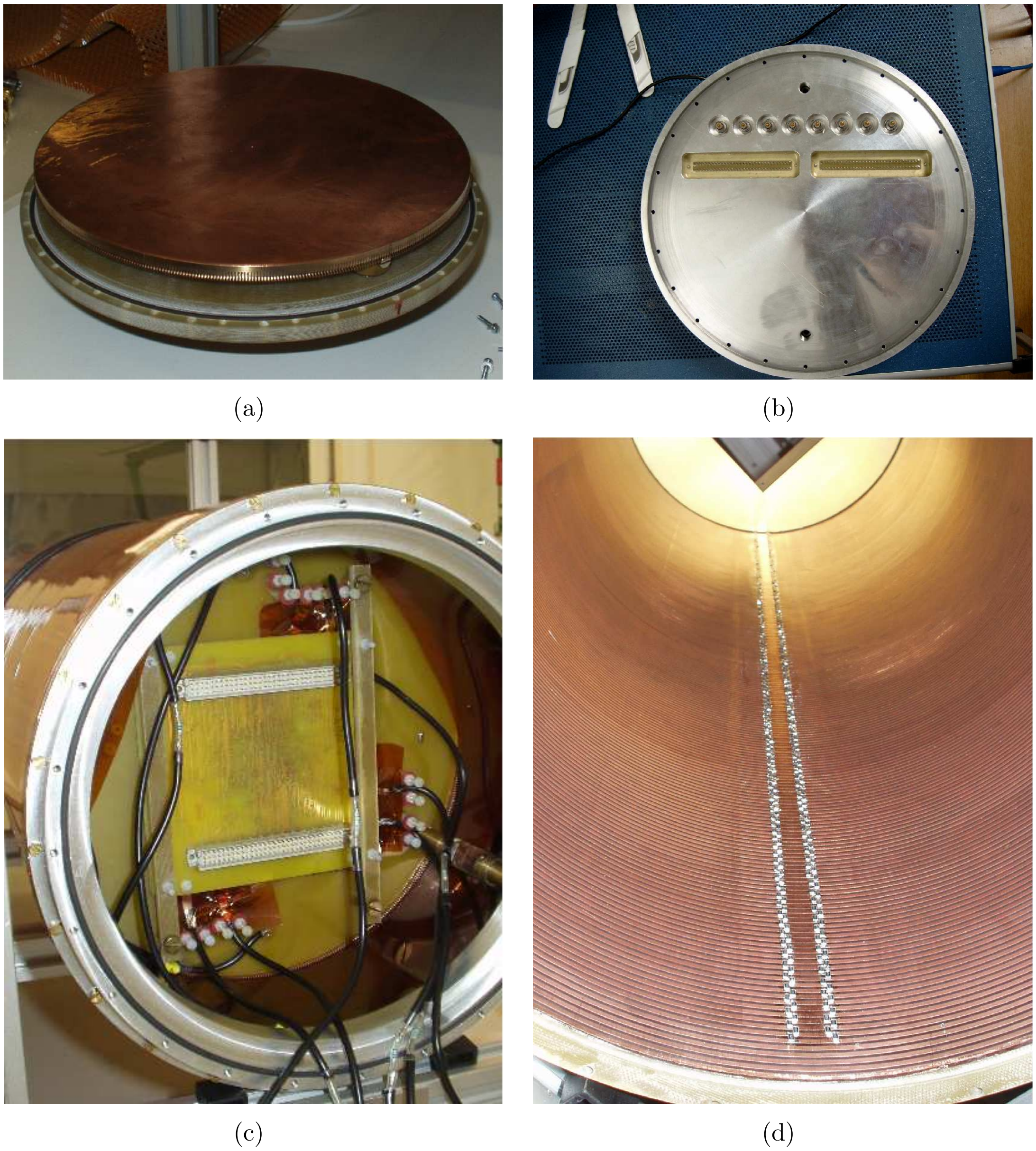

Figure 3.3: *Different parts of the prototype: (a) cathode of the chamber (b) endplate of the shield side (c) GEM module with shield (d) field cage strips with resistor chain.*

3.1.1 Field Cage

The aim was to build a stable and self supporting field cage, which at the same time should be as thin as possible. Additionally the field cage has to withstand the high electric gradient between the inner surface (at up-to 16 kV), and the outer surface, which is at ground. There are different approaches possible to achieve this [18, 20, 37]. For the TPC prototype a sandwich structure for field cage walls was chosen, which is similar to the structure used for ALEPH. Fig. 3.4 (a) shows the original design. The first inner layer is the Kapton foil coated on one side with copper strips, followed by three further layers of Kapton, a layer of carbon reinforced plastic (CFK) and a Nomex honeycomb structure. The field cage is completed in the radial direction by a second layer of CFK. In principle this CFK layer should act as an RF shield, but due to connection problems, a layer of aluminium or a copper coated Kapton foil respectively was later wrapped around the field cage. The final design of the prototype is shown in fig. 3.15.

HV Stability

As a first step, flat probes were built to test the HV stability, these consisted of the strip foil, the layers of Kapton and the first CFK layer. Fig. 3.5 (a) shows one of the probes. Afterwards one side of the probe was connected to up to 30 kV, while the other side was grounded. In a short term test no problems occurred, while in a long term tests a voltage breakdown after a few days was observed. The probe was thereby permanently destroyed. This behaviour might have been caused by the adjustment of the molecules within the dielectric. Fig. 3.5 shows the result of a spark. Therefore, the first layer of CFK was removed. This was also motivated by the results of simulations [47, 48], which indicate that a ground plane very close to the drift region disturbs the electric field inside the chamber. Afterwards the HV tests were continued with the structure shown in fig. 3.4 (b). This example withstood 10 days at 25 kV and 4 days at

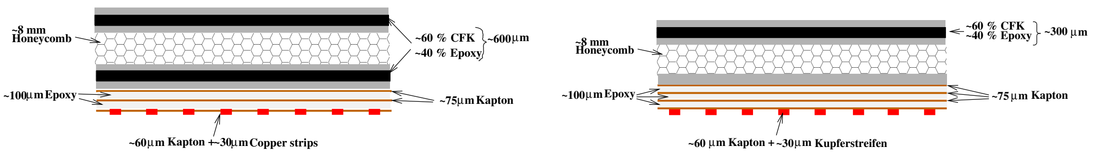

(a) (b)

Figure 3.4: *Field cage structure: (a) original design, (b) design used for the construction.*

29 kV before it was destroyed permanently due to a spark after 2 days at 30 kV. This was acceptable for the prototype and the chosen gas. Since it was planned to have the resistor chain inside the gas volume, a further HV test were performed. For this a small gas volume was constructed and an approximately 25 cm long probe was built. The field cage strips were connected via *Surface Mountable Device* (SMD) resistors. One end of this resistor chain was connected to 25-30 kV, while the other was connected to ground. Then it was tested for discharges at the edges of the SMD resistors, but none were observed.

Design of the Field Cage Strips and the Resistor Chain

Because of the limitation of the outer radius of the prototype the resistor chain between the strips was placed inside the gas volume. Furthermore the gradient between the cathode and the shield should be smooth. This implied the use of a large number of strips. The logical choice for the resistors were in this case SMD elements. This

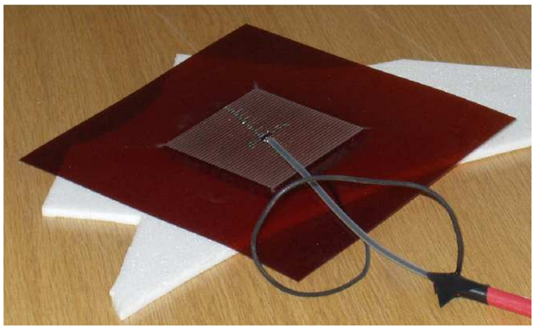

(a)

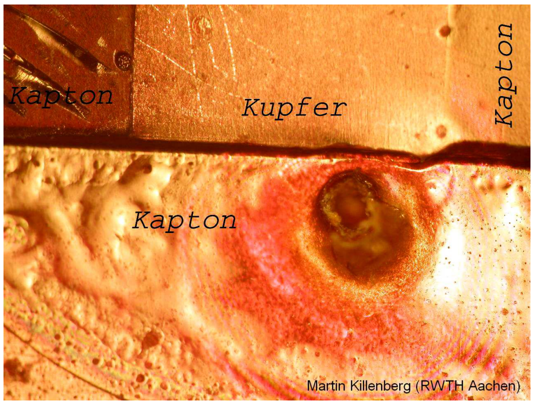

(b)

Figure 3.5: *(a) probe used for HV tests. (b) shows the result of a spark through the Kapton.*

also lead to the choice of the width and the pitch of the copper strips. The width is 1.6 mm and the pitch 2.8 mm. The resistors each have resistance of 810 kΩ. For reliability reasons not only one resistor chain was mounted, but four in parallel. This reduces the resistance between two strips to ≈ 200 kΩ. The total resistance between the shield and the cathode is therefore ≈ 50 MΩ over almost 250 strips. This value was confirmed by direct measurements. An important point to consider is the released power in the resistor chain. With a total resistance in the resistor chain of $R_{total} \approx 50$ MΩ and a operational potential difference of 13500 V between cathode and shield, the released power $P \approx 3.5$ W, which is not negligible. If the gas is taken as an ideal gas with $c_p = \frac{5}{2}R$ and it is assumed that the whole power is deposited in the gas, the gas temperature would change at a gas flow of $f = 13$ l/h of

$$\begin{aligned} \Delta T &= \frac{P\ [\frac{J}{s}] \cdot V_M\ [\frac{l}{Mol}] \cdot 3600\ [\frac{s}{h}]}{c_p\ [\frac{J}{K \cdot Mol}] \cdot f [\frac{l/h}{}]} \\ &= \frac{3.5\ [\frac{J}{s}] \cdot 22.4\ [\frac{l}{Mol}] \cdot 3600\ [\frac{s}{h}]}{\frac{5}{2} \cdot 8.31\ [\frac{J}{K \cdot Mol}] \cdot 13\ [\frac{l/h}{}]} \\ &\approx 1045^\circ\ K\ . \end{aligned} \tag{3.1}$$

Here, $V_M \approx 22.4$ l is the mol volume for a ideal gas. This is obviously an unrealistic value, which signifies that a large part of the energy transport is through the field cage and the endplates respectively. Since one should not underestimate this problem, a temperature measurement on the outer surface of the chamber was performed. The temperature sensors were aligned in two rows: one along the resistor chains and one with the maximal distance to them. It was observed, that the temperature raises within the first two hours until an equilibrium was reached. The sensors, which were not along the chains, shows a temperature increase of around 1° C. The difference to the sensors along the resistor chains was around 2° C. The interesting point was then, if a variation of the gas temperature could be observed within the pad area. The results of this study are presented in sec. 4.3.6.
Since only a small area in the middle of the chamber is read out for simplification

reasons it was resigned to use shielding electrodes (sec. 2.5.1).

Production of the Field Cage

As a first step the field cage strips were produced by etching from a Kapton foil coated with copper. A rotatable mandrel was build (fig. 3.6) and afterwards the foil was inversely mounted on the mandrel. The $\sim$ 1000 SMD resistors were then soldered manually to the strips. The foil was turned and the three further Kapton layers of 75 μm thickness, the honeycomb (8 mm) and the outer CFK layer (200 μm) were glued to each other step by step. As it turned out, in contrast to the flat examples, it was not possible to avoid air bubbles between the different layers. These air bubbles might reduce the maximum voltage able to be withstood by the walls, so that the operation voltage of the chamber was limited to 16 kV. Afterwards G10 rings were glued into the field cage. These contain the holes for the fixation of the intermediate flange and the endplates. Finally the intermediate flange and the endplates were aligned.

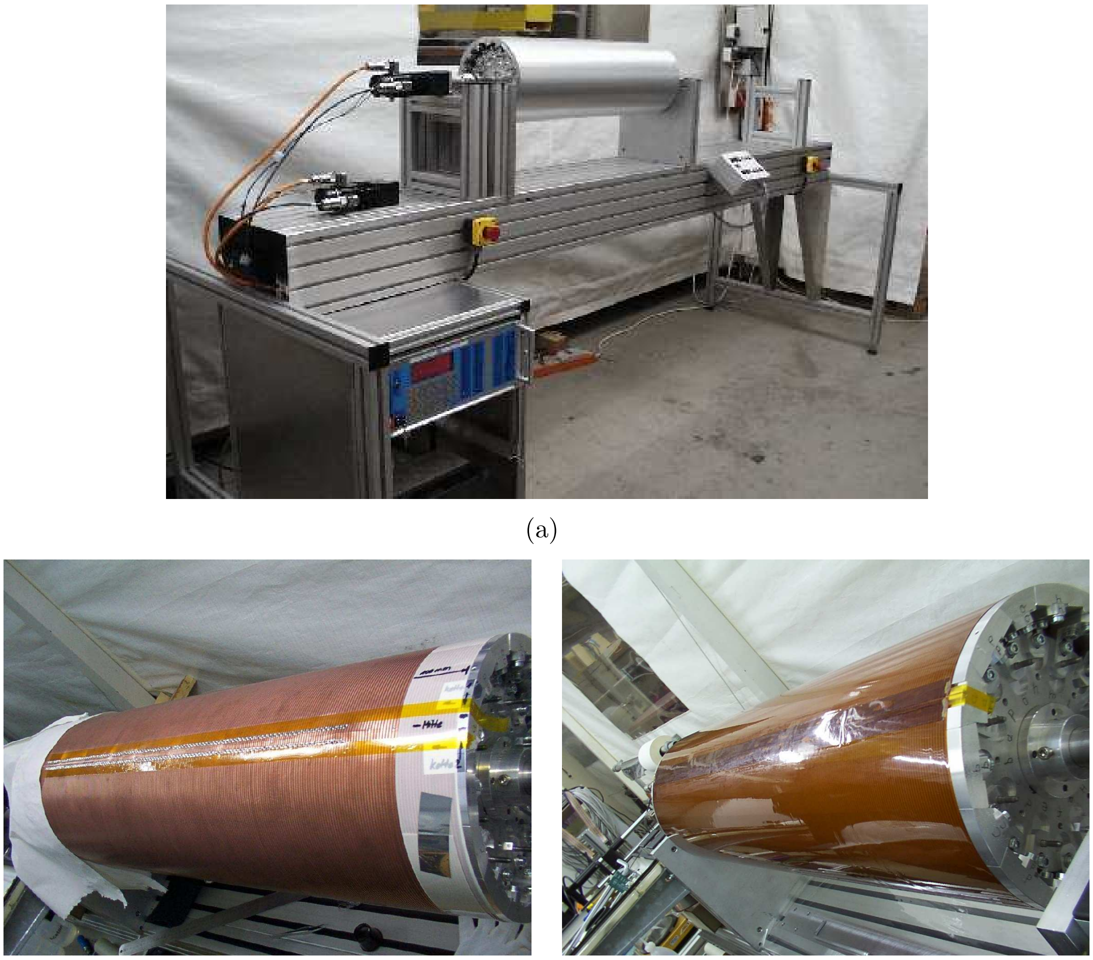

(a)

(b) (c)

Figure 3.6: *Production steps of the field cage: (a) the mandrel before the start of the production process, (b) during the soldering of the resistor chain, (c) after the three layers of Kapton were glued.*

Material	X_0 [cm]	d [μm]	X_0 [%]
CFK	18.8	200	0.11
Epoxy	19.4	1000	0.36
Kapton	25	275	0.09
Nomex Hexacomb	1430	8 mm	0.06
Copper	1.43	30	0.21
Sum			≈ 0.83

Table 3.2: *Material budget of the TPC prototype [1, 18, 49]*

Material Budget

The material budget of the field cage was calculated. Tab. 3.2 gives an overview of the materials used, their radiation length X_0 in cm, their thickness d and the relative radiation length X_0 in percent. A total radiation length of $\approx 0.8\%$ was achieved showing promise for the design aims of a TPC for a future linear collider.

3.1.2 GEM Module

The GEM module consists of a GEM tower with three 10×10 cm^2 standard GEMs from the CERN workshop and 2 printed circuit boards connected by SMD connectors. Fig. 3.7 shows a schematic view of the module. The electric field between two GEMs is called the *transfer field*, while the field between GEM1 and the pad plane is the *induction field*. The transfer gaps are 2 mm, while the induction gap is 3 mm. The field strength was chosen as 1.5 kV/cm for the transfer fields and 3 kV/cm for the induction field. The values are based on experience from the successful operation of previous setups. On PCB2 the pads are coated, while on PCB2 the signal wires are grouped to simplify the pad mapping. Finally the signal were directed out the chamber via two 96 pin connectors.

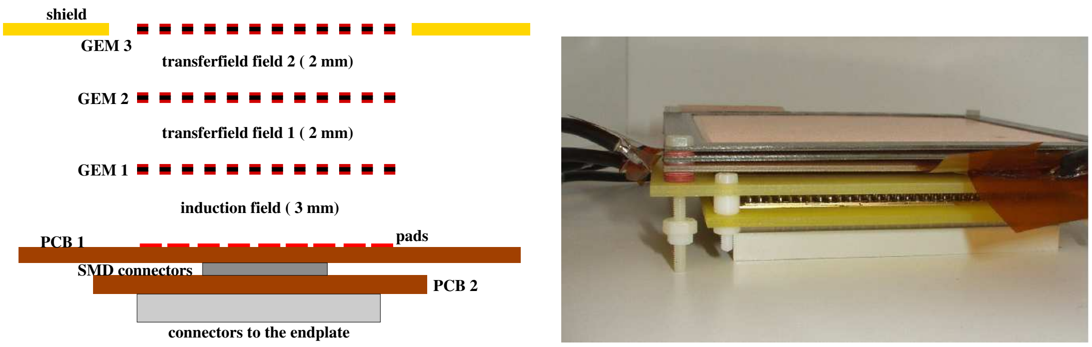

(a) (b)

Figure 3.7: *(a) schematic view of the GEM module. (b) photo.*

Pad Geometry

For the measurements two different pad geometries were used: non-staggered and staggered pads (see sec. 2.5.2). From the point of R&D they represent two extreme cases which appear in a full size TPC. In such a TPC the pads are arranged in a way, that they point towards the interaction point. As a consequence the geometry of the pad plane will be neither purely non-staggered nor purely staggered with a shift of half of the pitch between two pads. Therefore, the goal has to be to achieve results which agree for both pad geometries. This ensures that conclusion can be drawn which are also valid for the full size TPC.
The pad geometries used for the measurements are both based on rectangular conducting areas. These have a length of 6 mm and a width of 2 mm. The distance between two pads is 0.2 mm, so that the effective size of a pad is 6.2×2.2 mm^2. The values are mainly driven from simulations performed for the TESLA TDR [17]. 192 pads are read out, which are arranged in 8 rows and 24 columns. The *effective readout area* is therefore 49.6×52.8 mm^2, so that only a part of the GEM area of 10×10 cm^2 is covered. The remaining area is covered by a large outer plane and two lines of pads. These pads are connected via resistors of 100 kΩ or 150 kΩ respectively to the outer plane (fig. 4.6). The outer plane has the purpose of guaranty a homogeneous induction field, while the two lines of pads together with the resistors should avoid cross talk with the first line of the read out pads. This design is not optimal, as is discussed in sec. 4.3.2. A view of the pad plane with staggered pads is shown in fig. 3.8.

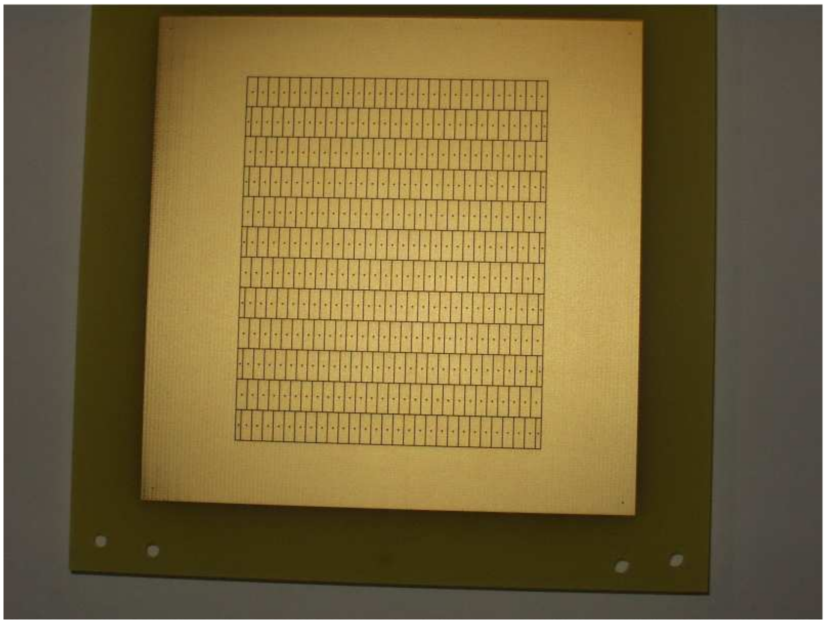

Figure 3.8: *Photo of the pad plane. The picture shows the pad plane with staggered pads. The coated region has a size of* 10×10 *cm*^{2}.

3.1.3 HV supply

Two independent HV power supplies are used to operate the TPC prototype. A power supply yielding up-to 35 kV is used to supply the cathode together with the field

cage strips and the shield with HV. To supply the GEM module with HV a multi-channel HV power supply (CAEN 127) is used. Each GEM surface was independently connected to a channel of the power supply. This setup has the advantage, that the settings of the various fields and the voltages over the different GEMs can be easily adjusted. In front of each GEM surface a 10 MΩ protection resistor is placed. This reduces the probability, that the GEM is permanently damaged due to a discharge. Without this limitation of the discharge current, a spark might release enough energy to burn a carbon tunnel or to melt the copper, which then flows into the holes and produces a permanent connection with a resistance between a few Ω and ≈ 100 MΩ between both sides of a GEM. In this case the GEM has to be replaced. It seems, that the position of this protection resistor is not arbitrary, but should be placed as close as possible to the GEM surface. A more detailed discussion of this point can be found in [50]. As a further protection mechanism the HV power supply was set, so that in case of a discharge with a current above a certain threshold the HV was switched off and automatically slowly ramped up again. For this the control system of TPC RWTH Aachen group was used.
An important point is, that the potential on shield and the GEM surface pointing to the drift volume have to be at the same potential U_{GS}. To ensure this a variable resistor R_s was placed between the shield and ground. The value of R_s is calculated by:

$$R_s = \frac{U_{GS}}{U_c - U_{GS}} \cdot R_{cage} \ . \tag{3.2}$$

Here, R_{cage} is the total resistance of the field cage and U_c the voltage at the cathode.

3.1.4 Gas

The chamber was operated with two different gas mixtures. One gas mixture, which is referred to as *TDR gas* consists of 93% argon, 5% CH_4 and 2% CO_2 and was optimised for the experimental conditions at the planned TESLA collider [51].
For reference measurements also a second gas mixture consisting of 95% argon and 5% CH_4 (*P5 gas*) was used. In fig. 3.9 one can see the differences between these gases in drift velocity and transverse diffusion.

3.1.5 Data Acquisition System

For the readout a data acquisition system (DAQ) based on well established electronics used at the ALEPH TPC at LEP [18] were adapted [52]. This readout system is based on a *Flash Analog Digital Converter* (FADC) system. Each of the 192 pads in the TPC is connected to one of the twelve preamplifiers, which integrates the charge deposited on the pad and converts it into a voltage signal. The integration time constant of the preamplifiers is 2 μs. The output signal from the preamplifier is sent to a digitising unit, *Time Projection Digitisation* (TPC), via a twisted pair cable. The digitiser consists of a receiver/shaper, followed by a 8 bit FADC. The sampling speed is 12.5 MHz and it has storage depth of 512 time slices (≈ 41 μs). The digitised information is written into a memory bank. The FASTBUS crate, which contains the TPDs, is controlled and read out through a VME based CPU (*Fast Intelligent Controller* (FIC 8234)) which

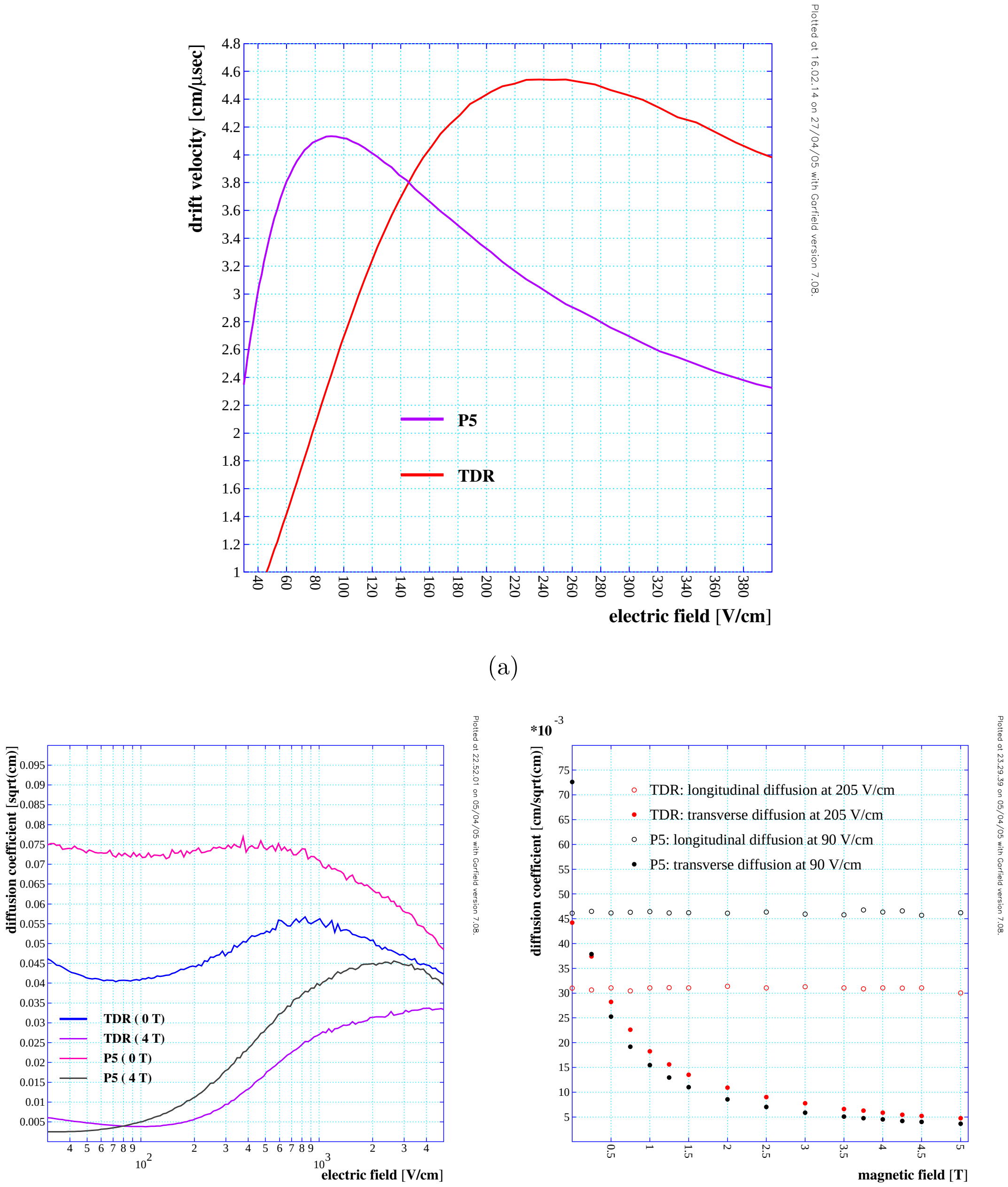

(a)

(b) (c)

Figure 3.9: *Comparison of TDR and P5 gas: (a) drift velocity as a function of the applied electric field. (b) dependence of the transverse diffusion coefficient on the electric field applied. (c) longitudinal and transverse diffusion coefficient as a function of the magnetic field applied.*

acts like a master to a FASTBUS-VSB-Interface (FVSBI 9210), which is the slave. The complete system is steered by an external computer, running under SUSE linux 7.3. Fig. 3.10 shows the basic system. In order to minimise the load of the FIC CPU and to keep the data transfer through the slow TCP connection as low as possible, a server client approach was chosen for the data handling. The data processed by the FIC CPU are sent via a TCP connection to the server, which is running on the linux PC. The server has the ability to forward the data to several other clients, that are connected to it. One client has been implemented to dump the data in a LCIO (*Linear Collider Input Output*) file [53, 54]. For the future it is planned to implement also a client for the online monitoring of the data.

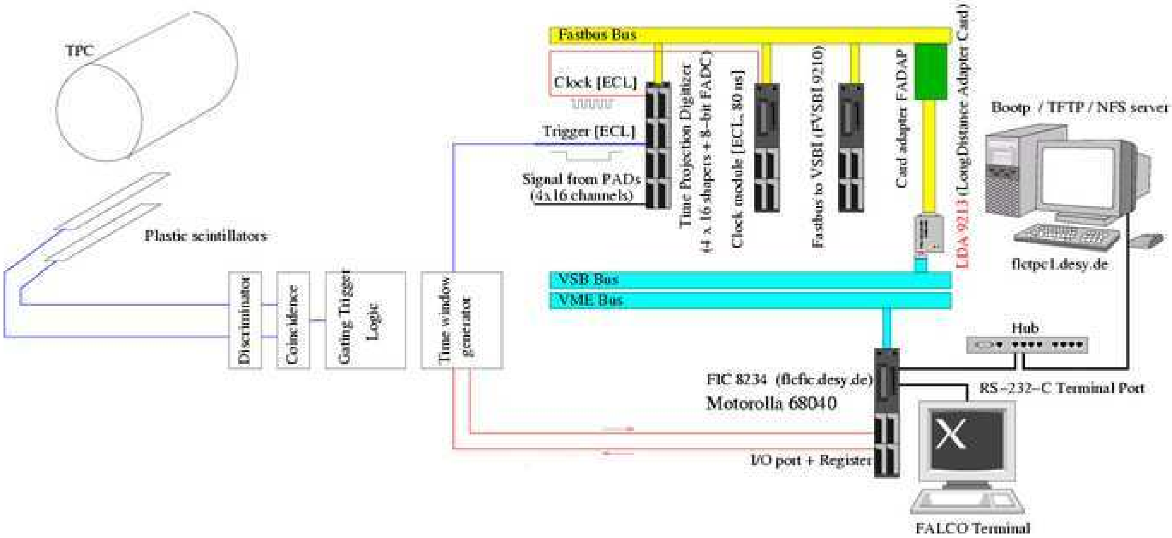

Figure 3.10: *Sketch of the DAQ system.*

3.2 High Magnetic Test Facility

A superconducting solenoid magnet with a large aperture has been set up as a high field test facility for the detector development for a future linear collider. The magnet can be operated at currents of up-to 1000 A corresponding to a magnetic field of 5.25 T. The coil has a length of 1.2 m and consists out diameter of 5083 turns arranged in 18 layers. The surrounding cryostat has a length of 1.86 m and an inner diameter of 28 cm and an outer of 104 cm. The calibration curve was measured using several NMR probes. Fig. 3.11 shows the result of the measurement in the centre of the coil. Unfortunately the produced field is not absolutely homogeneous. Fig. 3.12 shows the magnetic field along the magnet. Apart of an extensive electrical and network infrastructure a cosmic trigger system was installed by the TPC group of the RWTH Aachen. It consists of two scintillators, which are installed above and below the cryostat as shown in fig. 3.13. Here, the problem of this setup is also clearly visible. Because of the Helium supply the scintillators can not be centred according to the coil. To also obtain tracks at short drift distances, the prototype was not positioned in the centre of the coil, but so that the start of the sensitive volume was concordant with the end of the scintillators.

3.3 Cosmic Radiation

During R&D of particle detectors cosmic radiation is often used as a natural source of ionising radiation. It has its origin partly in solar flares and partly outside the solar

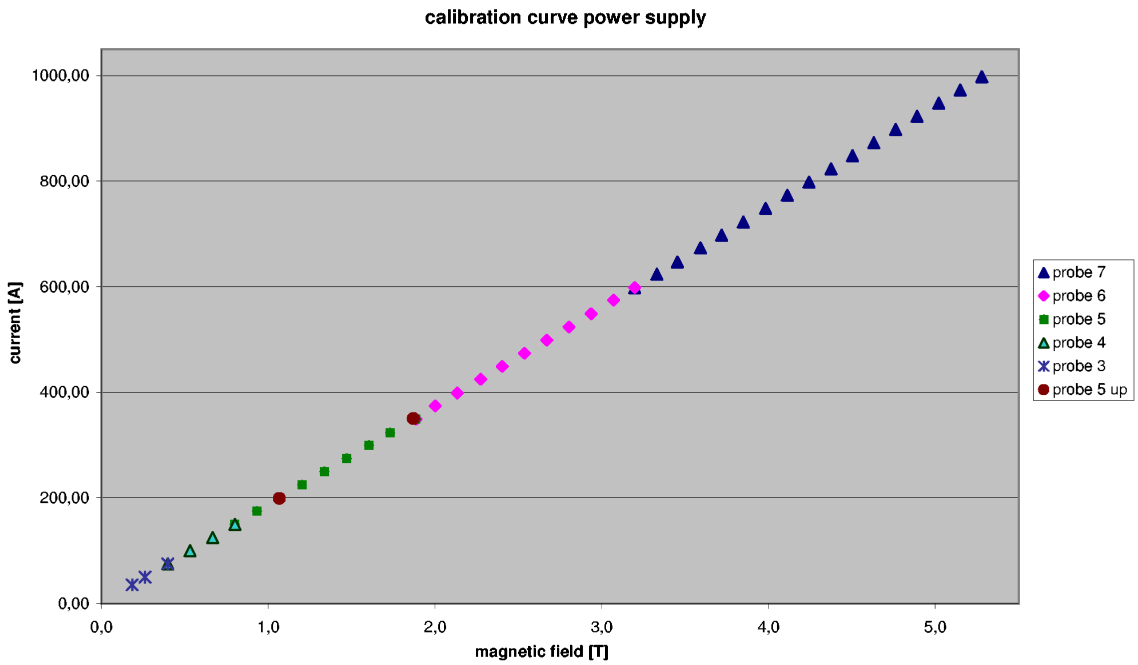

Figure 3.11: *Dependence of the current measured at the power supply and the magnetic field. The curve was measured using several NMR probes.*

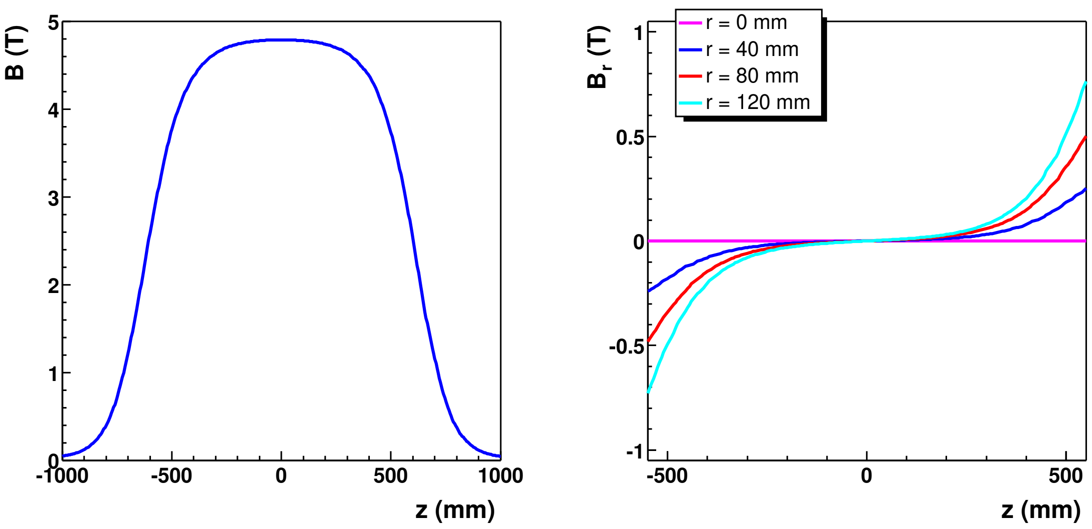

Figure 3.12: *Distribution of the magnetic field: longitudinal (left) and radial (right) [55].*

system, e.g. in Supernovas and consists of all particles which have a lifetime above 10^6 years. However, this primary cosmic radiation does not reaches the surface of the earth, but mostly interacts with the atmosphere producing short lived mesons. It is the decay product, mostly muons, of the mesons which reach ground level. The energy

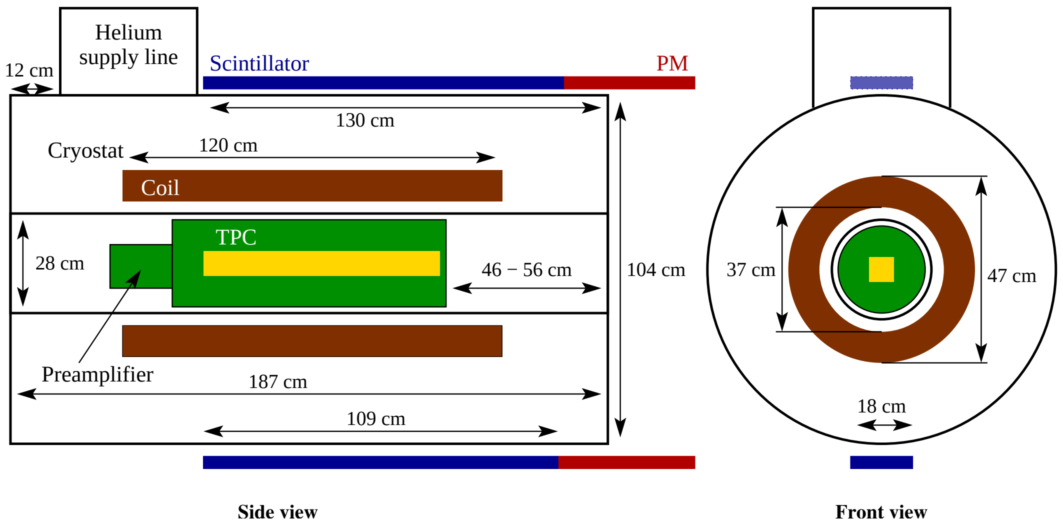

Figure 3.13: *Dimensions of the 5 T magnet and positioning of the TPC prototype in the magnet [50].*

spectrum of the muons has a mean value of 4 GeV with a steep falling slope for higher energies. The angular distribution depends on the energy of the muons. For muons with 3 GeV the distribution is well described by $\approx \cos^2 \Theta$ [1]. For other energies it can be described by a polynomial [56]. The momentum spectrum of cosmic muons at sea level for two different θ angles is shown in fig. 3.14

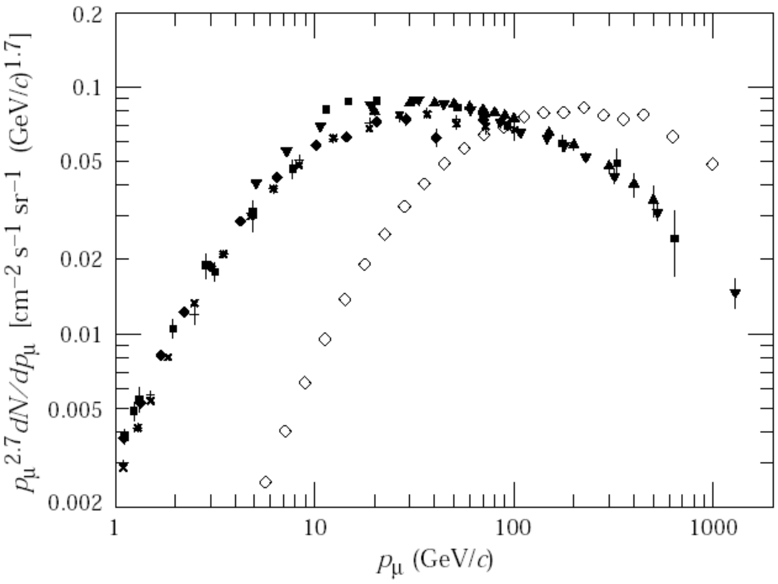

Figure 3.14: *Momentum spectrum of cosmic muons at $\theta = 0°$ (solid markers) at $\theta = 75°$ (open markers). Both distributions were measured at sea level [1].*

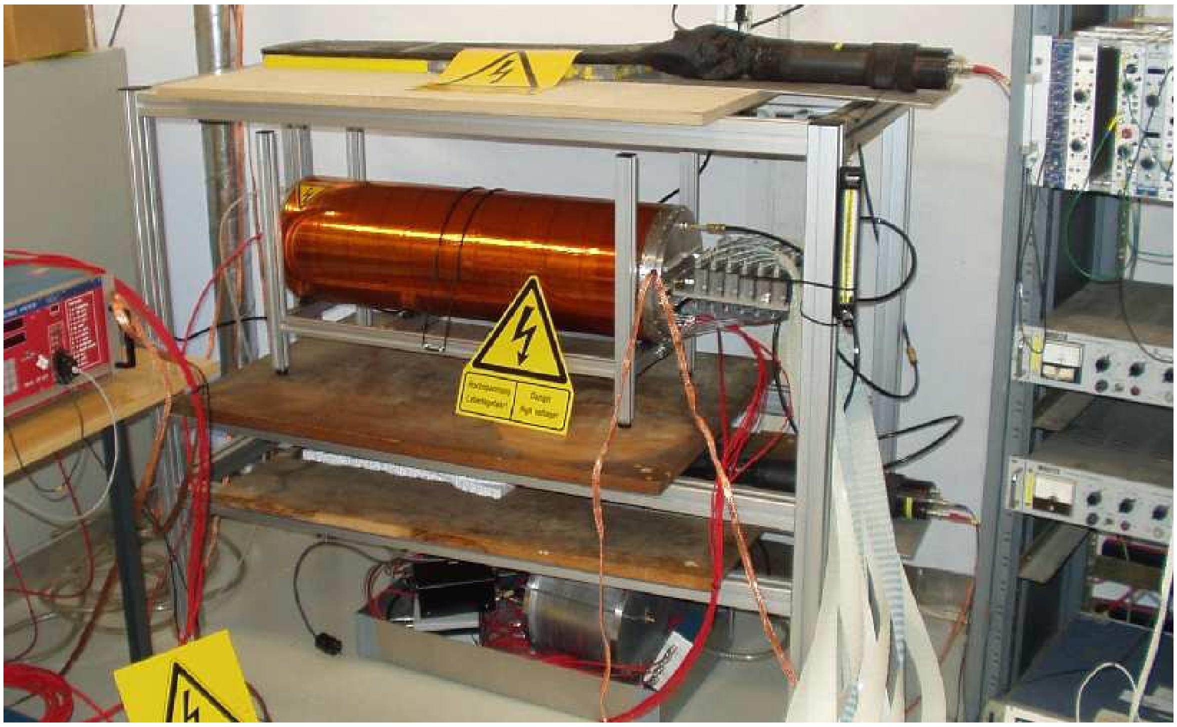

Figure 3.15: *Final design of the TPC prototype.*

Chapter 4

Performance Studies

In this chapter first the basics of the reconstruction and analysis software are introduced. That is followed by an overview of the used data sample, before measurements concerning the performance of the setup are presented.

4.1 Reconstruction and Analysis Software

The data taken with the DAQ system (sec. 3.1.5) is stored as raw data in the LCIO format. As a topic of a diploma thesis [50] the program package *MultiFit* was developed to reconstruct the tracks of the charged particles. The reconstructed data was afterwards analysed using the framework of ROOT [57].

4.1.1 MultiFit

The program packages *MultiFit* is written in C++ and consists of three independent modules: the *ClusterFinder*, the *TrackFinder* and the *TrackFitter module*. In the following a short overview of the modules is given. Fig. 4.1 illustrates the basic principle of the program. The used version is an improved version of the program developed within a diploma thesis [50]. A more detailed description of the basics of the program can be found there.

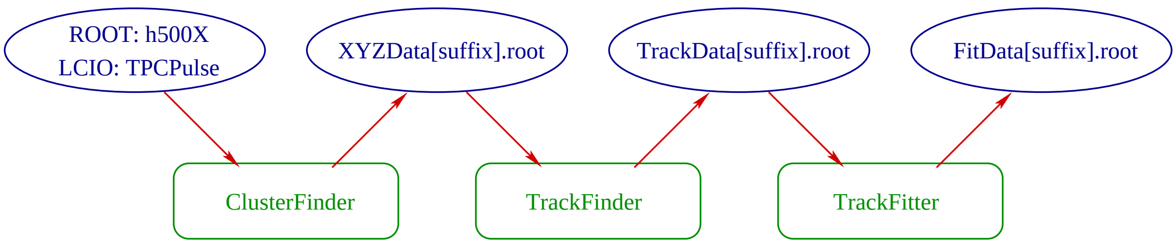

Figure 4.1: *Working principle of the MultiFit program package*

ClusterFinder

The ClusterFinder reads in the data stored from the DAQ system in the LCIO format. The ClusterFinder then uses the ADC information of the deposited charge, the time

bins and the channel number to reconstruct the three dimensional *hits* (also referred to as *points*). As a first step every channel number is assigned to a pad. The assignment is achieved via a steering file. This file also contains information about the pedestal for each channel and the pad geometry, including the arrangement of the pads, their width and length and the gap between two pads. Furthermore, also the length of the time bins and the drift velocity are given in the steering file. This information is required for the conversion of the drift time information to a z coordinate.
The reconstruction of the three dimensional hits is done row by row assuming that the tracks are transversing the chamber only along the long side of the pads (from the top). For cosmic muons this is a valid assumption. The algorithm used is called *HitMerge method*. It determines the hit coordinates in two steps: first it investigates the ADC spectrum for each pad alone searching for signals (*pulses*). A pulse is identified if the ADC value in a time bin i is above a certain threshold, which depends on the noise level in the data sample. All $i + n$ time bins for which the condition that their ADC values are above the threshold is fulfilled are merged into the pulse. For each pulse the total charge is calculated. Furthermore for each pulse the time information corresponding to the mean of the rising edge of the ADC spectrum is determined. In a second step the single pulses are combined into hits taking into account their spatial and time vicinity and the total charge of the pulses. As a starting point the pulse with the largest total charge is taken. Then the neighbouring pulses are investigated: if their total charge is below the total charge of the starting pulse, they are merged with the hit. Afterwards the iteration is repeated starting with the last added pulses until there are no more pulses with smaller total charge in the vicinity. Additionally the pulses have to lie inside of a time window around the pulse with the largest total charge. The algorithm takes into account variations of the pulse charge due to statistical fluctuations of the primary ionisation and damaged channels.
Afterwards the three dimensional coordinate for each hit is calculated. The y coordinate is taken as the centre of the row, while x is calculated from the centre-of-gravity of the total charge of the pulses. The time information for each pulse is converted to a z coordinate. The conversion factor corresponds to the drift velocity which is given in the steering file. The z coordinate of the hit is afterwards calculated as the charge weighted mean of the z coordinates of the single pulses. As an output the information related to the various hits are stored in a ROOT file.

TrackFinder

The TrackFinder module takes as input the output file from the ClusterFinder and searches for tracks using the hit information stored from the ClusterFinder module. It is assumed, that the tracks enter the chamber from the top and that the tracks can be approximated by a straight trajectory. The basic principle of the algorithm is the following: First two hits with a suitable minimum distance in y are used to initialise the algorithm and tracks are fitted to these hits in the xy and yz plane. Using this as a starting point the most probable position of a hit in the row below the top row is calculated. If a hit is found in a defined search window around this position, the hit is combined into the track, the track parameters are again calculated and the algorithm proceeds with the next row. In the case that more than one hit is found in the search window, only the hit yielding the smallest χ^2 of the fit is added. If no hit is found in the search window, the row is left out and the TrackFinder continues with the next row. When the lowest row is reached, the search is continued upwards in the rows where not yet hits were found. After reaching the top row the algorithm starts again searching for further tracks. In this second cycle only hits are considered which were not already combined into a track. Finally all information about such tracks, which pass the cut on the maximum number of rows left out and also a quality cut on the corresponding fit are stored in a ROOT file.

TrackFitter

The information about the hits combined into tracks are used by the TrackFitter module to perform the final fit. For this purpose both straight and curved fits can be used according to the flag set in the steering file. The following implementations are available:

ChiSquared: In the xy and independently thereof in the yz plane a straight line is fitted to the points using an analytic χ^2 minimisation and the x and z axis intercept and the slopes are calculated.

ChiSquaredRoot: Similar to the ChiSquared method, but using the ROOT libraries. The χ^2 is in this case minimised numerically.

ChiSquaredCurved: This method takes the curvature of the trajectory in the xy plane due to a magnetic field into account. Like for the ChiSquaredRoot method the program package ROOT is used. In the xy plane a circular arc is fitted to the hits, while in the xz plane a straight line fit is used.

At the moment the pad response function as mentioned in sec. 2.6 is not considered in these methods.
An additional feature of MultiFit is the graphical interface, which allows at any point the visual inspection of the results of the different modules. The fig. 4.2 shows for one event the graphical output of the TrackFinder module.

4.1.2 Analysis Software

The data as stored from the program MultiFit was afterwards investigated using the features of the ROOT framework. To investigate the various aspects of the data in each case an appropriate ROOT script was developed.

4.2 Data Sample

With the experimental setup as described in Chapter 3 various measurement series were taken between February 2004 and January 2005. Each of these measurement series were divided in several *runs*, which are data taking periods without changes e.g. in the applied GEM voltages. New runs were also started after technical problems e.g. network problems, so that some runs with equal electric and magnetic field settings

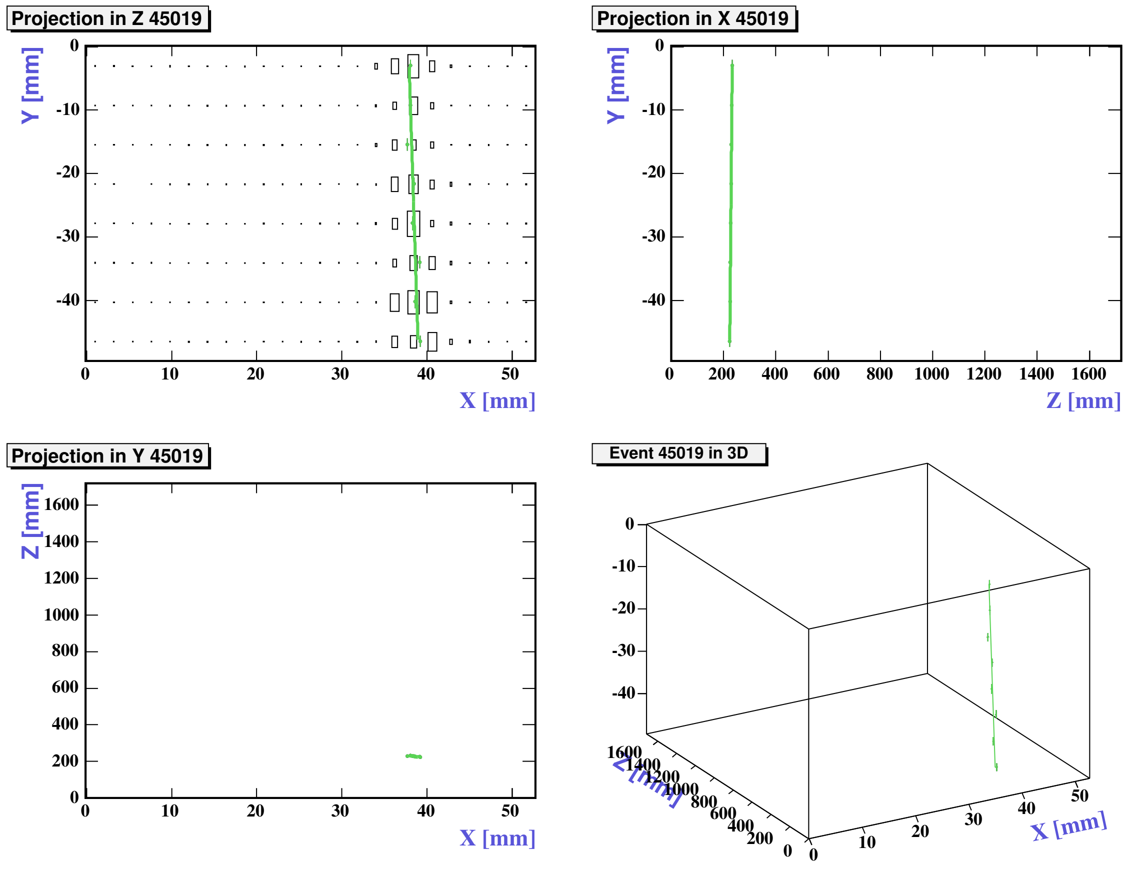

Figure 4.2: *Graphical output of the TrackFinder module. Shown is a typical event at 0 T.*

were afterwards combined into *analysis runs*. An overview of the different analysis runs is given in tab. 4.1. The data was reconstructed using mainly the ChiSquared method which is approbate for the performance studies and the chosen method to determine the point resolution.

4.3 Performance Studies

Before reliable point resolution studies were possible, the behaviour of the chamber had to be understood. For this several different studies were performed. First the distribution of the points in the chamber and the ϕ and θ distributions of the tracks were investigated. Also the working performance of the pad plane was studied including the pulse shape and the number of pulses for each pad, and the field homogeneity was tested. Since the drift velocity is required for the conversion from time information to a spatial coordinate also the time dependence of the drift velocity was studied. Another important point was the stability of the gain both spatial and in time. In addition the stability of the GEM concerning discharges was investigated. The data analysis was performed in two steps: first the data was reconstructed using standard settings for the MultiFit program. Then the pads which were not working properly were determined

pads: non-staggered				gas: TDR		
analysis run	runs	B (T)	drift field (V/cm)	GEM1/2/3 (V)	induction field (kV/cm)	transfer field (kV/cm)
A	12	0	203	335	3.0	1.5
B	13	1	203	335	3.0	1.5
C	17	4	203	325	3.0	1.5
pads: staggered				gas: TDR		
analysis run	runs	B (T)	drift field (V/cm)	GEM1/2/3 (V)	induction field (kV/cm)	transfer field (kV/cm)
D	6	0	203	330	3.0	1.5
E	7,8	1	203	325	3.0	1.5
F	9	2	203	320	3.0	1.5
G	3	4	203	320	3.0	1.5
pads: staggered				gas: P5		
analysis run	runs	B (T)	drift field (V/cm)	GEM1/2/3 (V)	induction field (kV/cm)	transfer field (kV/cm)
H	9,10,11	0	91	335/340/340	3.0	1.5
I	6,7,8	1	92	330	3.0	1.5
J	5	2	92	325	3.0	1.5
K	2,3,4	4	92	325	3.0	1.5

Table 4.1: *Overview of the analysis runs.*

and the drift velocity was calculated. Afterwards the reconstruction was rerun using the information gained through the first analysis of the data.

4.3.1 Hit and Track Distributions

The distributions of the hits as given by the ClusterFinder module in x,y and z are shown in fig. 4.3. It is noticeable, that the x distributions has a flat plateau in the middle and shows significant increases at the edges. An explanation for this behaviour is given in sec. 4.3.2. Since the y coordinate is set to the middle of each row, the y distribution shows a discrete spectrum with no large variation in the number of points except in the third row. The excess in this row is due to two broken pads causing that hits which include such a broken pad are in each case identified as two hits. For the measurements presented later it was considered during the reconstruction, that these pads were broken, so that this effect disappeared. The distribution of the points as a function of z shows a rising slope until it reaches a maximum followed by a sharp falling edge. This falling slope corresponds to the end of the chamber and can be used to calculate the drift velocity (sec. 4.3.3). The shape of the distribution is driven by the acceptance of the trigger system at the Magnet Test Facility. The fig. 4.4 shows the angle distribution of the tracks as given by the TrackFitter module. The ϕ distribution is well described by the $\cos^2\phi$ fit (solid line) as expected (see sec. 3.3). It is also obvious, that the chamber was not well aligned during this data taking period yielding an offset of around 4°. The θ distribution shows an excess of negative θ values compared to the

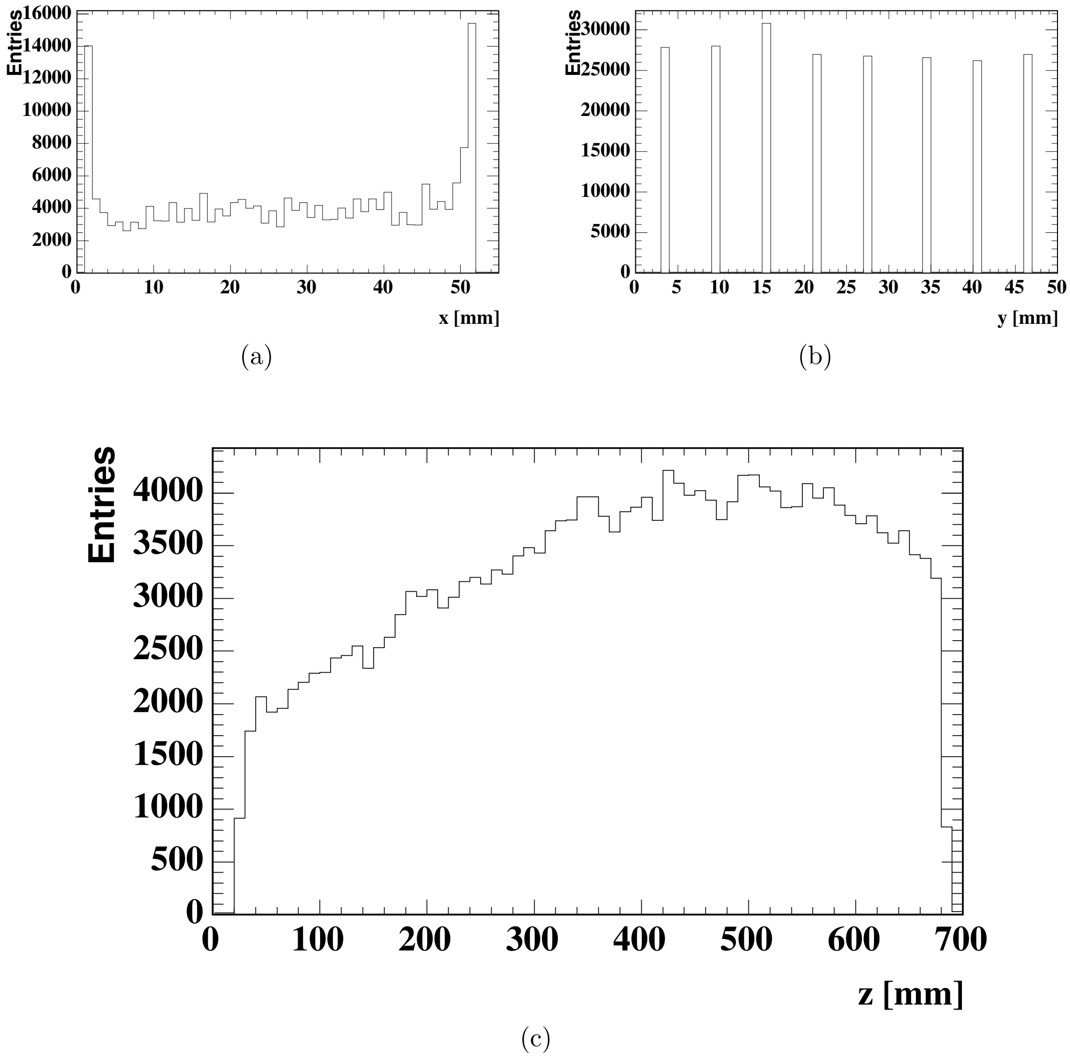

Figure 4.3: *Spatial distribution of the hits: (a) in x, (b) in y, (c) in z.*

$\cos^2\theta$ distribution. This can be explained like the shape of the z distribution by the acceptance of the trigger system which prefers tracks with negative θ values.

4.3.2 Pad Systematics

For the resolution studies it has to be taken into account which pads are working properly. One possibility to test the functionality of the pads is to investigate the number of pulses per pad. For the cosmic muons it is expected that the number of tracks for all pads is the same within statistical fluctuations. Noisy pads can be identified easily by this method due to an excess of pulses, while broken pads show a lack of pulses. Fig. 4.5 (a) shows the number of pulses as a function of the pad number, where the numbering of the pads is row wise starting with the top row. One can see that two pads are broken. Another conspicuity is, that the first and the last 24 pads as well as some pads between them show a significant excess in the number of pulses. The situation becomes much clearer in a three dimensional representation

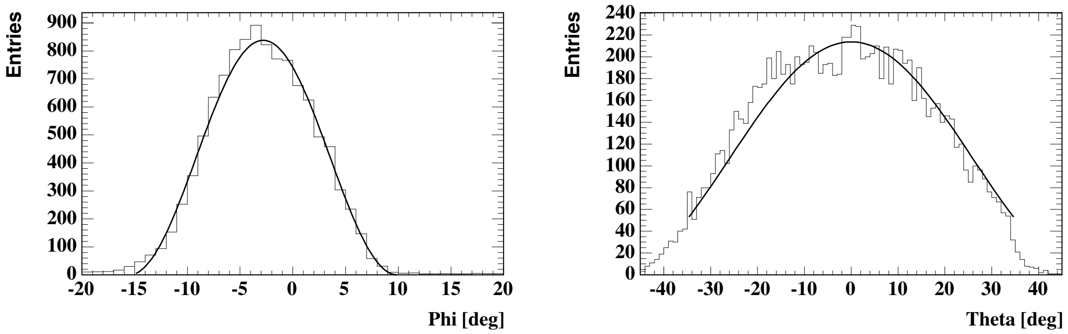

(a) (b)

Figure 4.4: *Angular distributions: (a) shows the ϕ distribution and (a) the θ distribution of the tracks. The solid line corresponds to a $\cos^2 \alpha$ fit to the data.*

(fig. 4.5 (a)). The y axis represents the number of the row, the x axis the number of the column and the z axis the number of pulses for each pad. The two holes in the second row due to the broken pads are clearly visible. Also it turns out that the excess of the number of pulses is restricted to the edge pads, while in the middle is a flat plateau. An explanation of this behaviour might be found in the surrounding

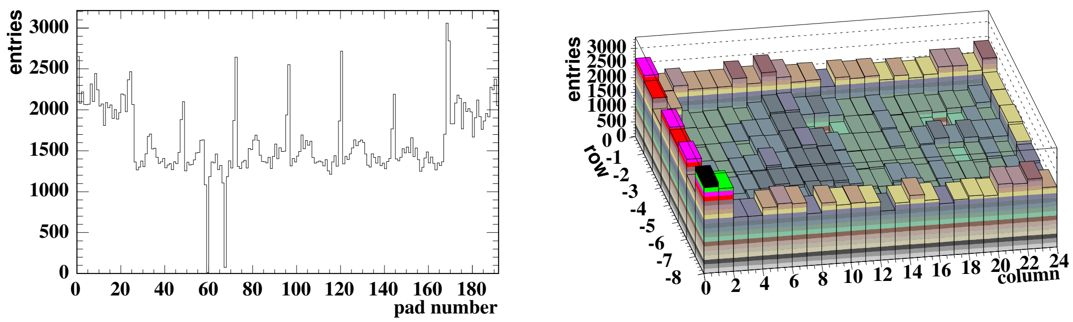

(a) (b)

Figure 4.5: *Number of pulses: (a) as a function of the pad number (b) as located in the pad plane*

pad plane. The charge cloud drifting through the induction gap produces an induction signal before it reaches the pad plane. This induction signal is much broader than the direct electron signal and might be therefore unverifiable with the $2.2 \times 6.2\,\mathrm{mm}^2$ pads. On the surrounding pad plane with its large size the signal might be sufficiently large to cause crosstalk to the outer readout pads. Fig. 4.6 illustrates this. Studies related to the signal creation process in a GEM readout system are ongoing. However, there are two indications that the reason for the excess in the number of hits is caused by an induction signal: on the one hand an excess of events was observed, in which only on both ends of the sensitive volume tracks occur. An explanation within the concept of the induction signal could be, that the true track was outside of the sensitive volume, but within the surrounding pad plane causing a large induction signal. Another hint for an induction signal is the time structure. The signal on the outer readout pads arrives earlier than the signal on a middle pad.

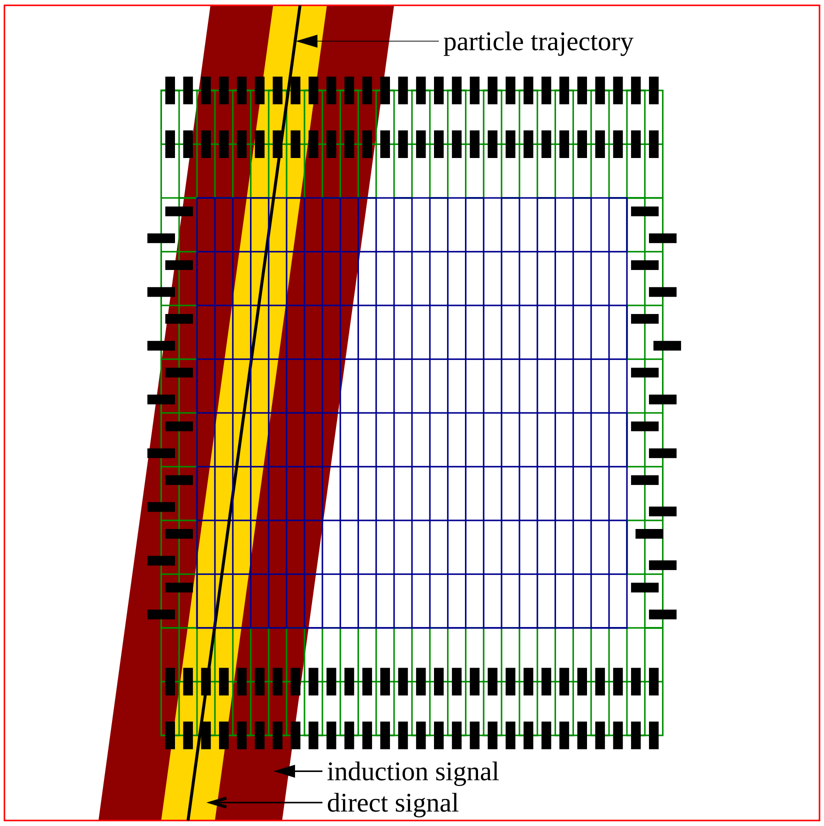

Figure 4.6: *Illustration of the edge effects. A particle transversing the sensitive area (black line) causes a direct electron charge cloud signal (yellow area) and also a much broader induction signal (indicated by the red area) [50].*

4.3.3 Drift Velocity

For each run the drift velocity was determined from the position of the falling edge as shown in fig. 4.3 (c). This edge corresponds to the end of the sensitive volume. From the position of this edge in the data and the maximal possible drift length given my the geometry of the chamber the drift velocity can be calculated. Thereby, it has to be considered, that the maximal possible drift length is a composition of the length of the sensitive volume l_{sens} and the depth of the GEM module. Since in the gaps of the GEM module the field strength is much higher, corrections have to be applied leading to the introduction of an *effective length* l_{eff} of the chamber. The effective length depends on the chosen gas and is for the TDR gas 676 mm and for P5 683 mm and is given by

$$l_{eff} = l_{sens} + \frac{v_D(E_{ind})}{v_D(E_d)} \cdot l_{ind} + 2 \cdot \frac{v_D(E_{tr})}{v_D(E_d)} \cdot l_{trans} \ . \tag{4.1}$$

Here, $v_D(E_x)$ is the drift velocity in the drift volume, in the transfer gaps or in the induction gap respectively as predicted by MAGBOLTZ. The corresponding widths of the gaps are l_{ind} for the induction gap and l_{tr} for the transfer field gaps. The method used to calculate the drift velocity is explained in detail in [50].

Change of the Drift Velocity over Time

In a further study the change of the drift velocity over time was investigated for both measurements with staggered pads: TDR and P5 gas. For each 8 hours the drift velocity was calculated. The results for both are shown in fig. 4.7. The solid line corresponds to the predictions from Garfield. For some hours during the measurement

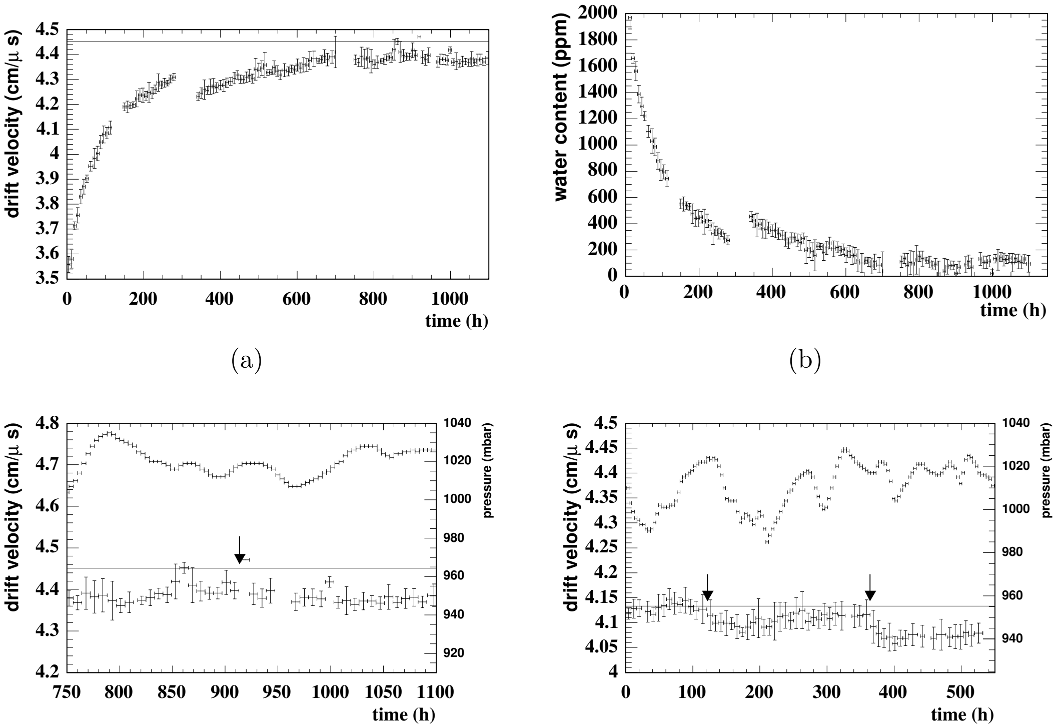

(a) (b)

(c) (d)

Figure 4.7: *Drift velocity versus time: (a) TDR gas. The measurement started on the 22th October. (b) Corresponding water content according to the predictions from MAGBOLTZ. (c) Pressure and drift velocity for TDR gas at stable conditions. (d) The corresponding plot for the measurement with P5 gas. The starting time was on the 13th December. (pressure values: [58]).*

time the chamber was not operated because of network problems and modification of the gas system. This appears as gaps in the measurements. The gap due to the modification of the gas system is clearly visible from the drop in the measured drift velocity (at ≈ 245 h). The solid arrows corresponds to the times, where the gas bottle was exchanged. It is noticeable, that for the measurement with the TDR gas it took almost two weeks to get stable conditions for the drift velocity. An obvious explanation for this behaviour is that it is caused by water pollution. There are two possible sources for the water. The chamber itself, which was before open for almost three months, sufficiently long so that the Kapton of the field cage, which is hydrophilic, could absorb a significant amount of water. The second source could be the ≈ 25 m of the tubes of the gas system, which are copper. Copper has a rough surface and water can be captured there for a long time. Before the measurements had been started, the gas system has

not been used for 2 months and has been exposed to air during this time. A better material choice for the tubes of the gas system would have been stainless steel.
Using predictions from the Garfield program package the dependence on the drift velocity can be converted into a dependence on the water content neglecting the effects due to pressure or temperature changes. Fig. 4.7 (b) shows the distribution for the TDR gas. It seems that the water content at the starting time of the measurements with the TDR gas was around 2000 ppm and at the end around 100 ppm. This result was also confirmed by direct measurements via the dew point of the gas yielding a maximal water content of below 200 ppm. The following measurements with the P5 gas yield a water content a little bit below this value ($\approx$ 70 ppm). This might be caused on one hand that for both measurements no corrections for changes of the pressure and the temperature are applied, which might be not identical for both gases. Also uncertainties in the calibration due to the MAGBOLTZ predictions might play a role.
Finally the correlation between the pressure, measured at the airport Fuhlsbüttel, and the drift velocity was investigated. Therefore, the relative change in the drift velocity versus the relative change in the pressure are plotted (fig. 4.8). A correlation would be

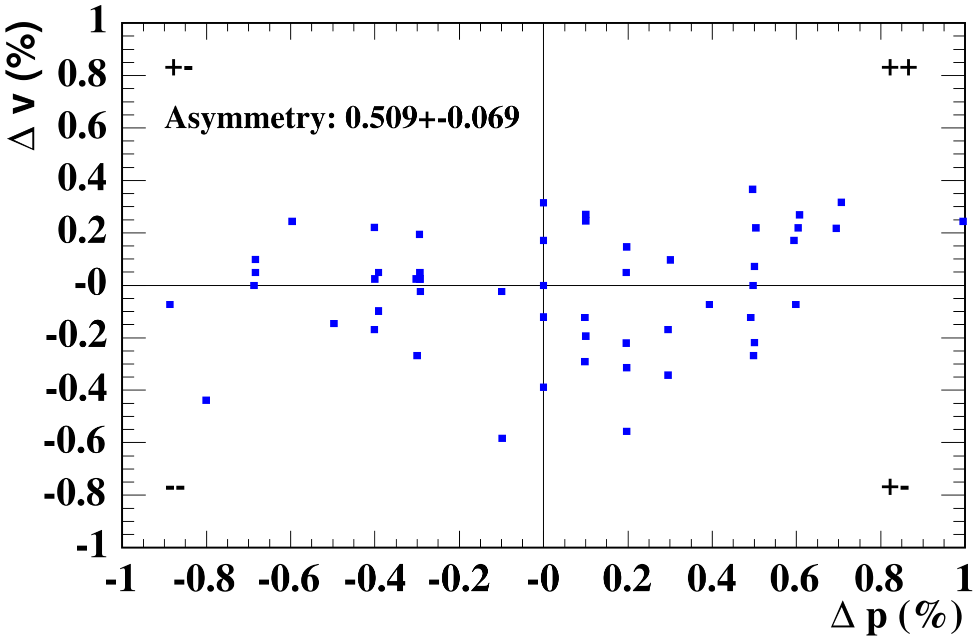

Figure 4.8: *Correlation plot between relative change of the drift velocity and relative change in the pressure.*

visible as an excess of data points in the $+-$ regions, while a anti correlation would yield an excess in the $++$ and $--$ region. In the case that neither correlation nor anti correlation is given, the data points should be distributed uniformly. The quantity a is a gauge for this:

$$a = \frac{\#\text{ data points in } ++ \text{ and } --}{\text{total } \# \text{ of data points}} \quad (4.2)$$

$$= 0.51 \pm 0.07\,. \quad (4.3)$$

Therefore, at the moment no indication of an anti correlation which is expected can be found.

Measurement of the Drift Velocity versus Drift Field

In the previous sections the drift velocity was only determined for the operational drift field of ≈ 200 V/cm (TDR) or ≈ 90 V/cm (P5). An interesting question is, if also of the shape of the distribution $v_D(E)$ as predicted from Garfield is well described by the measurements. Since the measurements should be performed for E fields below and above the maximum, for this measurement the P5 gas mixture was used. Due to time limitations only six data points were taken, which describes the shape of the curve well. The result is shown in fig. 4.9. The three lines corresponds to 0 ppm, 50 ppm and 100 ppm water content.

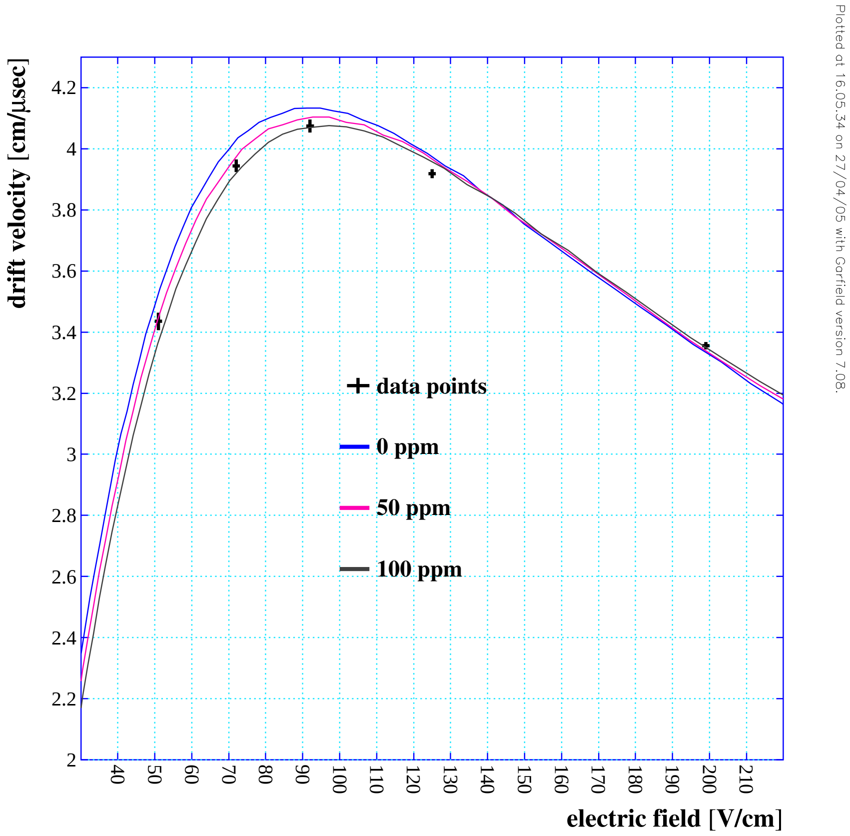

Figure 4.9: *Drift velocity as a function of the electric field. The three curves correspond to different values of the water content in the gas.*

4.3.4 Hit Charge Distribution

In fig. 4.10 the distribution of the charge per hit is presented. For thin absorber it is expected that this distribution can be well described by a Landau function (sec. 2.3.2). The solid line shows the fit of a Landau distribution to the data. It is obvious, that there a small differences, especially in the tail of the distribution. This indicates that the assumptions for the derivation of the Landau distribution are not completely fulfilled. The effect was also observed in other studies and nowadays numerical methods are used to describe the hit charge distribution in gaseous detectors [30].

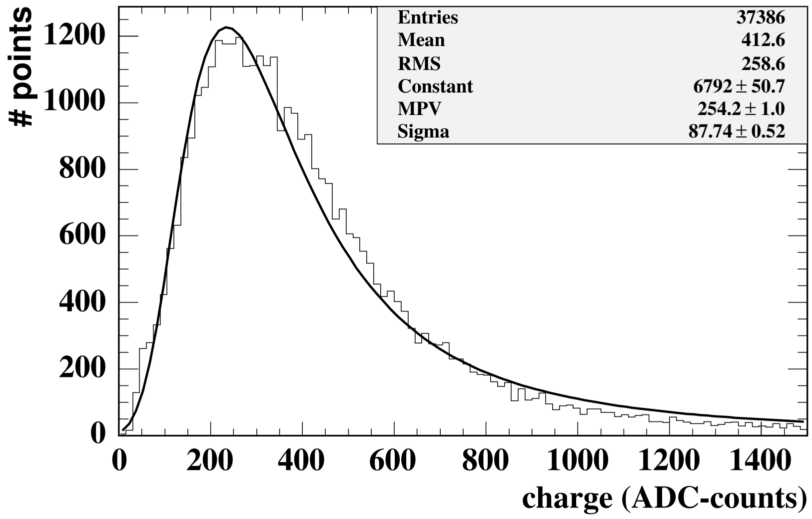

Figure 4.10: *Distribution of the charge per hit. The solid line corresponds to a Landau distribution fitted to the data.*

4.3.5 Field Distortions

For the measurements of the point resolution the electric field homogeneity is very important. Therefore, for each row the difference between the position as predicted from the track fit and the reconstructed position of the hit in this row was plotted. For this study the row, which was investigated, was excluded from the fit. The results are shown in fig. 4.11. The measurement was performed in nine different time bins separately. The average of all time bins is shown in red. Small statistical fluctuations are visible, but no systematic behaviour is observed, so that no significant impact on the point resolution is expected. For example field distortions due to a potential difference between shield and GEM surface would be visible in a *banana* shaped distribution in z, where the position of the reconstructed hits of most outer rows are always behind these from the position predicted from the track fit. Such a banana shaped distribution is shown in fig. 4.12 as it was observed in a previous study [24] The different scale has to be noticed.

4.3.6 Gain Stability

Also the gain stability was investigated, thereby it was distinguished between local variations and variations in time. Former is an indication for local variations of the temperature, while latter is important to prove the dE/dx capability of a GEM readout.

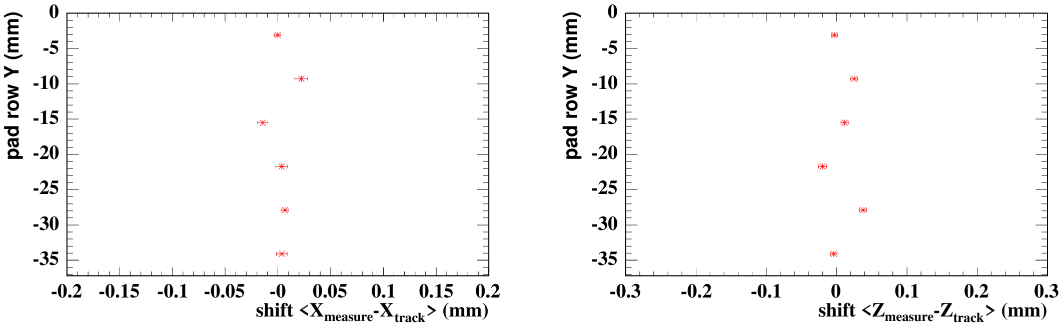

(a) (b)

Figure 4.11: *Study of systematic shifts in the reconstruction of the hit position, which would be a hint for field distortions: (a) in the xy plane and (b) in the yz plane. The mean values of all time bin measurements are shown as red points.*

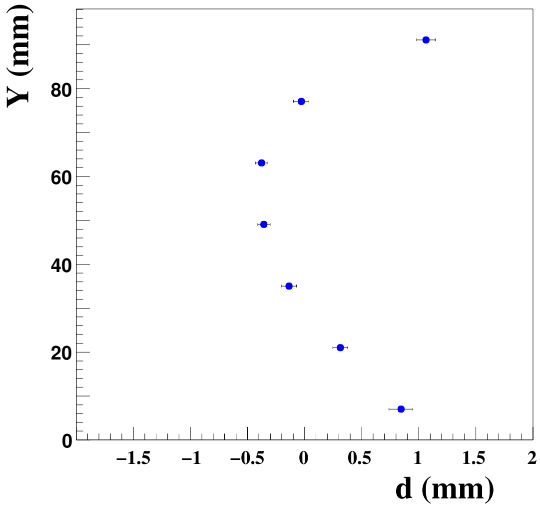

Figure 4.12: *Illustration of the effect of field distortions: banana shaped distribution in the yz plane as it was observed in a previous study [24]. One has to take into account the different scale compared to fig. 4.11.*

For both one has to consider, that the electronics were not calibrated. Without the calibration the variation in the gain is of the order of 7-8 % as shown in fig. 4.13. The figure shows the average charge per pulse for every pad normalised to the average charge per pulse of all pads. This quantity, in the following referred to as normalised or relative gain, is proportional to the gain.

Local Variation

Fig. 4.14 shows the same quantity per pad as it is located on the pad plane for two different analysis runs. An inhomogeneous temperature distribution due to the resistor chain should be visible as an excess in the gain on two opposite positions in the pad plane corresponding to the two positions of the resistor chains. In both figures this was

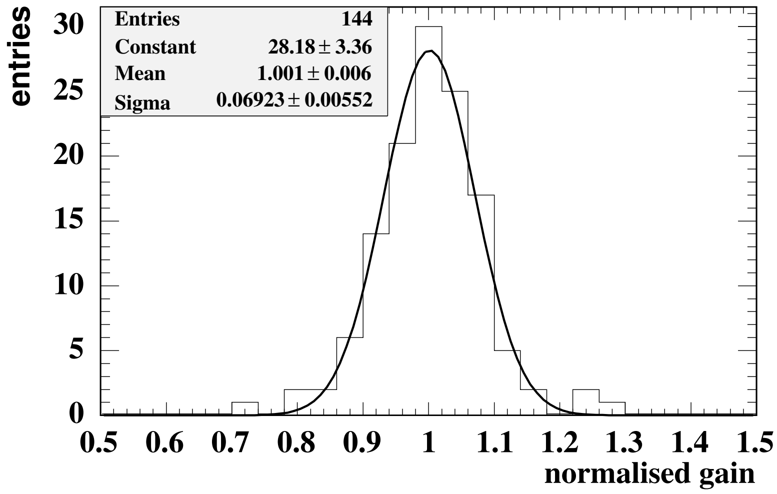

Figure 4.13: *Distribution of the gain normalised to the average gain over all readout channels. The solid line corresponds to a fit of a Gaussian to the data.*

not observed. The observed variations in the gain can be explained by the different properties of the preamplifiers used and TPD respectively of which at least the latter were exchanged between the two data taking periods.

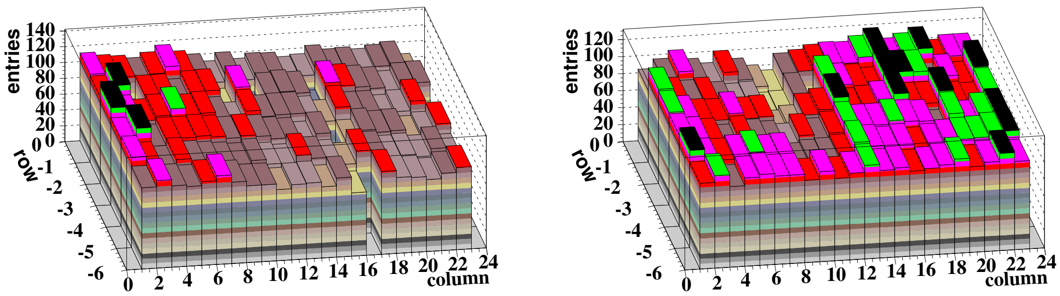

(a) (b)

Figure 4.14: *Gain distribution on the pad plane for two different analysis runs. The TPD modules were exchanged between these two measurements. The average of all pads corresponds to 100 %.*

Time Stability and Pressure Dependence

The normalised gain was also investigated over time. Since changes of the GEM voltage settings and also of the magnetic field affects the gain, this study was, in contrast to the drift velocity measurement, carried out only per analysis run. Due to this limitations in statistics the change of the normalised gain for each pad was not measured, but the change of the average gain of all working pads normalised to the first time window. Fig. 4.15 (a) shows the normalised gain as a function of the time. The change of $\approx \pm 4\%$

can be well explained by the change in pressure(fig. 4.15 (b)). This becomes obvious

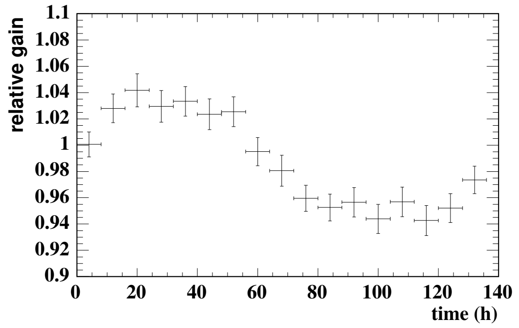

(a)

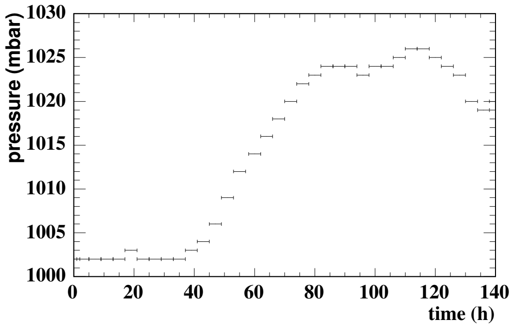

(b)

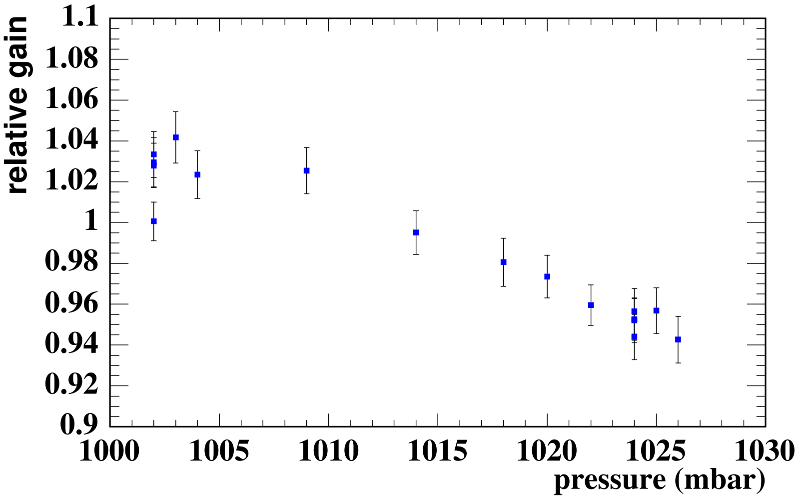

(c)

Figure 4.15: *Dependence of the relative gain on time and pressure. (a) shows the variation of the relative gain as a function of the time. (b) dependence of the pressure on the time. The relative gain as a function of the pressure is shown in (c).*

in fig. 4.15 (c) where the normalised gain versus the pressure is plotted. The gain decreases with increasing pressure which is expected assuming that the temperature in the experimental hall was stable [59]. However, since the gain has also an influence on the measured point resolution (see sec. 4.3.8 and fig. 5.7) the installation of a gas slow control system for the gas pressure and temperature is required to allow for corrections of these effects and thus guaranteeing stable operation conditions.

4.3.7 GEM Discharge Stability

An important issue for using a GEM readout in a full size detector is the reliability. Here, the stability against discharges is an important point. Even for a large TPC the GEMs will be divided in several parts, which are connected independently to the HV supply, it is desired, that the spark rate is low to avoid temporally dead areas in the detector. Therefore, the rate of discharges were controlled. A higher discharge rate was observed, when new GEMs were built in, when the chamber was open before for some weeks or when the gas system was exposed before to air respectively. That the discharge probability is higher with new GEMs is not unexpected, since new GEMs have to be "trained", which means some defects on the copper surfaces are removed by sparks. The high rate of several sparks per hour which was observed at the beginning of the measurement with staggered pads and TDR gas and which made it almost impossible to start the measurements can on the other hand not only be explained by this effect. Apart from small dust particles due to the exposing of the detector to air which can also cause discharges, another main role may be the high water content. Also in other studies this observation was made [60]. This assumption is assured due to the fact, that the discharge rate was decreased to almost zero after some time according to the reduction of the water content in the gas.

4.3.8 Effect of the Magnetic Field

To illustrate the effect of the magnetic field on the width of the charge cloud the average number of pulses of a hit (charge sharing) as a function of the B field is shown in fig. 4.16. The two distributions corresponds to the measurements with staggered and

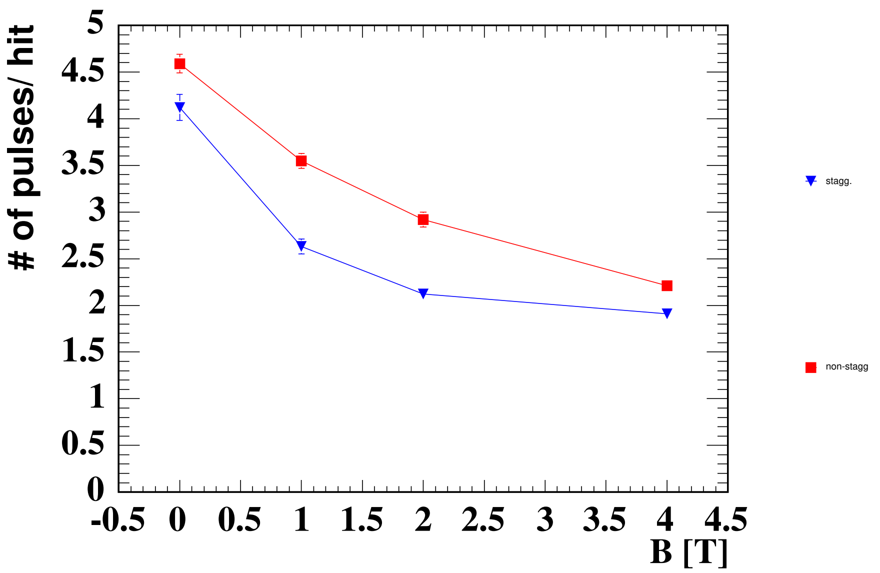

Figure 4.16: *Number of pulses of a hit as a function of the applied B field.*

non-staggered pads with TDR gas. Both distributions show a clear falling slope. For higher magnetic fields the slope of the distribution of the measurement with staggered pads becomes almost flat. In this region the number of pulses of a hit does not reflect anymore the width of the charge cloud, but the number of pulses of a hit is mainly driven by the pad geometry.

However, since the measurements were performed with the same gas the expectation is, that both distributions should be identical for low magnetic fields because in this

region the average number of pulses of a hit depends mainly on the diffusion coefficient. For higher magnetic fields and similar operational conditions it is expected that in measurements with staggered pads in average more pulses belong to a hit due to the fact, that in every second row charge sharing between two pads is enforced.
Small variations between these two distributions might be caused by different water contents in the gas during the measurements. Indeed the effect observed is too large to be explained by this. A more obvious explanation of this effect is the different gain at which the chamber was operated during the measurements. The gain has an influence on the observed charge sharing due to the applied threshold. At low gain a larger part of the Gaussian shaped charge cloud is below the threshold and therefore it is not detected. On the other hand a high gain may yield an amount of charge which is out of the range of the ADC spectrum leading to not well reconstructed hits.
The influence of this to the measurement of the point resolution is shown in fig. 5.7. The pros and cons of a higher operational gain are discussed in Chapter 5.

Chapter 5

Resolution Studies

The main task of the prototype is to measure the point resolution as a function of the drift distance. As mentioned in sec. 1.4 this is an important parameter concerning the momentum resolution. In this thesis the *Triplet method* is used to determine the point resolution. This method will be introduced first. Then the results of the measurements are presented and afterwards discussed.

5.1 The Triplet Method

A robust and simple method to determine the point resolution is the Triplet method. In this method the point resolution is determined via three neighbouring rows. A straight line is defined through the reconstructed hits of the outer rows and the residual between the position of the hit on the middle row and the line is measured. The point resolution σ_{res} is defined as follows:

$$\sigma_{res} = \sqrt{\frac{2}{3}}\sigma_{gaus} \ , \tag{5.1}$$

where σ_{gaus} denotes the width of the Gaussian fitted to the distribution of the residual. For eq. 5.1 it is assumed, that the error for each of the three hits is the same. The method is illustrated in fig. 5.1.

Various cuts are applied to the data:

The position of the used hits has to be reconstructed in the x range $11 < x < 41.8$ mm corresponding to a removal of 5 columns on each side. This ensures that even at 0 T where the charge cloud is broadest the complete signal of a hit is well reconstructed. Even when the Triplet method only requires reconstructed hits in three adjacent rows, a cut on the number of tracks in an event of $n_{track} = 1$ is implemented ensuring that noise events are not selected. In addition a ϕ cut on the track angle of $|\phi| < 5°$ is applied. The ϕ cut is motivated by the fact, that in a full size TPC the pads will be arranged in a way, that they are pointing to the interaction region, so that large ϕ angles will not occur in general. Furthermore only hits which do not include damaged pads are considered. Hits with ADC counts above the range of the ADC (*overflow hits*) are on the other hand not excluded to keep reasonable statistics. An illustration of the cuts is given in fig. 5.2. Using a simple MC generator the method was studied concerning systematic effects such as biases, and a comparison was made with other

established methods. The MC generator simulated curved tracks with a radius between 500 mm and 2000 mm. The positions of the hits were then smeared around the track according to a point resolution of 200 μm. The result of this study is presented in fig. 5.3. The *residual* and the *distance method* which are compared with the Triplet method are based on a track fit taking into account the information of the hit position in each row. In the case of the residual method the row in which the point resolution is determined is excluded from the fit. Thus, the point resolution is larger than the input ones. For the distance method all rows are used leading to a resolution better than the predicted ones. Both methods show edge effects which are suppressed if more rows or a longer lever arm is used.
The Triplet method on the other hand reproduces the input resolution very well, although the tracks simulated were curved. Therefore, this method is chosen for the determination of the point resolution. However, it will be shown later that this method is quite sensitive to biases in the reconstruction of the hit positions.

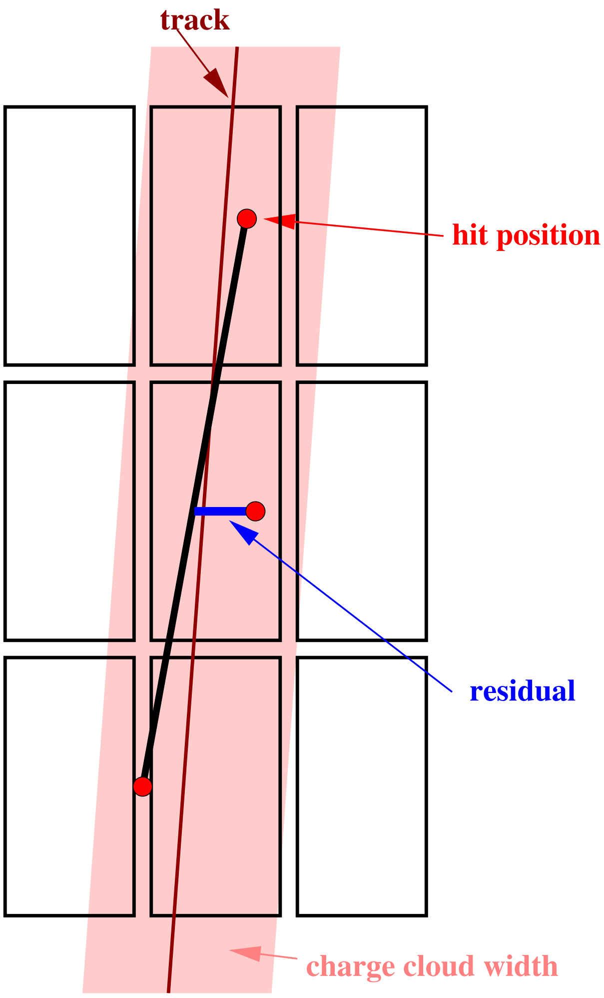

Figure 5.1: *Triplet method: a straight line is defined by the hit position in the outer rows and the residual in the middle row is measured.*

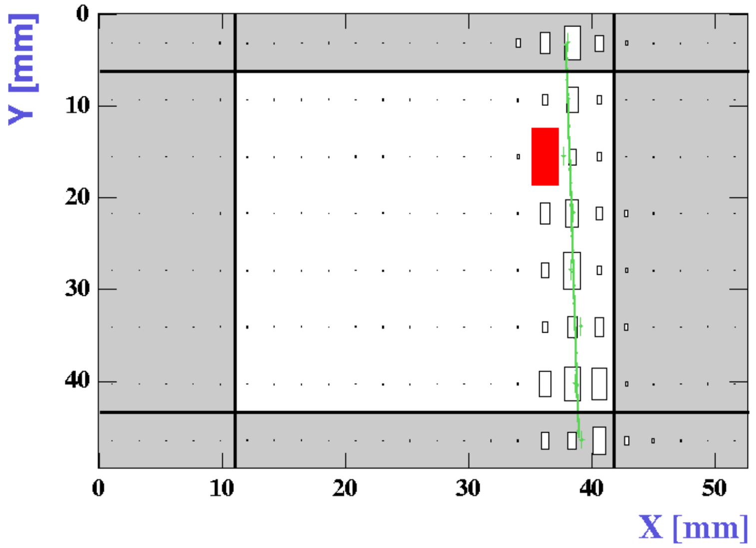

Figure 5.2: *Illustration of the coordinate system and the applied cuts. Hits whose position is within the white area are considered for the determination of the point resolution. The top and bottom rows are already removed during the reconstruction. The red pad indicates a broken channel and therefore the corresponding hit is excluded from the measurement of the point resolution.*

5.2 Non-staggered Pads

The first measurements with non-staggered pads using TDR gas in the magnet were performed between February and May 2004. The point resolution as a function of the drift length for these measurements are presented in fig. 5.4. For 0 T the resolution is dominated entirely by the diffusion of the charge cloud and showing the $\sqrt{z}$ dependence (see also fig. 5.7 (a)). For 1 T this effect is reduced, but still visible. For 4 T the point resolution is mainly determined by the defocussing term σ_0 (sec. 2.6) and the influence of the diffusion is visible only due to a small increase of the point resolution with z, since the charge cloud is distributed in average only on ≈ 2 pads (see fig. 4.16).

5.3 Staggered Pads

With the staggered pads two measurement series were taken between October 2004 and January 2005: first with the TDR gas mixture and secondly with the P5 gas.

5.3.1 Measurements with TDR Gas

The results of the point resolution studies with staggered pads and TDR gas are shown in fig. 5.5. For 0 T the shape of the distribution is similar to the results of the study with non-staggered pads. This is expected since due to the large diffusion the charge cloud is smeared over a wide range of pads and the reconstruction of the hit position is

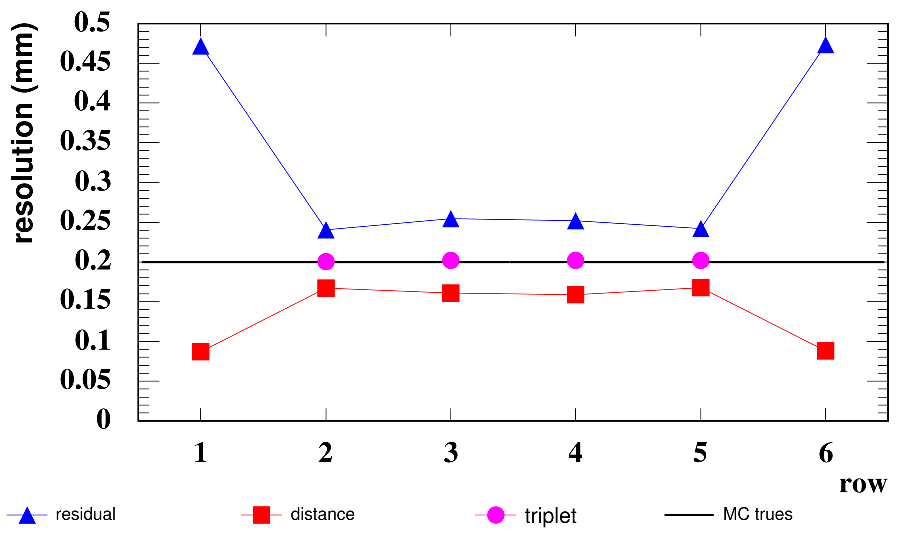

Figure 5.3: *Investigation of systematic effects on the point resolution due to the determination method, not considering biases due to the reconstruction of the hit position.*

therefore not limited by the pad geometry. The results in the presence of a magnetic field are surprising. For the 1 T data the resolution first improves and then follows the dependence due to diffusion. At 2 T the resolution for short drift distances is worse than for the 1 T data and improves afterwards to the same optimal value of about 200 μm. This is still worse than the best result of the measurement with the non-staggered pads. For long drift distances the resolution decreases slightly. At 4 T the dependence of the point resolution shows a falling slope from 700 μm for short drift distances to around 300 μm at the end of the chamber.

5.3.2 Measurements with P5 Gas

The results of the measurements with P5 gas are shown in fig. 5.6. The 0 T data shows the typical behaviour, whereabout the resolution is worse compared to the measurements with TDR gas due to the larger diffusion coefficient of P5. The measurement point with the largest drift distance could not be reconstructed sufficiently, since in this case the reconstruction software tends to reconstruct more than one track in one event. This effect appears also for shorter drift distances due to an increase of the errors. The larger error for large drift lengths is also caused by the large diffusion coefficient. At higher magnetic fields the behaviour is similar to the TDR measurement, but with a better resolution for short drift distances. For long drift distances it agrees with the TDR gas measurements, since the transverse diffusion at 4 T is quite similar for both gases (fig. 3.9) at the particular drift field. There are two effects which explain this behaviour: on the one hand the transverse diffusion coefficient of P5 in the induction and transfer field is larger than for TDR gas yielding a larger defocussing term. This term becomes more important at smaller drift distances. In addition the larger longitudinal diffusion in P5 gas reduces the

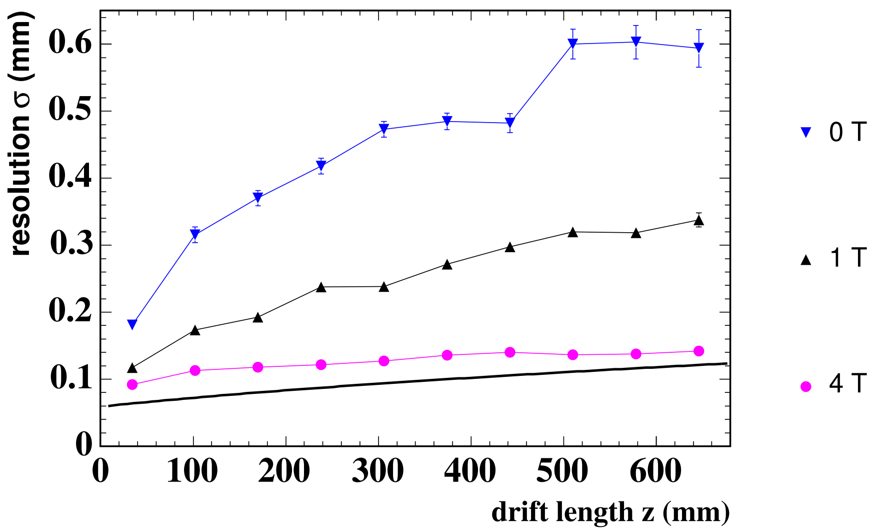

Figure 5.4: *Transverse point resolution as a function of the drift length for various magnetic fields. The measurement was performed using non-staggered pads and TDR gas. The solid line corresponds to the requirements for a TPC at the ILC.*

number of overflow hits compared to the TDR gas. In overflow pulses the deposited charge in at least one time bin is above the range of the ADC. Therefore, the charge is not completely reconstructed leading to incorrectly reconstructed position of the complete hit.

A direct comparison of the different measurements at 0 and 4 T is shown in fig. 5.7. The difference in the resolution for the measurements at 0 T with staggered and non-staggered pads and TDR gas is caused by the different gains used during the measurements as discussed in sec. 4.3.8. This conclusion is also justified by the fact, that the diffusion coefficient D determined by fitting the function

$$\sigma_P = \sqrt{\frac{D^2 \cdot z}{n_t} + \sigma_0} \tag{5.2}$$

(see eq. 2.18 eq. 2.11, eq. 2.19 and eq. 5.1) to the data agrees within 2.4 standard deviations for both measurements. The result for the measurement with non-staggered pads is $D = 191 \pm 3$ μm/$\sqrt{\text{cm}}$ and for the measurement with staggered pads $D = 203 \pm 4$ μm/$\sqrt{\text{cm}}$. For the fit the number of primary released electrons n_t is assumed to be $n_t = 60$, which is calculated from the commonly used value of $\approx$ 100 electrons per cm [31]. The discrepancy of these values to the prediction of MAGBOLTZ which is $D^{TDR}_{MAG} = 442$ μm/$\sqrt{\text{cm}}$ is remarkable. The diffusion coefficient obtained from the measurements with P5 is $D = 331 \pm 12$ μm/cm, which compared to the value predicted from MAGBOLTZ ($D^{P5}_{MAG} = 724$ μm/$\sqrt{\text{cm}}$) is also much too small. It is interesting that for all measurements the ratio R of measured to predicted diffusion coefficient is $R \approx 45\%$. This suggests the introduction of a correction factor c_D to the term

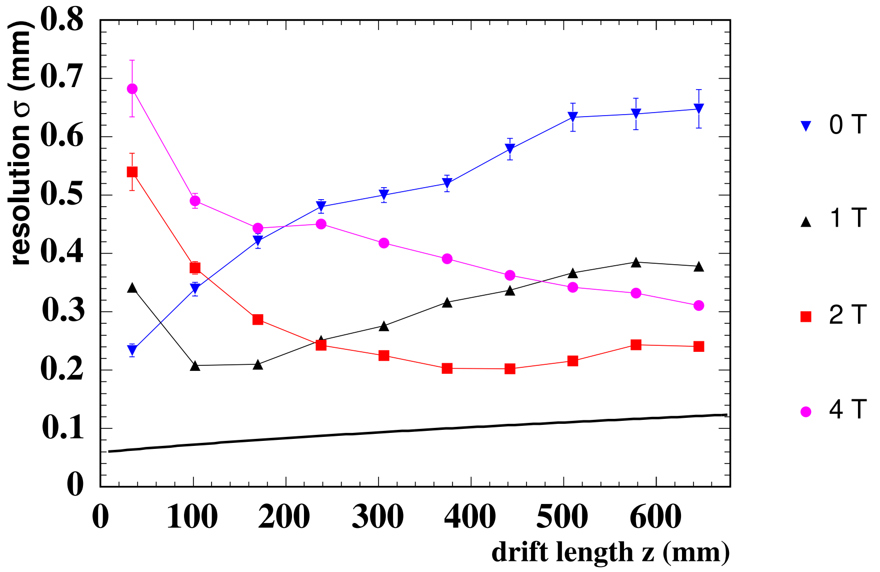

Figure 5.5: *Point resolution as a function of the drift length for staggered pads and TDR gas. The results of the measurements at 0, 1, 2 and 4 T are shown. The solid line corresponds to the requirements for a TPC at the ILC.*

$\frac{D^2 \cdot z}{n_t}$ of eq. 5.2. The value of c_D as deduced from the comparison of measured and predicted diffusion coefficient is $c_D \approx 4.75$. The justification of this correction factor and especially its value requires further investigations.
Since the fit yields for both measurements with TDR gas a similar result and only a discrepancy in the constant term σ_0 was observed, one can deduce that this term can be reduced using higher operational gains. This has of course limitations. If the gain is too high the number of overflow pulses will be increased, especially for short drift distances. This will decrease the point resolution as mentioned above. The application of another DAQ system with wider ADC range or a reduction of the electric noise level would also help.
Considering also the result of the determination of the diffusion coefficient of P5, which yields a larger value for the defocussing term than the measurement with TDR gas, this suggests to express the defocussing term by:

$$\sigma_0^2 = \sigma_1^2 + \sigma_2^2 \ . \tag{5.3}$$

Here, σ_1 corresponds to the part of the defocussing term caused by the operational gain and includes also the influence of the electronics. The second term, σ_2, reflects the influence of the diffusion in the induction and transfer gaps on the defocussing term. For this contribution the gas, the width of the induction and transfer gaps and the field strengths in these gaps are relevant.
The optimisation of both contributions has to be investigated for future measurements.

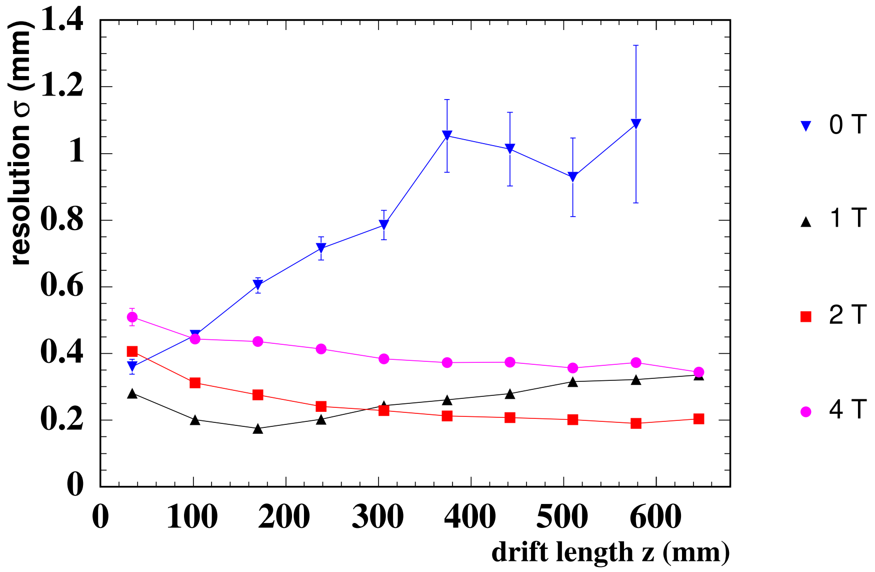

Figure 5.6: *Point resolution for staggered pads and P5 gas. The results for the measurements at 0, 1, 2 and 4 T are shown.*

5.4 Discussion of the Results

The point resolution was measured with two different pad geometries and gas mixtures. The measurements with TDR and P5 gas agree with each other in general, the results of the measurements with staggered and non-staggered pads using TDR gas differ significantly. While for non-staggered pads it seems to be possible to reach the aim for the ILC TPC, considering that building in the pad response function in the reconstruction and corrections due to temperature and pressure variations will slightly change the result. And also optimised electronics e.g. better noise reduction might help to improve the point resolution, so that it fulfils the requirements for the ILC TPC.

The results of the measurements with staggered pads on the other hand yield a completely different picture. The achieved point resolution degrades at high magnetic fields and is far above the required point resolution.

To understand this problem the reconstructed hit position as a function of the true hit position was studied. In fig. 5.8 this function is shown for the case that the width of the charge cloud is 14 % of the pad width and track angle $\phi = 0$. This charge cloud width corresponds to the TDR gas for a drift length of $\approx$ 30 cm at 4 T. The flat plateau in the middle indicates the region, where the whole charge is collected on one pad only. Considering the more realistic case, that a threshold for the collected charge is applied, this plateau becomes even broader. As a result this means for the case of non-staggered pads and tracks under small angle that the reconstructed position is shifted for all rows in the same direction leading to a bias in the reconstructed track. It is important to stress that this is not in contradiction to the considerations in sec. 5.1 concerning a possible bias of the Triplet method, since the bias is not caused

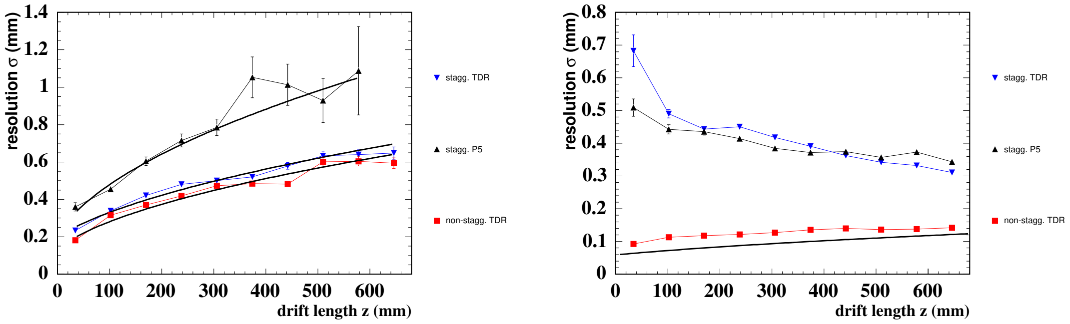

(a) (b)

Figure 5.7: *Comparison of non-staggered and staggered pads. (a) shows the measurements at 0 T. Also the fits to the data as explained in the text are shown. (b) shows the measurements at 4 T.*

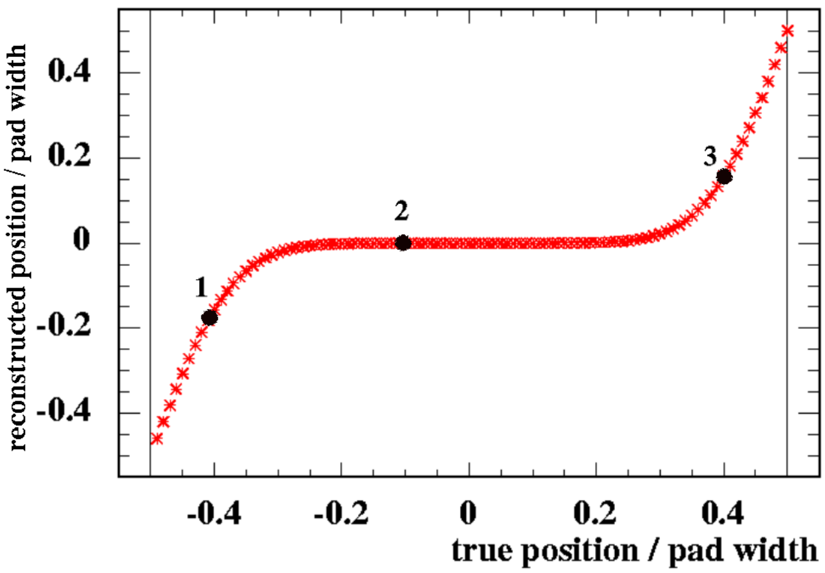

Figure 5.8: *Dependence of the reconstructed hit position, relative to the centre of the pad, on the true hit position also relative to the centre of the pad. The points 1, 2 and 3 refer to the different situations explained in the text and in fig. 5.9*

by the Triplet method, but occurs during the reconstruction of the position of the hit and is not visible in the measured point resolution. This situation is illustrated in fig. 5.9 (a). All hit positions in the three adjacent rows are distributed around the point 1 in fig. 5.8 and their reconstructed position is shifted with respect to their true position relative to the centre of the pad. This kind of bias does not affect the measured point resolution. Depending on the position the measured point resolution is either overestimated or underestimated.
The case of staggered pads is illustrated in fig. 5.9 (b). In the top and the bottom row the situation matches point 3 in fig. 5.8. There is charge sharing between two

neighbouring pads, but the reconstructed hit position is shifted slightly to the centre of the pad. In the middle row the charge is collected only on one pad thus leading to a reconstruction of the hit position in the centre of the pad. This corresponds to point 2 in fig. 5.8. Due to the offset of half of a pad this shift is in the opposite direction than for the adjacent rows. Therefore, the measured point resolution is worse than in the case of non-staggered pads, since the measured point resolution is a convolution of the "true" point resolution as measured for the non-staggered pads and a bias due to the reconstruction of the hit position. As long as the charge cloud is collected only on one pad, the improvement of the result by implementing the pad response function in the reconstruction is limited. The considerations quoted above

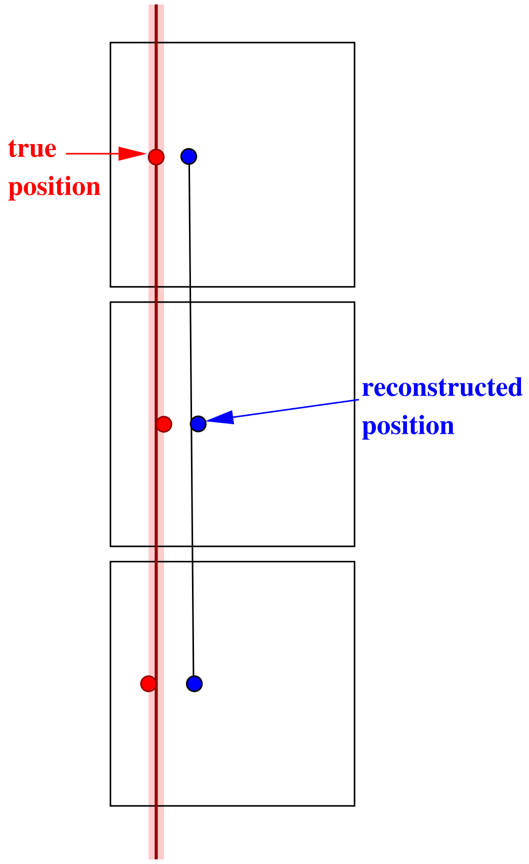

(a)

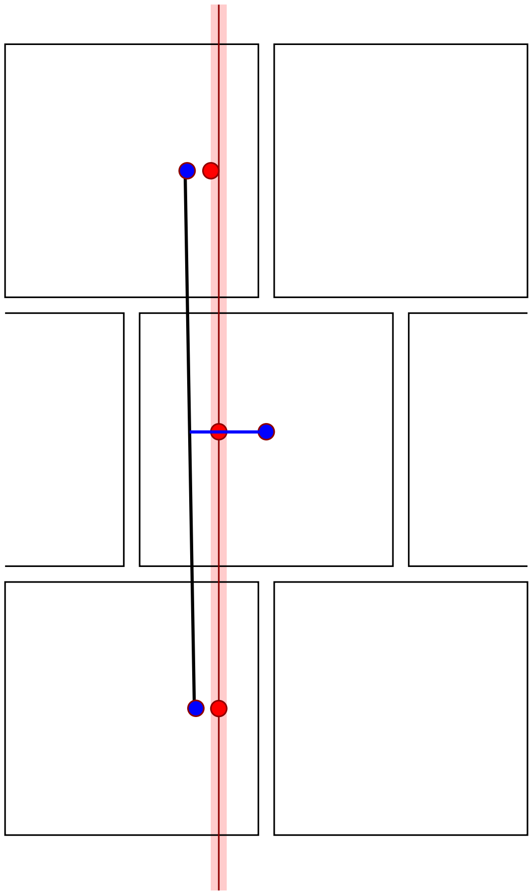

(b)

Figure 5.9: *(a) shows the situation in the case of non-staggered pads. The reconstructed track intercept has a bias relative to the true track and also the true residual is underestimated. (b) illustrates the corresponding situation for staggered pads. The hits defining the track intercept are shifted in one direction, while the hit used for the determination of the residual is shifted towards the opposite direction.*

are also supported by the residual distributions for both pad planes. Fig. 5.10 shows the residual distributions for various drift distances for TDR gas and staggered pads at 4 T. The top left distribution corresponds to the shortest drift distance and the bottom right distribution to the largest drift distance. The residual distributions

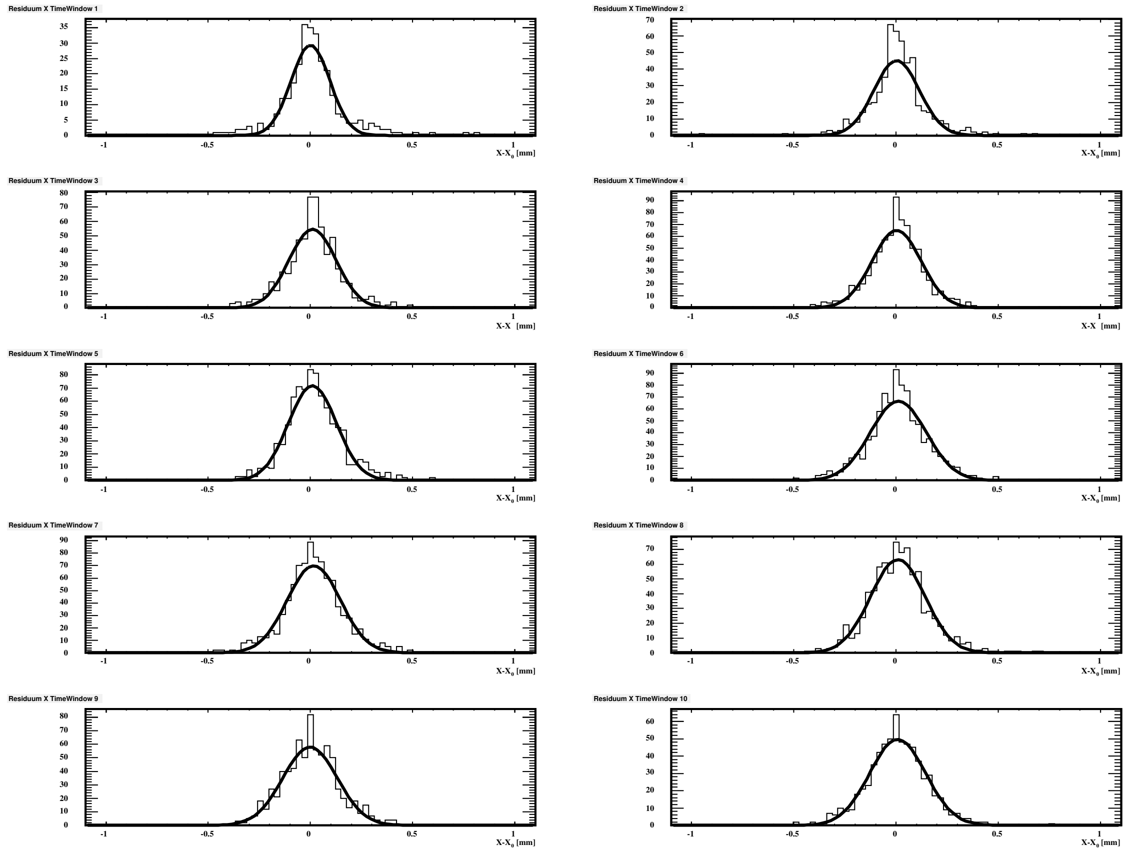

Figure 5.10: *Residual distributions for analysis run C for various drift distances starting in the top left graph. The factor $\sqrt{2/3}$ from eq. 5.1 is included in the plot. The peak in the middle of the distribution is caused by the fraction of events, in which in every row only one pad is hit.*

follow a Gaussian. The peak in the middle of the respective distribution is obvious. This corresponds to the number of events, where in each row only one pad is hit. At larger drift distances the peak becomes less significant due to the diffusion, but is still visible at the end of the chamber.

For the staggered pads these residual distributions have a completely different shape as shown in fig. 5.11. In contrast to the residual distribution for the non-staggered pads, no Gaussian distribution for the residual can be observed. While for short drift distances no structure at all is visible, the distribution has the form of a double Gaussian for longer drift distances. This double Gaussian starts to merge with increasing drift distance to one Gaussian, but does not disappear completely. This double Gaussian distribution can be easily explained with the arguments mentioned above. Depending on the position of the track relative to the centre of the pad in the middle row as shown in fig. 5.9 (b) the residual distribution follows a Gaussian with a shift relative to zero. The shift can either be positive or negative. The superposition of the Gaussians with positive and negative shift results in the observed shape of the distribution.

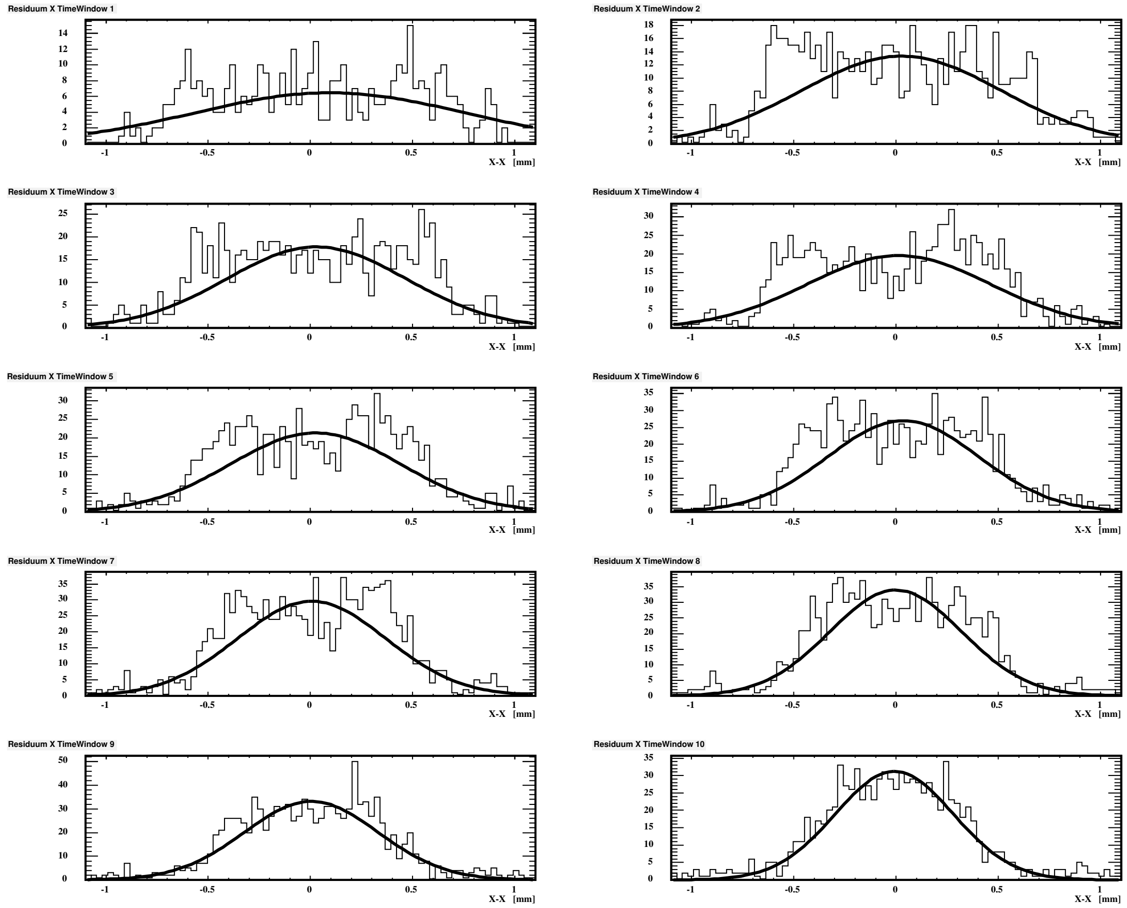

Figure 5.11: *Residual distributions for analysis run G for various drift distances starting in the top left graph (staggered pads).The factor* $\sqrt{2/3}$ *from eq. 5.1 is included in the plot.*

Chapter 6

Conclusion and Outlook

For the study presented in this thesis a new TPC prototype was designed, built and successfully commissioned. It was shown that a stable operation of a TPC with GEM readout at high magnetic fields is possible. This was seen during data taking of 800,000 events (500,000 events at the 5 T magnet and 300,000 events in the 6 GeV electron testbeam at DESY) in 2004 with this prototype. The data taken was used to carry out detailed performance studies for the TPC prototype showing that the chamber works reliably and that its behaviour is well understood.
However, from the results of the gain and drift velocity stability measurements it can be concluded that the development of a slow control system for the gas properties such as temperature and pressure, could assist greatly in the interpretation of the results. Further improvements of the gas system, e.g. the replacement of the copper tubes by stainless steel tubes, are required to drive the prototype to its performance limit.
The design of such a system is already in progress and it is expected to be available already for the next measurements with the prototype. From the investigation of the edge effects we also conclude that a change of the pad plane design is mandatory to reduce the cross talk effects and therefore to exploit the full capability of the chamber for point resolution studies.

Using the Triplet method first results of the point resolution as a function of the drift length in the presence of magnetic fields up to 4 T were presented.
The measurements with both non-staggered and staggered pads using a gas mixture of argon (93 %), methane (5%) and carbon dioxide (2%) are affected dramatically by bias effects due to the reconstruction of the hit position.
In the case of the non-staggered pads this bias leads to a shift in the reconstructed track position, but the measured point resolution still reflects the width of the charge cloud. The achieved point resolution reaches almost the goal for a TPC at the ILC.
For staggered pads this is not valid anymore and the measured point resolution is a convolution of the point resolution due to the width of the charge cloud and the bias effects due to the reconstruction of the hit position.
Since in a full size TPC the pad arrangement will vary between the extreme cases of staggered and non-staggered pads used in the presented study, this result arouses concerns about the feasibility to use rectangular pads of $2.2 \times 6.2\ \mathrm{mm}^2$ for a GEM based readout in a TPC.

This result agrees with the simulation shown in fig. 1.8, which indicated that rectangular pads of 2×6 mm^2 are too large to reach the the goals for a TPC at the ILC.

Following the study presented in this thesis, three recommendations can be made to fulfil possibly the requirements:

Introduction of new track fit methods: Since the reconstruction of the hit position is limited by the fact that the charge cloud is frequently collected only on one pad, new track fit methods have to be investigated, which take into account the charge distribution on all rows at the same time [61].

Different pad geometries: The use of more sophisticated pad geometries such as chevrons has to be studied. A simulation study related to the optimisation of such a pad geometry is currently ongoing [62].

Reduction of the pad size: A further possibility to improve the point resolution, which has to be investigated, is the reduction of the pad size. This leads of course to an increase of the number of readout channels and therefore to an increase of the costs of a full size TPC. Following this recommendation the design of a new pad plane for the TPC prototype with smaller pads is already in progress and further measurements will be performed soon. As concluded from the measurements of the diffusion coefficients at 0 T the operational settings, such as the gain, should be revised for these measurements.

The results of the study presented here constitute a platform for further studies needed for the development of a TPC with GEM readout, which is able to fulfil the requirements for a TPC at the ILC.

A study of the double track resolution in the presence of high magnetic fields, which for example is important for the concept of particle flow (PFLOW), using a laser setup will apply this prototype for the measurements [63]. The according modifications of the TPC prototype are currently performed.
Another topic which has to be investigated is the capability of a GEM readout in a TPC to measure dE/dx. The presented TPC prototype might also contribute to this study.

Part II

Measurement of Beauty Cross Sections in Deep Inelastic Scattering at HERA

Chapter 7

Introduction

In the preface already a short overview of the Standard Model was given. This part of the thesis focuses on the strong force which acts only between quarks and gluons. As a consequence of the strong force the quarks are bound into composite hadrons and can not be observed as free particles. Within the SM the strong force is described by *Quantum Chromodynamics* (QCD). The study of the production of *heavy quarks* gives a good opportunity to test the reliability of QCD. The *charm*, *bottom* and *top quark* belong to the class of heavy quarks, since their mass is larger than the energy scale at which quarks are confined into hadrons ($\Lambda_{QCD} \approx 200$ MeV). The other quarks are accordingly referred to as *light quarks*.

At the HERA collider in Hamburg with a centre-of-mass energy of around $\sqrt{s} \approx 320$ GeV it is only possible to produce charm and beauty quarks as heavy quarks. Various measurements of their cross section were performed or are ongoing at both high energy experiments H1 and ZEUS. While the results of the measurements of the charm cross section are compatible with the predictions of QCD, previous measurements indicate a beauty production rate, which lies above the theoretical predictions (fig. 7.1). An excess was also observed in $\gamma\gamma$ reactions at LEP and at the $p\overline{p}$ collider Tevatron.
The previous study in the kinematic region of deep inelastic scattering (DIS) ($2 < Q^2 < 100$ GeV^2) by. J. Kroseberg [64] suffered from limited statistics. In this thesis, for the first time, a sufficiently large data sample is available allowing for the measurement of differential beauty cross sections to evaluate QCD. In a parallel study the measurement was performed also in the *photoproduction region* ($Q^2 \approx 0$ GeV^2) exploiting the same event topologies, but with a three times larger statistics. This gave the opportunity to test both the experimental tools and partly the systematics with better precision.

The process investigated in this study is the semi-muonic beauty decay in high-energy *ep* scattering with one jet in the Breit frame or two jets in the laboratory frame, respectively:

$$ep \rightarrow eb\bar{b}X \rightarrow e\mu j(j)X \; . \tag{7.1}$$

Since the production of beauty is heavily suppressed at HERA energies in comparison to the background processes such as charm and misidentified light quarks, a separation between signal and background on an event by event basis is not possible. Fortunately

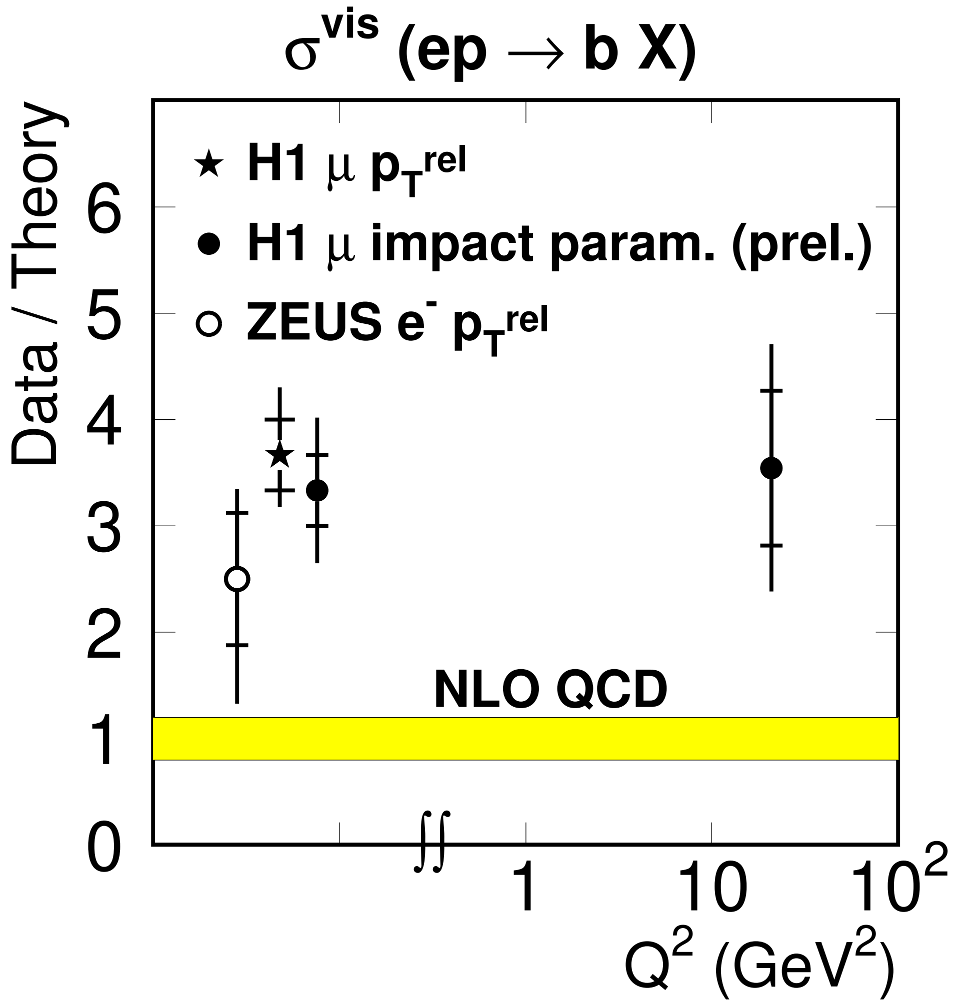

Figure 7.1: *Ratio of measured beauty production cross section over the result of Next-To-Leading order calculations. (Status 2001).*

there are two established techniques to enrich the inclusive muon sample with the beauty signal. The p_t^{rel} method exploits the large beauty mass by measuring the relative transverse momentum between muon and the associated jet. The second method is based on the long beauty life time and is called *signed impact parameter* δ .

The second part of this thesis is structured in the following way: In Chapter 8 the theoretical background of *ep* scattering and beauty physics is presented. Chapter 9 includes a description of the HERA collider and the subdetectors of the H1 detector most relevant for this analysis. The reconstruction procedure and the selection criteria are introduced in Chapter 10, while the results of the beauty cross section measurements are presented in Chapter 11. Finally, in Chapter 12 the results are compared with Next-to-Leading order calculations and discussed. Chapter 13 includes the conclusions and outlook.

Chapter 8

Theoretical Framework

8.1 Quantum Chromodynamics

In the sixties *quarks* were introduced as the constituents of hadrons to explain in a simple way the large number of discovered hadrons. This simple quark-parton model (QPM) demands that baryons consist of three quarks and mesons of a pair of quark and anti-quark. This model had two significant problems: 1) due to their small mass single quarks should be produced easily in a large number and therefore should have been seen in experiments and 2) also it could not explain the existence of e.g. the Δ^{++}, consisting of three u quarks, since due to the Pauli principle three identical quarks could not occupy the same state. The suggested solutions for these problems were the assumption that the quarks are confined in the hadrons and that an additional quantum number exists. The quantum number was called colour and can take the values *red, green* and *blue.* In this way it is possible to construct an asymmetric total wave function for the nuclear resonances Δ^{++}. The *Quantum Field Theory* (QFT) of colour interactions is *Quantum Chromodynamics* (QCD). The underlying gauge group is the non-abelian *SU(3).* While in *Quantum Electrodynamics* (QED) the interaction between two charged particles is mediated by the electrically neutral photon, in QCD the gauge mediator is the gluon. In contrast to the photon, which has no electrical charge, the gluons are not colour neutral, each gluon carries colour and anti-colour. With three colours and three anti-colours it is expected, that nine different gluons exist, forming a colour-octet and a colour-singlet, but the colour-singlet is not realized in nature. The gluons are massless and have spin 1. The existence of gluons and the colour charge is well supported by experimental results. The existence of gluons was e.g. confirmed in three jet events at the PETRA collider in Hamburg, and the number of colours was measured by the ratio R of the cross section $e^+e^- \rightarrow hadrons$ and the cross section $e^+e^- \rightarrow \mu^+\mu^-$

$$R = \frac{\sigma(e^+e^- \rightarrow hadrons)}{\sigma(e^+e^- \rightarrow \mu^+\mu^-)} = N_c \sum_{2m_q<E_{cm}} Q_q^2 \tag{8.1}$$

yielding $N_c = 3$ [65].

Calculations of particle scattering cross sections within QCD are accomplished using perturbation theory, *perturbative QCD* (pQCD), thereby one expands into a power series of the *strong coupling constant* α_s and sums over all contributing Feynman diagrams. Some Feynman diagrams beyond *leading order* (LO) cause divergences in the cross section. The *ultraviolet divergences* arise from Feynman diagrams including internal loops, as shown in fig. 8.1. Since one has to integrate over the whole phase space,

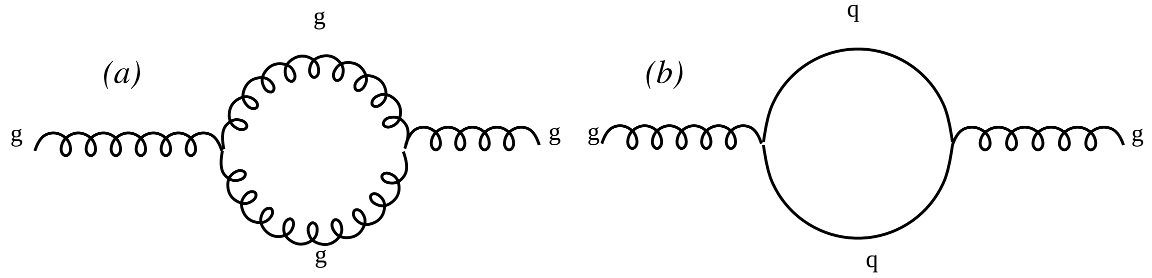

Figure 8.1: *One-loop diagrams which contribute to ultraviolet divergences [64].*

the momentum $k \to \infty$ of these loops yield singularities in the cross section. Another divergence is caused by soft gluons, which are emitted under a small angle $\theta \to 0$ to the quark propagation direction. This is called *infrared* or *collinear divergence*.
A *regularisation* is carried out, which means that the four-dimensional integrals are replaced by $4 + \epsilon$ dimensional ones. After the integration the transition $\epsilon \to 0$ is accomplished. The remaining simple pole divergences can be removed by introducing an arbitrary renormalisation scale μ_R. For all measurable quantities it is required that they are independent of the choice of the renormalisation scale. This can be achieved by replacing the bare parameters of the theory, e.g. the coupling, by the renormalised quantities, which are identical to the measured observable. The dependence of the parameters on μ_R is described by the renormalisation group equation

$$\beta(\alpha_s) = \frac{\partial \alpha_s(\mu_R)}{\partial \mu_R)} \ , \tag{8.2}$$

which defines the β function. Integration of eq. 8.2 yields in first order for the dependence of the strong coupling constant α_s at the scale μ_R:

$$\alpha_s(\mu_R^2) = \frac{12\pi}{(33 - 2n_f)\ln(\mu_R^2/\Lambda_{QCD})} \ . \tag{8.3}$$

Here, n_f is the number of quarks with a mass below μ_R and Λ_{QCD} is a parameter, which has to be determined experimentally. The world average value for α_s at the mass of the Z^0 is [1]:

$$\alpha_s(M_Z) = 0.116^{+0.003}_{-0.005}(exp.) \pm 0.003(theo.) \ . \tag{8.4}$$

Fig. 8.2 gives an overview of the results of the various α_s measurements. This corresponds to a value of $\Lambda_{QCD} = 202$ MeV [66]. Eq. 8.3 shows, that the strong coupling gets large for small values of μ_R (see also fig. 8.3), which corresponds to large distances and soft interactions. For this reason α_s is also called running coupling. This property of the strong coupling explains, that one has never discovered single quarks. The effect that the quarks can not leave the hadron is called *confinement*. The composite hadron

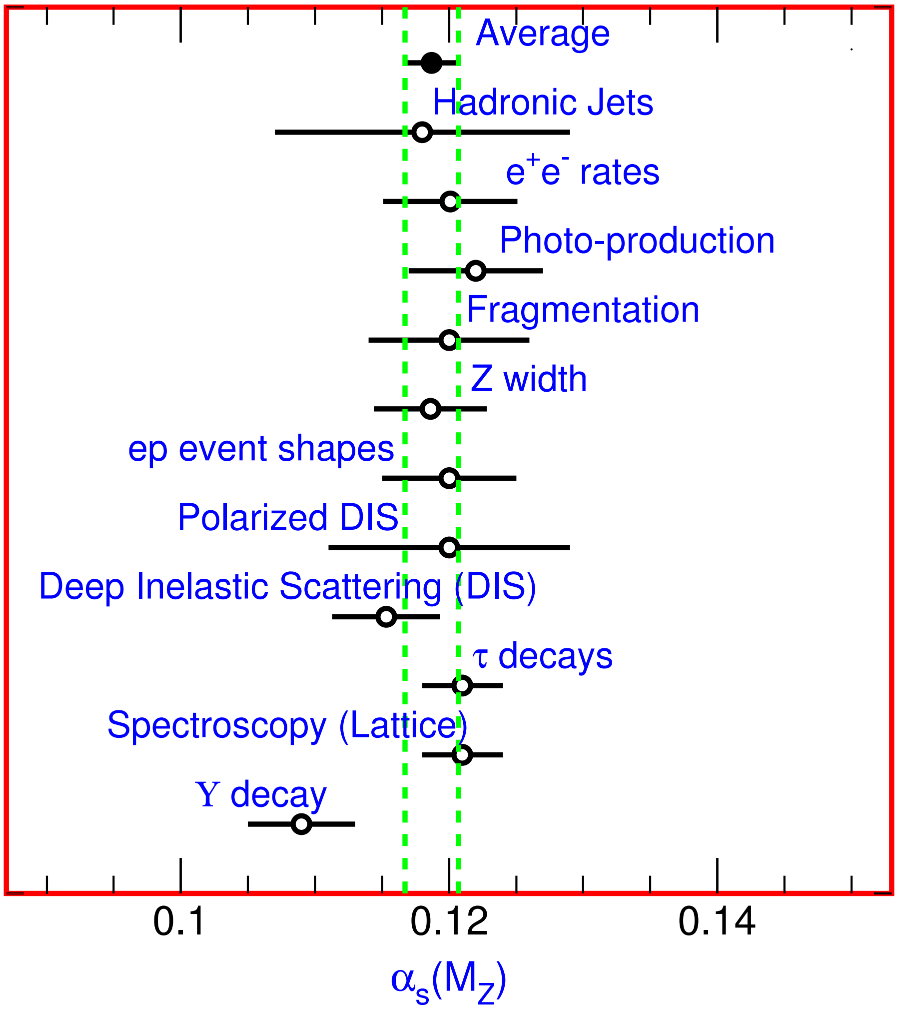

Figure 8.2: *Collection of available measurements of α_s in various physics processes [1].*

is colour-less, as opposed to the quarks. On the other hand hard interactions, which means interactions taking place on a large scale corresponding to small distances, imply that the quarks within a hadron react almost like free particles. This behaviour is known as *asymptotic freedom*.
It is important to remember that pQCD is only applicable, if $\alpha_s \ll 1$. For all other cases phenomenological models or *lattice QCD* have to be used.
A more detailed introduction to QCD is given in [66, 67]

8.2 Kinematics of *ep* Physics

A good test of pQCD is given by the electron- or positron-proton scattering processes

$$ep \rightarrow lX \ . \tag{8.5}$$

Fig. 8.4 shows the basic diagram and kinematics. The interaction is described by a single virtual gauge boson exchange. Depending on the charge of the exchange particle

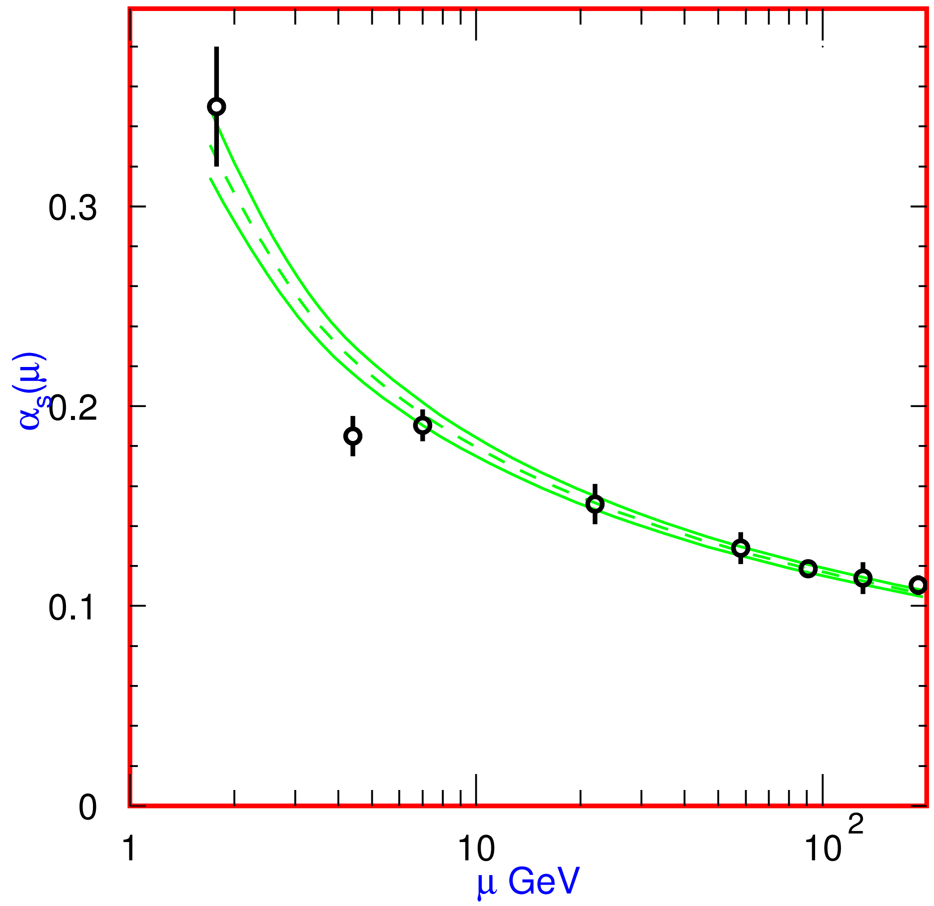

Figure 8.3: *Scale dependence of α_s [1].*

one distinguishes between *neutral current processes* (NC), $ep \to eX$, if the boson is a γ or a Z^0 and *charged current processes* (CC), $ep \to \nu X$, if the exchange particle is a $W^{\pm}$. Here, X denotes the hadronic final state. These processes can be characterised by a small set of Lorentz-invariant variables. One is the gauge boson virtuality

$$Q^2 = -q^2 = -(k - k')^2 \ . \tag{8.6}$$

For the virtuality $Q^2 \geq 0$ holds. Depending on the virtuality Q^2 the ep collisions are classified in two categories. The case $Q^2 \approx 0$ GeV^2 is called *photoproduction*, since the photon is almost real, while if $Q^2 \geq$1-2 GeV^2 one refers to as *deep inelastic scattering* (DIS).
Another invariant quantity is the square of the centre-of-mass energy

$$s = (p + k)^2 \tag{8.7}$$

The relative energy transfer y at the positron-boson vertex in the proton rest frame is given by

$$y = \frac{p \cdot q}{p \cdot k} \tag{8.8}$$

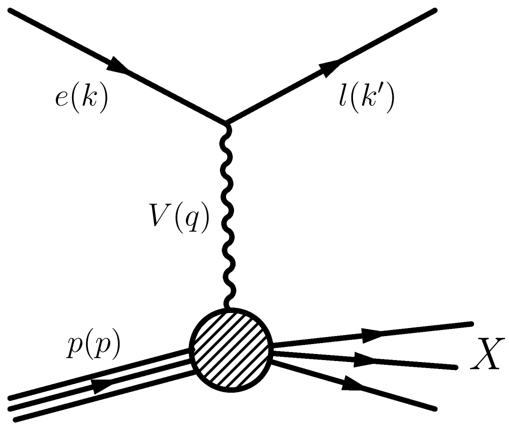

Figure 8.4: *Basic diagram of an ep scattering process. In the case of a NC process the exchange boson V is either a γ or a Z. In a CC process V is a $W^{\pm}$ boson.*

with $0 \leq y \leq 1$. Finally the *Bjorken scaling variable* x is given by

$$x = \frac{Q^2}{2p \cdot q} \ , \tag{8.9}$$

where $0 \leq x \leq 1$. In the QPM it is assumed that the quarks, also called partons, in a fast moving hadron are almost independent of each other and that they have a negligible transverse momentum. Each parton is carrying a fraction x_i of the total four-momentum of the hadron: $p_i = x_i P$. Deep inelastic scattering off the proton is interpreted as elastic scattering off partons , and x is identified as the momentum fraction x_i.
If the masses of the particles involved in the interaction are negligible compared to the centre-of-mass energy $\sqrt{s}$, these Lorentz invariant kinematic variables fulfil

$$Q^2 = xys \ . \tag{8.10}$$

A more detailed overview of *ep* physics can be found in [68, 69].

8.3 DIS cross section and Proton Structure

In this thesis only NC processes are investigated. In this case the double differential cross section $\frac{d^2\sigma^{NC}}{dx\ dQ^2}$ is given by:

$$\frac{d^2\sigma^{NC}}{dx\ dQ^2} = \frac{4\pi\alpha^2}{xQ^4}(xy^2F_1^{NC}(x,Q^2) + (1-y)F_2^{NC}(x,Q^2) + y(1-\frac{1}{2}y)F_3^{NC}(x,Q^2)) \ . \tag{8.11}$$

F_1^{NC}, F_2^{NC} and F_3^{NC} are called *structure functions*. The structure functions arise from the fact, that the proton enters the interaction as a composite object.
In the case that $Q^2 \ll M_Z^2$ the contribution from Z exchange can be neglected and, considering also that there is only a small contribution from longitudinal polarised

photons, eq. 8.11 is reduced to

$$\frac{d^2\sigma}{dx\ dQ^2} = \frac{2\pi\alpha^2}{xQ^4}(1+(1-y)^2)F_2^{em}(x,Q^2) \tag{8.12}$$

When the DIS processes occur in the infinite momentum frame, $|\vec{p}|^2 \ll m_p^2$, the scattering can be described in good approximation in the QPM. In this model the electron scatters elastically with a single quark, while the two other quarks are not affected and, therefore, called *spectator quarks*. They form the *proton remnant*. If these assumptions are fulfilled, the cross section can be calculated by summing over all transition amplitudes for the elastic scattering of an electron with a quark within the proton. In this case the structure function F_2^{em} is given by

$$F_2^{em}(x,Q^2) = x\sum_j c_j^2 \cdot f_j(x,Q^2)\ , \tag{8.13}$$

where the sum runs over all quark and anti-quark flavours j, c_j is the charge of the quark flavour j and f_j describes the probability to find a quark (anti-quark) with momentum fraction x in the proton. In the naive QPM, where the proton only consists of two u and one d quarks, the *valence quarks*, F_2^{em} depends only on x. This behaviour is known as *scaling*. The experimental data, though, show a *scaling violation*, which is caused by the fact that not only the valence quarks, but also gluons and gluon-induced quark pairs (*sea quarks*) are constituents of the proton.

8.3.1 Factorisation and Parton Density Functions

As mentioned before pQCD only applies if $\alpha_s \ll 1$, this suggests to divide the *ep* process in two parts: a short distance part, which describes the hard interaction between the electron and the parton and which can be calculated within pQCD and a long distance part, which includes low energy processes and also collinear divergences as mentioned in sec. 8.1.

The structure function F_2 can then be expressed as a convolution of *coefficient functions* C^i, which can be calculated perturbatively, and *parton density functions* $f_i(\xi)$ (PDFs), which describe the probability of finding a parton of type i with a fraction ξ of the momentum of the proton:

$$F_2 = \sum_{i=partons} \int_x^1 d\xi C^i\left(\frac{x}{\xi}, \frac{Q^2}{\mu_R}, \frac{\mu_F}{\mu_R}\right) f_i(\xi,\mu_F,\mu_R) \tag{8.14}$$

In principle the PDFs depends in first order only on x, but, since these *bare PDFs* are experimentally not accessible, a factorisation scale μ_F is introduced in analogy to the renormalisation scale μ_R absorbing the collinear divergences. The division in hard and soft processes is, therefore, defined by the scale μ_F. The way how singularities are absorbed in the PDFs depends on the chosen *factorisation scheme*.

Nevertheless, if the factorisation scheme and scale are fixed, the PDFs must be independent of the actual scattering process, they must be *universal*.

8.3.2 Parton Evolution Equations

As mentioned before the PDFs cannot be calculated within the framework of pQCD, but what can be calculated perturbatively is the dependence of the PDFs on the chosen scale μ_F. The differential equations, which describe this dependence are called *parton evolution equations*. The knowledge of them allows to extract the PDFs from a fit to the experimental structure function data (fig. 8.6).
The calculations are equivalent to summing over *ladder diagrams*. Fig. 8.5 illustrates such a ladder diagram, where $k_{t,i}$ and x_i are the transverse momentum and the longitudinal momentum fraction of the virtual parton, while the transverse momentum of the produced parton is labelled $p_{t,i}$. The longitudinal momentum fraction z of the parton $i+1$ from the momentum of the parton i is given by $z = x_{i+1}/x_i$.
For the calculations of them an integration over all internal momenta has to be performed. These can be simplified by introducing an *ordering scheme* in the emission process. Due to this approximation, there are different solutions for the parton evolution equations depending on the investigated phase space. In the following two models, which are relevant for this thesis, are shortly presented.

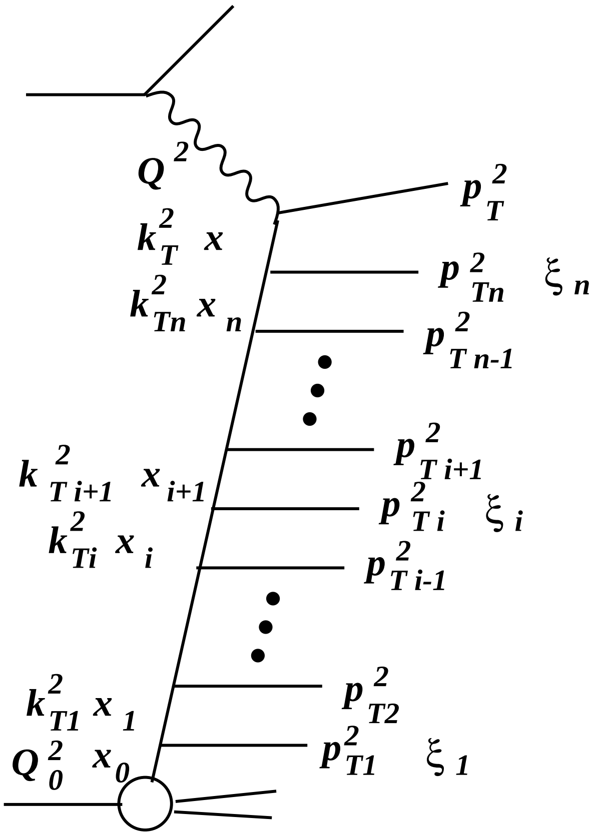

Figure 8.5: *Ladder diagram illustrating parton evolution [70].*

DGLAP model

The Dokshitzer-Gribov-Lipatov-Altarelli-Parisi (DGLAP) evolution [71–75]. is based on the *leading-log approximation* in which the sum is performed over all terms proportional to $(\alpha_s^2(Q^2)\ \ln(Q^2/Q_0^2))^n$. Terms of the form $\alpha_s^2(Q^2)\ \ln(1/x)$ are neglected. This is a valid approximation for the case that $\ln Q^2 \gg \ln(1/x)$ and corresponds to a strong ordering of the transverse momenta $k_{t,i}$:

$$Q_0^2 \ll k_{t,i} \ll k_{t,i+1} \ll \cdots \ll k_{t,n} \ll Q^2 \tag{8.15}$$

Here, Q_0^2 denotes a suitably chosen starting scale. The DGLAP equations are given in leading order by

$$\begin{aligned}
\frac{df_{qi}(x,Q^2)}{d\ln(Q^2)} &= \frac{\alpha_s(Q^2)}{2\pi}\int_x^1 \frac{d\xi}{\xi}\left[P_{qq}\left(\frac{x}{\xi}\right) f_{qi}(\xi,Q^2) + P_{qg}\left(\frac{x}{\xi}\right) f_g(\xi,Q^2)\right] , \qquad (8.16)\\
\frac{df_g(x,Q^2)}{d\ln(Q^2)} &= \frac{\alpha_s(Q^2)}{2\pi}\int_x^1 \frac{d\xi}{\xi}\left(\sum_i\left[P_{gq}\left(\frac{x}{\xi}\right) f_{qi}(\xi,Q^2) + P_{gg}\left(\frac{x}{\xi}\right) f_g(\xi,Q^2)\right]\right) ,
\end{aligned}$$

where f_{qi} is the quark density, while f_g describes the gluon density. The *splitting functions* $P_{mn}(z)$ represent the probability of finding a parton of type m with momentum fraction z of the mother parton (type n), which carries the momentum fraction x of the proton.
Fig. 8.6 shows that the data can be described with the DGLAP equations even to very low values of x and Q^2 . This was not expected, but it was assumed that in this kinematic region the data should be described better by the CCFM model, which is introduced in the next section.

CCFM model

The evolution model introduced by Ciafaloni, Catani, Fiorani and Marchesini (CCFM) [79–82] is based on a different ordering scheme than the DGLAP one. In this scheme the evolution is not performed in Q^2 and x, but in the polar angle of the emitted parton relative to the incoming proton.

$$\theta_i < \theta_{i+1} \ . \tag{8.17}$$

This corresponds to order according to

$$Q_0 \ll z_i\zeta_i \ll z_{i+1}\zeta_{i+1} \ll \cdots \ll z_n\zeta_n \ll \overline{\zeta} \ . \tag{8.18}$$

Here, the variable ζ is given by

$$\zeta_i = \frac{p_{t,i}}{1-z} \ , \tag{8.19}$$

$\overline{\zeta}$ is an additional scale related to the maximum allowed emission angle. The gluon density $f_g(x,Q^2)$ can be extracted from the *unintegrated gluon density* $\mathcal{A}_g$ by integrating over k_t:

$$f_g(x,Q^2) = \frac{1}{x}\int_0^{Q^2}\frac{dk_t^2}{k_t^2}\mathcal{A}_g(x,k_t^2,\overline{\zeta}) \ . \tag{8.20}$$

The evolution equation which describes the dependence of $\mathcal{A}_g$ on the scale $\overline{\zeta}$ is given by

$$\overline{\zeta}^2\frac{d}{d\overline{\zeta}}\frac{x\mathcal{A}_g(x,k_t^2,\overline{\zeta})}{\Delta_S(\overline{\zeta},Q_0)} = \int_0^{2\pi}\frac{d\phi}{2\pi}\int_x^1 dz\frac{\overline{P}(z,\overline{\zeta},k_t)}{\Delta_S(\overline{\zeta},Q_0)}\frac{x}{z}\mathcal{A}_g(x/z,k_t'^2,\overline{\zeta}) \ , \tag{8.21}$$

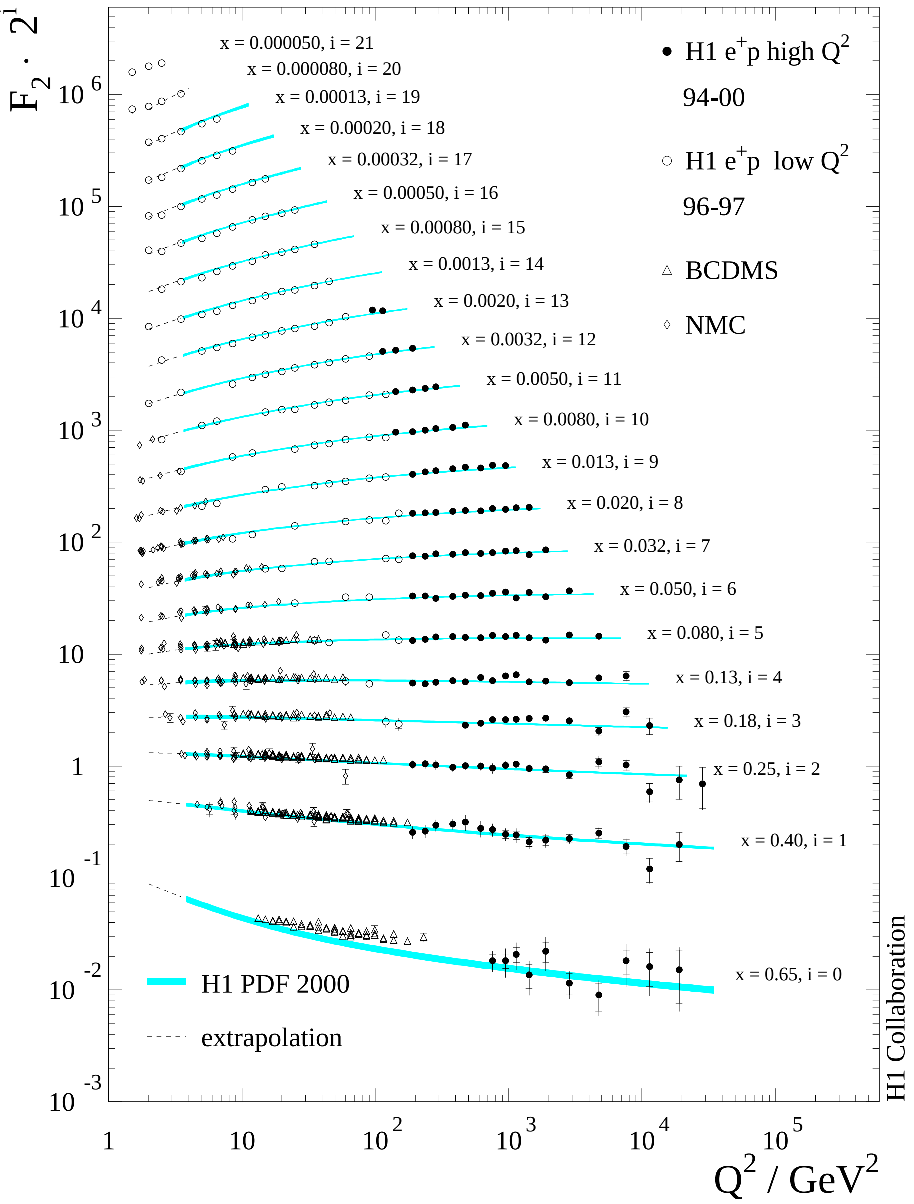

Figure 8.6: *Structure function $F_2(x, Q^2)$ as a function of Q^2 at fixed values of x (H1 data from [76, 77], see also [78]).*

with $\vec{k}_t' = ((1-z)/z)\vec{\zeta}+\vec{k}_t$ and $\vec{\zeta}$ calculated at a azimuthal angle ϕ. The factor Δ_S is the so called *Sudakov form factor* [83] and $\overline{P}$ is the relevant unintegrated splitting function. The corresponding equation that describes the quark evolution is not reported here. Since the CCFM equations also take into account the terms proportional to $\alpha_s \cdot \ln(\frac{1}{x})$, it should also cover the region where $\ln Q^2 \ll \ln\frac{1}{x}$ is. For larger values of x it agrees with the results from the DGLAP model.

8.4 Hadron Fragmentation and Jets

As mentioned in sec. 8.1 single quarks have never been observed due to colour confinement. In the detectors only colour-neutral hadrons are detected, which are a result of the *fragmentation* (also called *hadronisation*) of produced partons. Apart from the partons from the hard interaction further partons are produced in *parton showers*. While the parton showers occur at energies which justify the use of perturbative approaches, the final fragmentation process itself has to be described by phenomenological models.

8.4.1 Parton Showers

The production of a large number of partons in the parton showers is modelled by multiple emission processes. The probability that a parton m emits a parton n is described by the splitting functions introduced in sec. 8.3.1. For the calculations also the virtuality of the emitting parton is relevant. One distinguish two cases:

Initial state parton shower: In this case the virtuality of the parton coming from the proton is negative. The parton emits time-like or real partons until it enters the hard subprocess. In Monte Carlo generators (sec. 8.6.2) this is usually implemented in the form of a *backward evolution*, where one starts from the parton entering the scattering process and evolves towards the incoming proton.

Final state parton shower: Every outgoing parton of the hard subprocess can be the source of a *final state parton shower*. After each step of emitting a time-like parton the virtuality of the emitting parton decreases to lower virtualities.

The parton shower, also referred to as *parton cascade*, stops, when the virtuality of the outgoing partons reaches a minimum of around 1 GeV. Below this value perturbative methods cannot longer be applied and one has to rely on phenomenological hadronisation models.

8.4.2 Hadronisation Models

There are some models available, which describe the transition from partons from the parton shower to hadrons, which are detectable in the experiment. The models are only phenomenological without any strong theoretical justification [84]. Two different models are presented in the following:

Independent fragmentation: The simplest scheme of generating hadron distributions is the independent fragmentation model. In this model all outgoing partons hadronise independently from each other. Fig. 8.7 gives a schematic representation. The probability that a quark i forms a hadron h with momentum fraction z of the longitudinal momentum of the quark is given by the *fragmentation function* $D_i^h(z)$. It is assumed that the transverse momenta of the hadrons with respect to the flight direction of the original quark is a Gaussian distribution. New $q\overline{q}$ pairs emerge from the interaction of the original partons with the vacuum. This process is repeated as long as the available energy is large enough.

String fragmentation: A more advanced model of fragmentation is the string fragmentation model. In this model the original $q\bar{q}$ pair is connected via strings, representing the colour field. The string has a uniform energy per unit length. If the distance between them is large, the energy becomes sufficiently large to break up the string in hadron-sized pieces through spontaneous $q\bar{q}$ pair production in its intense colour field. Gluons are introduced in this model as "kinks" in the strings.

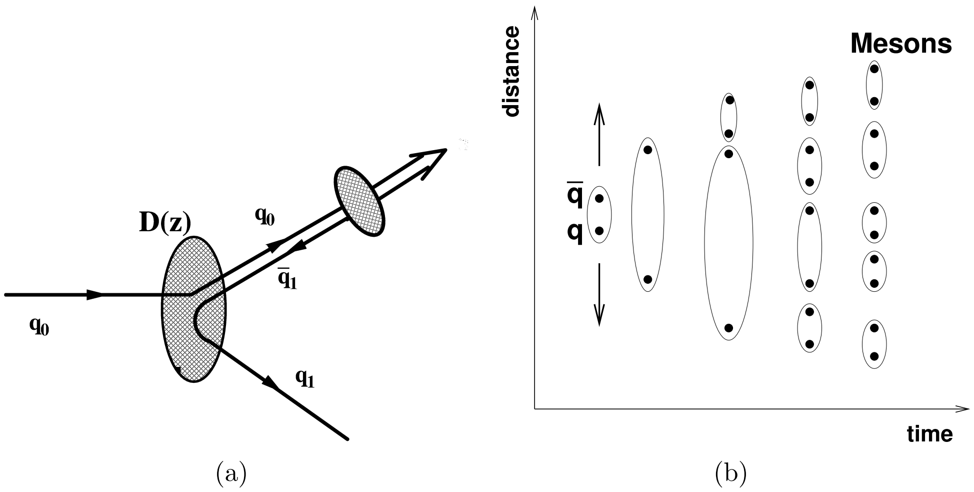

Figure 8.7: *Hadronisation models: (a) independent model, (b) string model [66].*

8.4.3 Jets

As discussed in the previous section each of the outgoing partons of a hard sub process produces hadrons. If the momenta of the outgoing partons are high enough, these groups of hadrons are not uniformly distributed, but collimated in *jets*.
Although higher order QCD processes have to be considered in the process of jet fragmentation, it is expected that the investigation of the jet topology allows to draw conclusions on the underlying partonic process. To be able to compare experimental jet-based observables with theoretical predictions, it is necessary to use a well-defined procedure to group the hadrons into jets. There exist several different *jet algorithms* to perform this task [85–87]. Also an adequate algorithm to calculate the jet momentum from the momenta of the particles has to be chosen (*recombination scheme*).
The measured jet properties depend on the reconstruction method. To ensure that the measurements are nevertheless comparable with pQCD the jet algorithm has to fulfil several requirements:
It must be *collinear* and *infra-red safe*, which means that the jet observable should not be influenced by collinear or soft parton emission.
The jet topology should reflect the partonic final state quite well, in order to have small *hadronisation corrections* between the jet based observables and the corresponding quantities on the parton level. Furthermore, the jet algorithm should preserve factorisation (sec. 8.3.1) between the beam fragmentation and the hard process. A suitable algorithm is the *longitudinally invariant k_t algorithm* [87] as presented in sec. 10.4.1.

8.4.4 Jets in the Breit Frame

In the factorisation the perturbatively calculable coefficient functions C^i depend only on the ratio x/ξ and can, therefore, be calculated without any reference to the momentum P of the incoming proton. To preserve this feature, the jet algorithm should not introduce any other form of dependence on x or ξ. The coefficient functions must be Lorentz-invariant and can only depend on the involved parton i, its momentum ξP, the polarisation p of the virtual photon and on the momentum of the virtual photon q.

$$C_p^i = C_p^i(\xi P \cdot q, q^2) \ . \tag{8.22}$$

In [87] it is shown, that for a well-defined jet algorithm an auxiliary vector v has to be introduced. The jet coefficient functions are then given by

$$C_P^i = C_p^i(\xi P \cdot q, q^2, \xi P \cdot v, q \cdot v, v^2, d_{cut}) \ . \tag{8.23}$$

Here, d_{cut} denotes a scalar resolution variable related to the jet algorithm. Furthermore, to preserve the y dependence of the total cross section (eq. 8.12) the auxiliary vector v should be written as a linear combination of P and q: $v = \alpha P + \beta q$. The coefficients α and β can in principle be any function of x and Q^2. The simplest example of a suitable vector is

$$v = 2xP + q \ . \tag{8.24}$$

In this case $v^2 = Q^2$ and $v \cdot q = 0$, i.e. the virtual photon momentum is purely space-like in the rest frame of v, which is called *Breit frame*.
The z direction of the Breit frame is generally chosen such, that it coincides with the direction of the incoming proton. The momentum q of the photon is then given by

$$q = (0, 0, 0, -Q) \tag{8.25}$$

Fig. 8.8 (a) shows the back-scattering of an incoming quark on a photon in the Breit frame according to the QPM description. The momentum of the quark before (p) and after ($p^{'}$) the reaction is given by

$$\begin{aligned} p &= (Q/2, 0, 0, Q/2) \ , \\ p^{'} &= (Q/2, 0, 0, -Q/2) \ . \end{aligned} \tag{8.26}$$

In the head-on collisions zero transverse momenta are measured both in the initial and in the final state. The situation changes in the case of *Boson-Gluon-Fusion* (BGF) processes, which is discussed in sec. 8.5.1. The process is shown in fig. 8.8 (b). In this case particles with net transverse momenta can arise from the hard process, while the transverse momentum sum is still zero. Since BGF processes are thought to be the main source of heavy quark production in ep collisions, this has to be taken into account, when measuring the cross section of beauty in DIS [1].

[1]For further information about the Breit frame see also [88–91].

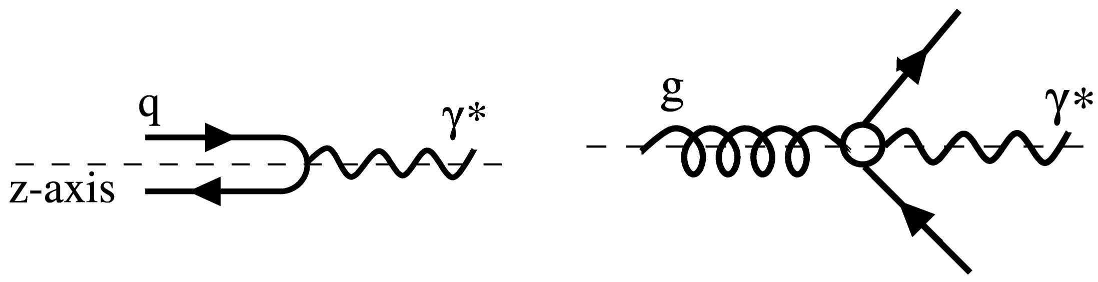

(a) (b)

Figure 8.8: *Breit frame: (a) in QPM, (b) in BGF. [91]*

8.5 Beauty Production and Decay

Beauty and charm quarks are here referred to as *heavy quarks*, because of their masses ($m_b \approx 4.75$ GeV and $m_c \approx 1.5$ GeV) being much heavier than the masses of the *light quarks* u, d and s. Since the mass can provide a hard scale, especially in the case of the b quark, the measurement of the heavy quark production rate is a good test of pQCD even at relatively small Q^2 values.

8.5.1 Production Processes

In the following the two main production processes of beauty quarks in leading order are discussed: BGF and *resolved photon processes.* A non negligible contribution to the cross section comes also from *next-to-leading order* (NLO) processes.

Boson-Gluon-Fusion

In the BGF process a photon coming from the electron and a gluon from the proton produce a $b\bar{b}$ or a $c\bar{c}$ pair as illustrated in fig. 8.9. The cross section in this case can be calculated, according to [92] and [64], via

$$\sigma_{BGF} = \frac{2\pi c_q^2 \alpha_{em} \alpha_s}{\hat{s}} \left((2 + 2\omega - \omega^2) \ln \left(\frac{1+\chi}{1-\chi} \right) - 2\chi(1+\omega) \right) , \tag{8.27}$$

where $\hat{s}$ is the photon gluon centre-of-mass energy, c_q is the charge of the produced quark and:

$$\begin{aligned} \omega &= \frac{4m_q^2}{\hat{s}} \\ \chi &= \sqrt{1-\omega} \end{aligned} \tag{8.28}$$

From eq. 8.27 follows directly, that due to the larger mass and the smaller charge the beauty production is heavily suppressed compared to the charm production. The kinematic region close to the beauty production threshold is strongly favoured, which leads to small transverse momentum p_t of the b quarks relative to the beam axis.

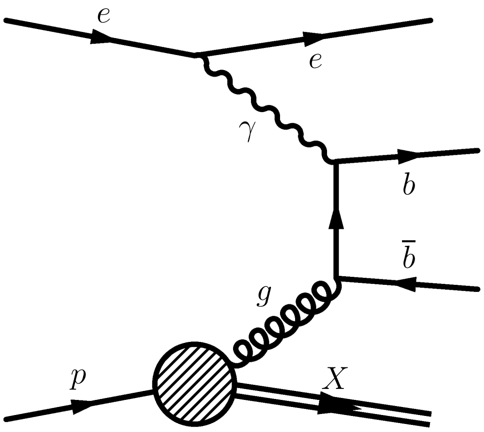

Figure 8.9: *Boson-Gluon-Fusion process in ep scattering.*

Resolved Photon Processes

Heavy quarks are also produced when the virtual photon from the lepton fluctuates into a $q\overline{q}$ pair. Fig. 8.10 shows two examples in LO.

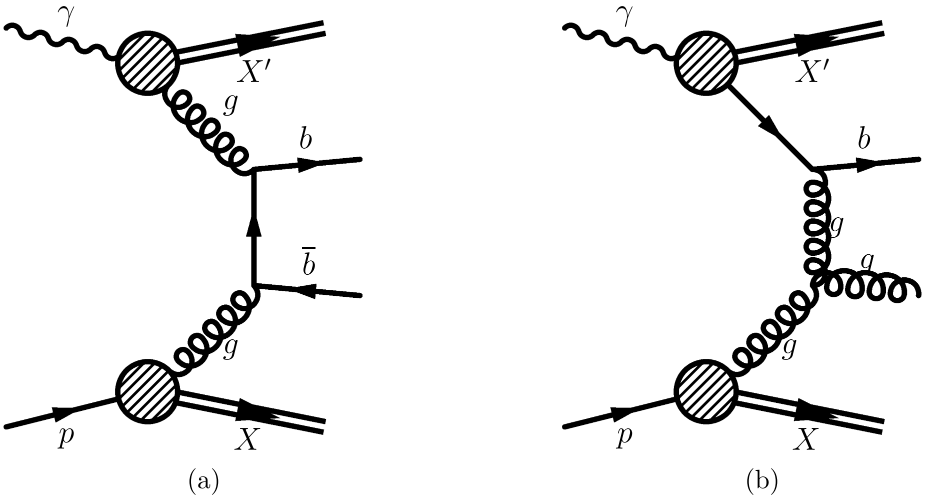

Figure 8.10: *Resolved Photon Diagrams which contribute to beauty production in ep scattering: (a) gluon-gluon fusion (a) excitation in the photon*

NLO Contributions

The production of beauty quarks does not only arise from LO processes, but a significant contribution comes from NLO diagrams, as shown in fig. 8.11. The calculations of these diagrams can be performed with two different approaches, depending on the ratio of the mass and the transverse momentum:

massive scheme: In the massive scheme only light quarks and gluons are considered as partons within the proton, while heavy quarks can only be produced dynamically in a hard subprocess. This approach is favourable, if the transverse momentum p_t of the heavy quark is comparable to or smaller than its mass.

massless scheme: If the mass of the heavy quark is much smaller than its transverse momentum the massless scheme should offer more reliable predictions. Due to collinear gluon emission from a heavy quark and gluon or photon splitting into a heavy quark pair, large terms proportional to $\ln(p_t^2/m_q^2)$ appear in the perturbative calculations, which might prevent the convergence of the perturbative series. This can be avoided by absorbing the collinear singularities into the fragmentation functions and PDFs. As a consequence the quark masses have to be set to zero, so that the heavy quarks are treated as constituents of the proton and can be produced in excitation processes.

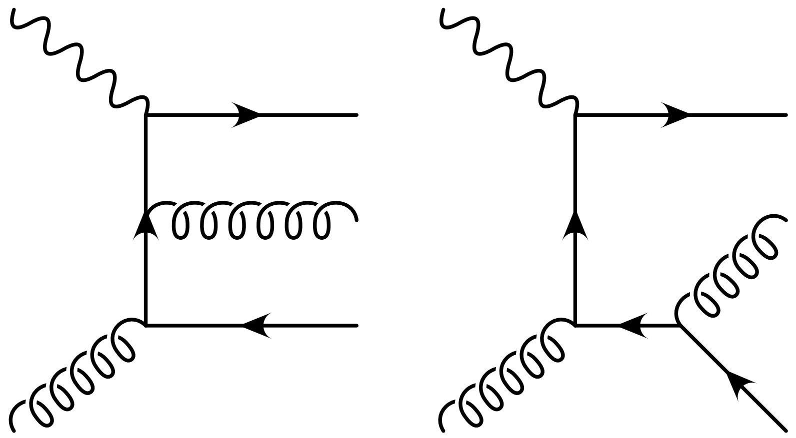

(a) (b)

Figure 8.11: *Two examples of NLO diagrams contributing to the heavy flavour production [64].*

8.5.2 Beauty Flavoured Hadrons

As already mentioned b quarks can not be produced as free particles, but only hadrons can be experimentally observed. In the following some important quantities of the b quark fragmentation and the formed beauty hadrons are summarised.

Fragmentation of Heavy Quarks

There are several different models available [93–96] which describe the fragmentation of heavy quarks in hadrons.
A simple and widely used model to describe hadronisation is based on the independent fragmentation (sec. 8.4.2). The *Peterson fragmentation function* [93] which describes in this model the probability of producing a hadron h with quark momentum fraction z is given by

$$\mathcal{D}_q^h(z) = \frac{1}{z}\left(1 - \frac{1}{z} - \frac{\epsilon_q}{1-z}\right)^{-2}, \tag{8.29}$$

where ϵ_q is a quark flavour dependent parameter which has to be determined experimentally [97]. Fig. 8.12 shows the shape of the Peterson function for beauty and charm.

Another fragmentation model, which is used for systematic studies in this thesis is the *Lund symmetric model* [98, 99], which uses the string fragmentation approach. The *Lund fragmentation function*, which corresponds in this model to the Peterson fragmentation function, is given by

$$\mathcal{D}_q^h(z) = \frac{1}{z}(1-z)^a \exp\left(-\frac{bm_t^2}{z}\right) \ . \tag{8.30}$$

Here, a is a quark flavour dependent parameter, b a universal parameter and m_t the transverse mass of the created hadron in the hadronisation process.

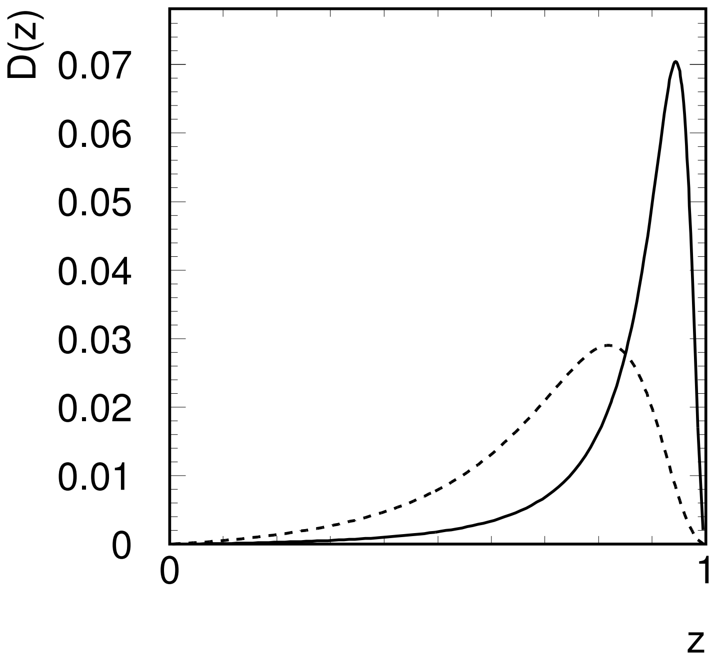

Figure 8.12: *Peterson fragmentation function: the solid line correspondents to the beauty quark while the dashed line describes the distribution for the charm quark. [66]*

Properties of Beauty Flavoured Hadrons

As mentioned above the b quark is considerably heavier than the c and especially much heavier than the light quarks. This is also reflected in the masses of hadrons with different flavour, which varies from $\approx$ 5.4 GeV for beauty flavoured hadrons to $\approx$ 1.9 GeV for charm flavoured hadrons and to $\approx$ 0.140-1.0 GeV for light flavoured hadrons.

In addition there is a significant difference in the lifetime between hadrons consisting of heavy and of light quarks, which arise from the different forces and available phase space for the decay. The decay of heavy flavoured hadrons arises mainly from the weak interaction.

There is also a significant difference in the lifetime between beauty and charm flavoured hadrons, which can not be explained by the mass difference between these quarks. The reason for this can be found in the different values for the corresponding elements V_{ij}

hadron	quark content	mass [MeV]	τ	$c\tau$
B^0	bd	5279.4 ± 0.5	1.536 ± 0.014 ps	460 μm
$B^{\pm}$	bu	5279.0 ± 0.5	1.671 ± 0.018 ps	501 μm
B_s^0	bs	5369.6 ± 2.4	1.461 ± 0.057 ps	438 μm
Λ_b^0	udb	5624.0 ± 9.0	1.229 ± 0.080 ps	368 μm
D^0	cu	1864.6 ± 0.5	0.410 ± 0.002 ps	123 μm
$D^{\pm}$	cd	1869.4 ± 0.5	1.040 ± 0.007 ps	312 μm
$D_s^{\pm}$	cs	1968.3 ± 0.5	0.490 ± 0.009 ps	147 μm
Λ_c^+	cud	2284.9 ± 0.6	0.200 ± 0.006 ps	60 μm
$\pi^{\pm}$	ud	139.6 ± 0.0004	26.033 ± 0.005 ns	7.805 m
$K^{\pm}$	us	493.7 ± 0.016	12.384 ± 0.024 ns	3.713 m
Λ^0	uds	1115.7 ± 0.006	$0.2632 \pm .0002$ ns	0.0789 m

Table 8.1: *Overview of a collection of beauty, charm and light flavoured hadrons [1].*

in the *Cabbibo-Kobayashi-Maskawa* (CKM) matrix. The CKM matrix elements offer a prediction for the probability of a certain decay channel. For the heavy quarks the most relevant decay channels are: $b \to cW^-$ and $c \to sW^+$. The corresponding matrix elements are [1]

$$\begin{aligned} |V_{cb}| &= 0.0413 \pm 0.0015 \ , \\ |V_{cs}| &= 0.996 \pm 0.013 \ . \end{aligned} \tag{8.31}$$

Both mass and lifetime are exploited in this thesis to distinguish between b quark events and background from c and uds hadrons. An overview about the relevant properties of the different flavoured hadrons is given in tab. 8.1.

8.5.3 The Semi-Muonic Beauty Decay

Although beauty flavoured hadrons are classified as *long-lived* particles, their lifetime is still too short to observe them directly in the detector. Therefore, it is strongly advised to choose a decay channel which yields a clean signature in the detector. A good candidate for this is the semi-muonic decay channel. As mentioned before the most relevant decay channel of a b quark is the decay in a c quark (the matrix element for $|V_{ub}|$ is approximately only 10% of $|V_{cb}|$) and a virtual W^-. With a probability of (10.68 ± 0.12)% [1] the W decays into a muon μ and the corresponding anti-neutrino ν_μ. Apart from this direct (*prompt*) decays, there is also a contribution from *cascade processes*, where the charm quark from a beauty decay decays muonically. Fig. 8.13 shows the corresponding diagrams.

A commonly used model to describe the hadron decay is the *spectator model*, which is quite similar to the QPM. In this model the b quark decays independently of the other partons in the hadron. The process is sketched in fig. 8.14.

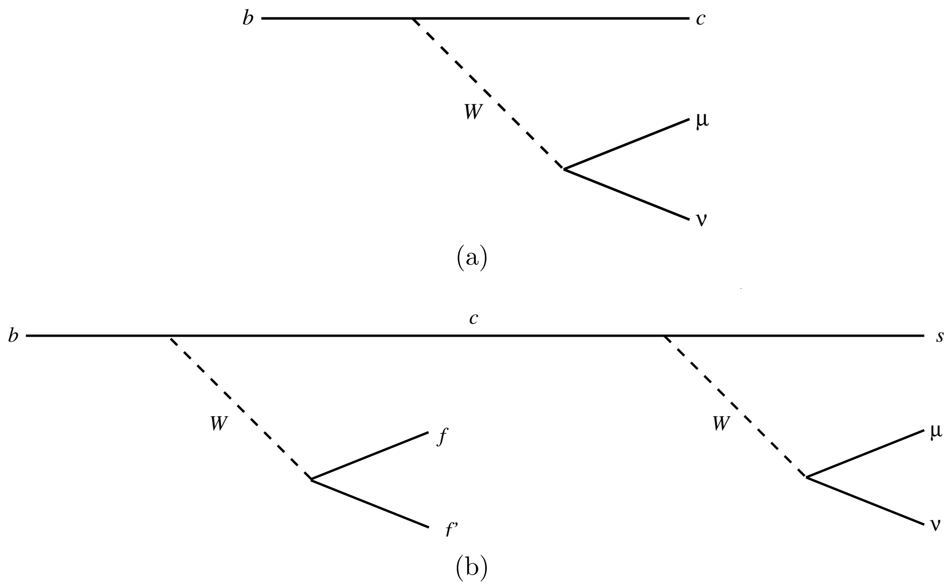

Figure 8.13: *Semi-muonic decay of a b quark: (a) prompt, (b) cascade.*

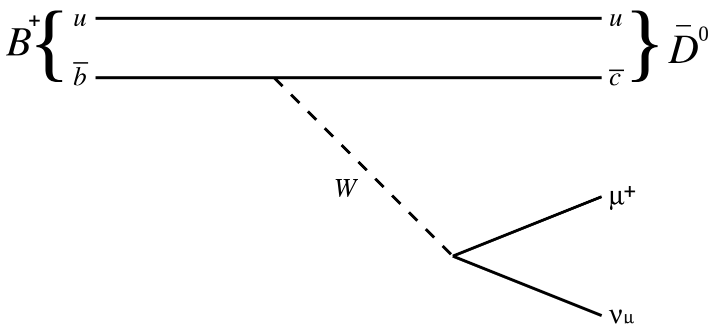

Figure 8.14: *Decay of a b flavoured hadron in the spectator model.*

8.6 Monte Carlo Programs

To compare the experimentally obtained results of measurements with the theoretical predictions two different kinds of programs are used: Monte Carlo integration programs, which are based on NLO calculations, and Monte Carlo event generators, which include LO calculations and parton showers.

8.6.1 HVQDIS

For the comparison with NLO calculations the FORTRAN program HVQDIS was used. This program is based on the calculations of Harris and Smith [100–102] who investigated the production of heavy quarks in the DIS region. The calculations were performed in the massive scheme (sec. 8.5.1). HVQDIS uses MC methods to obtain the beauty production cross section in LO and NLO. An overview about the used parameters and functions for the calculations in this analysis are given in sec. 12.1.

8.6.2 Monte Carlo Event Generators

For a better understanding of the experimental data in comparison to theoretical models, a detailed understanding of event topology and detector effects is needed. This requires an event-by-event simulation of the whole final state. This is at the moment not feasible for NLO programs, i.e. HVQDIS, even though studies are ongoing to implement this possibilities particularly with regard to LHC physics [103].
Event generators, which are also based on MC methods, are used for this purpose. Fig. 8.15 illustrates the principle of a MC event generator considering as example a BGF process. Starting from the *matrix element* (ME) in LO of the hard partonic subprocess, initial and final state parton showers (sec. 8.4.1) are produced. The originated partons are in a further step grouped to form hadrons. In this analysis the hadronisation is performed using the program JETSET [104, 105]. A complete overview about the MC event generators used for this thesis is given in sec. 11.3.

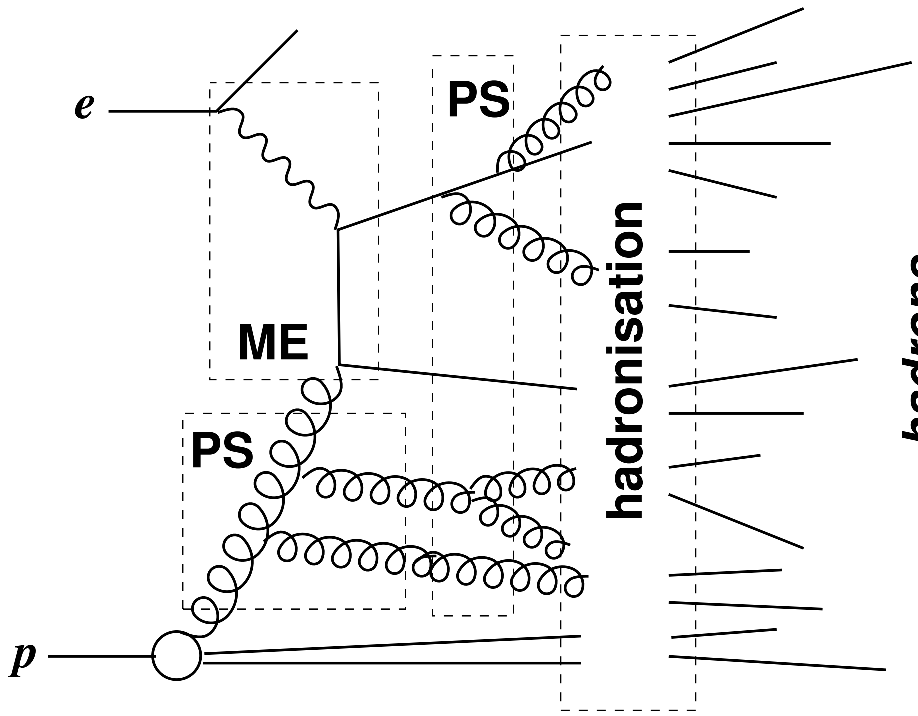

Figure 8.15: *Principle of an ep event generator [64]*

Chapter 9

HERA and the H1 experiment

At HERA (*Hadron-Elektron-Ring-Anlage*) in Hamburg positrons and protons are brought to collision. The positrons and the protons are accelerated in two separate storage rings at energies of 27.5 GeV and 920 GeV respectively. The corresponding centre-of-mass energy is around 318 GeV. A schematic overview of HERA and its pre-accelartors is shown in fig. 9.1. The accelerated particles are pooled in bunches, which

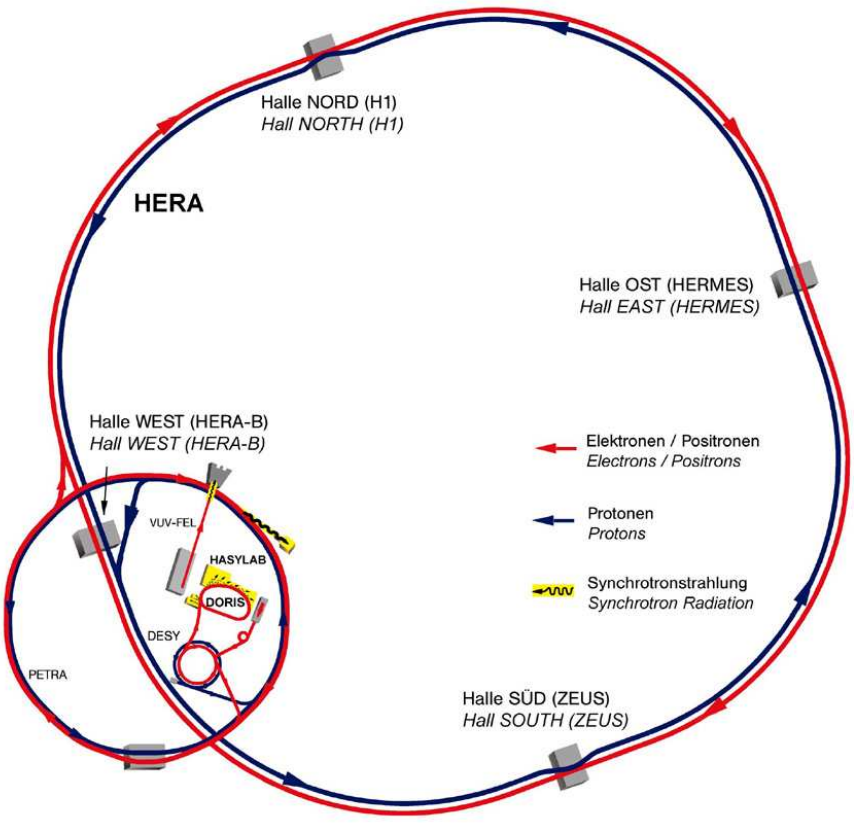

Figure 9.1: *The HERA ring, its pre-accelerators and also the four experiments H1, ZEUS, HERMES and HERA-B are shown.*

collide in two interaction regions with a separation in time of 96 ns. The achieved luminosity in 1999/2000 was of the order of 2×10^{31} cm^{2}s^{-1}.

At the two interaction regions two multi-purpose detectors are located to investigate the physics of *ep* scattering. The north hall hosts the H1 experiment and the south hall the ZEUS experiment. There are two other experiments HERMES and HERA-B which are using either the electron or the proton beam for physics studies. HERMES is located in the east site, where the electron beam is passed through a gas target to investigate the nucleon spin structure. HERA-B was located in the West Hall. It used the proton beam halo together with a wire target to study QCD and CP violation in the B system.
Since the data of this analysis was taken at the H1 detector, in the following section the components of the H1 detector most important for this thesis are discussed in more detail, which are the *central silicon tracker* (CST), the *central tracking detectors* (CTD), the *liquid argon calorimeter* (LAr), the *spaghetti calorimeter* (SpaCal) and the muon system. Fig. 9.2 shows a schematic view of the detector.

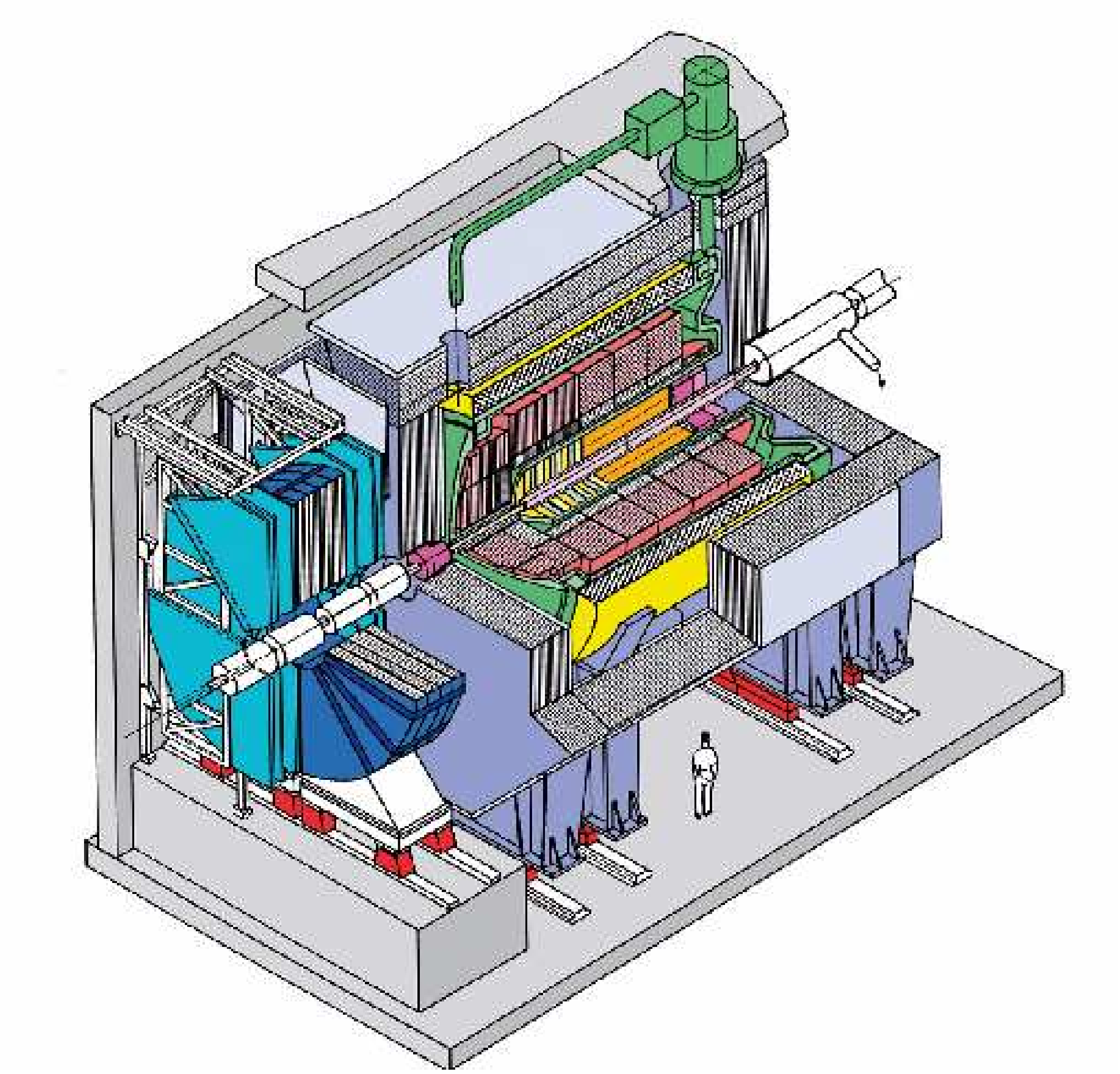

Figure 9.2: *Sketch of the H1 detector. The most relevant subdetectors are described in the text.*

	radial		z		polar	
	min[mm]	max[mm]	min[mm]	max[mm]	min[°]	max[°]
CJC2	530	844	-1125	1075	26	155
COZ	460	485	-1105	1055	24	157
CJC1	203	451	-1125	1075	11	170
CIZ	174	200	-1080	720	14	171
CST	57.5	95	-175	175	30	150

Table 9.1: *Overview about the dimension of the H1 tracking system consisting of the CST, CIZ, CJC1, COZ and CJC2.*

The asymmetric structure is due to the large energy difference of the colliding particles. This has the consequence that the produced particles have a large boost in the direction of the proton beam. The direction of the proton beam, called forward direction, also defines the z-axis of a right handed coordinate system. In this coordinate system the ϕ angle is measured in the xy-plane of the detector, while the polar angle θ is defined with respect to the z-axis. Thereby, $\theta = 0$ means forward direction. A more detailed description of the detector can be found in [106, 107].

9.1 Central Tracking System

As described in more detail in part I of this thesis the purpose of the tracking chambers is the reconstruction of the trajectories of charged particles. With a strong magnetic field it is also possible to measure the transverse momentum of the charged particle. Additional information about vertices, like the position of the ep interaction (primary vertex) and the decays of long lived particles (secondary vertices) can be obtained by extrapolating the reconstructed tracks back to the beam axis.
Two different technologies are in use for tracking detectors: silicon detectors, which yield an excellent resolution, but only few track points and gas detectors, which have a worser resolution, but deliver many track points.
The central tracking system of the H1 detector covers the polar angular region $10° \leq \theta \leq 170°$ and consists of the *central silicon tracker* (CST) close to the beam pipe, two *central jet chambers* (CJC1, CJC2), two z chambers, *central inner* and *central outer z-chambers* (CIZ, COZ) to improve the z and θ resolution and two multiwire proportional chambers, *central inner* and *central outer proportional chamber* (CIP, COP) for triggering purposes (see fig. 9.3 and tab. 9.1).

9.1.1 Central Silicon Tracker CST

The CST has been built to provide precise vertex information of charged particle tracks close to the interaction point.
During the data taking period 1999–2000 the CST consisted of two layers of double sided silicon strip sensors. Fig. 9.4 shows the $r\phi$ plane of the detector. The first layer consists of 12 *ladders* at a radius of 5.75 cm, while the second is formed from 20 ladders

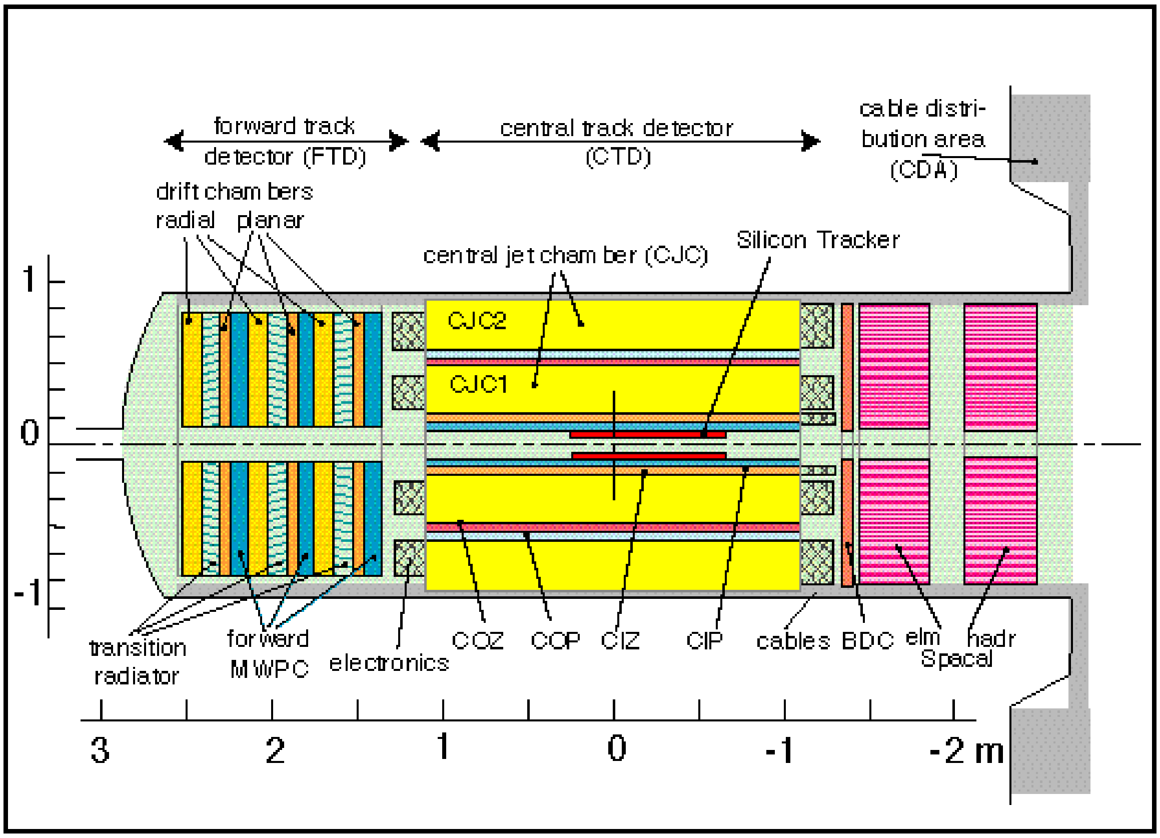

Figure 9.3: *Side view of the Tracking System.*

at a radius of 9.75 cm. Each of the ladders consists of two electrical units, the *half-ladders*. A half-ladder consists of three silicon sensors of 300 μm and a ceramic hybrid of 635 μm thickness carrying the front-end electronics.
On the outer *p-side* 12 μm wide strips with a pitch of 25 μm running parallel to the z-axis are implanted. Every second strip is read out leading to a ϕ-resolution of 12 μm. Electrons are collected on the n-side via 12 μm wide strips spaced by 88 μm. The orientation of the strips is perpendicular to the beam axis. The obtained resolution in z depends on the angle of the track. The minimum value for tracks with $\theta \approx 90°$ is 22 μm. The CST has an active length of 35.6 cm and a polar acceptance range of $30° \leq \theta \leq 150°$ for tracks originating from the nominal IP [108].

9.1.2 Central Jet Chamber CJC

The CJC is divided by the COZ and COP into two concentric cylinders: CJC1 with a radius from 20.3 cm to 45.1 cm and CJC2 with a radius from 53.0 cm to 84.4 cm. The active length is 220 cm ($-112.5\text{cm} \leq z \leq 107.5\text{cm}$) corresponding to a polar angle range of $11° \lesssim \theta \lesssim 170°$ for CJC1 and $26° \lesssim \theta \lesssim 155°$ for CJC2. The anode and cathode wires are grouped in cells. The CJC1 (CJC2) contains 30 (60) cells consisting of 24 (32) sense and 49 (66) cathode wires. A radial cross section is shown in Fig. 9.6. The jet cells are tilted by about 30°, so that the electron drift direction is almost perpendicular to tracks originating from the IP. With the CJC a $r\phi$-resolution of 140

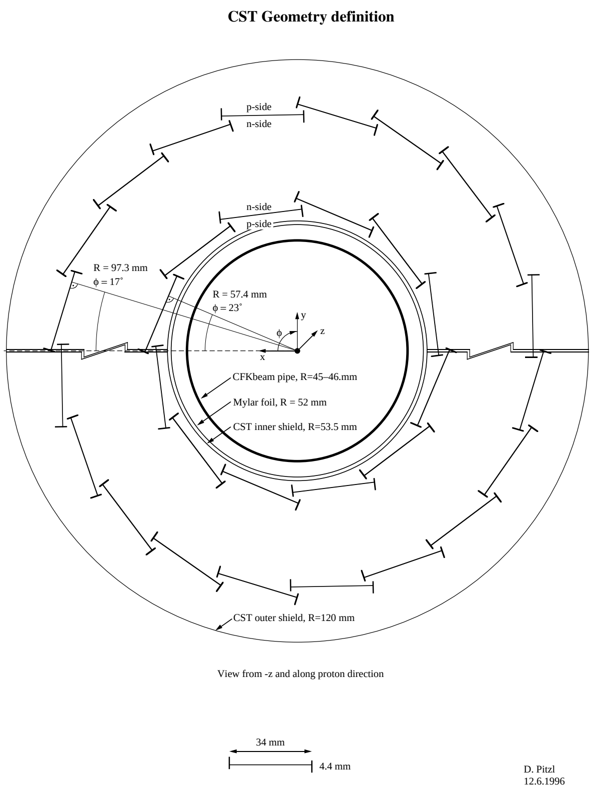

Figure 9.4: *$r\phi$ side view of the CST [108]. Both layers and the overlapping between the ladders are clearly visible.*

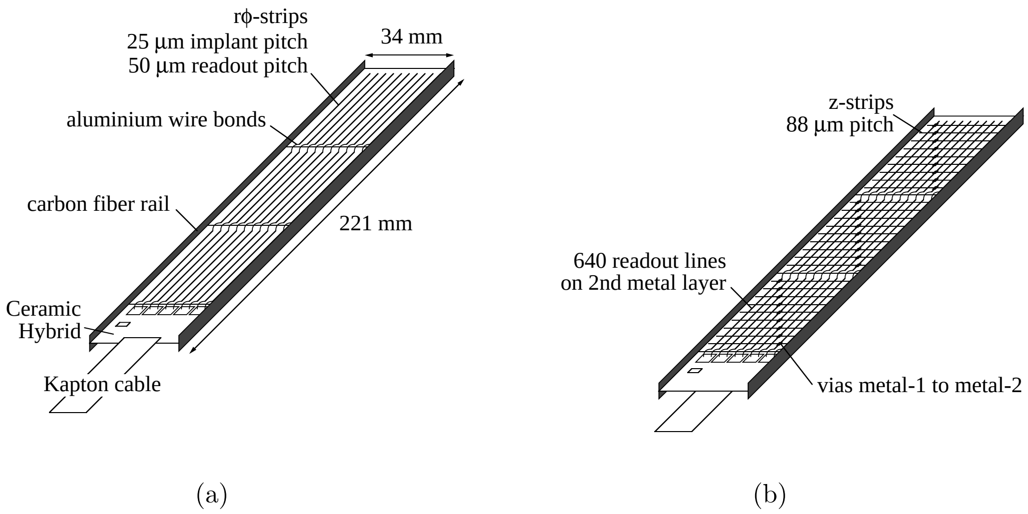

Figure 9.5: *CST half-ladders: (a) shows the p-side and (b) the n-side.*

μm and an intrinsic z-resolution of about 3 cm (by charge division) is achieved. The z-resolution can be improved to 380 μm using the information from the z-chambers (CIZ, COZ).

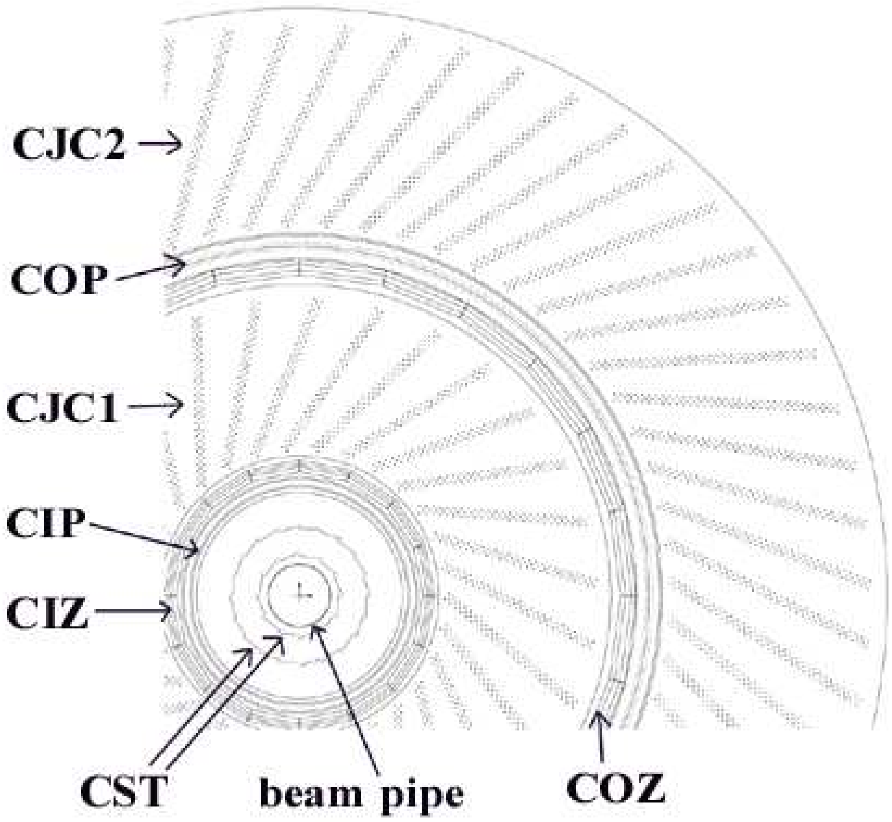

Figure 9.6: *Radial view of the central tracking detectors. The information about the size of the various chambers can be found in tab. 9.1.*

9.2 Calorimeters

For measurements of the particle energy several calorimeters are installed almost hermetically outside of the tracking system. The LArC and the SpaCal, which are of special interest for this analysis, are discussed in the following. The LArC is used for the reconstruction of the hadronic final state, while the SpaCal is important to distinguish between photoproduction and DIS events and to measure the momentum of the scattered positron.

9.2.1 Liquid Argon Calorimeter LArC

The LArC surrounds the tracking detectors and covers the polar acceptance of $4^\circ \lesssim \theta \lesssim 153^\circ$. It is composed of an inner electromagnetic and an outer hadronic part. The inner electromagnetic region is optimised to detect electrons and photons and has for this reason a high granularity. To measure the energy of hadronic particles the calorimeter is completed by a part with smaller granularity. The absorber material in the electromagnetic region is lead, while it is stainless steel in the hadronic part. In both regions liquid argon is used as active material [109]. The LArC is a non-compensating calorimeter, which means that for the same input energy strongly interacting particles deposit a smaller energy, than electromagnetically interacting ones. This effect has to be considered during the reconstruction. The systematical error on the scale of the hadronic energy is currently $\approx 4\%$. The achieved energy resolution is $\frac{\sigma(E)}{E} \approx \frac{12\%}{\sqrt{E[GeV]}}$ for electrons and $\frac{\sigma(E)}{E} \approx \frac{50\%}{\sqrt{E[GeV]}}$ for pions. Fig. 9.7 shows a side view of the LArC.

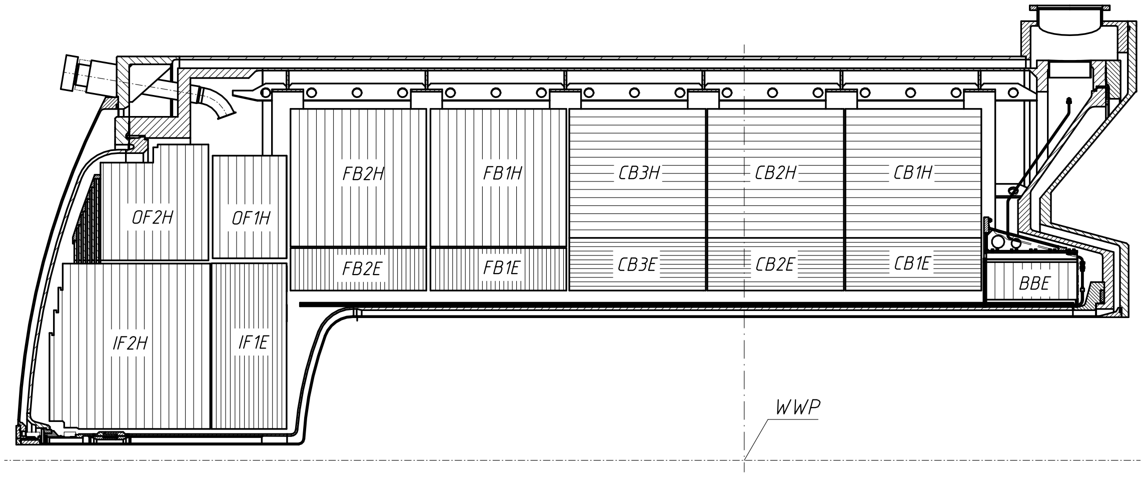

Figure 9.7: *Side view of one half of the LAr calorimeter.*

9.2.2 Backward Calorimeter SpaCal

The SpaCal consists of a lead-scintillating fibre matrix. The SpaCal is divided into an electromagnetic and a hadronic part, but only the electromagnetic region is relevant for this analysis. The electromagnetic section is subdivided in 1192 cells (fig. 9.8), each $4 \times 4\text{cm}^2$ yielding a resolution for a shower of < 4 mm. Since also an excellent resolution in time is achieved, the SpaCal is also used for triggering purposes. Fig. 9.9 shows the position of the SpaCal within the H1 detector. The energy resolution for electrons is $\frac{\sigma(E)}{E} \approx \frac{7\%}{\sqrt{E[GeV]}} \bigotimes 1\%$ [110].

9.3 Central Muon System

The muon system is the outermost detector which is located outside of the superconducting magnet, which yields a magnetic field of 1.15 T. For the detection of the muons, which are in general the only particles transversing the whole detector, and the measurement of the energy leaking from the calorimeter the iron return yoke of the magnet is instrumented with 16 layers of streamer tubes. Fig. 9.10 shows the cross section view of the iron yoke. For $\theta = 90^\circ$ muons have to have an energy of 1.2 GeV to reach the first layer and 2.0 GeV to transverse the whole structure.

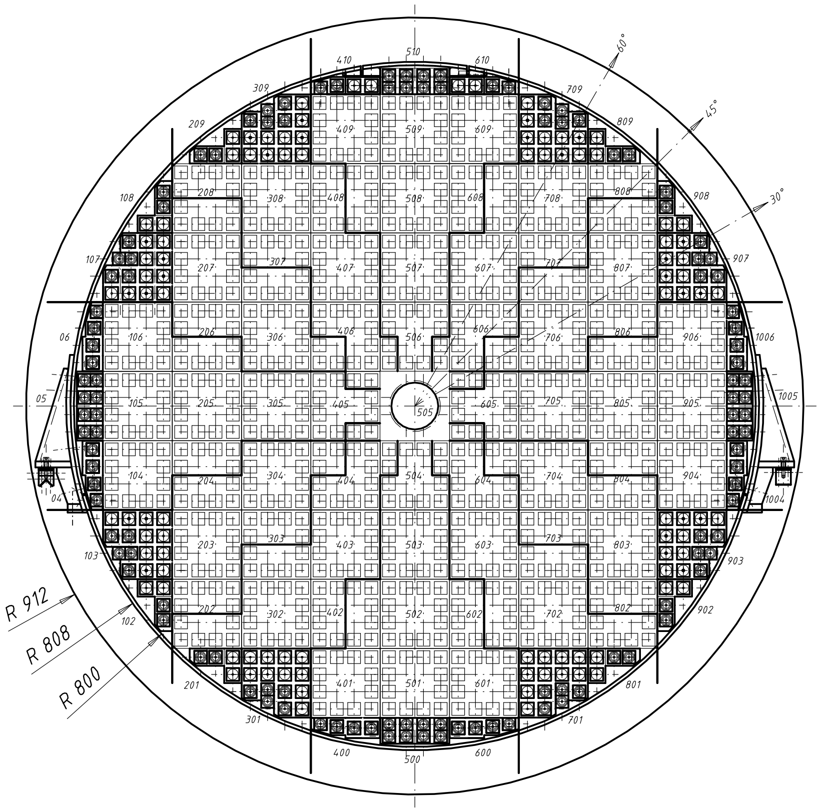

Figure 9.8: *xy view of the SpaCal showing also the cells.*

9.4 Luminosity System

The reaction used for the determination of the luminosity is the Bethe-Heitler process:

$$ep \rightarrow ep\gamma$$

This process has a high cross section and can be precisely calculated within the theory of QED. The main background process is bremsstrahlung from interactions of the electron beam with the residual gas in the beam pipe. For the calculation of the luminosity this is determined by using electron bunches, which have no counterpart in the proton train (*pilot bunches*). Experimentally the measurement is performed by measuring an $e\gamma$ coincidence in two detectors in the HERA tunnel: the photon detector (PD) at $z \approx 107$ m and the electron tagger (ET33) at $z \approx 33$ m. The whole system is illustrated in fig. 9.11.

9.5 Trigger System

While the crossing frequency of the beams is 10.4 MHz, corresponding to 96 ns, the rate of useful physics events is much lower ($\approx$ 100 kHz). Additionally there is a high rate of background events, mainly due to collisions of beam particles with the residual gas and the beam pipe wall, synchrotron radiation from the positron beam and also cosmic muons, which penetrate the H1 detector with a rate of $\approx$ 1 kHz. Since the

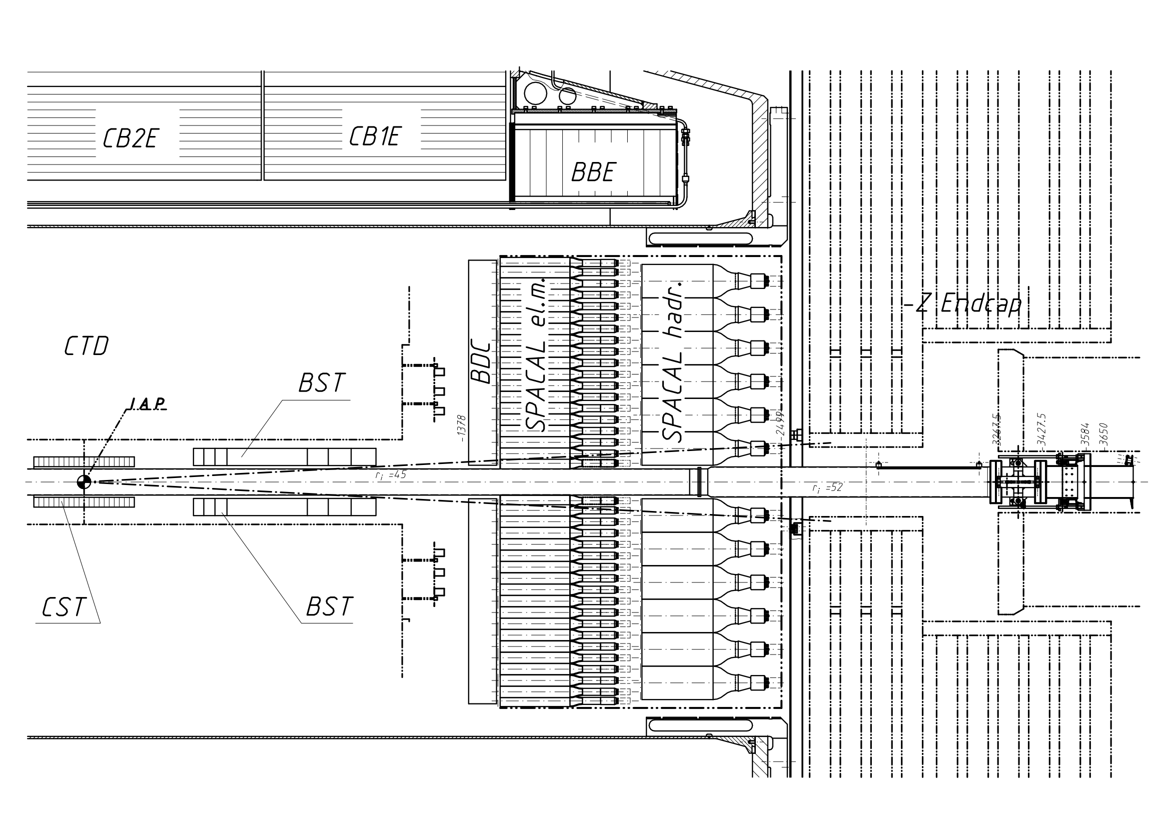

Figure 9.9: *Lateral view of the SpaCal in the H1 detector.*

bandwidth for writing the data to tape is limited, a *trigger system*, which distinguishes online between physics and background events, has to be used to reduce the data rate. Fig. 9.12 shows the H1 trigger system. It consists of four levels (L1 to L4). The first level (L1) is a hardware logic, which decides on the basis of information from the various subdetectors (*trigger elements*) if an event should be kept or rejected. The trigger elements (TE) relevant for this analysis are:

DCrϕ trigger This trigger is based on the $r\phi$ information of the CJC and allows to select tracks with a transverse momentum of $p_t \gtrsim 800$ MeV (DCRPh_THig), a track from a negatively charged particle (DCRPh_TNeg), etc.

zVtx trigger The *zVtx trigger* uses the information from the proportional chambers. If a track is reconstructed, which points to a region (-44cm $< z <$ 44cm) around the expected interaction point, a histogram is filled corresponding to the z-position. The information, if a significant maximum as an indication for a physics event is found, is stored in the zVtx_sig trigger element.

SpaCal IET The *SpaCal inclusive electron trigger* (IET) consists of overlapping trigger towers, each corresponding to 16 neighbouring cells within the electromagnetic part of the SpaCal. Because of the earlier mentioned good time resolution of the SpaCal, the SpaCal can be used to distinguish between *ep* interaction and proton-induced upstream background by measuring the deposited energy within a certain

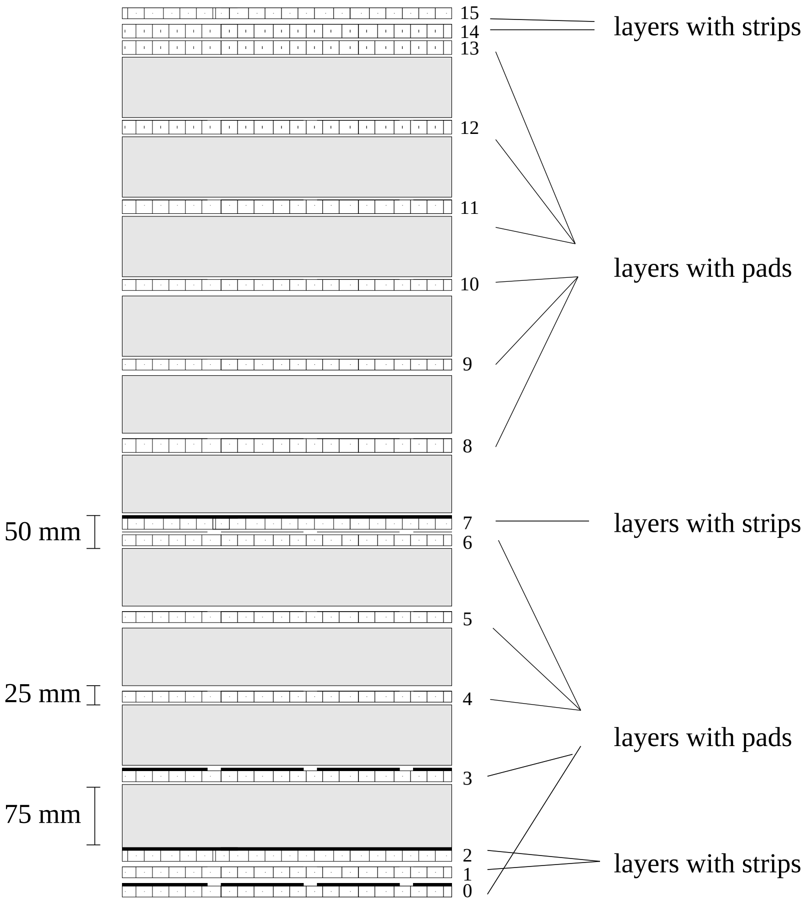

Figure 9.10: *Cross section view of the instrumented iron yoke.*

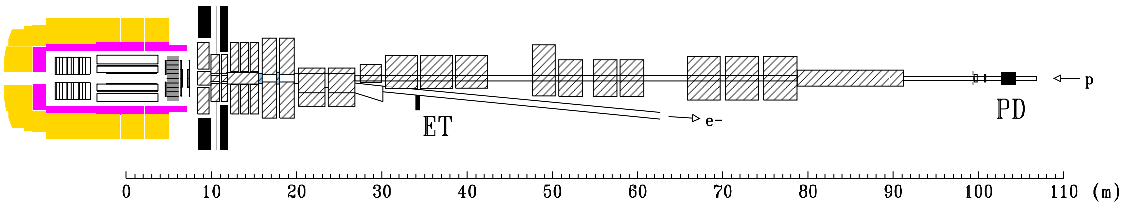

Figure 9.11: *Measurement principle of the luminosity at the H1 detector.*

time window. The amount of the deposited energy is compared with three different thresholds (0.5, 2 and 6 GeV) and the trigger elements SPCLe_IET for the outer part of the SpaCal ($R > 16$ cm) and (SPCle_IET_Cen_1, SPCle_IET_Cen_2, SPCle_IET_Cen_3) for the central part ($R < 16$ cm) are set accordingly.

With a combination of the TE it is possible to create up to 128 so called L1 subtriggers (s0 to s127). For a positive L1 decision at least one subtrigger condition has to be fulfilled. Since this would still lead to a data rate, which is too high for the available bandwidth, some subtriggers have to be prescaled by a factor n, which means that only

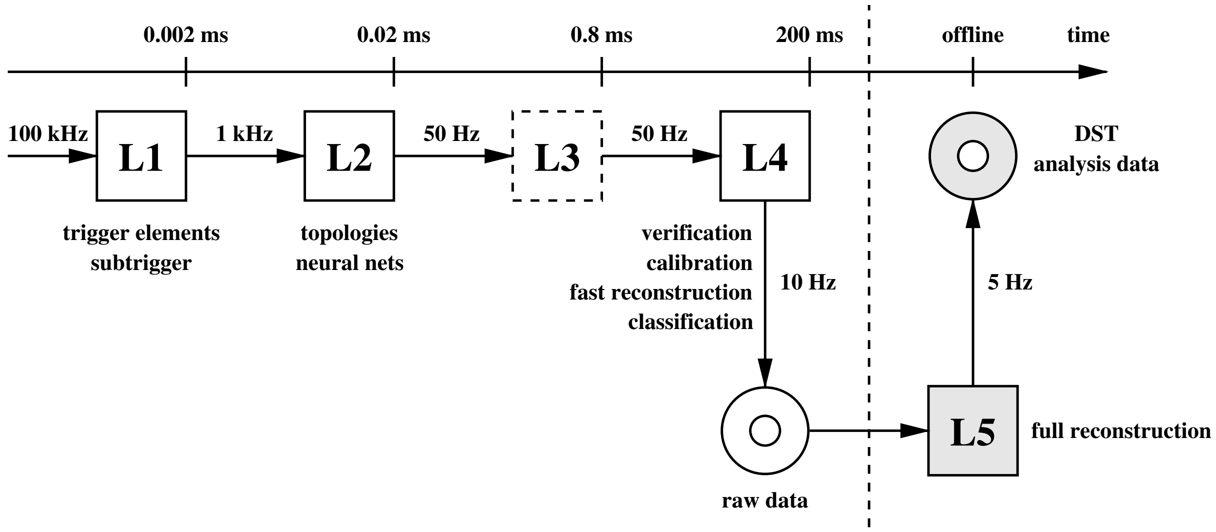

Figure 9.12: *Overview of the H1 trigger system.*

every nth fulfilling event, which fulfils the subtrigger condition is accepted (*L1 keep* signal).
The second level trigger (L2) verifies the decision of the L1 trigger and reduces the data rate further. Within 20 μs a L2 decision based on topology considerations is made. This is done either by a matrix operation (L2TT) or by a neural network (L2NN). After a positive decision the *L2 keep* signal is sent. During the data taking period the L3 trigger was not implemented. The L4 trigger is running on a farm of processors. The whole event is reconstructed, calibration factors are determined and, in case the event is accepted, it is classified in several physics groups. The output of L4 is written with a moderate rate of 10 Hz to the *production output tapes* (POT). With the L4 trigger the online analysis is completed and the L5 step follows. The event reconstruction is repeated using all available calibration factors. The output of L5, including an unique run and event number for each event, is finally written in the form of tables (*banks*) to the *data summary tapes* (DST), from which the data can later be accessed for analysis using the BOS software package [111, 112].

9.6 Detector Simulation

To be able to compare the results from the experimental measurements with the predictions from MC generators as presented in sec. 8.6.2, the use of detector simulation programs is necessary. The four-vectors from the MC particles are the input for the detector simulation, which adds the effect of detector acceptance and efficiencies. The correct detector description in the MC is well proven by test-beam and cosmic muons measurements and by comparison of real and simulated ep events.
The output of the simulation undergoes afterwards the same reconstruction software as the data, so that in this way data and MC predictions can be directly compared. For modelling the H1 detector the GEANT3 software package [113] is used.

Chapter 10

Event Reconstruction and Selection

The aim of this analysis is to measure the b cross section in DIS. For this measurement the semi-muonic decay channel of the b quark is chosen, which has an acceptable branching ratio of about 10% and, more important, a quite clean signature due to the muon signal in the instrumented iron. The following process is investigated:

$$ep \to eb\bar{b}X \to e\mu j(j)X \ . \tag{10.1}$$

The muon originates in most cases directly from the b decay and only a small contribution is due to muons from c cascade decays which fulfil the cuts introduced later on the transverse muon momentum p_t^μ [64]. As discussed in sec. 8.5.1 the main production process of $b\bar{b}$ in ep collisions is BGF. If the quarks have sufficiently high momenta each of them will form a jet. Due to detector acceptance and efficiencies not in all events both jets are reconstructed. Therefore, to improve the statistics, in this analysis one jet in the Breit frame is required. As a cross check also a data sample was selected containing two jets in the laboratory frame.

10.1 Muon Reconstruction

For the reconstruction of the muon candidate track information from the tracking devices (including the CST) and the instrumented iron are demanded. In a first step in both systems tracks are independently reconstructed and afterwards combined, whereas a quality cut on the combined fit of 0.1 is applied.

Tracks in the Central Detector

In this analysis only tracks within the polar angle acceptance of the CST ($35° < \theta < 130°$) are selected. Furthermore, the selected tracks must be fitted to the primary vertex using information from CJC, CIZ and COZ. A cut of 2.5 GeV on the transverse momentum of the muon is applied. This ensures that the muons reach the iron and traverse it. For the impact parameter also information from the CST has to be used. Since the CST consists of only two layers, a track reconstruction with the CST alone is not possible in multi-track events. On the other hand the resolution of the drift chamber does not allow to distinguish by using only information from the drift chambers, whether a certain track has its origin in the primary vertex or in the secondary vertex from the decay of a heavy flavoured hadron. Therefore, a combination of information from the drift chambers and the CST is needed. It is provided by a track fit which uses the drift chamber track information as starting value and improves the track fit with the CST hits. To ensure reasonable track quality it is required that the drift chamber tracks do not start at a radius larger than 35 cm, corresponding to a starting point within CJC1. The fitting procedure is explained in detail in [64].

Reconstruction in the Instrumented Iron

A detailed discussion of the track reconstruction within the instrumented iron can be found in [114]. In this analysis only tracks in the barrel detector are considered, since the track has to be within the acceptance range of the CST. At least four hits are requested in the 16 layers. The first hit has to be within the first five layers and the last hit within the last nine layers. Furthermore, the reconstructed track should point to the interaction region. Additionally a cut of 0.05 is applied on the linking probability for tracks in the central tracking detectors and in the iron of 0.05 is applied. Fig. 10.1 shows the distribution of the transverse momentum of the muon (a) and the corresponding ϕ distribution (b). Both are well described by the MC (RAPGAP). For these and for all following plots the fractions of the different contributions as given by the δ-p_t^{rel} fit (sec. 11.4.2) for the 1 jet analysis are taken.

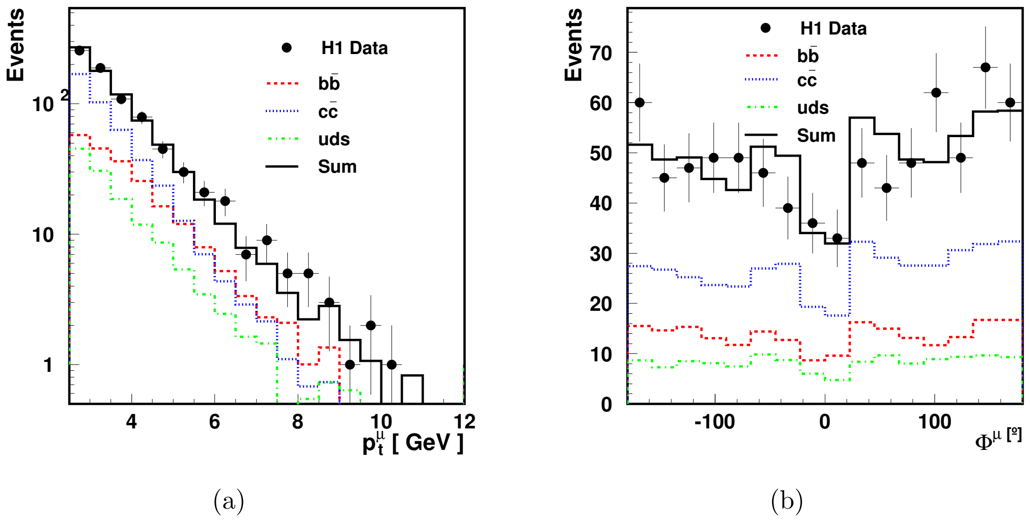

Figure 10.1: *The distribution for the transverse muon momentum p_t^μ (a) and the ϕ angle (b). The data points are extracted from the one jet analysis and the fractions of beauty, charm and uds are determined by the δ-p_t^{rel} fit . The predictions from RAPGAP are represented by the histograms.*

10.2 Reconstruction of the Primary Vertex

The transverse profile of the interaction region (beam spot) has a width of 145 μm in x direction and 25 μm in y direction. The event wise determination of the primary vertex is done in a iterative way. In a first step the average x and y vertex coordinates of the ep reaction for each run are determined from the data. This *run vertex* is used as a starting point for a fit to selected tracks, which are used to determine the *event vertex*. In the H1 standard software the program package *CSPRIM* [115] is used for this purpose. To ensure a high reconstruction quality of the event vertex special requirements are demanded for the tracks accepted as input for the fit, e.g. the tracks have to point within two standard deviations to the run vertex to avoid secondary particle tracks. For the same reason also the muon candidate track is excluded from the fit. A detailed description of the fit procedure can be found in [64]. The distribution of a probability-like control variable $\mathcal{P}(\chi^2)$ of the vertex fit in $r\phi$ is shown in fig. 10.2. The data points are well described by the MC.

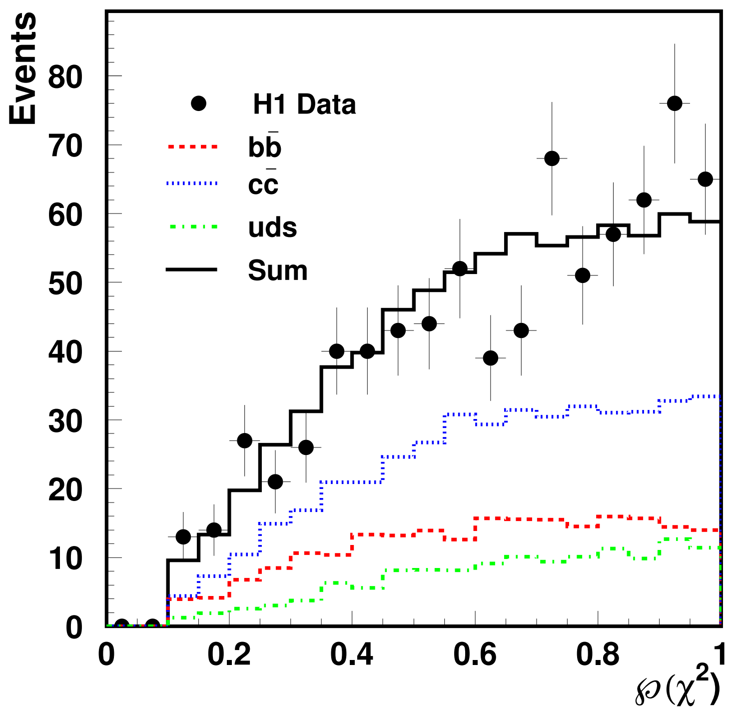

Figure 10.2: *Distribution of a probability-like control variable $\mathcal{P}(\chi^2)$ for the primary vertex fit in $r\phi$.*

10.3 Reconstruction of the Scattered Positron

The reconstruction of the scattered positron is achieved with the information of the SpaCal using the *QESCAT* package [116] within the H1 standard software.
The energy deposited in the cells is measured and neighbouring cells above a certain threshold are combined to *clusters*. If the maximum cluster energy is above 8 GeV, the cluster is accepted as a positron candidate. The four-momentum of the scattered

positron is determined from the cluster energy, the position of the cluster in the SpaCal and the z-position of the event vertex. Fig. 10.3 shows the energy (a) and the θ (b) distribution of the scattered positron. While the θ distribution is well described by the MC, the energy distribution shows small differences between MC and data. However, this should be covered by the conservative estimation of the systematic error.

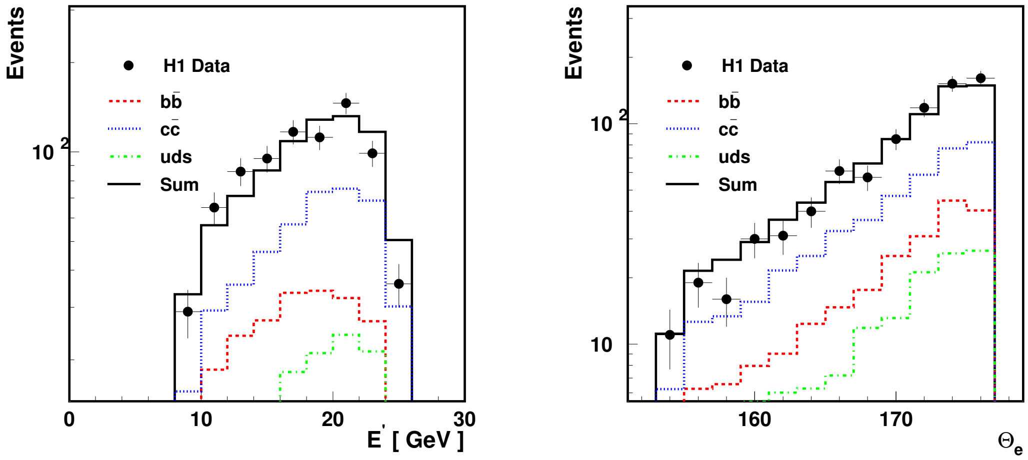

(a) (b)

Figure 10.3: *Observables of the scattered positron: (a) energy distribution, (b) θ distribution. The data points are extracted from the one jet analysis. The histograms represent the MC prediction (RAPGAP).*

10.4 Jet Reconstruction

Starting point of the jet reconstruction are the hadronic final state particles, which are identified using a sophisticated combination of track information from the tracking detectors and the clusters in the calorimeters. These hadronic final state objects are afterwards combined to jets using an appropriate jet algorithm and in this way conclusions can be drawn on the underlying partons. The muon is included in the jet reconstruction, but since it deposits only a small fraction of energy in the calorimeter, its energy is determined from the track parameters calculated from the information given by the tracking detectors.

10.4.1 The longitudinally invariant k_t clustering algorithm

The k_t algorithm was originally introduced for e^+e^- collisions, but was later also adopted for $p\overline{p}$ and ep reactions. It is based on an iterative clustering procedure starting from the list of hadronic final state objects:

1. In a first step for each object the value d_i is calculated.

$$d_i = E_{t,i} \tag{10.2}$$

There $E_{t,i}$ is the transverse momentum of the particle i. Also for each pair of objects the value d_{ij} is computed.

$$d_{ij} = \min(E_{t,i}^2, E_{t,j}^2)[(\eta_i - \eta_j)^2 + (\phi_i - \phi_j)^2] \tag{10.3}$$

η_i is the pseudo-rapidity and ϕ_i the ϕ angle of the particle i.

2. Afterwards the minimum d_{min} of all d_i and d_{ij} is determined.

3. If d_{min} is one of the d_{ij}, the particles i and j are merged to a new *pseudo*-particle k:

$$E_{t,k} = E_{t,i} + E_{t,j} \tag{10.4}$$
$$\eta_k = \frac{E_{t,i}\eta_i + E_{t,j}\eta_j}{E_{t,i} + E_{t,j}} \tag{10.5}$$
$$\phi_k = \frac{E_{t,i}\phi_i + E_{t,j}\phi_j}{E_{t,i} + E_{t,j}} \tag{10.6}$$

4. If d_{min} is one of the d_i the particle cannot be merged.

5. The clustering process is continued until all particles have been used.

As a result one gets the E_t, the η and the ϕ of the jet. To ensure that the jet is coming from a hard process, an additional cut on the transverse momentum of the jet has to be applied. This also removes the beam remnant jet. The applied p_t^{jet} cut for the reconstruction was $p_t^{jet} > 4$ GeV. For the one jet selection a cut on the transverse momentum alone is not sufficient, but the jet finding has to be performed in the Breit frame. Also, it has to be considered, that the jets are within the polar acceptance of the detector. An overview about the applied selection criteria can be found in tab. 10.1.

10.4.2 Boosting to the Breit Frame

As discussed in sec. 8.4.4 the transformation from the laboratory to the Breit frame is performed via an auxiliary vector v, which depends on the momentum p of the incoming proton, the variable x and the momentum q of the exchanged photon given by $q = k_i - k_f$. Here, k_i is the four momentum of the initial positron and k_f the four momentum of the scattered positron. The latter can be reconstructed measuring the energy E' and the angles ϕ_e, θ_e of the scattered positron, as:

$$\begin{aligned}
k_{f,0} &= E'_e \ , \\
k_{f,1} &= E'_e \sin\theta_e \cos\phi_e \ , \\
k_{f,2} &= E'_e \sin\theta_e \sin\phi_e \ , \\
k_{f,3} &= E'_e \cos\phi_e \ .
\end{aligned}$$

10.4.3 Selection Criteria for the Jets

As mentioned before cuts have to be applied on the jets to suppress soft processes and to ensure, that the whole jet is in the acceptance range of the detector. For the two jet analysis at least 2 jets are required with a transverse momentum $E_{t,jet}$ of $E_{t,jet1} > 6$ GeV and $E_{t,jet2} > 5$ GeV for the first and second jet respectively. While in the laboratory frame single jets with sufficient p_t can also be produced due to QPM processes, in the Breit frame only BGF processes contribute to this. Therefore, in the one jet analysis a cut on the transverse momentum $E_{t,jet}^{Breit} > 5$ GeV in the Breit frame is used. For both selections a cut on the polar angle of the jet in the laboratory frame is applied: $15° < \theta_{jet} < 165°$. Furthermore at least one muon has to be associated with one jet in the event.
The distributions of the transverse momentum in the Breit frame and the number of jets are presented in fig. 10.4. Both are well described by the MC.

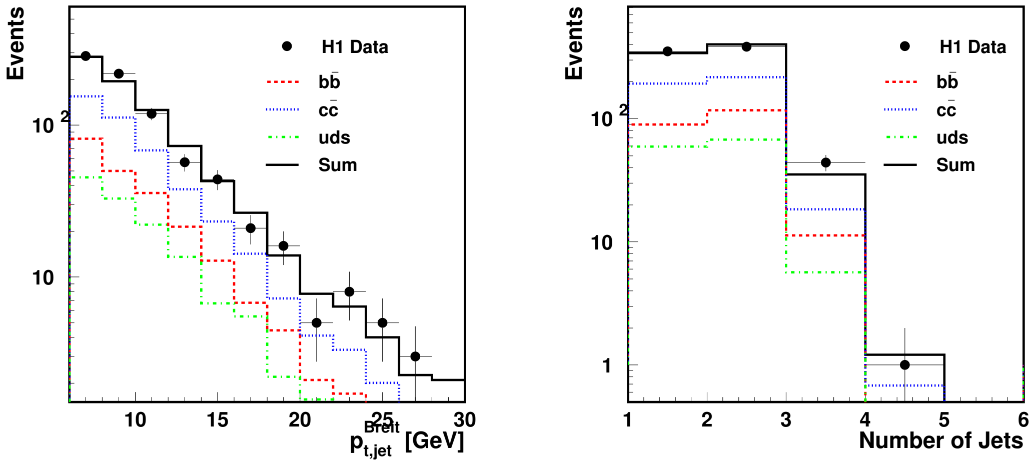

(a) (b)

Figure 10.4: *Jet observables: (a) transverse momentum of the jets in the Breit frame, (b) number of jets distribution. The data points are extracted from the one jet analysis. The histograms are obtained from the RAPGAP MC.*

10.5 Reconstruction of the Kinematic Variables

The kinematic variables Q^2, y and x can be reconstructed from the energy E'_e and the polar angle θ_e of the scattered lepton and from the four-momentum $(E_h, p_{x,h}, p_{y,h}, p_{z,h})$ of the hadronic final state particles, given the energy of the incoming positron E_e and proton E_p. There are different methods available [91], but here only the $e\Sigma$ method is discussed, which is used in this analysis.

The $e\Sigma$ method

In the $e\Sigma$ method the relevant kinematic variables are given by:

$$Q^2 = 2E_eE'_e(1+\cos\theta_e) \tag{10.7}$$

$$y = \frac{\sum_h(E_h - p_{z,h})}{\sum_h(E_h - p_{z,h}) + E'_e(1-\cos\theta_e)} \tag{10.8}$$

$$x = \frac{Q^2}{4E_eE_py} \tag{10.9}$$

This method optimises on one hand the Q^2 resolution, while it is on the other hand insensitive to initial state radiation. The distributions of Q^2 , y, and x_{bj} are shown in fig. 10.5. The agreement between data and MC is reasonable.

Kinematic Requirements

Cuts are applied on Q^2 and y. The Q^2 range is constrained by the acceptance of the SpaCal to:

$$2\ \text{GeV}^2 < Q^2 < 100\ \text{GeV}^2$$

The y range is restricted to:

$$0.1 < y < 0.7$$

where the upper cut is determined by the chosen minimum positron energy of 8 GeV. The kinematic plane in y and Q^2 is shown in fig. 10.6.

10.6 The Data Sample

For this analysis the statistics collected in 1999/2000 is used. Previous data, which were investigated in the thesis of J.Kroseberg [64], are not considered, since the benefit in statistics is only of the order of 10 pb^{-1}, while at the same the time the centre-of-energy $\sqrt{s}$ was different. Restrictions are made concerning the detector status and the subtrigger.

Detector Status

The data is subdivided in *runs* taken within up-to two hours in stable experimental conditions. Each run is classified considering the status of the slow control and detector as *poor, medium* or *high quality.* For this analysis only runs with a medium or high quality are selected and, additionally, the subdetectors described in chapter 9 had to work properly.

Subtrigger s2/s61

As discussed in sec. 9.5 only events are accepted, which fulfil at least one of the L1 subtriggers. For an analysis of heavy quark production in the DIS region the subtrigger

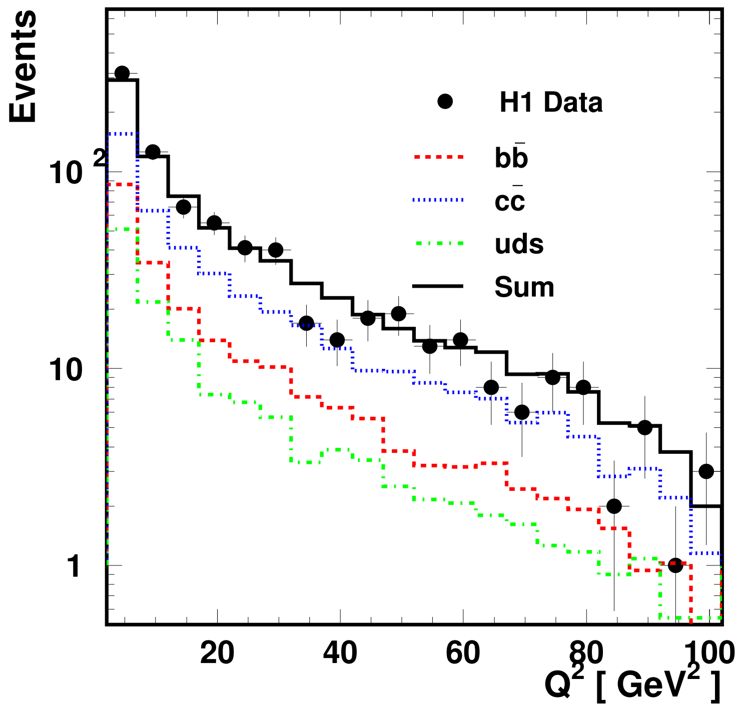

(a)

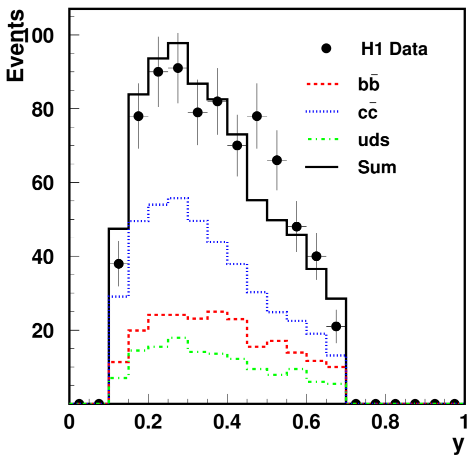

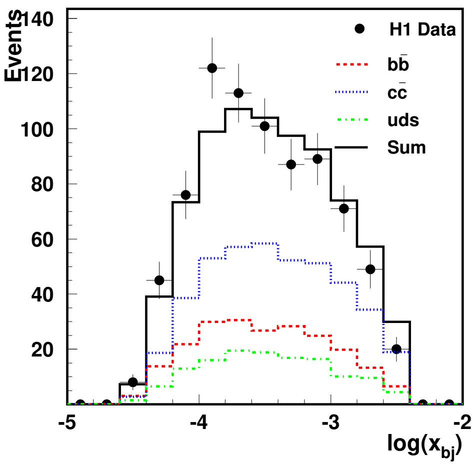

(b) (c)

Figure 10.5: *The distribution for Q^2 (a), y (b) and x (c) using the $e\Sigma$ method for reconstruction. The data points are extracted from the one jet analysis.*

s61 was designed, which requires a high energy deposition in the SpaCal, together with track and vertex activity in the central region. Expressed in the H1 trigger elements:

$$\text{DCRPh\_THig} \ \wedge \ \text{zVtx\_sig} > 0 \ \wedge (\text{SPCLe\_IET} > 2 \ \vee \ \text{SPCLe\_IET\_Cen\_3})$$

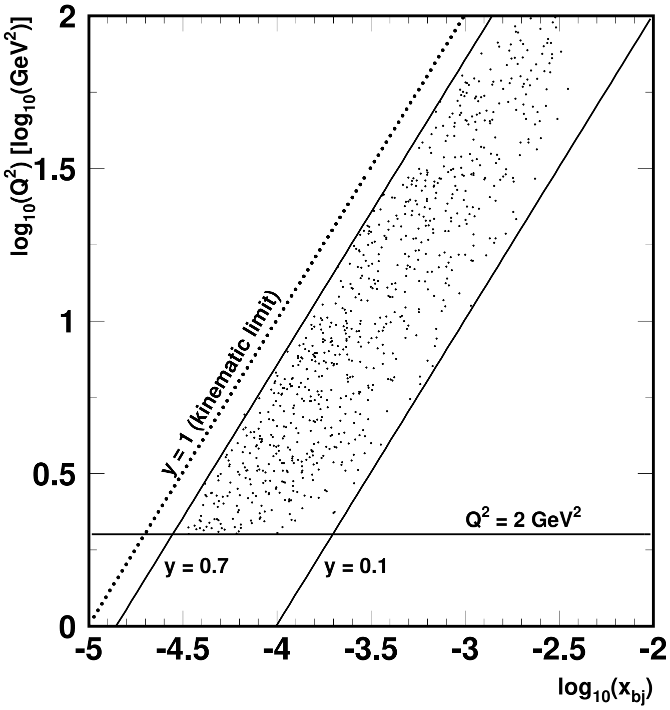

Figure 10.6: *The distribution of events (data) in the kinematic plane fulfilling the cuts for the 1 jet selection.*

Furthermore timing information is used to suppress background from non-*ep* events.

10.7 Suppression of γp and ISR Events

To avoid a contamination of the DIS sample with photoproduction and *initial state radiation* (ISR) events a new quantity, $\mathcal{S}$, is introduced, which exploits the energy and longitudinal momentum conservation in the scattering process. $\mathcal{S}$ is given by:

$$\mathcal{S} = E - p_z \tag{10.10}$$

For the initial value $\mathcal{S}_i$ of *ep* collisions at HERA this means:

$$\begin{aligned}\mathcal{S}_i &= \mathcal{S}_p + \mathcal{S}_e \\ &= (920 \text{ GeV} - 920 \text{ GeV}) + (27.5 \text{ GeV} - (-27.5 \text{ GeV})) \\ &= 55 \text{ GeV}\end{aligned}$$

The final $\mathcal{S}_f$ can be reconstructed from the particles of the hadronic final state and the scattered positron.

$$\begin{aligned}\mathcal{S}_f &= \mathcal{S}_h + \mathcal{S}_{e'} \\ &= \sum_h (E_h - p_{z,h}) + E'_e(1 - \cos\theta_e)\end{aligned}$$

	Variable	Cut
Positron	energy	$E'_{e,min} > 8$ GeV^2
Muon	transverse momentum	$p_t^\mu > 2.5$ GeV
	polar angle	$30° < \theta^\mu < 130°$
Jets	transverse momentum (1 jet selection)	$p_t^{Breit} > 6$ GeV^2
	or (2 jet selection)	$p_{t,jet1}^{lab} > 6$ GeV^2
		$p_{t,jet2}^{lab} > 5$ GeV^2
	polar angle	$15° < \theta_{lab}^{jet} < 165°$
Kinematic	Q^2	2 GeV$^2 < Q^2 < 100$ GeV^2
	y	$0.1 < y < 0.7$

Table 10.1: *Overview about the most relevant cuts for the 1 and 2 jet selection*

The beam remnant, which escapes undetected in the beam pipe, plays no role for this quantity, since for it E and p_z are almost equal in the $m = 0$ approximation. Due to the limited resolution and acceptance of the detector a cut of 45 GeV is applied to $\mathcal{S}_f$

$$45 \text{ GeV} < \mathcal{S}_f$$

Larger deviations from this cut value indicate a photoproduction or ISR event, where the scattered positron or the photon escapes in the beam pipe, leading to much lower values of $\mathcal{S}_f$.

Chapter 11

Cross Section Measurement

It is obvious that not only signal events survive the selection cuts discussed in the previous chapter, but also background events. In this chapter first the most relevant background processes are described, before the measurement of the total and differential cross sections is presented. Finally the systematic uncertainties of the measurement are addressed.

11.1 Background Processes

The largest contribution to the background in this analysis is from semi-muonic decay of charm hadrons and from in-flight decays and punch-through of light mesons. Further background sources, like cosmic muons and heavy vector meson decays, were already ruled out in a study for the measurement in the photoproduction region.

Semi-Muonic Charm Decays

Charm quarks are produced in BGF processes as the b quarks, but with a much higher production cross section than beauty. They decay with a branching ratio of $\sim 7\%$ in the semi-muonic mode which , leading to a final state topology, which is similar to the one of beauty events.

uds

Another significant contribution to the background is from the light quarks *uds*, which include events from in-flight decays and punch-through of light mesons. As described in sec. 10.1 the muon identification is based on a signal in the barrel region of the muon chambers and on a drift chamber track related to this signal. In rare cases not only muons reach the instrumented iron, but also light hadrons from the interaction region create a signal in the iron (*punch-through*) and are identified as muons. Even when such a process only occurs rarely, the contribution to the background is quite large, since the cross section for light quarks exceeds the one for beauty by several orders of magnitude.
Additionally also *in-flight decays* of light mesons, pions and kaons, contribute to the

background. Both, pions and kaons, are abundantly produced in *ep* collisions at HERA and decay preferably into muons.

11.2 Analysis Observables

Since it is not possible to discriminate between signal and background events on an event-by-event basis, statistical methods are used to extract the fraction of beauty events. For this the definition of appropriate observables is a crucial point. In this analysis two observable are used: the *relative transverse momentum* p_t^{rel} between the muon and the jet associated to the muon and the *signed impact parameter* δ . The former exploits the large mass of beauty hadrons, while the latter makes use of their long lifetime.

11.2.1 p_t^{rel}: Mass Information

Hadrons containing beauty quarks are significantly heavier than those containing charm or light quarks. This has an impact on the decay kinematics and the final state topology and can be measured in the detector.
The observable, which exploits the mass difference in the best way, is the relative transverse momentum p_t^{rel} of the muon with respect to the decaying hadron. Fig. 11.2 shows the p_t^{rel} distribution for beauty, charm and light quarks. It is directly related to the momentum spectrum of the muon in the rest frame of the decaying hadron. The true p_t^{rel} is given by:

$$p_{t,true}^{rel} = \left| \frac{\vec{p}_{\mu,true} \times \vec{p}_h}{|\vec{p}_h|} \right| , \tag{11.1}$$

where $\vec{p}_{\mu,true}$ is the momentum of the muon and $\vec{p}_h$ the momentum of the decaying hadron. Since $\vec{p}_h$ is experimentally not accessible, the flight direction of the hadron can be approximated by a *reference axis* $\vec{A}_{jet}$, which is calculated from the jet properties. The measured p_t^{rel} is given by:

$$p_t^{rel} = \left| \frac{\vec{p}_{\mu,true} \times \vec{A}_{jet}}{|\vec{A}_{jet}|} \right| . \tag{11.2}$$

In this analysis the reference axis $\vec{A}_{jet}$ used is the reconstructed jet vector excluding the muon. The p_t^{rel} method is illustrated in fig. 11.1.

11.2.2 Signed Impact Parameter δ: Lifetime Information

A second observable, the impact parameter δ , can be defined, which exploits the long lifetime τ of beauty-flavoured hadrons. Tab. 8.1 shows the lifetimes for various hadrons. In the laboratory frame the decay length L_D is given by:

$$L_D = \beta\gamma c\tau \ . \tag{11.3}$$

Here, γ denotes the boost parameter from the rest frame of the hadron to the laboratory frame and c is the velocity of light. For experimental reasons a 3 dimensional reconstruction of the decay length is not possible with good efficiency, only the projection

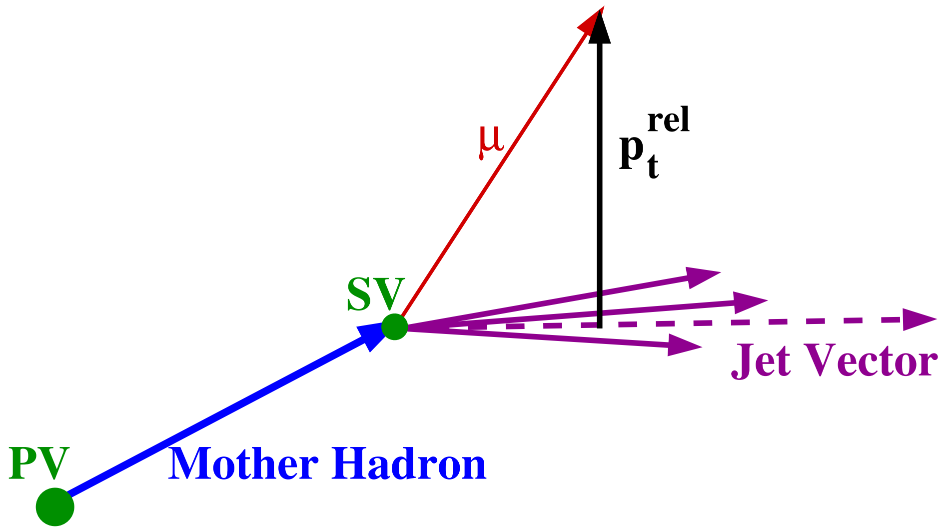

Figure 11.1: *Definition of the relative transverse momentum p_t^{rel} between the muon track and the associated jet* PV denotes the primary vertex and SV the secondary vertex.

$L_{r\phi}$ of L_D in the $r\phi$-plane is reconstructed:

$$L_{r\phi} = L_D \sin\theta \;, \tag{11.4}$$

where θ is the polar angle of the decaying hadron. In order to exploit this method it is necessary to reconstruct in addition to the *primary vertex* (PV) also the decay vertex (SV). A robust method, which allows to extract the lifetime information without reconstructing the decay vertex, is the *signed impact parameter method*. The impact parameter δ of a particle coming from the decay vertex of the hadron is the closest distance between the particle trajectory, in this analysis the trajectory of the muon, and the production vertex of the hadron in the $r\phi$-plane. The relation between δ and $L_{r\phi}$ is given by

$$\delta = L_{r\phi} \sin\alpha \;, \tag{11.5}$$

where α is the opening angle between the flight direction of the decaying hadron, reconstructed by the jet axis, and the direction of the muon from the decay. Fig. 11.3 (a) illustrates the impact parameter method. While δ is by construction a positive quantity, it is useful to assign a sign to it depending on the position relative to the primary vertex, where the muon track and the jet vector intersect. The sign can be expressed by

$$sign(\delta) = \begin{cases} +1 & \text{if } |\Delta\phi| \leqslant \pi/2 \\ -1 & \text{if } |\Delta\phi| > \pi/2 \;. \end{cases}$$

The quantity $|\Delta\phi|$ is given by

$$|\Delta\phi| = \arccos\left(\frac{\vec{A}_{jet}\cdot\vec{d}_{pv,\mu}}{|\vec{A}_{jet}|\cdot|\vec{d}_{pv,\mu}|}\right) \tag{11.6}$$

with $\vec{A}_{jet}$ the jet based reference axis and $\vec{d}_{pv,\mu}$ the vector between the primary vertex and the point of closest approach of the muon track (fig. 11.3(b)). The generated δ distributions for beauty and charm are shown in fig. 11.4.

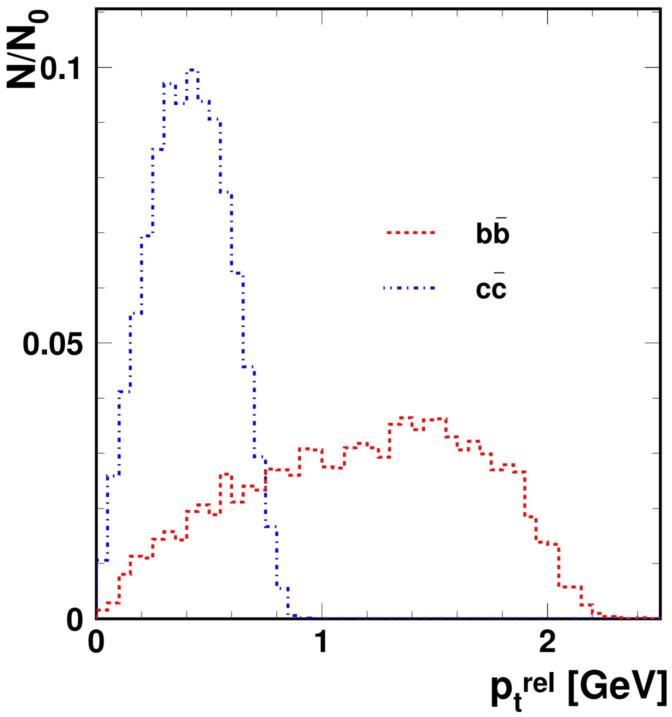

Figure 11.2: *Normalised distributions of p_t^{rel} for beauty and charm as predicted by RAPGAP. It is clearly visible that for $p_t^{rel} > 1$ GeV on generator level only beauty contributes.*

11.2.3 δ-p_t^{rel} Fit

To extract the fractions of the different sources in the data a maximum likelihood fit is used (Appendix C). For the 1 jet analysis the fit results for δ alone are

$$\begin{aligned} f_b &= [25.5 \pm 6.3]\% \,, \\ f_c &= [61.2 \pm 13.4]\% \,, \\ f_f &= [13.3 \pm 10.0]\% \,, \end{aligned} \tag{11.7}$$

and for p_t^{rel} alone

$$\begin{aligned} f_b &= [32.4 \pm 8.4]\% \,, \\ f_c &= [41.1 \pm 23.5]\% \,, \\ f_f &= [26.5 \pm 28.8]\% \,. \end{aligned} \tag{11.8}$$

Here, f_b, f_c and f_f denote the fractions of the different contributions to the signal. As shown in fig. 11.5 the data is for both observables well described by the fit. The fit also indicates, that with these observables it is not possible to determine also the charm and uds fractions in the data, since both distributions are too similar. The b fraction on the other hand is for both observables comparable within the statistical

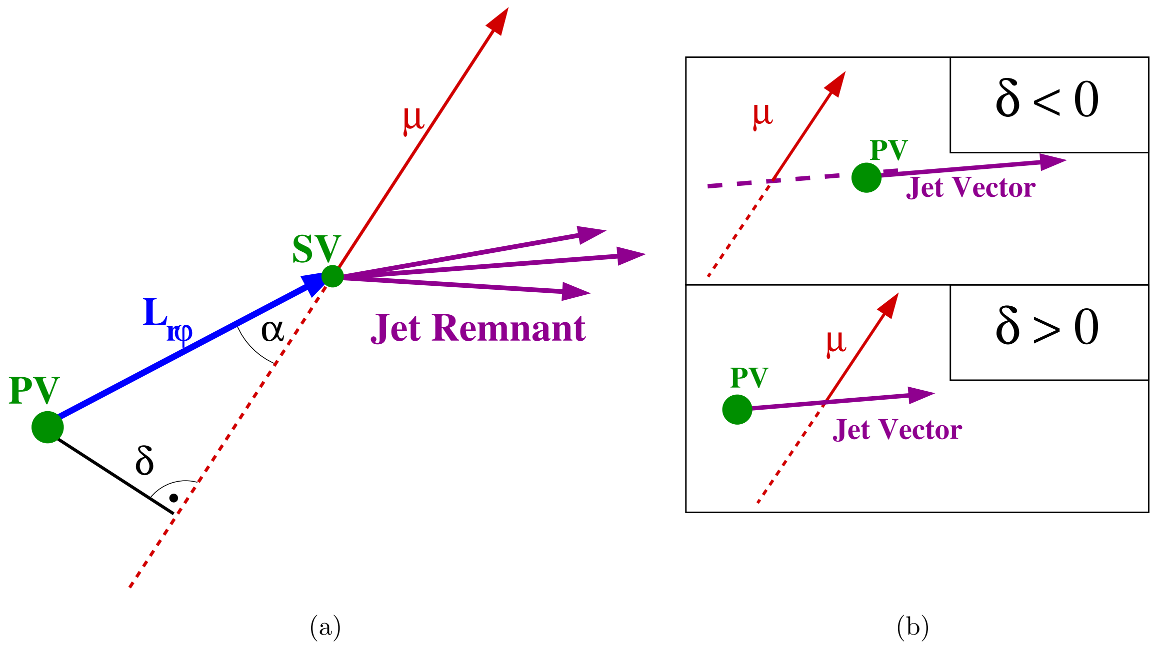

Figure 11.3: *Illustration of the signed impact parameter method. The left picture shows the magnitude of δ , whereby PV is the primary vertex and SV the secondary. The graph on the right shows the definition of the sign of δ . If the muon track and the jet are in the same hemisphere related to the PV the sign of δ is positive otherwise negative.*

error and also the relative error is of the same size showing that both observables have similar sensitivity for b events.
δ and p_t^{rel} are not correlated, which means that a high value for δ does not imply a high p_t^{rel} value. Fig. 11.6 illustrates this fact by showing the generated value of p_t^{rel} against δ for beauty and charm. In this case it is possible to enhance the separation power by using a two-dimensional fit with both observables simultaneously. This is particularly advantageous, if only low statistics is available.
Fig. 11.7 shows the input distributions for the two-dimensional fit (δ-p_t^{rel} *fit*). Apart from the fractions (see eq. 11.18), the data , the summed MC and the pull distributions are given as output. The pull distributions (fig. 11.8) also do not show any significant structure in the central region. This demonstrates that the two-dimensional distribution is well described by the data.
An additional possibility to show the consistency of this method is to restrict the range of one observable and plot the other. Fig. 11.9 shows these *high purity plots* for $p_t^{rel} > 1.2$ GeV and $\delta > 0.01$ cm. The data is for both observables well described by the δ-p_t^{rel} fit . This allows to test that the beauty signal itself is well described by the MC. For uds and charm this description of the data can be checked independently with other data samples.
In the following only results obtained from the δ-p_t^{rel} fit are presented.

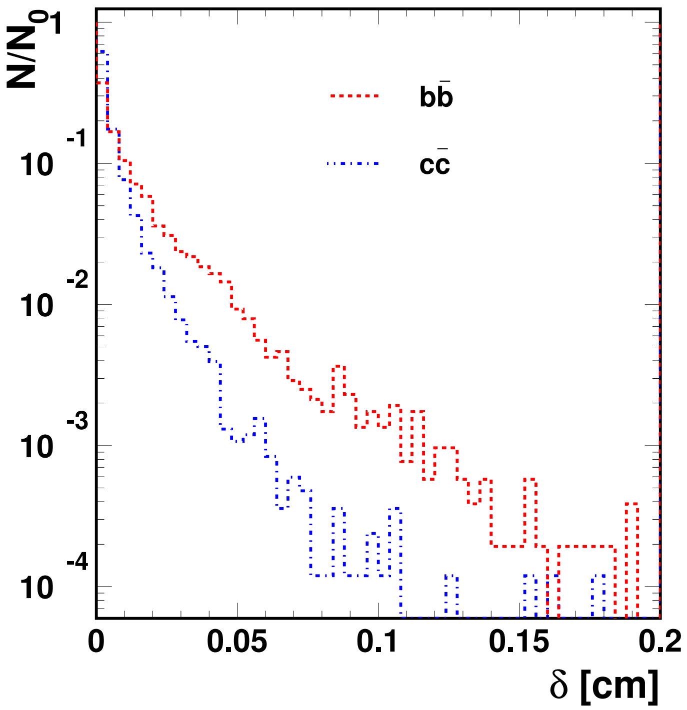

Figure 11.4: *Normalised distributions of δ for beauty and charm on generator level as predicted by RAPGAP. The excess of b events for large δ values is clearly visible.*

11.3 Event Samples

The selection criteria described in Chapter 10 lead to the following samples for data and MC simulation.

H1 Data

The data sample used in this analysis was recorded with the H1 detector in 1999/2000 and corresponds to an integrated luminosity of 43.4 pb^{-1} considering the prescale factor of s61. The one jet sample contains 781 muon candidates and the two jet sample 547. Fig. 11.10 shows the event display of a selected event.

MC Samples

For the signal and background MC the event generator RAPGAP [117] was used. For beauty an event sample corresponding to 2227.41 pb^{-1} was generated yielding 5026 muon candidates for the one jet and 3753 for the two jet selection. To describe the background coming from events containing charm quarks, 1895.66 pb^{-1} were generated, out of which 8175 muon candidates survive the one jet selection and 5363 pass the two jet selection. For the uds background 200.26 pb^{-1} were produced yielding 1454 muon candidates for the one jet and 967 for the two jet selection. The RAPGAP MC contains

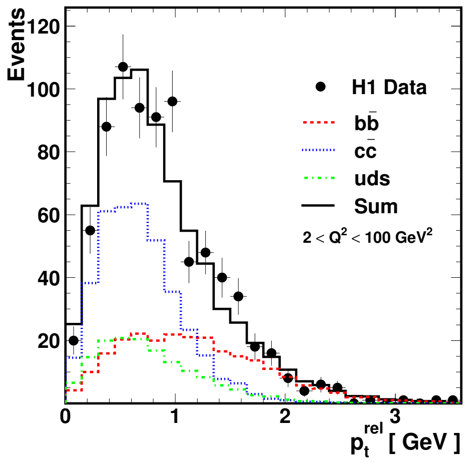

(a)

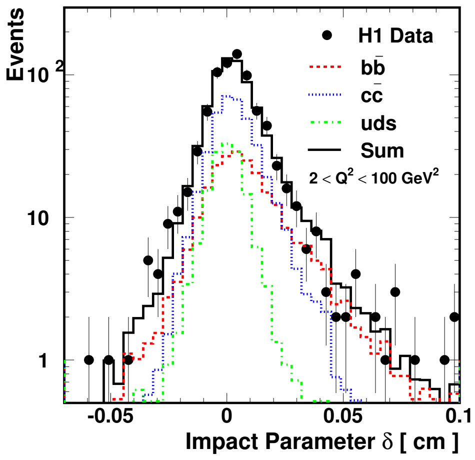

(b)

Figure 11.5: *Results for the one-dimensional fits. (a): p_t^{rel} distribution, (b): δ distribution.*

only events from direct processes. Further MC generators with different fragmentation models (Peterson or Lund) and different parton evolution equations (CCFM instead of DGLAP) , e.g. CASCADE [118], were used for systematic studies.

11.4 The total Cross Section

After the definition of the visible cross section, the results for the one jet and the two jet selection are presented. The fit fractions were determined using the δ-p_t^{rel} fit .

11.4.1 Definition of the visible Cross Section

In this analysis the definition of the visible cross section follows the argumentation from [64]. The visible cross section is given by

$$\sigma^{vis}(ep \to b\bar{b}X \to e\mu j(j)X) = \frac{f_b N_\mu}{2\epsilon\mathcal{L}} \;, \tag{11.9}$$

where f_b is the fraction of beauty as determined by the δ-p_t^{rel} fit , N_μ is the number of muon candidates in the data sample, $\mathcal{L}$ is the corresponding integrated luminosity and ϵ denotes the efficiency for a b event to survive the selection and trigger conditions. The factor 2 is due to the fact, that no distinction has been made between muons produced in b or $\bar{b}$ decays. The visible range is given by the cuts on the transverse momentum p_t^μ, the polar angle θ^μ of the muon and the cuts on the jets as described in chapter 10, which are summarised again:

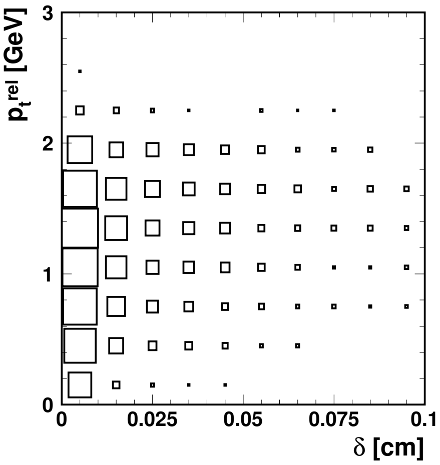

(a)

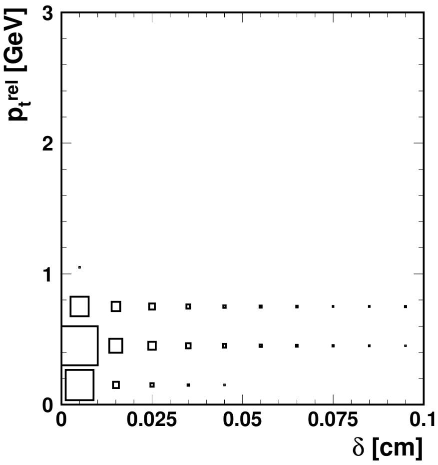

(b)

Figure 11.6: *Correlation plot for beauty and charm on generator level (RAPGAP) for events, which fulfil the selection criteria.*

$$\begin{aligned} 2.5\text{ GeV} &< p_t^{\mu} \\ 35^\circ &< \theta^{\mu} < 130^\circ \\ 15^\circ &< \theta_{jet} < 165^\circ \end{aligned} \tag{11.10}$$

and the kinematic cuts

$$\begin{aligned} 2\text{ GeV}^2 < &\ Q^2 < 100\text{ GeV}^2 \\ 0.1 < &\ y < 0.7 \end{aligned} \tag{11.11}$$

The visible cross section is extracted from the comparison to MC generated events according to:

$$\begin{aligned} \sigma^{vis} &= \frac{\sigma_{data}}{\sigma_{mc}^{reco}}\sigma_{mc}^{gen} , \\ &= \frac{f_b N_\mu \mathcal{L}_{mc}}{N_{mc}\mathcal{L}_{data}} \cdot \sigma_{mc}^{gen} . \end{aligned} \tag{11.12}$$

Here, σ_{mc}^{gen} denotes the cross section on generator level.

11.4.2 Results for the one Jet Selection

In addition to the cuts mentioned in eq. 11.10, eq. 11.11 in the one jet selection a cut on the jet momentum in the Breit frame is applied

$$E_{t,jet}^{Breit} > 6\text{ GeV} . \tag{11.13}$$

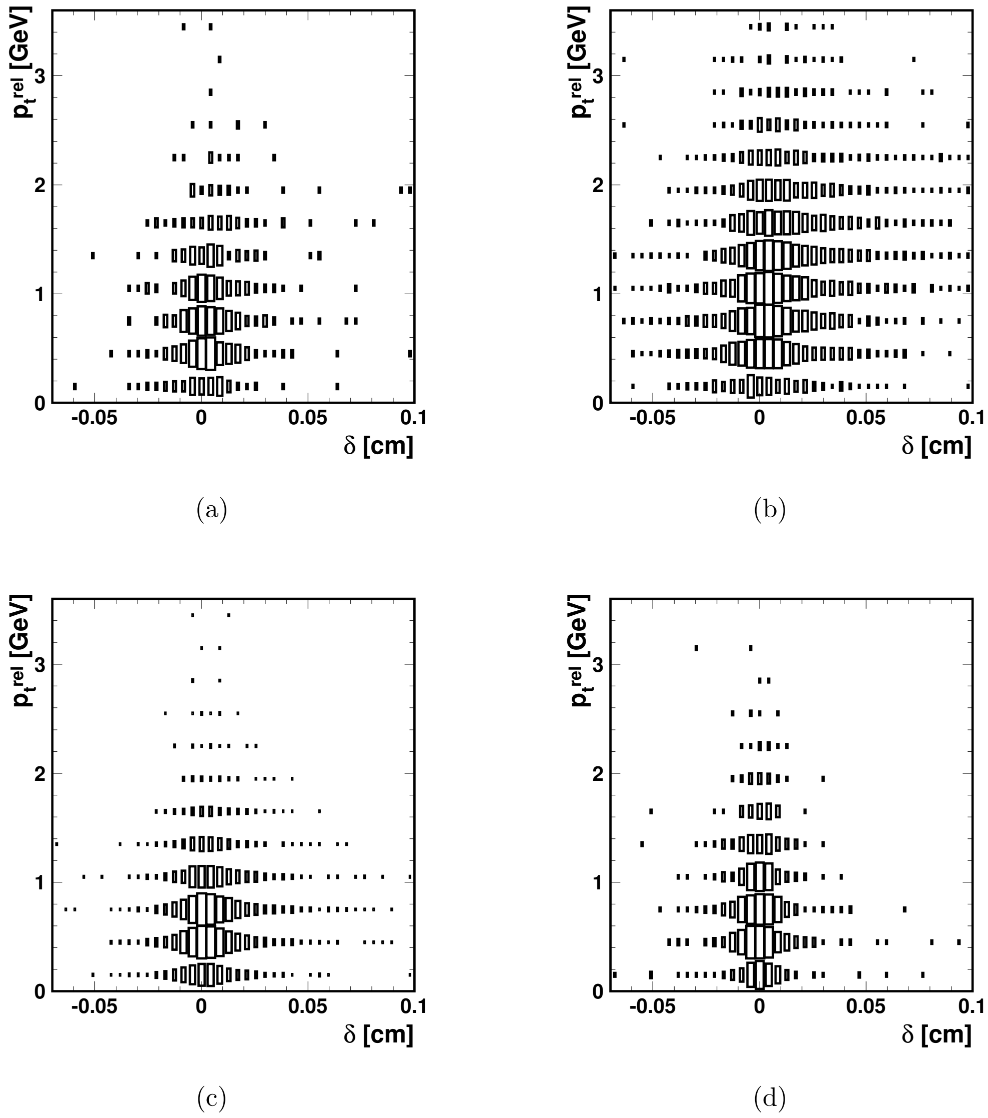

Figure 11.7: *Two-dimensional distribution for reconstructed* p_t^{rel} *and* δ *as delivered as input to the* δ-p_t^{rel} *fit : (a): H1 data, (b): beauty, (c): charm, (d): uds.*

The δ-p_t^{rel} fit yields the following fractions for b quark production in the presented kinematic region (eq. 11.11, eq. 11.10).

$$
\begin{aligned}
f_b &= [31.7 \pm 3.7]\% \ , \\
f_c &= [49.7 \pm 7.2]\% \ , \\
f_f &= [19.2 \pm 7.0]\% \ ,
\end{aligned}
\tag{11.14}
$$

This result for the b fraction is comparable within the statistical errors with the results from the 1-dimensional p_t^{rel} and δ fits (eq. 11.7 resp. eq. 11.8). This yields an inclusive cross section of

$$\sigma^{vis}(ep \to eb\bar{b} \to e\mu jX) = (16.3 \pm 2.0(stat.) \pm 2.3(sys.)) \text{ pb} \ . \tag{11.15}$$

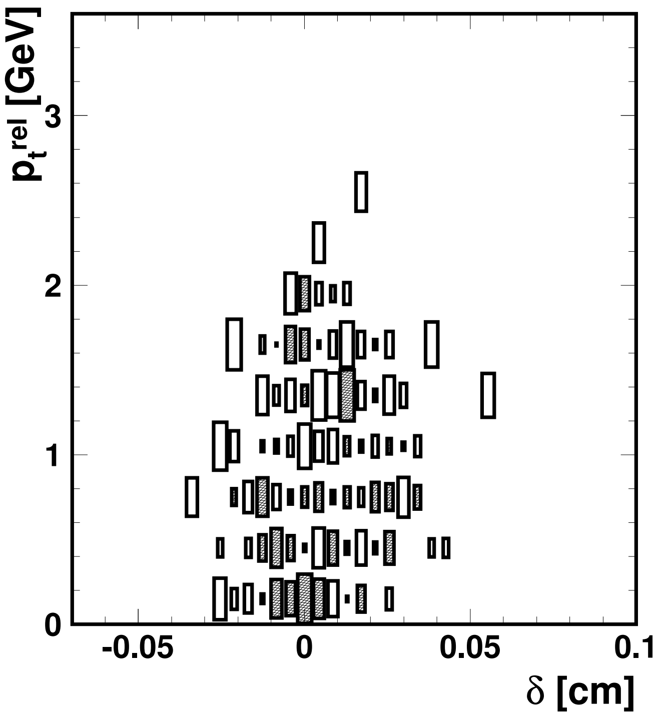

Figure 11.8: *Pull distribution as given by the δ-p_t^{rel} fit . The filled boxes indicate the regions, where the prediction of the fit is above the data, while in the regions of the open boxes the fit underestimates the data.*

11.4.3 Results for the two Jet Selection

For the two jet selection the cut 11.13 was replaced by

$$E_{t,jet}^{Lab} > 6\text{GeV} \tag{11.16}$$

for the first and

$$E_{t,jet}^{Lab} > 5\text{GeV} \tag{11.17}$$

for the second jet. With these cuts the relative fractions from the δ-p_t^{rel} fit are

$$\begin{aligned} f_b &= [35.7 \pm 4.6]\% \ , \\ f_c &= [52.0 \pm 8.2]\% \ , \\ f_f &= [12.3 \pm 7.6]\% \ . \end{aligned} \tag{11.18}$$

This leads to an inclusive cross section of

$$\sigma^{vis}(ep \rightarrow eb\bar{b} \rightarrow e\mu jjX) = (12.9 \pm 1.6(stat.) \pm 1.8(sys.)) \text{ pb} \ . \tag{11.19}$$

11.5 Differential Cross Sections

Differential cross sections of b production have been measured as a function of the virtuality of the exchanged photon Q^2 , the Bjorken scaling variable x_{bj} and the fraction

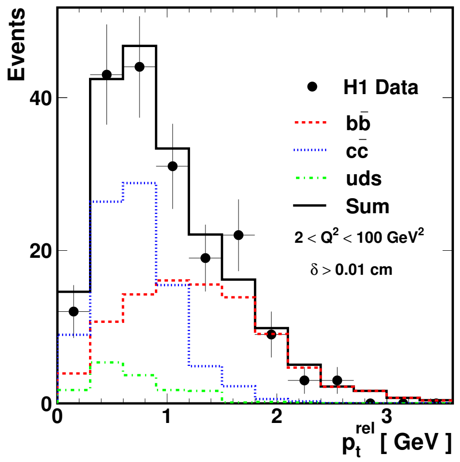

(a)

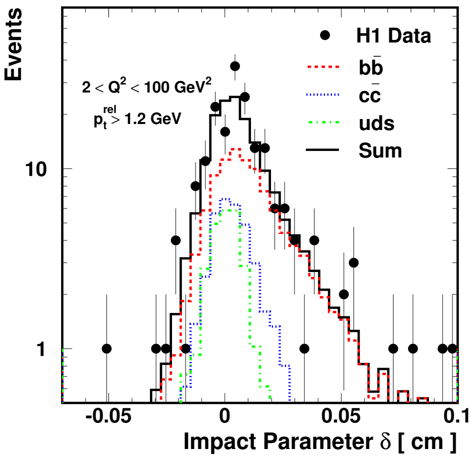

(b)

Figure 11.9: *High purity plots for* p_t^{rel} *(a) and* δ *(b). The fractions were obtained from the* δ-p_t^{rel} *fit to the full data sample.*

Bin	Q^2 range [GeV^2]	Q^2_{bin} [GeV^2]	Purity [%]	f_b [%]	$d\sigma/dQ^2$ [pb/GeV^2]
1	2.0-5.0	3.5	90.5 ± 0.8	33.9 ± 6.5	1.55 ± 0.37
2	5.0-18.0	9.5	95.7 ± 0.5	21.4 ± 5.4	0.297 ± 0.086
3	18.0-100.0	45.0	97.1 ± 0.4	35.9 ± 6.2	0.091 ± 0.020

Table 11.1: *Overview of the different bins of the* $d\sigma/dQ^2$ *measurement. The purity was obtained from the RAPGAP MC.*

x_γ of the photon momentum. The fraction of b events was determined in each bin of the differential cross section by the δ-p_t^{rel} fit . The differential cross section in a bin of width Δx_i is calculated via eq. 11.10 divided by the bin width Δx_i:

$$\frac{d\sigma^{vis}}{dx_i} = \frac{f_b^i N_\mu^i \mathcal{L}_{mc}}{N_{mc}^i \mathcal{L}_{data}} \cdot \sigma_{mc}^{gen,i} \cdot \frac{1}{\Delta x_i} \tag{11.20}$$

11.5.1 Measurement of $d\sigma/dQ^2$

For the determination of the differential cross section the 1 jet selection was used. The total Q^2 range was divided in three bins, each with approximately the same number of events (2 GeV^2 $< Q^2 <$ 5 GeV^2, 5 GeV^2 $< Q^2 <$ 18 GeV^2 and 18 GeV^2 $< Q^2 <$ 100 GeV^2). Tab. 11.1 shows the results of fraction, differential cross section and the purity for each bin. The purity is defined as the fraction of events which are generated and reconstructed in the same bin relative to the number of events generated in that bin. Fig. 11.11 shows the measured differential cross section as a function of Q^2. The data points are significantly underestimated by the predictions from the MC.

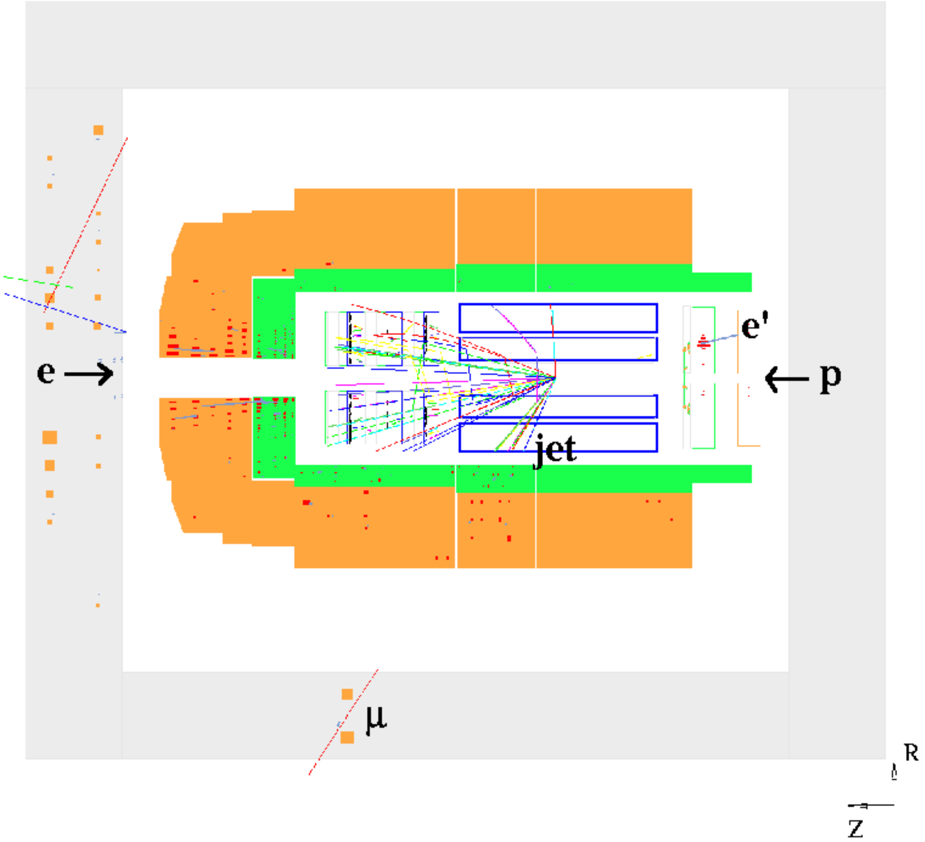

Figure 11.10: *H1 event display of a selected event (run: 254037, event: 78610). The positron e and the proton p of the initial state and also the jet, the scattered positron e′ and the muon candidate μ of the final state are shown.*

11.5.2 Measurement of $d\sigma/d\log x_{bj}$

The differential cross section $d\sigma/d\log x_{bj}$ was measured in the range $10^{-4.5} < x_{bj} < 10^{-2.4}$ also using the 1 jet sample. This range was also divided in three bins with approximately the same number of events ($10^{-4.5} < x_{bj} < 10^{-3.8}, 10^{-3.8} < x_{bj} < 10^{-3.1}$ and $10^{-3.1} < x_{bj} < 10^{-2.4}$). For each bin a purity of $\approx 90\%$ was observed. An overview of the different x_{bj} bins is given in tab. 11.2. $d\sigma/d\log x_{bj}$ is shown in fig. 11.12.

Bin	$\log(x_{bj})$ range	$\log(x_{bj,bin})$	Purity [%]	f_b [%]	$d\sigma/d\log(x_{bj}$ [pb]
1	-4.50--3.80	-4.15	94.1 ± 0.6	30.5 ± 6.3	6.40 ± 1.60
2	-3.80--3.10	-3.45	92.2 ± 0.6	30.9 ± 5.4	9.72 ± 2.18
3	-3.10--2.40	-2.75	94.2 ± 0.7	31.2 ± 6.7	6.68 ± 1.71

Table 11.2: *Overview of the different bins of the differential cross section $d\sigma/d\log(x_{bj})$. The purity was determined using the RAPGAP MC.*

The shape of the data is well described by by the MC prediction, but like for $d\sigma/dQ^2$

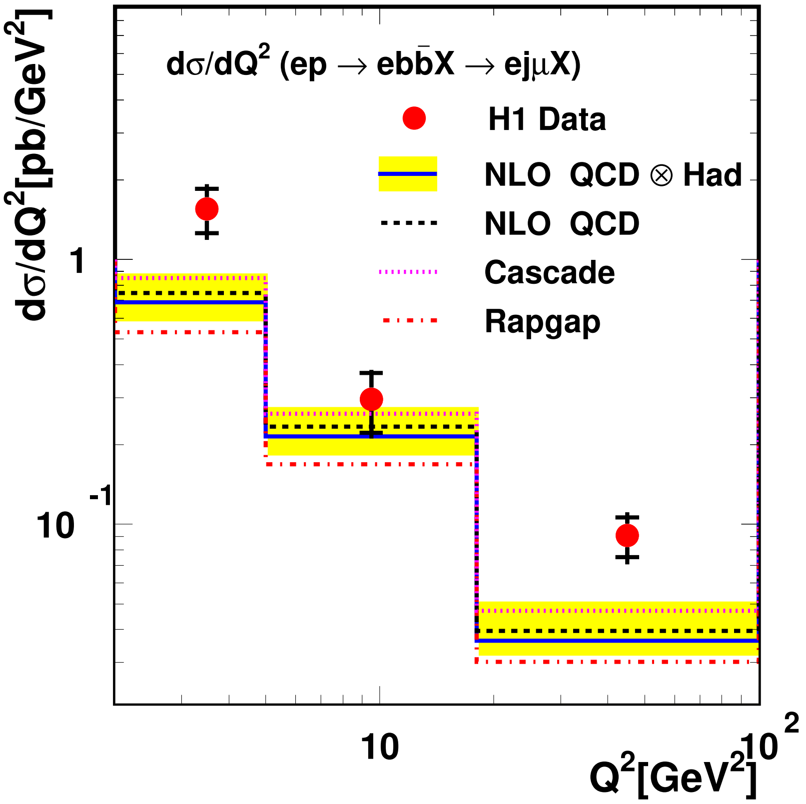

Figure 11.11: *Differential cross section $d\sigma/dQ^2$ as a function of the photon virtuality Q^2 in the in Chapter 10 discussed kinematic range. The inner error bars show the statistical error, the outer error bars represent the statistical and systematic uncertainties added in quadrature. The NLO QCD predictions at parton level (dashed line) are corrected to the hadron level using the RAPGAP generator (solid line). The shaded bands around the hadron level predictions indicate the systematic uncertainties as estimated from scale variations (see Chapter 12). Predictions from the Monte Carlo generator programs CASCADE (dotted line) and RAPGAP (dash-dotted line) are also shown.*

the data lie significantly above the MC.

11.5.3 Measurement of $d\sigma/d\eta^\mu$

Furthermore the differential cross section $d\sigma/d\eta^\mu$ of the pseudorapidity of the muon η^μ was measured. The pseudorapidity η^μ is defined as

$$\eta^\mu = -\ln(\tan(\theta_\mu/2)) \ . \tag{11.21}$$

Here, θ_μ is the θ angle of the muon, which is directly measured in the detector. The pseudorapidity has the characteristic that it is additive under Lorentz transformations corresponding to a boost along the z direction. The result of the measurement is presented in fig. 11.13. In the backward and the central region the shape of the measured

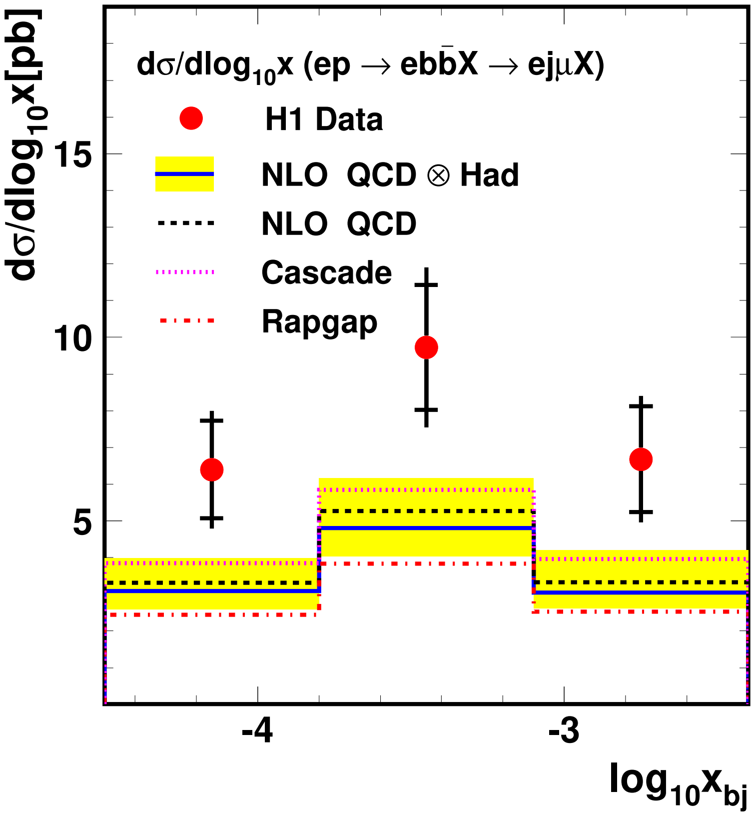

Figure 11.12: *Measurement of the differential cross section $d\sigma/d\log x_{bj}$ as a function of the Bjorken scaling variable x_{bj}.*

differential cross section is well described by both MC generators, while in the forward region a significant excess in the data is visible. A summary of the three bins is given in tab. 11.3.

11.5.4 Measurement of $d\sigma/dx_\gamma$

To investigate the fraction of the resolved and direct processes the introduction of the variable x_γ is appropriate. The observable x_γ corresponds to the fraction of the photon energy entering the hard interaction and can be estimated experimentally via

$$x_\gamma^{obs} = \frac{\sum_{Jet_1}(E-p_z) + \sum_{Jet_2}(E-p_z)}{\sum_h (E-p_z)} \ . \tag{11.22}$$

The sums in the numerator include all particles associated with the two jets, while the sum in the denominator runs over all detected hadronic final state particles. For direct processes $x_\gamma \approx 1$ is valid, while for resolved processes x_γ can be small. Since this calculation requires two jets the measurement of differential cross section $d\sigma/dx_\gamma$ were carried out using the 2 jet data sample. Due to the smaller statistics in the 2 jet

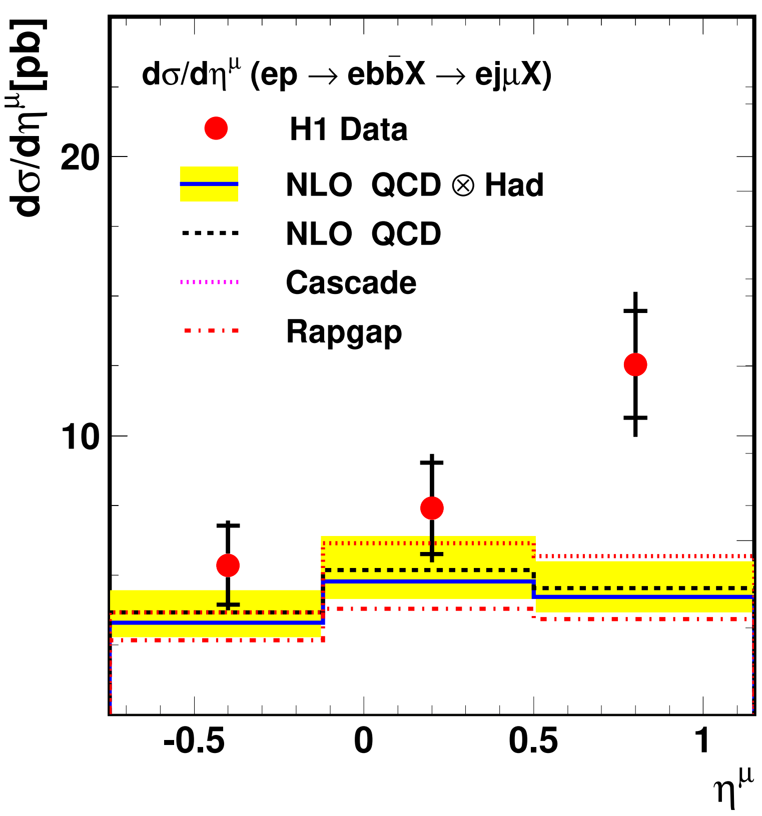

Figure 11.13: *Measurement of the differential cross section $d\sigma/d\eta^{\mu}$ as a function of the pseudorapidity η^{μ}.*

selection the data sample is only divided in two bins ($0 < x_{\gamma} < 0.75$ and $0.75 < x_{\gamma} < 1$). The bin boundaries are as in the photoproduction analysis [119]. Tab. 11.4 shows the relevant information for the two bins. Fig. 11.14 shows the measured differential cross section as a function of x_{γ}. While RAPGAP and CASCADE show a similar behaviour in the range $0 < x_{\gamma} < 0.75$, where both underestimate the data, the prediction of the cross section in the range $0.75 < x_{\gamma} < 1$ of CASCADE lies significantly above the prediction of RAPGAP. But also in this range both underestimate the measured differential cross section.

11.6 Systematic Uncertainties

Possible sources of systematic uncertainties in this analysis were investigated, partly results from studies for the photoproduction analysis were adopted benefiting from the larger data sample in this kinematic region. The most relevant ones are present in more detail in the following. For the 1 jet and the two jet selection no significant difference in the systematic uncertainties was observed. This study was also performed for each bin of the measurement of the differential cross section. It is found that for each bin

Bin	η^μ range	η^μ_{bin}	Purity [%]	f_b [%]	$d\sigma/d\eta^\mu$ [pb]
1	-0.75--0.12	-0.4	80.3 ± 1.1	23.4 ± 6.2	5.36 ± 1.60
2	-0.12-0.50	0.2	81.6 ± 0.9	22.7 ± 5.0	7.40 ± 2.18
3	0.50-1.15	0.8	83.8 ± 0.9	45.7 ± 7.0	12.6 ± 2.6

Table 11.3: *Overview of the different bins of the differential cross section $d\sigma/d\eta^\mu$. The purity was determined using the RAPGAP MC.*

the systematic error is in the same order of about 14%.

11.6.1 MC and Fragmentation Model Dependence

Other MC event generators e.g. CASCADE were used to simulate signal and background events. Unlike RAPGAP, CASCADE uses the CCFM approach for the parton evolution, while RAPGAP is based on the DGLAP approach. This leads to a change in the total cross section of about 5%. The CASCADE MC generator was also used to estimate the effect of the used fragmentation model. Using the Lund fragmentation model instead of the Peterson causes changes in the measured cross sections of around 7%. Also varying the lifetimes and branching ratios of the b flavoured hadrons within the world average values for the MC simulation leads to an uncertainty of about 2%. Finally the composition of the uds MC was varied. Muons from light mesons decays exhibit a broad δ distribution. When the contribution of these events is varied by a factor of two up and down in the MC, the cross section changes by about 2%.

11.6.2 Hadronic and Electromagnetic Energy Scale

The systematic uncertainty coming from the energy reconstruction of the LAr calorimeter was considered by the variation of the hadronic energy scale of $\pm 4\%$ in the MC samples. This results in a change of the total cross section of 4%. In the same way the energy of the scattered positron was conservatively scaled by $\pm 3\%$ leading to a change in the total cross section of around $\pm 2\%$.

Bin	x_γ range	x_γ	Purity [%]	f_b [%]	$d\sigma/dx_\gamma$ [pb]
1	0.0-0.75	0.375	83.6 ± 1.0	50.5 ± 8.8	7.2 ± 1.6
2	0.75-1.0	0.875	72.5 ± 1.3	28.4 ± 5.1	30.2 ± 6.9

Table 11.4: *For each bin of the differential cross section $d\sigma/dx_\gamma$ the lower and the upper limit, the bin centre, the purity (as determined by PYTHIA MC), the b fraction and the result for the differential cross section are given.*

11.6.3 Trigger Efficiencies

The trigger efficiencies were determined using independent subtrigger conditions, while all other selection cuts had to be fulfilled. As discussed in sec. 10.6 the subtrigger s61 consists of four trigger elements (DCRPh_THig, zVtx_sig> 0 and (SPCLe_IET> 2 $\vee$ SPCLe_IET_Cen_3)). It turned out that with the applied cut on the energy of the scattered positron, which is significantly above the threshold of the SpaCal, the inefficiency of the SpaCal trigger elements is negligible. The other trigger elements were tested using independent trigger elements, which are based on the LAr calorimeter and the forward detectors. Tab. 11.5 shows the results for DCRPh_Thig , zVtx_sig and SPCLe_IET $\vee$ SPCLe_IET_Cen_3 for data and MC. The trigger efficiency for the two jet selection is slightly better than for the 1 jet selection and for both selection schemes the MC overestimates the trigger efficiency by about 4-5%. The MC is adjusted accordingly, the corresponding uncertainty was estimated to be ±3 %.

	Efficiency [%]			
	1 jet		two jet	
Trigger Elements	H1 Data	MC	H1 Data	MC
DCRPh_THig	99.0 ± 0.4	98.9 ± 0.1	99.5 ± 0.3	99.0 ± 0.2
zVtx_sig	92.0 ± 1.0	96.8 ± 0.3	92.9 ± 1.2	97.6 ± 0.2
SPCLe_IET $\vee$ SPCLe_IET_Cen_3	100.0	100.0	100.0	100.0
s61	91.1 ± 1.1	95.7 ± 0.3	92.4 ± 1.2	96.6 ± 0.3

Table 11.5: *Efficiency of the subtrigger s61 for H1 data and RAPGAP MC for both selection schemes.*

11.6.4 Muon and Jet Axis Reconstruction

The muon track reconstruction efficiency in the central drift chambers with the additional requirement of two hits in the CST is known to a precision of about 3%. The muon identification efficiency, which includes the reconstruction in the instrumented iron and the linking with the central track, leads to an uncertainty of about 5%.
To determine the uncertainty coming from the jet axis reconstruction, which is crucial for the measurement of p_t^{rel} , the resolution of the reconstructed jet directions in the MC was varied by 2 %. This variation yields a change in the measured cross section of about 2%.

11.6.5 Impact Parameter Reconstruction

To estimate the systematic uncertainty related to the impact parameter, the resolution of the impact parameter was smeared in the MC by 25 μm. Additionally the core and the tails of the impact parameter resolution were smeared separately. To determine the influence of the beam spot ellipse the data sample was divided into two independent samples containing either more horizontal or more vertical muons. All the variations

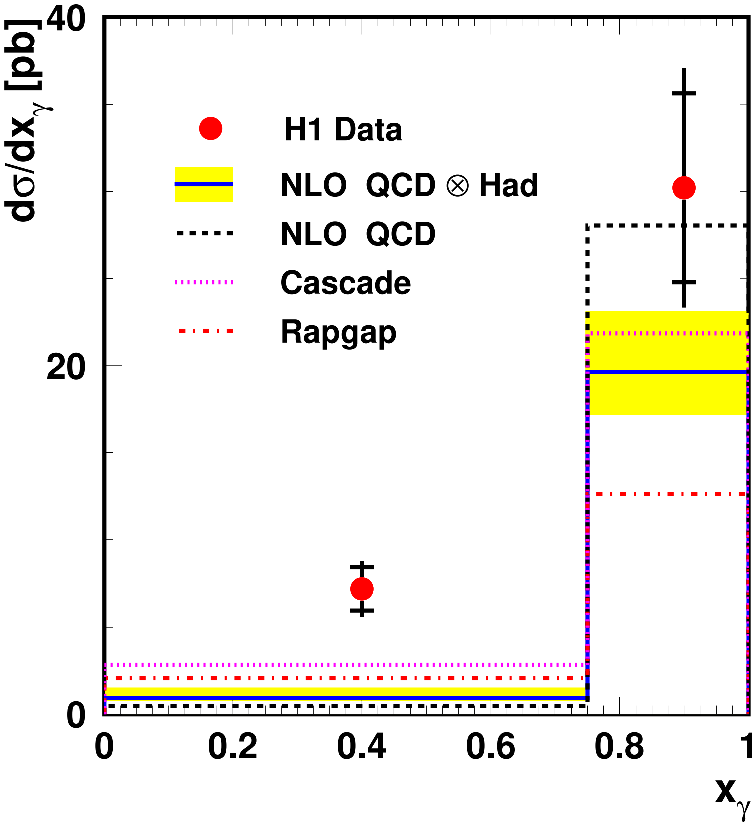

Figure 11.14: *Measurement of the differential cross section $d\sigma/dx_\gamma$ as a function of the fraction x_γ of the photon momentum.*

of the measured cross section in these checks are consistently covered by a systematic uncertainty of 7%.

11.6.6 Other Contributions and Further Studies

A further contribution to the systematic uncertainty of about 1.5% is due to the luminosity measurement. To determine the influence of the definition of the jet reference axis for the p_t^{rel} calculation various different definitions (e.g. thrust vector) including and excluding the muon track were tested. The observed variation in the measured cross section is covered by the statistical uncertainties and also no systematic shift to higher or lower values are observed. Therefore, this contribution was neglected.

Source	$\Delta\sigma/\sigma$ [%]
MC and Fragmentation Model Uncertainties:	
– RAPGAP : CASCADE	5
– Fragmentation (Peterson : Lund)	7
– **Fragm. Fractions, BR's & Lifetimes**	2
– K, π **Decays ($\pm$ factor 2)**	2
Energy Scale:	
– Electromagnetic Energy Scale	2
– Hadronic Energy Scale	4
s61 Trigger Efficiency:	
– Trigger Efficiency	3
Impact Parameter:	
– δ Resolution	7
Muon and Jet Axis Reconstruction:	
– **CST+CTD Tracks**	3
– **Muon Identification**	5
– **Jet Axis**	2
Other Contributions:	
– Luminosity	1.5
Total	14

Table 11.6: List of systematic uncertainties as discussed in section 11.6. The total systematic error is obtained by adding the various contributions in quadrature. Systematics adopted from the photoproduction analysis are shown in bold.

Chapter 12

Discussion of the Results

In this chapter the cross section measurements presented in Chapter 11 are compared with NLO QCD predictions and with results from other analyses.

12.1 NLO QCD Predictions

The calculations of the NLO QCD predictions were carried out using the program HVQDIS in the $\overline{MS}$ factorisation scheme.

12.1.1 Principle of the Calculations

The calculation is performed in four steps:

1. In a first step HVQDIS provides weighted parton level events with two or three outgoing partons, the b and $\overline{b}$ quarks and possibly an additional gluon or light quark.

2. Afterwards the b or $\overline{b}$ quark is fragmentated into a b -flavoured hadron with rescaled three-momentum using the Peterson fragmentation function.

3. In a third step the decay of the b -flavoured hadron into a final state including a muon is modelled. The muon momentum spectrum, as predicted by JETSET, includes direct and cascade decays of b -flavoured hadrons into muons. Additionally jets are reconstructed on parton level by applying the k_t jet algorithm to the outgoing partons.

4. To compare the NLO calculations on parton level directly with the data on hadron level further corrections have to be applied. For this RAPGAP parton level jets are reconstructed from the generated quarks and gluons after the parton showering process. Hadron level jets are reconstructed by applying the jet algorithm to all hadrons after the decay of the heavy-flavoured hadron. The jet and the muon selection cuts are applied to the generator samples. Finally the ratio hadron level cross section to parton level cross section is calculated and applied as a correction factor to the NLO calculation. The same procedure is performed for each bin

	Version	PDF	Λ_{QCD} [GeV]	μ_r^2	μ_f^2	m_b	ϵ_b
HVQDIS	1.4	CTEQ5F4	0.309	$m_b^2 + p_{tb\bar{b}}^2$	$m_b^2 + p_{tb\bar{b}}^2$	4.75	0.0033

Table 12.1: *Overview of the NLO parameters used for the calculations.*

of the differential cross sections, leading to a change in the NLO cross section between −30% and +5% labelled as $NLO \bigotimes Had$.

An overview about the parameters used and functions is given in tab. 12.1.

12.1.2 Theoretical Uncertainties

The theoretical uncertainties of the NLO calculations were estimated by a simultaneous variation of the b quark mass m_b and the renormalisation μ_r and factorisation scales μ_f from $m_b = 4.5$ GeV and $\mu_r = \mu_f = m_T/2$ to $m_b = 5$ GeV and $\mu_r = \mu_f = 2m_T$, where m_T is given by: $m_T = \sqrt{m_b^2 + p_{tb\bar{b}}^2}$. Here, $p_{tb\bar{b}}$ is the average of the transverse momenta of the two b quarks in the laboratory frame. This leads to a change in the cross sections of $15 - 20\%$. The uncertainty arising from the fragmentation parameter ϵ_b was estimated by varying the parameter by ±25% leading to a cross section variation below 3%. The total systematic uncertainty is calculated by adding all contributions in quadrature.

12.1.3 Total NLO Cross Section

The total cross section as predicted by NLO is calculated for both the one jet selection in the Breit frame and the two jet selection in the Lab frame. The parameters are shown in tab. 12.1. For the one jet selection the visible cross section is

$$\sigma_{NLO}^{1jet} = 9.0^{+2.6}_{-1.6} \text{ pb}, \tag{12.1}$$

which is around 1.8 standard deviations (including the contribution from statistics, systematics and theory) below the data. The resulting visible cross section for the two jet selection is

$$\sigma_{NLO}^{2jet} = 7.4^{+1.3}_{-1.2} \text{ pb}. \tag{12.2}$$

The deviation from the measured cross section is about 2.0 standard deviations.

12.1.4 Differential NLO Cross Sections

The differential cross sections for $d\sigma/dQ^2$ and $d\sigma/d\log x_{bj}$ in comparison to the NLO calculations are shown in fig. 11.11 and fig. 11.12 respectively. In both cases the data points lie above the prediction of the NLO calculations. The shape of the $d\sigma/d\log x_{bj}$ distribution is well described by the NLO prediction, while for $d\sigma/dQ^2$ the data point in the middle bin is somehow too low compared to the shape described by the NLO calculation. The data is in this bin compatible with the NLO predictions considering the uncertainties. The measurement of $d\sigma/d\eta^\mu$ is shown in fig. 11.13. While in the

backward and central region the data is compatible within the uncertainties with the NLO calculations, a large deviation between data and NLO is visible in the forward region, so that the shape of the distribution is not well described. This might be a hint, that this region is not well described for DIS events by pQCD. This conclusion is also justified by the fact, that this excess in the data is also observed in measurements at the ZEUS experiment e.g. [120]. For all these measurements the NLO calculations give similar results as CASCADE, while the predictions from RAPGAP lie below the data.
The 2 jet data sample was used to determine the differential cross section $d\sigma/dx_\gamma$. It is noticeable, that in the x_γ range $0 < x_\gamma < 0.75$ the measured cross section lies several standard deviations above the NLO calculations, while in $0.75 < x_\gamma < 1$ the data and the NLO are compatible considering both the uncertainties in the measurement and the uncertainties in the NLO calculations. Since any additional hadronic activity not included in the two jets, e.g. from gluon radiation, reduces the observed value of x_γ, this may be interpreted as a hint for missing higher order corrections in the theory.

12.2 Comparison with other Measurements

Beside the results reported in the present analysis further measurements of the b production rate in ep collisions were performed from both H1 and ZEUS. Fig. 12.1 shows the comparison of the different cross section measurements as a function of the photon virtuality Q^2. Since the measurements were carried out in different phase space regions, the results of the measurements are not compared directly but via the ratio of measured cross section and NLO prediction. The results of this analysis are in good agreement with the results of the ZEUS collaboration [121] and both lie significantly above the NLO predictions. In the photoproduction region this effect is smaller but also visible.

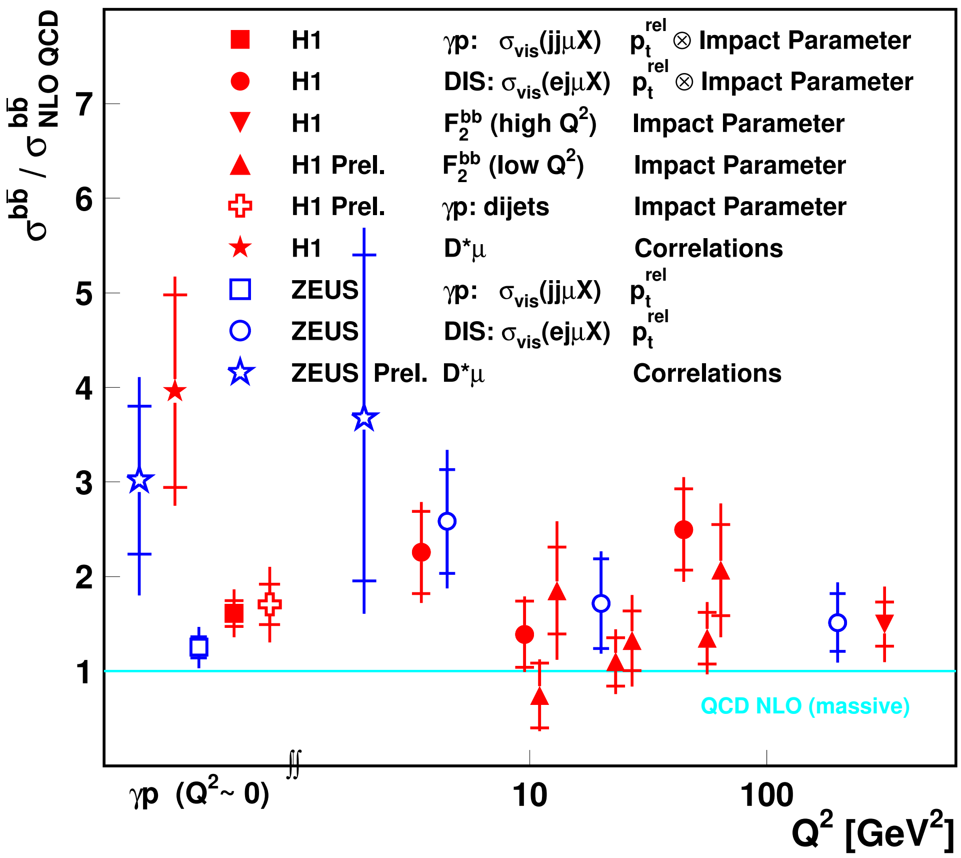

Figure 12.1: *Comparison of H1 and ZEUS measurements of the b cross section to the prediction of the NLO calculations. The red dots refer to the result of this analysis.*

Chapter 13

Conclusion and Outlook

In this thesis the measurements of the beauty production rate in DIS have been presented using data collected in 1999 and 2000 with the H1 detector. Established methods to enrich and separate beauty quarks, using p_t^{rel} and impact parameter δ as observables were applied. The investigated decay channel of the b quark was the semi-muonic mode. The results of the total cross section measurements of this analysis are summarised in tab. 13.1 and in the case of the 1 jet analysis were published together with the results of the photoproduction analysis [119]. Compared to the thesis of J. Kroseberg [64], which was the starting point for this analysis, the ratio of the measured cross section over NLO prediction became smaller (see fig. 7.1 and fig. 12.1), but it is still significantly above 1. The discrepancy in standard deviations is comparable for both studies.
However, for the interpretation of this comparison one has to take into account that the definition of the visible cross section was changed. In the study [64] it was extrapolated in a much wider kinematic region.
The available larger data sample also allowed for measurements of differential cross sections to investigate where QCD fails to describe the data. In general the shape of these distributions are well described by the NLO calculations. A significant discrepancy in the shape of the distributions can be found in the $d\sigma/d\eta^{\mu}$ distribution. Since this is also observed in a similar measurement from the ZEUS collaboration [120], this might be a hint, that in this region QCD is not capable to describe the physics correctly. In the x_γ distribution also a discrepancy between data and NLO prediction can be found, which needs further investigation.
To solve this problem and to investigate also the underestimation of data by the NLO

	1 jet selection σ [pb]	2 jet selection σ [pb]
Data	$16.3 \pm 2.0 \pm 2.3$	$12.9 \pm 1.6 \pm 1.8$
HVQDIS	$9.0^{+2.6}_{-1.6}$	$7.4^{+1.3}_{-1.2}$
RAPGAP	6.3	4.7
CASCADE	9.8	7.6

Table 13.1: Summary of the total cross section results

predictions in general further studies related to the beauty production rate are in progress. Thus, the beauty production cross section is measured at H1 in the forward direction using the p_t^{rel} method alone. Preliminary results of this study also indicates an excess in the measured cross section compared to the theoretical predictions [122]. On the other hand the measurement of $F_2^{b\bar{b}}$ [123, 124], which is the b contribution to the inclusive proton structure function F_2 yields a result with is compatible with the predictions from QCD. However, the analysis presented in this thesis sets higher requirements on the theory in the sense that due to the tighter cuts applied the theory is tested only in a particular phase space.

The data, which are currently collected at HERA II, will certainly help to solve this ambiguity benefiting from the expected increase in statistics. This will decrease on one hand the statistical error, but also, due to a better evaluation of the contributing effects, to a reduction of the systematic uncertainties.
However, the measurement of beauty cross sections at HERA but also at other colliders will be in the future a reasonable method to get a deeper understanding of the strong interaction and will help to answer the open questions.

Appendix A

Technical Drawing of the TPC Prototype

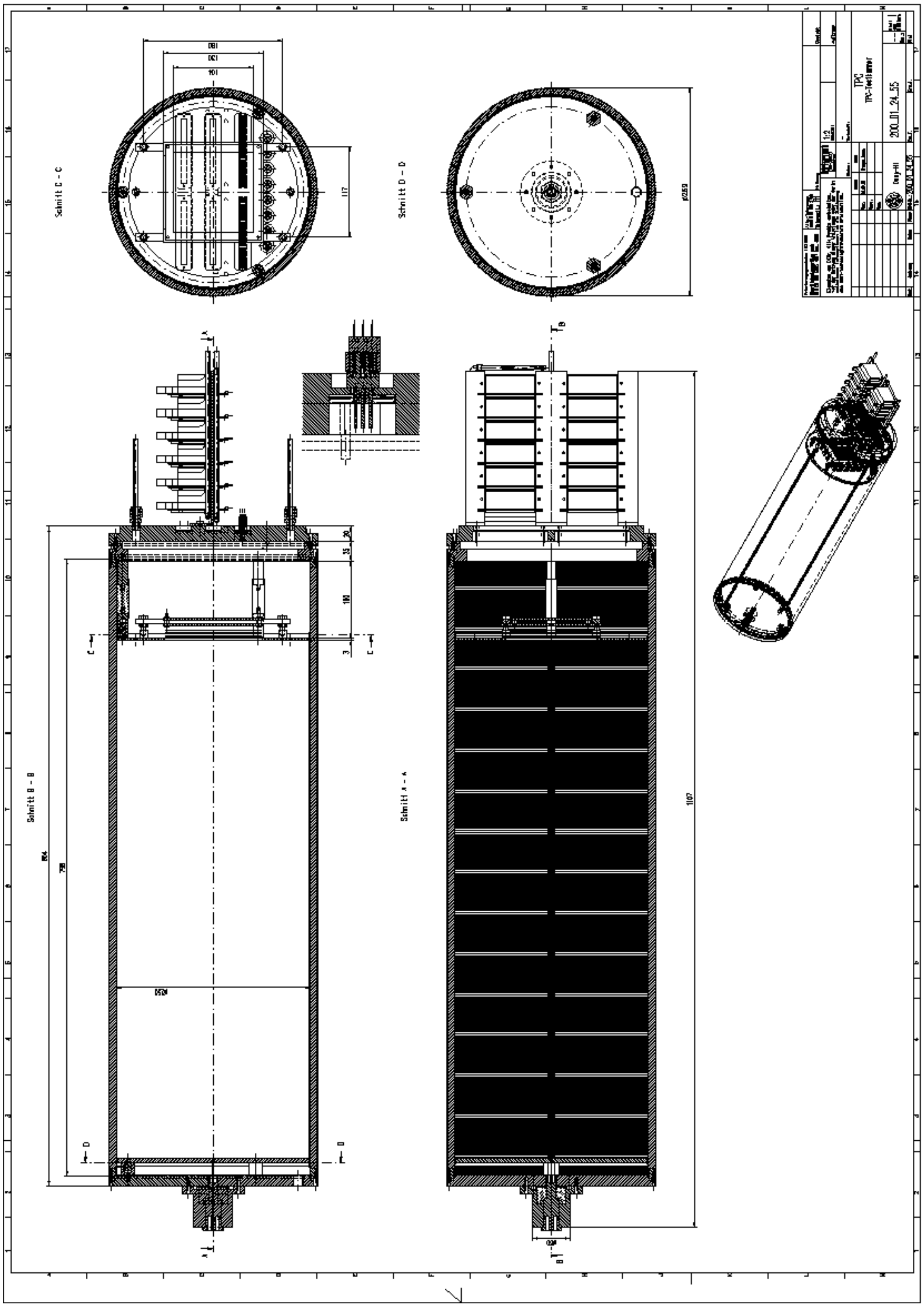

Appendix B

Parameters of the 5 T Magnet

COIL	
Length	1.2 m
Internal diameter	0.37 m
External diameter	0.47 m
Coil weight	630 kg
Coil layers	18
Turns	5083
Bmax on axis	5 T
Operating current	1000 A
Current density	4.2 kA/cm
Stored energy	1.5 MJ
CONDUCTOR	
Material	NbTi/Cu (1:7)
Filament number	600
Filament diameter	50 m
Twist pitch	50 mm
Dimensions	4.0x2.6 mm
Dimensions (with Kapton insulation)	4.3x2.9 mm
Critical current (at B=5.4 T, T=4.3 K)	1600 A
Heat load (60K)	15 W
Critical current density	1300 A/mm
CRYOSTAT	
Length	1,86 m
Internal diameter	0.28 m
External diameter	1.04 m
Iron yoke weight	4000 kg
Helium vessel weight	860 kg
Vacuum vessel weight	1300 kg
Heat load (4.3K)	5 W
Current leads (0 A)	1.6 W
Current leads (1000A)	2x0.070g/s

Table B.1: Overview of the main parameters of the 5 T magnet.

Appendix C

The Fit Method

Important for the determination of the beauty cross section is the determination of the signal fraction f_b contributing to the total data sample. In the following an overview of the used fitting method is given, which follows mainly the argumentation in [64]. Using m different MC samples to model all relevant signal and background processes, a prediction for the number of muon candidates n_i^P contributing to bin i can be calculated via

$$n_i^P = \sum_{j=1}^{m} f_j A_{ji} \ . \tag{C.1}$$

This prediction n_i^P is compared to the corresponding number of muon candidates n_i^D found in the data. Here, f_j corresponds to the fraction of the source j in the data and has to be determined and A_{ij} denotes the number of muon candidates expected from the contributing MC source j.
The fractions f_j can be estimated by maximising the following likelihood

$$\ln \mathcal{L} = \sum_{i=1}^{r} [n_i^D \ln(n_i^P) - n_i^P] \ . \tag{C.2}$$

The statistical errors of the fit are calculated by varying the f_j around the solution and determining the maximum variation for which $\ln \mathcal{L}$ stays within given bounds depending on the required confidence level.
In contrast to the fit method used in [64] the error due to finite MC sample was not taken into account (see also [125]).

List of Figures

List of Tables

Bibliography

[1] L. Alvarez-Gaume, *et al.* (Editors). *Review of Particle Physics*. Physics Letters B (2004).

[2] L. Maiani. *The Large Hadron Collider: A status report*. Int. J. Mod. Phys., A19, 1229–1239 (2004).

[3] S. Kuhlman, *et al.* (NLC ZDR Design Group and NLC Physics Working Group). *Physics and technology of the Next Linear Collider: A Report submitted to Snowmass '96* (1996). `hep-ex/9605011`.

[4] N. Akasaka, *et al. JLC design study*. KEK-REPORT-97-1, `http://www-jlc.kek.jp/2003oct/index.html`.

[5] F. Richard, J. R. Schneider, D. Trines, *et al. TESLA Technical Design Report Part I: Executive Summary* (2001). `hep-ph/0106314`.

[6] *The LEP Electroweak Working Group* (2005). `http://lepewwg.web.cern.ch/LEPEWWG/`.

[7] T. Behnke, S. Bertolucci, R. D. Heuer, *et al. TESLA: The superconducting electron positron linear collider with an integrated X-ray laser laboratory. Technical design report. Pt. 4: A detector for TESLA*. DESY-01-011.

[8] C. J. S. Damerell (LCFI). *A CCD-based vertex detector for TESLA*. LC-DET-2001-023, `http://www.desy.de/~lcnotes`.

[9] G. Deptuch, *et al. Design and testing of monolithic active pixel sensors for charged particle tracking*. IEEE Trans. Nucl. Sci., 49, 601–610 (2002).

[10] P. Fischer, *et al. A DEPFET based pixel vertex detector for the detector at TESLA*. LC-DET-2002-004, `http://www.desy.de/~lcnotes`.

[11] M. Battaglia, *et al. A pixel vertex tracker for the TESLA detector* (2001). LC-DET-2001-042, `hep-ex/0102046`, `http://www.desy.de/~lcnotes`.

[12] E. Garutti (2005). Talk, IFAE - Incontri di Fisica delle Alte Energie.

[13] J.-C. Brient. *Improving the Jet Reconstruction with the Particle Flow Method; an Introduction*
. `http://hal.ccsd.cnrs.fr/docs/00/02/82/00/PDF/ParticleFlow-Brient-V2.pdf`.

[14] E. Garutti, M. Groll, A. Karakash, *et al.* *Magnetic field dependence studies for silicon photomultiplier.* LC-DET-2004-025, `http://www.desy.de/~lcnotes`.

[15] R. L. Gluckstern. *Uncertainties in track momentum and direction, due to multiple scattering and measurement errors.* Nucl. Instrum. Meth., 24, 381–389 (1963).

[16] T. Behnke. *BRAHMS - a detector simulation program for TESLA.* Prepared for 5th International Linear Collider Workshop (LCWS 2000), Fermilab, Batavia, Illinois, 24-28 Oct 2000.

[17] M. Schumacher. *Pad readout geometries for a TPC with GEM readout for the TESLA linear collider.* LC-DET-2001-014, `http://www.desy.de/~lcnotes`.

[18] C. Bowdery. *ALEPH Handbook 1995, Volume 1, Chapter V.* ISBN 92-9083-072-7.

[19] Y. Sacquin. *The DELPHI Time Projection Chamber* (1992).
DELPHI 92-41 TRACK 70.

[20] e. a. M. Anderson. *The STAR time projection chamber: a unique tool for studying high mulitplicity events at RHIC.* NIM A, 499, 659–678 (2003).

[21] F. Sauli. *GEM: A new Concept for Electron Amplification in Gas Detectors.* Nucl. Instrum. Meth., A386, 531–534 (1997).

[22] S. Bachmann, *et al.* *Charge Amplification and Transfer Processes in the Gas Electron Multiplier.* Nucl. Instrum. Meth., A438, 376–408 (1999).

[23] Y. Giomataris, P. Rebourgeard, J. P. Robert, *et al.* *Micromegas: A High-Granularity Position-Sensitive Gaseous Detector for High Particle-Flux Environments.* Nucl. Instrum. Meth., A376, 29–35 (1996).

[24] M. Hamann. *Studies for a Linear Collider Drift Chamber and Search for Heavy Stable Charged Particles in e^+e^- Collisions up to $\sqrt{s} = 209$ GeV.* Ph.D. thesis, University of Hamburg (2003).

[25] D. R. Nygren. *A Time Projection Chamber.* Presented at the 1975 PEP Summer Study. Included in Proceedings.

[26] R. Veenhof. *GARFIELD - A Drift Chamber Simulation Program.* CERN Program Library W5050 (1984). `http://garfield.web.cern.ch/garfield/`.

[27] R. Veenhof. *GARFIELD, recent developments.* Nucl. Instrum. Meth., A419, 726–730 (1998).

[28] U. ANSOFT Co. Pittsburgh PA. *MAXWELL 2D/3D Electric Field Simulator.* `http://www.ansoft.com/products/`.

[29] I. Smirnov. *HEED Simulation Programme for Energy Loss.*

[30] W. Blum, L. Rolandi. *Particle Detection with Drift Chambers.* Springer (1993).

[31] F. Sauli. *PRINCIPLES OF OPERATION OF MULTIWIRE PROPORTIONAL AND DRIFT CHAMBERS*. CERN-77-09.

[32] D. Buskulic, *et al.* (ALEPH). *Performance of the ALEPH Detector at LEP*. Nucl. Instrum. Meth., A360, 481–506 (1995).

[33] W. Leo. *Techniques for Nuclear and Particle Physics Experiments*. Springer-Verlag (1994).

[34] A. T. Margarian. *FLUCTUATIONS AND PROBABLE VALUES OF IONIZATION ENERGY LOSSES OF RELATIVISTIC ELECTRONS IN THIN GAS LAYERS*. EFI-977-27-87-YEREVAN.

[35] E. Wagner, F. Davies, G. Hurst. *Time-of-flight investigations of electron transport in some atomic and molecular gases*. J. Chem. Phys., 47, 3138 (1967).

[36] P. A. Aarnio, *et al.* (DELPHI). *The DELPHI detector at LEP*. Nucl. Instrum. Meth., A303, 233–276 (1991).

[37] G. Dellacasa, *et al.* (ALICE). *ALICE Technical Design Report of the Time Projection Chamber*. CERN-OPEN-2000-183.

[38] A. Breskin, *et al. High flux operation of the gated multistep avalanche chamber*. Nucl. Instr. Meth., 178, 11 (1980).

[39] M. Li. *The Gas Electrom Multiplier (GEM) - A New Detector for Scanned Projection Radiography*. Ph.D. thesis, Carleton University (2000).

[40] A. Bondar, A. Buzulutskov, L. Shekhtman, *et al. Study of Ion Feedback in Multi-GEM Structures*. Nucl. Instrum. Meth., A496, 325–332 (2003).

[41] F. Sauli, S. Kappler, L. Ropelewski. *Electron Collection and Ion Feedback in GEM-based Detectors*. IEEE Trans. Nucl. Sci., 50, 803–808 (2003).

[42] S. Lotze. *Aufbau eines Teststandes und Messungen zum Betrieb einer TPC mit GEMs* (2001). Diploma thesis.

[43] T. Lux. *Bau und Test einer Mini-TPC mit GEM-Auslese zur Messung des Ionen-Rückflusses* (2001). Diploma thesis.

[44] *GAS DETECTORS DEVELOPMENT*. `http://gdd.web.cern.ch/GDD/`.

[45] M. Killenberg, *et al. Charge transfer and charge broadening of GEM structures in high magnetic fields*. Nucl. Instrum. Meth., A530, 251–257 (2004).

[46] A. Muennich. *Studies of Charge Broadening in Multi GEM Structures and Development of a TPC* (2004). International Conference on Linear Colliders.

[47] A. Krivchitch. *Results of the TPC FC electric field simulation*. Personal communication.

[48] G. E. Gavrilov, A. G. Krivshich, M. K. Dzharmakin. *Influence of external grounded screens on the electric field structure in a drift chamber*. Nucl. Instrum. Meth., A356, 189–195 (1995).

[49] K. Gadow. Personal communication.

[50] M. E. Janssen. *Resolution studies of a time projection chamber using a GEM gas amplification system. (In German)*. DESY-THESIS-2004-049.

[51] M. Gruwe. *Gas studies for the TPC of a detector for the future linear collider TESLA*. LC-DET-1999-003-TESLA, `http://www.desy.de/~lcnotes`.

[52] M. Ball, N. Ghodbane, M. E. Janssen, *et al. A DAQ system for linear collider TPC prototypes based on the ALEPH TPC electronics* (2004). `physics/0407120`.

[53] F. Gaede, T. Behnke, N. Graf, *et al. LCIO: A persistency framework for linear collider simulation studies*. ECONF, C0303241, TUKT001 (2003). `physics/0306114`.

[54] *LCIO*. `http://lcio.desy.de/`.

[55] P. Wienemann. `http://www.desy.de/~wiene/magnet/`.

[56] J. Kempa, I. M. Brancus. *Zenith angle distributions of cosmic ray muons*. Nucl. Phys. Proc. Suppl., 122, 279–281 (2003).

[57] R. Brun, F. Rademakers. *ROOT - An Object Oriented Data Analysis Framework*. Nucl. Instrum. Meth., A389, 81–86 (1997). `http://root.cern.ch/`.

[58] `http://www.wetteronline.de`.

[59] J. E. Bateman. *Gain stabilisation in proportional counters*. RAL-TR-1998-044.

[60] S. Bachmann, *et al. Discharge mechanisms and their prevention in the gas electron multiplier (GEM)*. Nucl. Instrum. Meth., A479, 294–308 (2002).

[61] D. Karlen. *Pad geometry study for a linear collider TPC*. Prepared for International Workshop on Linear Colliders (LCWS 2002), Jeju Island, Korea, 26-30 Aug 2002.

[62] A. Imhof. *PhD. thesis in preparation*. University of Hamburg.

[63] M. Ball. *PhD. thesis in preparation*. University of Hamburg.

[64] J. Kroseberg. *A Measurement of Beauty Production in High-Energy Positron-Proton Scattering*. Ph.D. thesis, University of Zurich (2002).

[65] M. Chemarin. *Number of neutrino families from LEP1 measurements*. Nucl. Phys. Proc. Suppl., 85, 67–71 (2000).

[66] S. W. Ellis, R.K, B. Webber. *QCD and Collider Physics*. Cambridge University Press (1996).

[67] A. M. F. Halzen. *Quarks and Leptons*. John Wiley & Sons (1984).

[68] H. Abramowicz, A. Caldwell. *HERA collider physics*. Rev. Mod. Phys., 71, 1275–1410 (1999). `hep-ex/9903037`.

[69] B. Foster. *Lectures on HERA physics* (2002). `hep-ex/0206011`.

[70] C. Risler. *Produktion seltsamer neutraler Teilchen in tiefinelastischer Streuung bei HERA*. Dissertation, Universität Hamburg (2003).

[71] V. N. Gribov, L. N. Lipatov. *Deep inelastic electron scattering in perturbation theory*. Phys. Lett., B37, 78–80 (1971).

[72] V. N. Gribov, L. N. Lipatov. *e+ e- pair annihilation and deep inelastic e p scattering in perturbation theory*. Sov. J. Nucl. Phys., 15, 675–684 (1972).

[73] V. N. Gribov, L. N. Lipatov. *Deep inelastic e p scattering in perturbation theory*. Sov. J. Nucl. Phys., 15, 438–450 (1972).

[74] G. Altarelli, G. Parisi. *ASYMPTOTIC FREEDOM IN PARTON LANGUAGE*. Nucl. Phys., B126, 298 (1977).

[75] Y. L. Dokshitzer. *CALCULATION OF THE STRUCTURE FUNCTIONS FOR DEEP INELASTIC SCATTERING AND E+ E- ANNIHILATION BY PERTURBATION THEORY IN QUANTUM CHROMODYNAMICS. (IN RUSSIAN)*. Sov. Phys. JETP, 46, 641–653 (1977).

[76] C. Adloff, *et al.* (H1). *Measurement and QCD analysis of neutral and charged current cross sections at HERA*. Eur. Phys. J., C30, 1–32 (2003). `hep-ex/0304003`.

[77] C. Adloff, *et al.* (H1). *Deep-inelastic inclusive e p scattering at low x and a determination of alpha(s)*. Eur. Phys. J., C21, 33–61 (2001). `hep-ex/0012053`.

[78] `http://www-zeus.desy.de/physics/sfew/PUBLIC/sfew_results/preliminary/moriond04/zeush1.php`.

[79] M. Ciafaloni. *COHERENCE EFFECTS IN INITIAL JETS AT SMALL Q**2 / s*. Nucl. Phys., B296, 49 (1988).

[80] S. Catani, F. Fiorani, G. Marchesini. *QCD COHERENCE IN INITIAL STATE RADIATION*. Phys. Lett., B234, 339 (1990).

[81] S. Catani, F. Fiorani, G. Marchesini. *SMALL x BEHAVIOR OF INITIAL STATE RADIATION IN PERTURBATIVE QCD*. Nucl. Phys., B336, 18 (1990).

[82] G. Marchesini. *QCD coherence in the structure function and associated distributions at small x*. Nucl. Phys., B445, 49–80 (1995). `hep-ph/9412327`.

[83] V. V. Sudakov. *Vertex parts at very high-energies in quantum electrodynamics*. Sov. Phys. JETP, 3, 65–71 (1956).

[84] P. Schmüser. *Feynman-Graphen und Eichtheorien für Experimentalphysiker.* Berlin, Heidelberg, New York: Springer (1995).

[85] G. Sterman, S. Weinberg. *JETS FROM QUANTUM CHROMODYNAMICS.* Phys. Rev. Lett., 39, 1436 (1977).

[86] S. Bethke, *et al.* (JADE). *EXPERIMENTAL INVESTIGATION OF THE ENERGY DEPENDENCE OF THE STRONG COUPLING STRENGTH.* Phys. Lett., B213, 235 (1988).

[87] B. R. Webber. *Factorization and jet clustering algorithms for deep inelastic scattering.* J. Phys., G19, 1567–1575 (1993).

[88] N. H. Brook (ZEUS). *The measurement of fragmentation functions in the Breit frame.* Prepared for International Workshop on Deep Inelastic Scattering and Related Phenomena (DIS 96), Rome, Italy, 15- 19 Apr 1996.

[89] *Fragmentation measurements in the Breit frame at HERA.* Contributed to 29th International Conference on High-Energy Physics (ICHEP 98), Vancouver, Canada, 23-29 Jul 1998.

[90] K. H. Streng, T. F. Walsh, P. M. Zerwas. *QUARK AND GLUON JETS IN THE BREIT FRAME OF LEPTON - NUCLEON SCATTERING.* Zeit. Phys., C2, 237 (1979).

[91] V. Chiochia. *Measurement of beauty quark production in deep inelastic scattering at HERA.* Ph.D. thesis, University of Hamburg (2003).

[92] L. M. Jones, H. W. Wyld. *CHARMED PARTICLE PRODUCTION BY PHOTON GLUON FUSION.* Phys. Rev., D17, 759 (1978).

[93] C. Peterson, D. Schlatter, I. Schmitt, *et al. SCALING VIOLATIONS IN INCLUSIVE e+ e- ANNIHILATION SPECTRA.* Phys. Rev., D27, 105 (1983).

[94] P. D. B. Collins, T. P. Spiller. *THE FRAGMENTATION OF HEAVY QUARKS.* J. Phys., G11, 1289 (1985).

[95] V. G. Kartvelishvili, A. K. Likhoded, V. A. Petrov. *ON THE FRAGMENTATION FUNCTIONS OF HEAVY QUARKS INTO HADRONS.* Phys. Lett., B78, 615 (1978).

[96] B. Andersson, G. Gustafson, C. Peterson. *ON QUARK FRAGMENTATION DISTRIBUTIONS.* In *Tabor 1978, Proceedings, Multiparticle Dynamics*, F121- f140.

[97] K. Harder. *Studies of QCD-Related Aspects of Event Evolution at e^+e^- Collisions.* Phd. thesis, University of Hamburg (2002). DESY report: DESY-THESIS-2002-030.

[98] B. Andersson, G. Gustafson, B. Soderberg. *A GENERAL MODEL FOR JET FRAGMENTATION.* Z. Phys., C20, 317 (1983).

[99] B. Andersson, G. Gustafson, G. Ingelman, *et al. PARTON FRAGMENTATION AND STRING DYNAMICS*. Phys. Rept., 97, 31 (1983).

[100] B. W. Harris, E. Laenen, S. Moch, *et al. Heavy quark production in deep-inelastic scattering at HERA* (1998). hep-ph/9905365.

[101] B. W. Harris, J. Smith. *Heavy quark correlations in deep inelastic electroproduction*. Nucl. Phys., B452, 109–160 (1995). hep-ph/9503484.

[102] J. Nelson, K. Heller (Editors). *Minneapolis Meeting of the Division of Particles and Fields of the American Physical Society*. World Scientific (1996).

[103] S. Frixone (Editor). *The Inclusion of Higher-Order QCD Corrections into Parton Shower Monte Carlos*. Strebsk Pleso, Slovakia (2004).

[104] T. Sjostrand. *PYTHIA 5.7 and JETSET 7.4: Physics and manual* (1995). hep-ph/9508391.

[105] T. Sjostrand. *The PYTHIA and JETSET programs*. Prepared for Particles & Fields 92: 7th Meeting of the Division of Particles Fields of the APS (DPF 92), Batavia, Illinois, 10-14 Nov 1992.

[106] I. Abt, *et al.* (H1). *The H1 detector at HERA*. Nucl. Instrum. Meth., A386, 310–347 & 348–396 (1997).

[107] H. Collaboration. *The H1 Detector at HERA*. Technical report, H1 (1996). http://www-h1.desy.de/h1/www/h1det/detpaper/nim.part1.ps http://www-h1.desy.de/h1/www/h1det/detpaper/nim.part2.ps.

[108] D. Pitzl, *et al. The H1 silicon vertex detector*. Nucl. Instrum. Meth., A454, 334–349 (2000). hep-ex/0002044.

[109] B. Andrieu, *et al.* (H1 Calorimeter Group). *The H1 liquid argon calorimeter system*. Nucl. Instrum. Meth., A336, 460–498 (1993).

[110] T. Nicholls, *et al. Performance of an Electromagnetic Lead/Scintillating-Fibre Calorimeter for the H1 Detector*. NIM, A 374, 149–156 (1996).

[111] V. Blobel. *THE BOS SYSTEM. DYNAMIC MEMORY MANAGEMENT*. HAMBURG DESY - INTERNAL REP. R1-88-01 (88,REC.FEB.) 40p.

[112] V. Blobel. *The BOS System* (2001).

[113] R. Brun, F. Bruyant, M. Maire, *et al. GEANT3*. CERN-DD/EE/84-1.

[114] C. Kleinwort, U.-P. Krüger. *Track Reconstruction in the Iron*. H1 Internal Software Note 35-08/92, H1 (1992).

[115] T. Kuhr, M. Kausch-Blecken von Schmeling. *CSPRIM: Primary Vertex Determination using CST Measurements* (2000).

[116] P. et. al., Bruel. *QESCAT - e identification software in H1PHAN* (1996). `https://www-h1.desy.de/iwork/iescale/qescat/qescat.html`.

[117] H. Jung. *Hard diffractive scattering in high-energy e p collisions and the Monte Carlo generation RAPGAP*. Comp. Phys. Commun., 86, 147–161 (1995).

[118] H. Jung. *The CCFM Monte Carlo generator CASCADE*. Comput. Phys. Commun., 143, 100–111 (2002). `hep-ph/0109102`.

[119] A. Aktas, *et al.* (H1). *Measurement of beauty production at HERA using events with muons and jets* (2005). `hep-ex/0502010`.

[120] S. Chekanov, *et al. Measurement of beauty production in deep inelastic scattering at HERA*. Phys.Letters, B 599, 173–189 (2004).

[121] S. Chekanov, *et al.* (ZEUS). *Measurement of beauty production in deep inelastic scattering at HERA*. Phys. Lett., B599, 173–189 (2004). `hep-ex/0405069`.

[122] H. Lüders. *PhD. thesis in preperation*. Ph.D. thesis, University of Hamburg (2005).

[123] A. Aktas, *et al.* (H1). *Measurement of F2(c anti-c) and F2(b anti-b) at high Q**2 using the H1 vertex detector at HERA* (2004). `hep-ex/0411046`.

[124] T. Klimkovich, A. Mehta, P. Thompson. *Measurement of $F_2^{c\bar{c}}$ and $F_2^{b\bar{b}}$ at Low Q^2 using the H1 Vertex Detector at HERA*. paper in preparation (2005).

[125] R. J. Barlow, C. Beeston. *Fitting using finite Monte Carlo samples*. Comput. Phys. Commun., 77, 219–228 (1993).

Danksagung

Diese Doktorarbeit, wie jede andere auch, basiert nicht nur auf meiner Arbeit, sondern eine große Anzahl von Menschen haben dazu beigetragen. Bei diesen möchte ich mich im folgendem bedanken.
Allen voran sei Prof. Dr. Rolf-Dieter Heuer und Dr. Ties Behnke gedankt, dass sie mir die Möglichkeit gaben meine Doktorarbeit in ihrer Gruppe durchzuführen und für die Unterstützung während dieser Zeit.
Prof. Dr. Beate Naroska, Prof. Dr. Caren Hagner und Prof. Dr. Götz Heinzelmann möchte ich für die Erstellung der Gutachten bzw. die Leitung der Disputation danken.
Steven John Aplin danke für interessante Diskussionen und das Korrekturlesen des TPC Teils. Felix Sefkow und Erika Garutti möchte danken, dass sie dasselbige für den Beauty Teil gemacht haben. Falls jemand noch zahlreiche Fehler in dieser Arbeit findet, so gehen sie ganz und gar zu meinen Lasten. Erika danke ich natürlich auch für die Bereitstellung der NLO Rechnungen und dafür, dass sie so ein dankbares Opfer meiner nicht ganz ernstgemeinter Sprüche war. Auch wenn ich klarstellen möchte, dass *Bastardo* nicht die korrekte Bezeichnung für mich ist.
Außerdem danke ich Peter Wienemann, Nabil Ghodbane und Thorsten Kuhl für ihre Betreuung bei meiner TPC Arbeit. Olaf Behnke und Andreas Meyer danke ich, dass sie mich bei meiner H1 Analyse betreut haben.
Desweiteren danke ich meinen TPC Kollegen Matthias Enno Janssen, Markus Ball, Alexandre Kaoukher und Markus Hamann für die tolle Zusammenarbeit, ohne die diese Doktorarbeit niemals erfolgreich beendet worden wäre.
Natürlich wäre diese Arbeit auch nicht ohne Karsten Gadow, Jörn Schaffran und Gert Falley möglich gewesen, die maßgeblich am Design und Bau des TPC Protypen und der dazugehörigen Infrastruktur beteiligt waren.
Auch den externen ILC TPC Gruppen aus Aachen, Karlsruhe, Ottawa und Victoria und auch Michael Hauschild und Ron Settles möchte ich für den regen Austausch an Gedanken und teilweise auch Geräten danken.
Meinen Ex-Kollegen von der FLC Gruppe danke ich für fast 5 schöne Jahre. Da ich aufgrund der Größe der Gruppe nicht alle namentlich erwähnen kann, hier nur eine kleine Auswahl stellvertretend für alle. Ramona, Andreas, Niels, Blanka und Klaus danke ich, daß sie die Organisation von vielen dienstlichen, aber auch vor allem außerdienstlichen Aktivitäten (Sommerfest, Betriebsausflüge, Doktorhüte, etc.) übernommen haben, wozu ich mich selber viel zu wenig habe aufraffen können und ohne die meine Zeit in der FLC Gruppe nicht so schön gewesen wäre. Wolfgang, Götz, Philip und Jörgen danke ich für ihre Arbeit als Linux-Systemadministratoren, die ich erst jetzt richtig zu schätzen weiß. Marius danke ich insbesondere für die wochenendliche Streßbekämpfung in "Kentucky Fried Chicken" und "Rosis Bar".

Meiner Familien, allen voran meinen Eltern und meinem Großvater gebührt besonderer Dank für ihre Unterstützung während meines Studiums. Ohne sie wäre ich sicherlich nicht da, wo ich jetzt bin.
Abschließend möchte ich mich bei allen bedanken, die mich auf meinem Weg begleitet haben und die ich hier nicht namentlich aufgeführt habe, entweder weil es den Rahmen gesprengt hätte oder aber, was weitaus schlimmer ist, weil ich sie beim Schreiben dieser Danksagung leider schlichtweg vergessen habe.

"Ich habe fertig!"
Giovanni Trapattoni